

CR
1981 NASA-ASEE SUMMER FACULTY PROGRAM AT
NASA-JOHNSON SPACE CENTER
TECHNICAL FINAL REPORT
(Copy #4 - Volume 2 of 2)
Co-Directors:
Nancy Robertson
C. J. Huang

(NASA-CR-768776) THE 1981 NASA ASEE SUMMER
FACULTY FELLOWSHIP PROGRAM, VOLUME 2 Final
Technical Report (Houston Univ.) 380 p
HC A17/MF A01 CACL 05I
G3/99
N82-25122
THRU
N82-23136
Unclas
19154

C22

N82 23123 D1

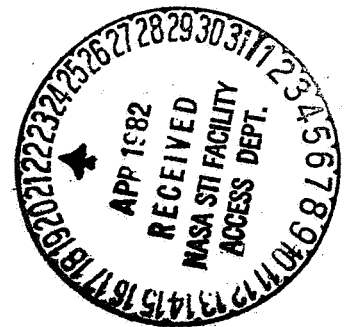
LANGMUIR PROBE THEORY
AND THE PROBLEM OF
ANISOTROPIC COLLECTION

by

A. Kyrala

A. Kyrala

Final Report of work on
NASA/ASEE summer fellowship
at NASA/JSC Houston, Texas 77058



ORIGINAL PAGE IS
OF POOR QUALITY

Table of Contents

1. Introduction
 2. Langmuir Probe Theory
 3. Plane Probe
 4. Spherical Probe
 5. Cylindrical Probe
 6. Probe of Arbitrary Shape
 7. Charge-Free Field of Infinite Strip
 8. Field of Infinite Strip with Space Charge
 9. Collection Trajectories of Ions in Free Space
 10. General Motion of Particles in Elliptic cylinder
Coordinates in Charge-Free Space
 11. Field of Charged Rectangular Plate at Constant Potential
 12. General Solution of Stationary Collisionless Boltzmann
Equation
 13. Physical Basis of Current Saturation
 14. Anisotropy of Current Collection
 15. Current Focussing for a Strip Collector
 16. Input Vectorial Velocity on Entry Ellipse
 17. Summary
- Appendix A: Elliptic Cylinder Differencing Scheme
for Trajectory Calculation
- Bibliography

ORIGINAL PAGE IS
OF POOR QUALITY

LANGMUIR PROBE THEORY AND THE PROBLEM
OF ANISOTROPIC COLLECTION
by A. Kyrala* +

1. Introduction

The objective of this study is to contribute to a more general understanding of Langmuir probe theory¹ by going beyond the arguments tied to particular coordinate systems insofar as possible. In particular it is desired to clearly delineate the role of initial velocities in the problem and to characterize the interaction between the velocity flow field and the electrostatic potential field both of which enter into the determination of particle trajectories.

The probe will be supposed to be negatively charged throughout and the ensuing region of positive space charge about it differs fundamentally from the plasma region beyond in the sense that the former represents a region in which deterministic trajectories dominate while the latter is a region dominated by statistical interactions largely controlled by the collisionless stationary Boltzmann² (Vlasov) equation.

In the present study a general solution of this Boltzmann equation will be given and its relationship to the problem of saturation current density in 3D will be elucidated.

This work has been particularly associated with the vacuum chamber experiments conducted by B. McIntyre at the JSC environmental testing laboratory. Since those experiments have concentrated on a probe geometry involving a probe in the form of a

*Physics Dept./Arizona State Univ./Tempe 85281/AZ

+This work has been supported by a NASA-ASCE fellowship at Johnson Space Center/Houston/TX 77058

long strip of constant width detailed specific calculations have been required for this case. To this end solutions suitable for this geometry have been studied and a report of these approaches is included in the present work.

Finally the physical picture of the problem of current collection and current "focussing" (anisotropic collection) is discussed.

2. Langmuir Probe Theory

Most treatments of this subject have emphasized differential equation approaches. Streamlined versions of these arguments will be initially given but it will be found that integral versions using the integral form of the mean value theorem offer more physical insight while cutting through the mathematical verbiage usually encountered. Thus the physical results may be expressed as averaging theorems which reduce to the classical results if the initial velocities are zero.

It should be clearly recognized that by including an initial velocity (see eq. (6)) in the problem we have opened the possibility of two extreme situations in which the value of the velocity magnitude at any point in the space charge region may be dominated by the electrostatic potential field or by the initial velocity depending upon the size of the latter.

3. Plane Probe

For a plane probe (which is a wall) which is negative with respect to an adjoining quasineutral plasma electrons will be

removed from a layer next to the probe because of their greater mobility than the positive ions. This leads to the development of a dark space containing positive ions and this space of thickness of the order of the Debye shielding length³

$$\delta = \frac{V_{\theta}}{\omega_p} \quad (1)$$

(V_{θ} = thermal velocity, ω_p = plasma angular frequency) is a region over which the approximate charge neutrality of the plasma does not obtain. It is here supposed that this region is sharply delineated by a well-defined surface separating the region of charge neutrality from that of positive charge. This is an idealization. The above argument is based on the assumption that there is no net flow velocity of the plasma with respect to the probe. The effects of such a net flow velocity will be shortly considered.

To determine the voltage as a function of position in the region of positive space charge one proceeds from the Poisson equation⁴ in 1-dimensional form

$$\phi'' = -\rho/\epsilon \quad (2)$$

where ϕ is the potential, $\rho \geq 0$ is the space charge density and ϵ is the permittivity assumed constant. The current density J is given by

$$J = \rho v \quad (3)$$

where v is the magnitude of the velocity of positive ions directed from the plasma toward the probe and J has the same direction. The energy of an ion is

$$E = \frac{mv^2}{2} + e\phi = \frac{mv_p^2}{2} + e\phi_p \quad (4)$$

where the subscript p refers to the value at the surface separating the quasineutral plasma from the region of positive charge density.

Substitution for ρ in the Poisson equation then yields

$$\phi'' = -J / \sqrt{v_p^2 + \frac{2e}{m}(\phi_p - \phi)} \quad (5)$$

where J is understood to be positive in the direction toward the probe. By the substitution

$$\psi = v_p^2 + \frac{2e}{m}(\phi_p - \phi) = v^2 \quad (6)$$

the Poisson equation then becomes

$$\psi'' = \frac{2e}{m} J / \sqrt{\psi} \quad (7)$$

For constant J one may write $k=4eJ/m$ and integrate this subject to the condition that the field be continuous at $x_p=d$ the plasma/space-charge interface so that $\psi'_p = 0$

$$\frac{(\psi')^2}{2} = -k \sqrt{\psi} \quad (8)$$

This may be written in the form (taking the negative square root because $\psi' < 0$)

$$\frac{\psi'}{\psi^{1/4}} = -\sqrt{2k} \quad (9)$$

which may be immediately integrated to yield (since $\psi'_p = 0$ at $x=d$)

$$\frac{4}{3} \psi^{3/4} = (d-x) \sqrt{2k} \quad (10)$$

which at $x=0$ on the probe gives

$$d = \frac{4}{3\sqrt{2\pi}} \psi_0^{3/4} = \frac{\sqrt{2}}{3} \sqrt{\frac{m}{eJ}} \left[V_p^2 + \frac{2e}{m} (\phi_p - \phi_0) \right]^{3/4} \quad (11)$$

which for $V_p=0$ is recognized as the 3/4 Law of Langmuir

theory. This may also be expressed by squaring as

$$J = \frac{2}{9} \left(\frac{m}{e} \right) \psi_0^{3/2} / d^2 \quad (12)$$

4. Spherical Probe

The Poisson equation is

$$\frac{1}{r^2} d_r (r^2 d_r \psi) = \frac{(r\psi)''}{r} = \frac{2eJ}{m} / \sqrt{\psi} \quad (13)$$

or

$$(r\psi)'' = \frac{2eJ}{m} r^{3/2} / \sqrt{r\psi} \quad (14)$$

Here $4\pi r^2 J$ is constant so

$$(r\psi)'' = \frac{eI}{2\pi m \sqrt{r}} / \sqrt{r\psi} \quad (15)$$

Replacing \sqrt{r} by its average $\langle \sqrt{r} \rangle$ for $r_0 \leq r \leq r_0 + d$ one has approximately

$$(r\psi)'' \approx \frac{eI}{2\pi m \langle \sqrt{r} \rangle} / \sqrt{r\psi} \quad (16)$$

which is similar to the plane probe case. This approximate

relation can be made exact by using the integral form of the

mean value theorem to replace $\langle r^{1/2} \rangle$ by $\sqrt{r_0} / \xi_1$ with ξ_1

$$1 \geq \xi_1 \geq \frac{\sqrt{r_0}}{\sqrt{r_0+d}}$$

an appropriate constant.

Hence,

$$\frac{4}{3} (r \psi)^{3/4} = (r_0 + d - r) \sqrt{2 \epsilon_1} \quad (17)$$

with

$$k = \frac{e I \epsilon_1}{\pi m \sqrt{r_0}} \approx \frac{e I}{\pi m \langle \sqrt{r} \rangle} \quad (18)$$

At $r=r_0$ this becomes

$$\frac{4}{3} (r_0 \psi_0)^{3/4} = d \sqrt{2 \epsilon_1} \quad (19)$$

or squaring

$$I = \frac{8 \pi}{9} \left(\frac{m}{e} \right) \left(\frac{r_0^2}{\epsilon_1} \right) \frac{\psi_0^{3/2}}{d^2} \quad (20)$$

or

$$J = \frac{2}{9} \left(\frac{m}{e} \right) \left(\frac{1}{\epsilon_1} \right) \frac{\psi_0^{3/2}}{d^2} \quad (21)$$

which exhibit the fact that the effective area of the probe is increased by the factor $(1/\epsilon_1)$.

5. Cylindrical Probe

The Poisson equation is

$$\frac{1}{r} d_r (r d_r \psi) = \frac{(r \psi')'}{r} = \frac{2 e I}{m \sqrt{\psi}} \quad (22)$$

or with $2 \pi r h J = 1 = \text{constant}$

$$(r \psi')' = \frac{e I}{\pi m h} \sqrt{\psi} \quad (23)$$

Then

$$(r\psi') (r\psi')' = \frac{e I r}{\pi m h} \frac{\psi'}{\sqrt{\psi}} \quad (24)$$

The integral mean value theorem then implies that there exists a constant ξ_2 such that $\langle r \rangle$ (which would yield an approximation when replacing r on the right side) may be replaced by r_0 / ξ_2 with

$$1 \geq \xi_2 \geq r_0 / (r_0 + d)$$

to yield the relation

$$\frac{(r\psi')^2}{2} = k_1 \sqrt{\psi} \quad (25)$$

with

$$k_1 = \frac{2e I r_0}{\xi_2 \pi m h} \quad (26)$$

so that

$$\frac{\psi'}{\psi^{3/4}} = - \frac{\xi_3 \sqrt{2k_1}}{r_0} = - \sqrt{2k_2} \quad (27)$$

where

$$k_2 = k_1 \xi_3^2 / r_0^2 \quad (28)$$

and

$$1 \geq \xi_3 \geq r_0 / (r_0 + d)$$

then

$$\frac{4}{3} \psi_0^{3/4} = d \sqrt{2k_2} \quad (29)$$

and

$$I = \frac{4}{3} \left(\frac{m}{e} \right) \frac{\pi r_0 h \xi_2}{\xi_3^2 d^2} \psi_0^{3/2} \quad (30)$$

6. Probe of Arbitrary Shape

Starting from the Poisson equation ($\rho \neq 0$ for ions)

$$\Delta \phi = -\rho/\epsilon \quad (31)$$

multiplication by the velocity \bar{v} of the ions yields

$$\bar{v} \Delta \phi = -\bar{J}/\epsilon \quad (32)$$

where \bar{J} is the electrical current density. Since $\bar{J} \parallel \bar{v}$ this implies

$$v \Delta \phi = -J/\epsilon \quad (33)$$

substituting

$$\psi = v_p^2 + \frac{2e}{m} (\phi_p - \phi) = v^2 \quad (34)$$

where v_p is velocity at sheath boundary and ϕ_p is electrostatic potential, there one has

$$\Delta \psi = -\frac{2e}{m} \Delta \phi \quad (35)$$

so that

$$v \Delta \psi = \frac{2e}{m\epsilon} J = \sqrt{\psi} \Delta \psi \quad (36)$$

Integrating over a volume bounded by the sheath boundary,

the probe surface and the surface along which $\bar{n} \cdot \nabla \psi = 0$

one has

$$\frac{2e}{m\epsilon} < J >_V V = \int \sqrt{\psi} \Delta \psi dV \quad (37)$$

Using the integral form of the mean value theorem there exists

a constant ξ_4 such that

$$\frac{2e}{m\epsilon} < J >_V V = \xi_4 (\sqrt{\psi_p} - \sqrt{\psi_{\min}}) \int \Delta \psi dV \quad (38)$$

From the Gauss divergence theorem this may be written

$$\frac{2e}{m\epsilon} < J >_V V = \xi_4 (\sqrt{\psi_p} - \sqrt{\psi_{\min}}) \oint \partial_n \psi dS \quad (39)$$

(note: V = volume \neq v = velocity)

($S_0 =$ probe surface)

$$\frac{2e}{m\epsilon} \langle J \rangle_V V = \frac{\epsilon}{4} (\sqrt{\psi_{\max}} - \sqrt{\psi_p}) S \left[\frac{d\psi}{dt} \right]_{S_0}^{S_p} \quad (40)$$

For a thin positive charge layer with $v_p = 0$ so that $\psi_p = 0$ and $\langle \frac{d\psi}{dt} \rangle_{S_p} = 0$ if there is not too much space charge $\psi_{\max} \approx \psi_0$

Hence

$$\frac{2e}{m\epsilon} \langle J \rangle_V = \frac{\epsilon}{4} \sqrt{\psi_0} \frac{\psi_0}{d} \frac{S_0}{V} \quad (41)$$

or

$$\langle J \rangle_V \approx \frac{m\epsilon}{2e} \frac{\epsilon}{4} \psi_0^{3/2} / d^2 \quad (42)$$

which then corresponds to the 3/4 law

$$d \approx \sqrt{\frac{m\epsilon \epsilon_0}{2e \langle J \rangle_V}} \psi_0^{3/4} \quad (43)$$

so that the general case includes the usual result by specialization.

For $v_p = \psi_p = 0$ there is an alternative derivation for the 3/4 law by averaging with respect to ψ and $\psi^{3/2}$. Thus

$$\frac{2e}{m\epsilon} J = \sqrt{\psi} \Delta \psi \quad (44)$$

multiplying by $d\psi$ this can be written

$$\frac{2e J d\psi}{m\epsilon} = \frac{2}{3} \Delta \psi d(\psi^{3/2}) \quad (45)$$

In terms of the averages (in the region between the probe and the plasma)

$$\langle J \rangle_\psi = \int_0^{\psi_0} J d\psi / \psi_0 \quad (46)$$

$$\langle \Delta \psi \rangle_{\psi^{3/2}} = \int_0^{\psi_0^{3/2}} \Delta \psi d(\psi^{3/2}) / \psi_0^{3/2} \quad (47)$$

one has

$$\langle J \rangle_{\psi} = \frac{m e}{3 e} \psi_0^{3/2} \frac{\langle \Delta \psi \rangle_{\psi}^{3/2}}{\psi_0} \quad (48)$$

or in terms of charge density

$$\langle J \rangle_{\psi} = \frac{2}{3} \psi_0^{3/2} \langle \rho \rangle_{\psi}^{3/2} / \psi_0 \quad (49)$$

$$\langle J \rangle_{\psi} \approx \frac{2}{3} \xi_5 \frac{\psi_0}{\psi_0 d^2} \psi_0^{3/2} \quad (50)$$

so that

$$\langle J \rangle_{\psi} \approx \frac{2}{3} \xi_5 \psi_0^{3/2} / d^2 \quad (51)$$

where ξ_5 is an appropriate constant.

7. Charge-Free Field of Infinite Strip

The field of an infinite strip maintained at constant potential $-\phi_0$ is most readily determined in elliptic cylinder coordinates. These are defined by

$$\begin{aligned} x &= c \cosh \eta \cos \psi \\ y &= c \sinh \eta \sin \psi \end{aligned} \quad (52)$$

in which elimination of ψ yields the elliptic cylinders for

$$\eta = \text{constant} \quad \left(\frac{x}{c \cosh \eta} \right)^2 + \left(\frac{y}{c \sinh \eta} \right)^2 = 1 \quad (53)$$

while elimination of η yields the hyperbolic cylinders for

$$\psi = \text{constant} \quad \left(\frac{x}{c \cos \psi} \right)^2 - \left(\frac{y}{c \sin \psi} \right)^2 = 1 \quad (54)$$

Corresponding to $\{y=0, x \geq c\}$ is $\psi = 0$

Corresponding to $\{y=0, x \leq -c\}$ is $\psi = \pi$

Corresponding to $\{x=0, y > 0\}$ is $\psi = \pi/2$

* ($\phi_0 > 0$) + coordinate ψ not to be confused with function ψ defined by (6)

Corresponding to $\{x=0, y<0\}$ is $\psi = 3\pi/2$

Corresponding to $\{y=0, x>0\}$ is $\eta = 0$

The arc length ds in this coordinate system is

$$ds^2 = \Lambda^2 (d\eta^2 + d\psi^2) \quad (55)$$

with $\Lambda^2 = c^2 (\cosh^2 \eta - \cos^2 \psi) = c^2 (\sinh^2 \eta + \sin^2 \psi)$

The gradient is given by

$$\Lambda \nabla \phi = \bar{u}_\eta \partial_\eta \phi + \bar{u}_\psi \partial_\psi \phi \quad (56)$$

The divergence is given by

$$c \Lambda (\nabla \cdot \bar{E}) = \partial_\eta (\Lambda E_\eta) + \partial_\psi (\Lambda E_\psi) \quad (57)$$

The Laplacian is given by

$$\Lambda^2 \Delta \phi = \partial_\eta^2 \phi + \partial_\psi^2 \phi \quad (58)$$

The magnitude of the curl is given by

$$\Lambda^2 |\nabla \times \bar{E}| = \partial_\eta (\Lambda E_\psi) - \partial_\psi (\Lambda E_\eta) \quad (59)$$

The unit vectors \bar{u}_η and \bar{u}_ψ are in the directions of increasing η and ψ respectively.

$$\bar{u}_\eta = \frac{c}{\Lambda} (\sinh \eta \cos \psi, \cosh \eta \sin \psi) \quad (60)$$

$$\bar{u}_\psi = \frac{c}{\Lambda} (-\cosh \eta \sin \psi, \sinh \eta \cos \psi)$$

The eccentricity of any particular ellipse given by a special value of η is

$$e = \operatorname{sech} \eta \quad (61)$$

while the oblateness is $\tanh \eta$. The semi-major axis a and

the semi-minor axis b are clearly read from (53)

$$\begin{aligned} a &= c \cosh \eta \\ b &= c \sinh \eta \end{aligned} \quad (62)$$

In these coordinates the solution of Laplace's equation reducing to zero on $\eta = \eta_s$ and to $-\phi_0$ on $\eta = 0$ becomes trivial. Since there is no ψ dependence Laplace's equation is

$$\frac{d^2 \phi}{d\eta^2} = 0 \quad (63)$$

with solution

$$\phi = A\eta + B \quad (64)$$

whence the boundary conditions yield

$$\phi = \phi_0 \left(\frac{\eta}{\eta_s} - 1 \right) \quad (65)$$

According to (62) $2a = 2c \cosh \eta$ so that the sum of the distances to the strip edges in rectangular coordinates is given by

$$\sqrt{(x-c)^2 + y^2} + \sqrt{(x+c)^2 + y^2} = 2c \cosh \eta \quad (66)$$

with the square roots non-negative. Thus the value of η is given by

$$\eta = \operatorname{arccosh} \left[(r_1 + r_2) / 2c \right] \quad (67)$$

with

$$\begin{aligned} r_1 &= \sqrt{(x+c)^2 + y^2} \\ r_2 &= \sqrt{(x-c)^2 + y^2} \end{aligned} \quad (68)$$

so that

$$\phi = \phi_0 \left[\frac{\operatorname{arccosh} \left[(r_1 + r_2) / 2c \right]}{\eta_s} - 1 \right] \quad (69)$$

where η_s may be replaced by any of

$$\operatorname{arccosh}\left(\frac{a+b\eta_s}{c}\right) = \eta_s = \operatorname{arcsinh}(b/c) = \operatorname{arccosh}(a/c) \quad (70)$$

Alternatively the potential may be obtained by mapping the semistrip $\{\operatorname{Im} w \geq 0, |\operatorname{Re} w| \leq \frac{\pi}{2}\}$ onto the upper half z -plane by a Schwartz - Christoffel transformation. Mapping $w = \pm\pi/2$ into $z = \pm c$ one has

$$\frac{dw}{dz} = A (c-z)^{-1/2} (c+z)^{-1/2} = \frac{A}{\sqrt{c^2 - z^2}} \quad (71)$$

which integrates to

$$w = A \operatorname{arcsin}(z/c) + B \quad (72)$$

Since $z=0$ is the image of $w=0, B=0$.

Since $w=\pi/2$ has $z=c$ as image

$$\pi/2 = A \operatorname{arcsin} 1$$

(see Fig 9)

implies $A = 1$. Hence

$$z = c \sin w \quad (73)$$

which corresponds to

$$\begin{cases} x = c \cosh v \sin u \\ y = c \sinh v \cos u \end{cases} \quad (74)$$

for $w = u + iv$ and $z = x + iy$. The potential for the given strip problem is then

$$\phi = \phi_0 \left(v / \operatorname{arccosh}(a/c) - 1 \right) \quad (75)$$

with

$$c \cosh v = (r_1 + r_2) / 2 \quad (76)$$

so that

$$\phi = \phi_0 \left[\frac{\operatorname{arccosh}[(\eta + r_2)/2c]}{\operatorname{arccosh}(c/c)} - 1 \right] \quad (77)$$

as in (65) and with a corresponding to η_s .

8. Field of Infinite Strip with Space Charge

The simplest way of incorporating space charge into the elliptic cylinder symmetry would be obtained with a space charge distribution of the form

$$-\rho/\epsilon = \frac{1}{2} \Lambda^2 / \sqrt{\psi} \quad (78)$$

So that (58) would become

$$d^2_{\eta} \psi = \frac{\Lambda^2}{2\sqrt{\psi}} \quad (79)$$

as in (7). This would then yield a 3/4 law in terms of η_s

$$\frac{1}{3} \psi_0^{3/4} = \sqrt{2\Lambda^2} \eta_s \quad (80)$$

Even without the assumption (78) one can expect that the charge density could be approximated by some appropriate η dependence between η_s and $\eta=0$. One could join two linear functions of η at some ellipse η_{in} between $\eta=0$ and $\eta=\eta_s$. The disadvantage of such a double linear fit (each portion of which satisfies Laplace's equation) is that it would imply a charge distribution crowded along the intermediate ellipse which is hardly likely physically. Going to fit quadratic or cubic in η provide a more realistic distribution

of charge and one could even go to higher degree if a "cathode glow" were desired in addition to a "cathode dark space".

It is not difficult to fit a parabola (in η) of the form

$$\phi = A(\eta_s - \eta)^2 + B(\eta_s - \eta) \quad (81)$$

to the conditions

$$\phi(\eta_s) = 0 ; \phi(0) = -\phi_0 ; \phi(\eta_m) = \phi_m$$

getting *

$$A = \left| \frac{-\phi_0}{\phi_m (\eta_s - \eta_m)} \right| / \Delta ; B = \left| \frac{\eta_s^2 - \phi_0}{(\eta_s - \eta_m)^2 - \phi_m} \right| / \Delta$$

which would then have a uniform charge density $2A$ in the dark

space. For more detailed specifications Lagrangian interpolation would suffice. These interpolated models however do not yield a charge density inversely proportional to square root of potential. (Fig 9)

9. Collection Trajectories of Ions in Free Space (see Appendix A)

If it be supposed that an ion be injected into the electrostatic charge-free field of a strip with a velocity below the escape velocity it will traverse a trajectory which is the image of an elliptical trajectory in the object plane in which the strip has become a circle. Thus if the strip plane be labeled W one has

$$W = \frac{c}{z} \left(z + \frac{1}{z} \right) \quad (82)$$

where c is the strip semiwidth. The strip $\{ \text{Im } w=0, |\text{Re } w| \leq c \}$

is the image of the unit circle $z^*z = 1$ in the Z -plane. A

collection trajectory then represents an ellipse with a "perihelion"

$$* \Delta = \eta_m \eta_s (\eta_s - \eta_m)$$

distance not greater than unity. The "escape velocity" is

$$v_p = \frac{2}{\pi} [q \phi_0 - 2 Q q \ln R]^{1/2} \quad (83)$$

where Q is the total charge of the strip and q is the charge in motion while R is the image circle for $\eta = \eta_s$.

In the Z -plane the elliptical trajectory is

$$\bar{z} = \frac{\epsilon k e^{i\theta}}{1 - \epsilon \cos(\theta - \alpha)} \quad (84)$$

while the image trajectory in the w -plane is

$$W = \frac{c}{2} \left\{ \frac{\epsilon k e^{i\theta}}{1 - \epsilon \cos(\theta - \alpha)} - \frac{1 - \epsilon \cos(\theta - \alpha)}{\epsilon k e^{i\theta}} \right\} \quad (85)$$

The "perihelion" distance is

$$r_p = \frac{\epsilon k}{1 + \epsilon} \leq 1 \quad (86)$$

for collection.

10. The General Motion of Particles in Elliptic Cylinder Coordinates in Charge-free Space

The unit vectors \bar{u}_η and \bar{u}_ψ are given by (60). In terms of these the vectorial velocity is

$$\bar{v} = \Lambda (\dot{\eta} \bar{u}_\eta + \dot{\psi} \bar{u}_\psi) \quad (87)$$

The directions of the unit vectors change with time during a trajectory and this must be considered to calculate the acceleration

$$\dot{\bar{u}}_\eta = \frac{c^2 F}{2\Lambda^2} \bar{u}_\psi; \quad \dot{\bar{u}}_\psi = -\frac{c^2 F}{2\Lambda^2} \bar{u}_\eta \quad (88)$$

$$F = \dot{\psi} \sinh(2\eta) - \dot{\eta} \sin(2\psi)$$

Using these the acceleration is found to be

$$\begin{aligned}\bar{a} &= a_\eta \bar{u}_\eta + a_\psi \bar{u}_\psi \\ a_\eta &= \Lambda \ddot{\eta} + \frac{c^2}{\Lambda} \dot{\eta} \dot{\psi} \sin(2\psi) + \frac{c^2}{2\Lambda} (\dot{\eta}^2 - \dot{\psi}^2) \sinh(2\eta) \\ a_\psi &= \Lambda \ddot{\psi} + \frac{c^2}{\Lambda} \dot{\eta} \dot{\psi} \sinh(2\eta) - \frac{c^2}{2\Lambda} (\dot{\eta}^2 - \dot{\psi}^2) \sin(2\psi)\end{aligned} \quad (88)$$

which give the η and ψ components of the acceleration explicitly.

For the electrostatic field of the strip $a_\psi = 0$ and $a_\eta = \frac{eE_\eta}{m\gamma^3} = \frac{e\phi_0}{m\eta\gamma^3\Lambda}$ so one has the equations of motion

$$\begin{aligned}\Lambda \ddot{\psi} + \frac{c^2}{\Lambda} \dot{\eta} \dot{\psi} \sinh(2\eta) - \frac{c^2}{2\Lambda} (\dot{\eta}^2 - \dot{\psi}^2) \sin(2\psi) &= 0 \\ \Lambda \ddot{\eta} + \frac{c^2}{\Lambda} \dot{\eta} \dot{\psi} \sin(2\psi) + \frac{c^2}{2\Lambda} (\dot{\eta}^2 - \dot{\psi}^2) \sinh(2\eta) &= \frac{e\phi_0}{m\eta\gamma^3\Lambda}\end{aligned} \quad (90)$$

which may also be obtained from the Lagrangian

$$L = \frac{m\Lambda^2(\dot{\eta}^2 + \dot{\psi}^2)}{2} + e\phi_0 \left(\frac{\dot{\eta}}{\eta\gamma} - 1 \right) \quad (91)$$

which suggests that Ritz Ansätze

$$\left\{ \begin{aligned} \eta &= \eta(t) \\ \psi &= \psi(t) \end{aligned} \right\} \quad (92)$$

may be used in a variational Hamilton principle using (91).

Finally it is readily calculated that the curvature of a trajectory any point is given by

$$K = \frac{|\bar{v} \times \bar{a}|}{v^3} = \frac{\dot{\psi} a_\eta}{\Lambda^2 (\dot{\eta}^2 + \dot{\psi}^2)^{3/2}} \quad (93)$$

so that

$$K = \frac{|\dot{\psi} [\Lambda \ddot{\eta} + \frac{c^2}{\Lambda} \dot{\eta} \dot{\psi} \sin(2\psi) + \frac{c^2}{2\Lambda} (\dot{\eta}^2 - \dot{\psi}^2) \sinh(2\eta)]|}{\Lambda^2 (\dot{\eta}^2 + \dot{\psi}^2)^{3/2}} \quad (94)$$

11. Field of Charged Rectangular Plate at Constant Potential

Here the Laplace equation is in Cartesian coordinates

$$\Delta \phi = (\partial_x^2 + \partial_y^2 + \partial_z^2) \phi = 0 \quad (95)$$

which by the Bernoulli separation argument and Fourier synthesis

has solutions of the form

$$\phi(\bar{R}, z) = \frac{1}{\pi^2} \int_0^{\infty} \int_0^{\infty} e^{-|z| \sqrt{m^2 + n^2}} \cos(mx) \cos(ny) \bar{\Phi}(m, n) \, dm \, dn \quad (96)$$

with $\bar{R} = (x, y)$. For $z = 0$

$$\phi(\bar{R}, 0) = \frac{1}{\pi^2} \int_0^{\infty} \int_0^{\infty} \bar{\Phi}(m, n) \cos(mx) \cos(ny) \, dm \, dn \quad (97)$$

while the charge density σ is

$$\sigma = -\frac{1}{2\pi} \left. \frac{\partial \phi}{\partial z} \right|_{z=0} = \frac{1}{\pi^2} \int_0^{\infty} \int_0^{\infty} \bar{\Phi}(m, n) \sqrt{m^2 + n^2} \cos(mx) \cos(ny) \, dm \, dn \quad (98)$$

Since the charge density is expected to be

$$\sigma = \frac{\sigma_0 \, a \, b}{\sqrt{(a^2 - x^2)(b^2 - y^2)}} \quad (99)$$

with σ_0 the minimum at $x = y = 0$ the Ansatz

$$\frac{1}{\pi^2} \bar{\Phi}(m, n) \sqrt{m^2 + n^2} = \sigma_0 \, a \, b \, J_0(am) J_0(bn) \quad (100)$$

is suggested because of the identity

$$\int_0^{\infty} J_0(am) \cos(mx) \, dm = \begin{cases} 1/\sqrt{a^2 - x^2} & |x| < a \\ 0 & |x| > a \end{cases} \quad (101)$$

* J_0 is zero order Bessel function ($1 \leq |x| \leq a$)

The potential reducing to ϕ_0 on the plate then becomes

$$\phi(\bar{R}, z) = \sigma_0 ab \int_0^\infty \int_0^\infty e^{-|z| \sqrt{m^2 + n^2}} \frac{J_0(am) J_0(bn) \cos(mz) \cos(ny) dm}{\sqrt{m^2 + n^2}} \quad (102)$$

It would be desirable to generalize this solution to include the effect of a space charge of the type to be expected in the dark space about such a plate, but this has not yet been accomplished.

12. The General Solution of the Collisionless Stationary Boltzmann Equation

This equation sometimes called the Vlasov equation is of the following form

$$\bar{\nabla} \cdot \bar{\nabla}_{\bar{R}} p + \bar{a} \cdot \bar{\nabla}_{\bar{V}} p = 0 \quad (103)$$

where $\bar{\nabla}_{\bar{R}}$ is the positional gradient operator and $\bar{\nabla}_{\bar{V}}$ is the velocity gradient operator while

$$p d\tau_{\bar{R}} d\tau_{\bar{V}} \quad (104)$$

(with $d\tau_{\bar{R}}$ volume element and $d\tau_{\bar{V}}$ velocity space volume element) represents the probability that a particle exists with position in $d\tau_{\bar{R}}$ about \bar{R} and with velocity in $d\tau_{\bar{V}}$ about \bar{V} . It is supposed that with $p \geq 0$ one has

$$\iiint p d\tau_{\bar{R}} d\tau_{\bar{V}} = 1 \quad (105)$$

over all position and velocity space.

For a particle total energy

$$E = \frac{mv^2}{2} + e\phi \quad (e > 0 > \phi) \quad (106)$$

one discerns by using the method of characteristics or by inspection that the general solution of the collisionless stationary Boltzmann equation is

$$p = f(E) \quad (107)$$

with f an arbitrary function which may be a posteriori verified by

$$\begin{aligned} \nabla_E p &= f'(E) \nabla_E E = f'(E) e \nabla_E \phi \\ \nabla_V p &= f'(E) \nabla_V E = f'(E) m \bar{V} \end{aligned} \quad (108)$$

assuming \bar{V} to be independent of position. Adding one then has

$$\bar{V} \cdot \nabla_E p + \bar{a} \cdot \nabla_V p = f'(E) \left(m \bar{V} \cdot \frac{d\bar{V}}{dt} + e \frac{d\phi}{dt} \right) = 0 \quad (109)$$

by conservation of energy.

For a classical thermodynamic gas f is taken to be of the form

$$f(E) = \lambda e^{-\lambda E} \quad (110)$$

which is a Poisson frequency function expressing the physical assumption of Boltzmann that a particle is exponentially unlikely to be in a high energy state. For such a gas $e\phi = 0$ and a Gaussian distribution in velocities, viz. the Maxwell-Boltzmann distribution, results. The temperature of the gas

is then proportional to the variance of this velocity distribution.

In cases where the particle velocities do not follow the Maxwell-Boltzmann distribution one can expect to characterize the form of the function f from experimental information about the actual velocity distribution.

13. The Physical Basis of Current Saturation

(Fig 2)

Although the problem of current saturation may not arise at low voltage levels it is important as a limiting situation more closely approached at high voltages. Therefore it seems appropriate to discuss this in a general (3D) way.

Starting from Maxwell's equations ¹³

$$\begin{aligned} \vec{J}/c &= \nabla \times \vec{H} - \partial_{ct} \vec{D} \\ \rho &= \nabla \cdot \vec{D} \\ \vec{0} &= \nabla \times \vec{E} + \partial_{ct} \vec{B} \\ 0 &= \nabla \cdot \vec{B} \end{aligned} \quad (111)$$

in Gaussian rationalized units it is clear that under stationary conditions obtaining at saturation all partial time derivatives will be zero and the equations become

$$\begin{aligned} \vec{J}/c &= \nabla \times \vec{H} \\ \rho &= \nabla \cdot \vec{D} \\ \vec{0} &= \nabla \times \vec{E} \\ 0 &= \nabla \cdot \vec{B} \end{aligned} \quad (112)$$

The stationary (saturation) state is thus characterized by the existence of an electrostatic potential ϕ with

$$\vec{E} = -\nabla\phi \quad (113)$$

So that for constant permittivity

$$-\frac{\rho}{\epsilon} = \Delta\phi \quad (114)$$

Poisson's equation results. If \vec{v} is the vectorial velocity of a charge

$$\vec{J} = -e\vec{v}\Delta\phi = \rho\vec{v} \quad (115)$$

and it is not necessary to use the Ampere circuital law to calculate current density \vec{J} . If this result be used in the plasma region where the collisionless stationary Boltzmann equation holds one has

$$\vec{J} = \rho\vec{v} = ne\vec{v} = n_0 e^{-\frac{(e\phi + \frac{mv^2}{2})}{kT}} e\vec{v} \quad (116)$$

Since (4) implies via (107)

$$n = n_0 e^{-\frac{(e\phi + \frac{mv^2}{2})}{kT}} \quad (117)$$

(106) is a deterministic relation*. If it be applied to an essentially stochastic situation where the expected velocity is zero (117) implies

*For the expectation \vec{v} to be detectable it must be larger than the thermal velocity which represents noise. This holds at low ϕ .

$$\bar{J} = n_0 e^{-e\phi/kT} e \bar{v} \quad (118)$$

One notes that $\langle \bar{v} \rangle$ may be taken to be zero for velocities of random direction with magnitudes less than their standard deviations producing a semilogarithmic behaviour of \bar{J} vs. ϕ . This holds a low ϕ . When ϕ increases sufficiently the general velocity will be increased due to the continuity of flow and the fall of particles into the elliptical funnel potential well they are approaching. In fact as ϕ increases this funnel will widen at the top. Under these conditions v cannot be set equal to zero, but because (106) is constant \bar{J} no longer depends on ϕ which is the peculiar property of saturation. What then determines \bar{J} ? Clearly \bar{v} as a factor outside the exponential.

Thus particles approaching the elliptical funnel potential well would in the absence of initial velocity simply fall down the sides of the well along the electric field lines for the strip. In the presence of initial velocity they would swirl around in the funnel as they fell. All this is true at not too high (saturation) voltage. Above saturation voltage the particles behave as if there were no potential well. Hence they simply move in the flow pattern of uncharged particles about the strip. There is thus a transition on saturation from a problem of ionic motion in an electrostatic field to one equivalent to a neutral gas dynamic flow about an obstacle (strip).

14. Anisotropy of Current Collection

(Fig 3)

In Langmuir probe theory one is usually interested only in

total current collected. Naturally such a variable contains no information about how the current density is distributed on a closed surface about the collector. To address the latter question one must set up a distribution of current density under the assumption that the current crosses the surface everywhere in the same sense. Then for total current I crossing the surface one has

$$\frac{1}{I} \oint \vec{J} \cdot \vec{n} \, dS = 1 \quad (119)$$

If \vec{R} represents the vectorial location of a point on the surface

$$\langle \vec{R} \rangle = \frac{1}{I} \oint (\vec{J} \cdot \vec{n}) \vec{R} \, dS \quad (120)$$

represents the expected location of current entry on the surface.

$$3\sigma_{\vec{R}}^2 = \langle \vec{R} \cdot \vec{R} \rangle - \langle \vec{R} \rangle \cdot \langle \vec{R} \rangle \quad (121)$$

$$\langle \vec{R} \cdot \vec{R} \rangle = \frac{1}{I} \oint (\vec{J} \cdot \vec{n}) (\vec{R} \cdot \vec{R}) \, dS \quad (122)$$

determines the standard deviation $\sigma_{\vec{R}}$ about the mean location of current entry. This then is a measure of current concentration or "focussing" on the surface.

15. Current Focussing for a Strip Collector

Returning to (32) and (34) and using elliptic cylinder coordinates (58) one finds from (87) current density crossing a particular ellipse corresponding to a specific value of η

$$(\vec{J} \cdot \vec{n}) = -\epsilon (\vec{n} \cdot \vec{v}) \Delta \phi \quad (123)$$

or

$$-(\bar{J} \cdot \bar{n}) = \epsilon \dot{\eta} d_{\eta}^2 \phi / \Lambda \quad (124)$$

where ϕ has been taken independent of ψ and only the η component of velocity has been used. To evaluate (124) requires not only that ϕ has been fitted as indicated in Section 8 but a knowledge of $\dot{\eta}$ as a function of η and ψ . If the particular ellipse chosen is η_s however assuming the input velocity \bar{V}_p is known vectorially one can write

$$-(\bar{J} \cdot \bar{n}) = (\bar{V}_p \cdot \bar{u}_{\eta}) d_{\eta}^2 \phi / \Lambda^2 \quad (125)$$

where $(\bar{V}_p \cdot \bar{u}_{\eta})$ is the component of input velocity normal to the ellipse η_s . Here the difficulty is that some (high-velocity) fraction of the particles may miss the collector invalidating the assumption that $(\bar{J} \cdot \bar{n})$ is single signed. To avoid this it seems reasonable to take an ellipse with η sufficiently close to zero that misses will be unlikely to enter it. With a parabolic fit

$$\phi = A(\eta - \eta_s)^2 + B(\eta - \eta_s) \quad (126)$$

$$d_{\eta}^2 \phi = 2A$$

$$-\phi_0 = A\eta_s^2 - B\eta_s$$

while with a cubic fit

$$\phi = A(\eta - \eta_s)^3 + B(\eta - \eta_s)^2 + C(\eta - \eta_s)$$

$$d_{\eta}^2 \phi = 6A(\eta - \eta_s) + 2B \quad (127)$$

$$-\phi_0 = -A\eta_s^3 + B\eta_s^2 - C\eta_s$$

and in either case $d_{\eta}^2 \phi$ is determined at the strip. The η in (124) must be integrated down to the normal component of impact velocity at the strip. Then integrating $(\bar{J} \cdot \bar{n}) ds$ about the strip will yield total current I per unit length of the strip. On the strip (55) reduces to $ds = \Lambda d\psi$ so

$$I = \epsilon \int_0^{2\pi} |\eta| |d_{\eta}^2 \phi| d\psi \quad (128)$$

is the total current into the strip. On the strip (122) becomes

$$\langle \chi^2 \rangle = \frac{\epsilon c^2}{I} \int_0^{2\pi} |\eta| |d_{\eta}^2 \phi| \cos^2 \psi d\psi \quad (129)$$

while (120) becomes

$$\langle \chi \rangle = \frac{\epsilon c}{I} \int_0^{2\pi} |\eta| |d_{\eta}^2 \phi| \cos \psi d\psi \quad (130)$$

Then σ_{η}^2 may be calculated via

$$\sigma_{\eta}^2 = \langle \chi^2 \rangle - \langle \chi \rangle^2 \quad (131)$$

as a function of applied voltage ϕ_0 . This describes the "focussing" as a function of applied voltage*. However, considering space charge it would be better to parallel this procedure numerically.

16. Input Vectorial Velocity on Entry Ellipse η_s (Figs 5, 6, 7, 8)

For the purpose of getting better input information on the velocity of flow into the potential (well) funnel.

Flow into a circular funnel from a point source in the
*If no space charge were present one could use the initial information on location of entry point and \bar{v}_p in the w-plane of Sec. 9 calculating image of impact point and impact angle to find η .

W-plane (into unit circle) at $W=i\sigma$ is described by the complex flow function (k is strength of flow)

$$F(W) = k \ln \left(\frac{W - i\sigma}{1 + i\sigma W} \right) \quad (132)$$

with velocity potential (zero for $|w| = 1$) ϕ and stream function ψ

$$\phi = k \ln \left| \frac{W - i\sigma}{1 + i\sigma W} \right| \quad (133)$$

$$\psi = k \arg \left(\frac{W - i\sigma}{1 + i\sigma W} \right) \quad (134)$$

By mapping this onto the z-plane according to

$$W = \frac{z}{c} + \sqrt{\left(\frac{z}{c}\right)^2 - 1} \quad (135)$$

the unit circle $|w| = 1$ becomes the slit $\{|z| \leq c, \text{Im } z = 0\}$

so one has flow into the slit from the image of the source

which is at $z = is$

$$\sigma = \frac{s}{c} + \sqrt{\left(\frac{s}{c}\right)^2 + 1} \quad (136)$$

and the complex flow function in the z-plane is

$$f(z) = k \ln \left\{ \frac{c \left[\frac{z}{c} + \sqrt{\left(\frac{z}{c}\right)^2 - 1} - i \left(\frac{s}{c} + \sqrt{\left(\frac{s}{c}\right)^2 + 1} \right) \right]}{c^2 + i \left(\frac{s}{c} + \sqrt{\left(\frac{s}{c}\right)^2 + 1} \right) \left(\frac{z}{c} + \sqrt{\left(\frac{z}{c}\right)^2 - 1} \right)} \right\} \quad (137)$$

and the (complex) velocity is found from

$$V^* = f'(z) \quad (138)$$

However what is desired is not a flow into the slit from

an isotropic source but rather a flow into an elliptical funnel from a dipole source. To get this the mapping from circle into ellipse may be used.

$$z = \frac{1}{2} \left\{ (a+b)W + \frac{(a-b)}{W} \right\} \quad (138)$$

maps $|W|=1$ onto the ellipse with maximum abscissa at $Z = a$ and maximum ordinate at $Z = ib$. To map the exterior of the ellipse onto the exterior of the circle the appropriate inverse mapping is

$$W = \frac{z + \sqrt{z^2 + b^2 - a^2}}{(a+b)} \quad (139)$$

The complex flow function from a dipole source at $W = i\sigma$ into a unit circle $|W|=1$ sink is

$$F(W) = \frac{i\sigma(1+W^2)}{(W-i\sigma)(1+i\sigma W)} \quad (140)$$

Substitution from (139) for w then yields the required complex flow function in the z -plane. From this the velocity can be calculated at the ellipse which forms "the edge of the funnel".

17. Summary (40)

A general relationship between current density, voltage and flow velocity has been obtained for Langmuir probes of arbitrary shape. Several particular cases (plane, cylindrical, spherical) have also been derived. The classical 3/4 law is recovered from the general case if initial flow velocity is zero.

It is argued that for sufficiently high applied voltage there will be a saturation effect in which current density

becomes independent of further voltage increases. The approach to saturation then involves a transition from a flow pattern dominated by the electrostatic field of the collector to one similar to flow past an uncharged object.

The question of anisotropic collection or current focussing is handled by treating the current density as a statistical distribution on any surface surrounding the collector. The standard deviation of this distribution is then a measure of the concentration of current about the mean entry location on the surface and the determination of this standard deviation as a function of applied voltage would solve the current focussing problem.

Arguments bearing on the numerical approaches to the problem are also given. It is believed that the theoretical aspects have been considerably clarified. The author wishes to express his appreciation to Bernard McIntyre for many useful discussions and much helpful guidance in approaching the problem. Also the assistance of Dino Zei in numerical modeling is gratefully acknowledged.

APPENDIX A

Elliptic Cylinder Differencing Scheme for Trajectory Calculation

$$\bar{R} = (x, y) = c(\cosh \eta \cos \psi, \sinh \eta \sin \psi) \quad (A-1)$$

$$\bar{v} = v_{\eta} \bar{u}_{\eta} + v_{\psi} \bar{u}_{\psi} = \Lambda (\eta \bar{u}_{\eta} + \dot{\psi} \bar{u}_{\psi}) \quad (A-2)$$

$$\bar{a} = a_{\eta} \bar{u}_{\eta}, \quad a_{\psi} = 0 \quad (A-3)$$

τ = time increment (+ indicates after τ)

$$v_{\psi}^{\dagger} = v_{\psi} \quad (A-4)$$

$$v_{\eta}^{\dagger} = v_{\eta} - a_{\eta} \tau \quad (A-5)$$

$$\eta^{\dagger} = \eta + \frac{v_{\eta}}{\Lambda} \tau \quad (A-6)$$

$$\psi^{\dagger} = \psi + \frac{v_{\psi}}{\Lambda} \tau \quad (A-7)$$

$$\Lambda^{\dagger} = \Lambda + \frac{c^2}{2\Lambda} \left\{ \sinh(2\eta)(\eta^{\dagger} - \eta) + \sin(2\psi)(\psi^{\dagger} - \psi) \right\} \quad (A-8)$$

ORIGINAL PAGE IS
OF POOR QUALITY

Bibliography

The notations:

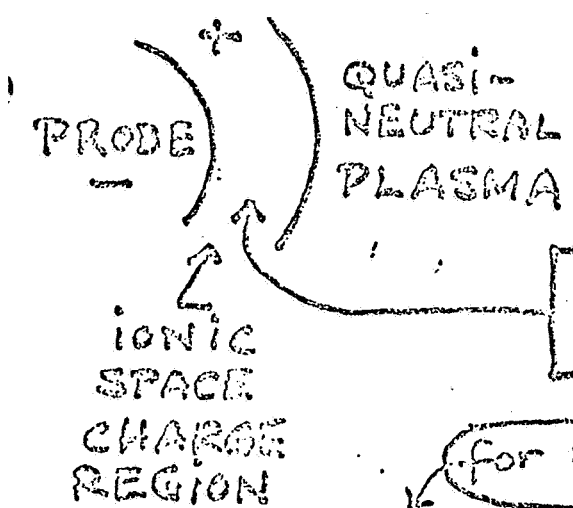
K1 = Theoretical Physics/Kyrala /1967/W.B.Saunders Co.

K2 = Applied Functions of a Complex Variable/Kyrala/1972
Wiley - Interscience

will be used.

1. Langmuir, I.: Phys. Rev. 21, 419 (1923).
Langmuir, I.: Phys. Rev. 2, 450 (1913).
Child, C.K.: Phys. Rev. 32, 492 (1911).
Laframboise, J.: Advances in Rarified Gas Dynamics , 1966.
2. K1: p. 335
3. Spitzer, L.: Physics of Fully Ionized Gases, 1956, Interscience
p. 17.
4. K1: p. 105
5. Knopp, K.: Theory and Application of Infinite Series, Hofner.1944
6. K1: p. 102
7. K1: p. 152
8. K2: p. 106
9. K1: p. 118
10. K1: p. 201
11. Watson, G.N. : Bessel Functions /1944/Cambridge Univ. Press
12. K1: p. 126
13. K1: p. 314
14. K2: p. 114

LANGMUIR PROBE THEORY



COLLISIONLESS STATIONARY
BOLTZMANN EQ.
 $\nabla \cdot \nabla_E p + \vec{a} \cdot \nabla_p p = 0$
 Sol. $p = f(E)$

$\vec{J} = \rho \vec{v} = -e \bar{v} \Delta \phi = n_0 e \bar{v} e^{-\frac{e\phi + \frac{1}{2}mv^2}{kT}}$

$E = \frac{mv^2}{2} + e\phi$

for zero flow

$\delta \approx \frac{v_0}{\omega_p}$ Debye shielding distance

$\psi = v_p^2 + \frac{2e}{m}(\phi_p - \phi) = v^2$

$v_0 =$ thermal velocity
 $\omega_p =$ plasma frequency

$v \Delta \psi = \left[\frac{2e}{m\epsilon} J = \sqrt{\psi} \Delta \psi \right]$

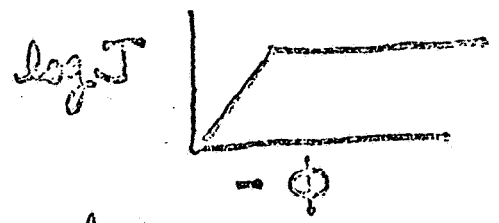
SATURATION AND CURRENT FOCUSSED

$\vec{J} = e \bar{v} n_0 e^{-E/kT} = e \bar{v} n_0 e^{-\frac{e\phi + \frac{1}{2}mv^2}{kT}}$

DETERMINISTIC STOCHASTIC

for $v < v_0$ can set $v = 0$ in deterministic energy expression $E = e\phi$ hence

$\vec{J} = e \bar{v} n_0 e^{-e\phi/kT}$



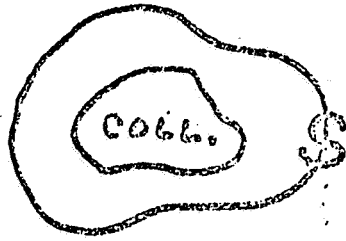
for $v > v_0$
 $\vec{J} = e \bar{v} n_0 e^{-E/kT} =$ no dependence on ϕ = saturation

(Fig 2)

As long as stochastic dominate we are not entitled to assume $E =$ constant.

STATISTICAL THEORY OF CURRENT FOCUSSED

For $\vec{J} \cdot \vec{n}$ single signed



$$\frac{1}{I} \oint (\vec{J} \cdot \vec{n}) dS = 1 \quad \text{normalization}$$

$$\langle \vec{R} \rangle = \frac{1}{I} \oint \vec{R} (\vec{J} \cdot \vec{n}) dS = \text{expected location of current entry on } S$$

$$\langle \vec{R} \cdot \vec{R} \rangle = \frac{1}{I} \oint (\vec{R} \cdot \vec{R}) (\vec{J} \cdot \vec{n}) dS$$

Fig 3

$$3\sigma_{\vec{R}}^2 = \langle \vec{R} \cdot \vec{R} \rangle - \langle \vec{R} \rangle \cdot \langle \vec{R} \rangle$$

$$\sigma_{\vec{R}} = F(\phi_0)$$

$\phi_0 = \text{applied voltage}$

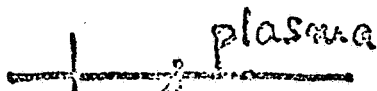
standard deviation $\sigma_{\vec{R}}$ is measure of current focussing on S

Physical Picture for Strip Collector

No Flow / No Space Charge plasma



Elliptic Cylinder Field For Charge Free Dark Space



Recharges fall into funnel along field lines

No Flow / Space Charge plasma



Some Equipotentials plasma ϕ potential (bump possible)

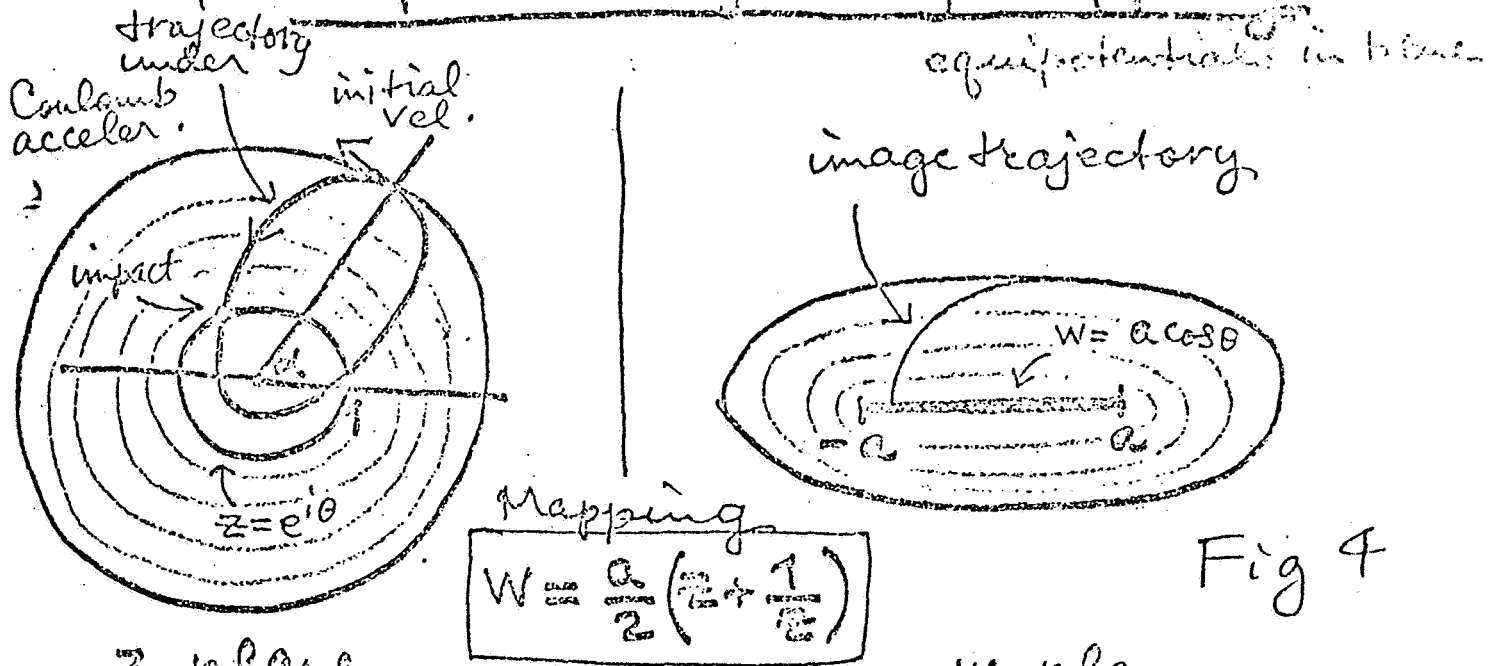
Flow / Space Charge plasma



at low ϕ charges still into funnel
at high ϕ charges tend to flow across strip

ORIGINAL PAGE IS OF POOR QUALITY

Ion Elliptical Trajectory Mapping



Mapping

$$W = \frac{a}{2} \left(z + \frac{1}{z} \right)$$

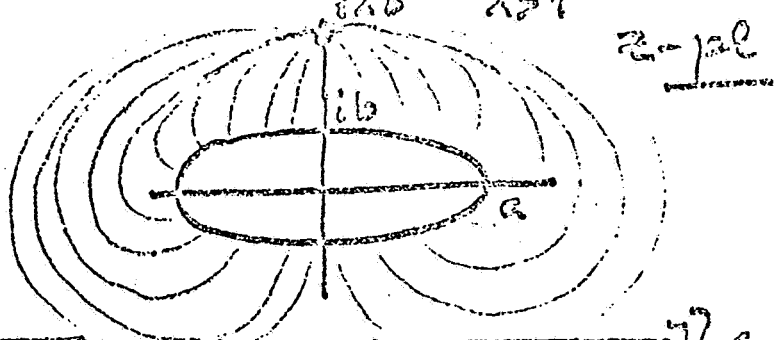
Fig 4

z-plane W-plane

$$z = \frac{a + i b e^{i\theta}}{1 - e \cos(\theta - \alpha)} \rightarrow W = \frac{a}{2} \left\{ \frac{a + i b e^{i\theta}}{1 - e \cos(\theta - \alpha)} + \frac{1 - e \cos(\theta - \alpha)}{a + i b e^{i\theta}} \right\}$$

Flow into Elliptical Funnel from Pt. Source

Complex Flow Function Fig 5

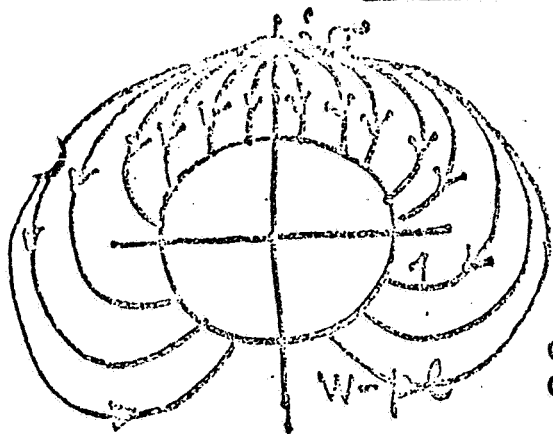


$$f(z) = c \ln \left[\frac{z + \sqrt{z^2 + b^2 - a^2} - i [\lambda b + \sqrt{(\lambda^2 - 1) b^2 + a^2}]}{(a+b)^2 + i [\lambda b + \sqrt{(\lambda^2 - 1) b^2 + a^2}] [z + \sqrt{z^2 + b^2 - a^2}]} \right] (a+b)$$

$V^* = f'(z) =$ conjugate complex (2D) velocity

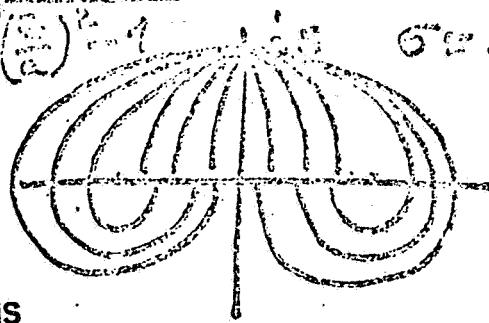
in terms of elliptic cylinder coords
 substitute $z = c \cosh \xi$ $\xi = \eta + i\psi$
 $c =$ semi focus = strip semi $b = c \sinh \xi = c \sinh(\eta + i\psi)$

Flow Pt. Source to Circular Funnel



$$w = \frac{z}{a} + \sqrt{\left(\frac{z}{a}\right)^2 - 1}$$

$$\sigma = \frac{z}{a} + \sqrt{\left(\frac{z}{a}\right)^2 - 1}$$



ORIGINAL PAGE IS OF POOR QUALITY

$z = pe$

$$f(w) = c \ln(w - i\sigma) - c \ln\left(w + \frac{1}{i\sigma}\right) - c \ln(i\sigma) \quad \text{Fig 6}$$

$$f(w) = c \ln\left(\frac{w - i\sigma}{1 + i\sigma w}\right)$$

velocity potential = $\phi = c \ln\left|\frac{w - i\sigma}{1 + i\sigma w}\right| = 0$ for w/σ

stream function = $\psi = c \arg\left(\frac{w - i\sigma}{1 + i\sigma w}\right)$ (used)

Conformal Mapping Circle \rightarrow Ellipse

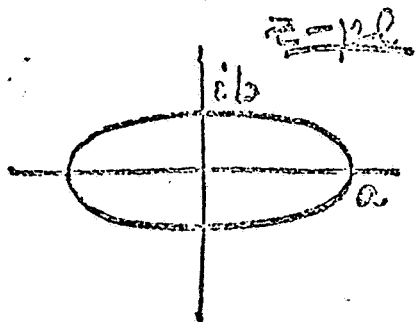
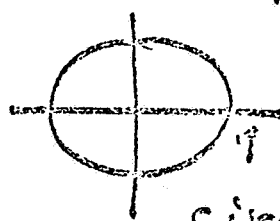


Fig 7



Circle $w^2 = 1$

$$z = \frac{1}{2} \left\{ (a+b)w + \frac{(a-b)}{w} \right\}$$

$w=0 \Rightarrow z = \infty$
 $w = \infty \Rightarrow z = \infty$

For $w = e^{i\phi}$ $z = \frac{1}{2} [(a+b)e^{i\phi} + (a-b)e^{-i\phi}] = a \cos\phi + ib \sin\phi$

Hence maps unit circle ($w = pe$) onto ellipse ($z = pe$)

Maps inside and outside of unit circle onto outside of ellipse

$$w = \frac{z}{a+b} + \sqrt{\left(\frac{z}{a+b}\right)^2 - \frac{b^2}{a^2}}$$

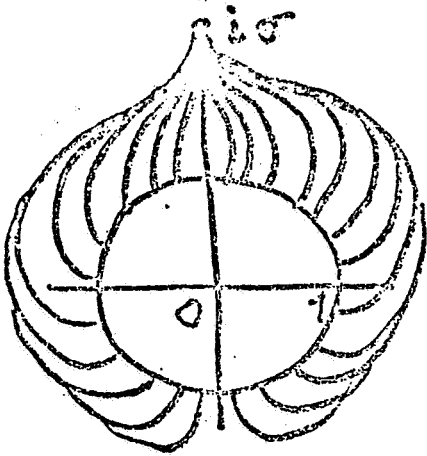
(a+b) \rightarrow outside \rightarrow inside of circle

$$w = \frac{z}{a-b} - \sqrt{\left(\frac{z}{a-b}\right)^2 - \frac{b^2}{a^2}}$$

(a-b) \rightarrow inside \rightarrow outside of circle

Flow into Circular Funnel From Dipole

(4)



ORIGINAL PAGE IS
OF POOR QUALITY

Fig 8

Substitute

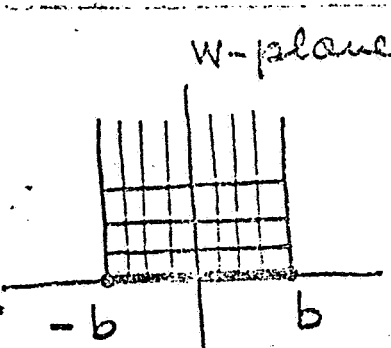
$$W = \frac{z + \sqrt{z^2 + b^2 - a^2}}{a + b}$$

to get flow from
dipole into
Elliptic Funnel

$$f(W) = \frac{ic(1+W^2)}{(W-i\sigma)(1+i\sigma W)}$$

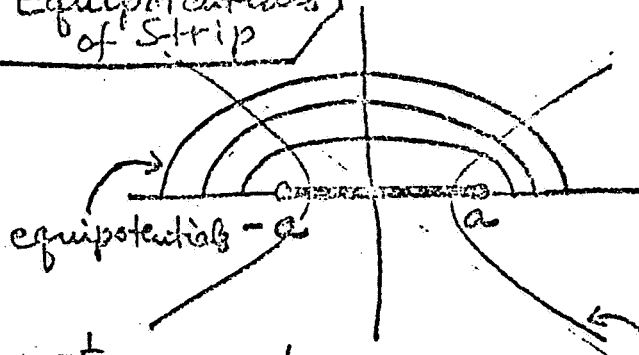
Complex
flow function

Schwarz-Christoffel
Mapping



Field and Equipotentials of Strip

z-plane



$$(z-a)^{\frac{\alpha}{\pi} - 1}$$

$$\alpha = \frac{\pi}{2}$$

$$(z-a)^{-1/2}$$

field lines

Fig 9

$$\frac{dw}{dz} = A(a-z)^{-1/2}(a+z)^{-1/2}$$

$$\frac{dw}{dz} = \frac{A}{\sqrt{a^2 - z^2}} \quad \int dw = A \int \frac{dz}{\sqrt{a^2 - z^2}}$$

$$W=0 \Leftrightarrow z=0$$

$$\downarrow$$

$$B=0$$

$$W = A \arcsin\left(\frac{z}{a}\right) + B$$

$$W = A \arcsin\left(\frac{z}{a}\right)$$

$$W=b \Leftrightarrow z=a \Rightarrow A = b / \arcsin 1 = \frac{2b}{\pi}$$

(over)

N82 23124

D2

Anthropometric Program Analysis

of

Reach and Body Movement

Charles J. McKinley Ph.D.

Supervisor: Barbara Woolford

Crew Station Design Section

Crew Station Branch

Spacecraft Design Division

NATIONAL AERONAUTICS AND SPACE ADMINISTRATION

LYNDON B. JOHNSON SPACE CENTER

HOUSTON, TEXAS

August 14, 1981

ABSTRACT

This was a multifaceted project involving several tasks related to anthropometric data collection and comparison.

Such data occurred in various forms, and included activities relating to human force and motion capabilities. Information was obtained from astronaut candidates doing certain force and motion activities. These individuals were suited, both in one-G and in neutral buoyancy of a water facility, and also unsuited, in a one-G environment.

Also involved was the review and comparison of several pieces of hardware used in quantification of the data collection. This hardware included a CYBEX II force and torque machine, and a three-dimension camera system(AMS) for measuring range of motion envelopes.

Preliminary comparison of collecting techniques was made to determine significant variables in the available data. Also, suggestions are offered for standardization of data collection in an attempt to better predict usefulness to various groups.

ACKNOWLEDGEMENTS

I wish to respectfully give my thanks to the following experts who gave so freely of their time and understanding to make this project a success: Dr. James Lewis, Head of Crew Station Design Section, encouraged me and helped direct me and focus my objectives. Also, Barbara Woolford, who patiently explained the mysteries of the computer software programs. My gratitude, especially, to Mr. John Jackson who hand-carried many references, introduced me to many other important people and helped me see the finer points to anthropometrics.

I am also grateful to the many others who let me into their facilities and labs, gave me special tours of the work stations and allowed inspection of WETF water tank. Without these, the job would have been impossible.

C. J. M.

INTRODUCTION:

It has long been recognized that the science of measurement has been important in the history of civilization. Even in our present-day technology, we easily forget this principle as it applies to the physical size of a person and his ability to function in our complex world.

Early researchers into body size, like Blumenbach (1752-1840), reported for the first time the complete body measurements. At about this same time the statistician Quetelet (1796-1874) carried out the first large-scale body measurement study, and is recognized as founding the science and coining the term "anthropometry".

Later, during the early part of the 20th century, extensive and rapid increases in anthropometric literature occurred. At this time, difficulties became evident as various investigators used differing terms in gaining measurements on the human body. More and more, knowledge of methodology became an important part of data interpretation and evaluation.

Today, what most people consider "normality" of body size is more accurately replaced with tables and charts of statistical values. In anthropometry today, statistical calculations are used to establish design criteria for specifying the range of each body dimension or function for which a product is to be designed.

These criteria will also determine the basis for selection standards used in screening a potential user population. This setting of anthropometric criteria or limits is essential if we are to insure proper fit of the man-machine system. However, we must recognize that variables of human beings are vastly different than those of machinery.

In both cases, too tight a tolerance excludes use by many, and may well raise the costs. On the other hand, a design that accommodates the full range of observed variations in the population, requires adjustments to the design, and will also raise the costs.

PROBLEM:

As in many engineering problems of measurement, the most direct approach to movement and range of motion capabilities is that of defining "final effects". At this level of the problem, the desired answer can be presented in a simple "yes" or "no" to a question such as: "can the individual reach and move a control?"

Given no prior knowledge, the likely approach to such a problem is to build a mockup of the situation and test a sample of individuals to observe if they are able to perform the given task.

This approach has its obvious limitations. After the answer is obtained, one still has knowledge of only a single, specific situation that may never be repeated.

At the next level, a more general solution may be sought in terms of defining a reachable spatial volume by determining its boundary surfaces, or its envelope. Within this defined envelope, several motion activities are possible.

Angular movement measurement is one of these, and has much in common with measurement of linear dimensions. Here, a variety of types of information regarding movement, may be obtained. These include

centers of rotation and angles as well as range of movement envelopes.

In each of the foregoing, for angular movement, a consistent use of scales, reference axes, planes and vectorial representation of links will reduce uncertainty and encourage consistency. These are important in that they will lead to more accurate design data and the development of clear specifications for mobility requirements.

In the cases involving dynamic recording and measurement of human movement, several measurement problems are compounded. According to J. A. Roebuck (1975) and others, the following are the minimum requirements for exact and objective methods of recording human movement:

1. Constant relationship and precision to the given dimension chosen.
2. Action of the subject must be unobstructed.
3. The range and sensitivity of the equipment must be sufficient to record changes in body position.
4. The data should be easily interpreted.

Further, as compared to anthropometric dimensions, strength data generally have a much greater variability between individuals. It also may be more easily influenced by a change in either mental or physical state of the subject.

Therefore, it has been stated that many of the published studies on muscular strength may suffer from shortcomings involving failure to consider the biomechanical, physiological, and the psychological aspects, as well as inadequate or improper instrumentation. This last deficit may also include failure

to report clearly the experimental procedures or statistical analyses.

Indeed, one of the most difficult problems in the assessment and application of human strength data is the presentation of this data. For strength data to be valid, a large number of variables must be kept constant. Their status must be clearly specified in the protocol or final report. The failure to specify such experimental conditions has caused the results of many studies to be of questionable validity and use.

CURRENT ANTHROPOMETRICS LABORATORY:

Given the brief background on anthropometrics and some of the recognized problems associated with the field, the present task at the Johnson Space Center and the Anthropometrics Laboratory (AML) may now be undertaken.

The primary concern was analyzing the usefulness of the AML facility in determining the kinds of problems that a suited astronaut might encounter in E.V.A. Immediate questions which came to the fore were: What information is vital? How can this information be obtained quickly and most accurately? And, what processing is available for the data reduction and analysis?

In order to answer these and other related questions, it became apparent that the task was multifaceted. Other researchers needed to be contacted. Suit facilities had to be seen. Various work stations needed to be visited, to understand how the real world of the E.V.A. could be demonstrated.

Questions as those above needed answers. As the list of "experts" from contacted laboratories grew, the evidence became clear that a large number of researchers were currently applying themselves to the problem of motion and force analysis. (See Table 1.0)

It also became clear that several important differences were present as to techniques and approach to the anthropometrics problem. Many such workers, it was discovered, have unique needs and therefore, have designed their techniques to that purpose. Sports medicine and physical education labs which were contacted had such a special purpose.

In addition, certain private lab facilities for anthropometric collection are available, and will tailor their techniques in an attempt to fit the needs of their clients.

One research unit contacted is using the method of stereophotogrammetry to re-configure the actual body proportions of an individual. These dimensions are then recorded digitally to later be displayed.

Several labs across the country are using two-dimensional and three-dimensional approaches with 16 mm cameras to record motion activities. Such film is later analyzed for angular and reach changes, to be digitized for reference on the test subject.

As noted earlier, the suit facility was a vital factor to further understanding of any motion analysis problems. At various times through the weeks, contacts and meetings were held with individuals of this facility. The attempt was to gain knowledge about the current suit model, with particular reference and attention to its fabrication and intended E.V.A. uses.

Several days were spent observing suited activities by astronauts performing tasks in the WETF water tank. Here, several different astronauts were in training to attempt a number of activities on the submerged shuttle cargo bay and air-lock. Participants were in neutral buoyancy to simulate zero-G effects. General suit

flexibility and cuff-ring mobility was observed during these tasks and activities.

At present, the current model of the E.V.A. suit has had only limited pilot runs of anthropometric data collected on it. One such collection was made using a two-dimensional reach onto a drawing board. This was a reach test done in the WETF water tank.

Also, a single demonstration, suited and in one-G was run, using a three-dimensional approach with T.V. cameras and a microprocessor analyzer.

Finally, while several unsuited force and torque measurements have been obtained using a CYBEX force machine, no such information is currently available using the present model E.V.A. space suit.

It is evident that the ability to do work should be the primary tool to evaluate any E.V.A. space suit. And, while it is more difficult to relate elementary force and torque functions to the more complex mission maneuvers, data from such elementary movements may be applied to understand the limits of a given space suit and the occupant within.

The anthropometrics laboratory (AML) at NASA-JSC is dedicated to the task of gathering vital information on reach and force of astronauts in both unsuited and suited configuration. To this end, the AML has several prototype pieces of equipment designed for such data collection. These include:

1. Automatic joint angle measurement device, consisting of a video camera, lights which attach to the subject, and a microprocessor for data acquisition. This system provides for direct angle readings from a joint, plus a hard copy print thru an electronic teletype-writer.

2. Automatic three-dimensional anthropometric video system, including 3 T.V. cameras, a lighting system attaching to the subject, and a microprocessor. Information gained from this system includes envelope of motion and velocity-acceleration. Data from this equipment is programed thru computers for use.

3. A CYBEX II dynamometer and recorder for force and torque data collection. This machine allows analysis of the various body joint movement and several types of motion data, including strength, torque, power endurance and other isokinetics.

When fully operational, the above equipment has the capability of collecting the many parameters of body movement and force data on both the unsuited and suited individual.

Used together, the CYBEX and the three-dimensional system can give information on both envelope of motion AND the type and endurance of many tasks at various body positions.

Clearly, one of the principle jobs in the study of dynamic anthropometry, is to describe quantitatively the translocations and rotations of the various body segments, and to relate them to the movement of the entire body. To be adequate, any such description requires not only that these body movements be measured in three-dimensions, but also that velocities and force be recorded and that the sequence of motion of various parts of the body be determined.

FUTURE SUGGESTIONS:

The Johnson Space Center's AML is currently in the early functional stages to begin collection of useful data on suited and unsuited functional reach and force activities.

A test plan outline has been received from the suit facility, and discussion begun for the start of a performance mapping profile on shuttle SSA suit at various pressure levels. The general procedure will include the following:

1. Establish baseline "nude body" range of movement measurements with selected subjects. Each subject will serve as his own control.
 - a) Use document No. ILS-J-SS-011 as a guide line to determine 22 basic body motions required, and the technique for deriving these 22 motions.
2. Conduct suited, pressurized mobility range measurements with three dimensional cameras, using:
 - a) above defined 22 motions.
 - b) shuttle space suit at following P.S.I.: 4.0, 5.0, and 6.0
3. Repeat steps 2a and 2b, using shuttle space suit without thermal micrometeoroid layer.
4. The following cautions are to be observed in each of the above experimental conditions:
 - a) Each position to be run three times, with average value of these taken as mean.
 - b) Care used not to degrade motions due to candidate fatigue.
 - c) Refer to appropriate standard text sources for defining each motion given.

It is further suggested that the suited reach (envelope) information be formatted in the manner given below and adapted from Kennedy (1978).

Using AML three dimension camera system, develop reach envelope in the prescribed manner. Then, for better data availability, determine the outside boundry values of this envelope. This may be done by slicing 15⁰ horizontal layers and 15⁰ vertical layers through the reach envelope. By using a standard reference point (such as SCYE or seat) reach numbers can quickly be obtained in 15⁰ intervals.

To gain further knowledge about a given model suit, additional reach data must be obtained in neutral buoyancy of WETF water tank. Alternative methods are suggested for collecting such data. Perhaps placement of reach boards at front, at 45⁰ each side and 90⁰ each side would give more useful reach data from the WETF tank approach. However, general format must be compatable if these data are to be comparable with the 3-D system.

Additionally, force and work information is vital on each suit. These data must also be obtained in one-G and in simulated 0-G environment.

Suggestions are also made to use Life Sciences Division for coordinating efforts for obtaining B.T.U.'s used and thermal loads developed during standard force and work tasks, while in a given model suit under the varying conditions.

A final reminder that data bases must be developed using as much standardized procedures as can be obtained for proper data comparison in the future.

TABLE 1.0

Laboratories and Individuals
Involved in Anthropometric Studies of
Motion and Force

Ken Kennedy and
Chuck Clauser
Anthropometric Unit
Wright Patterson A.F.B.
(87) 775-5779

Date collection on several types of flight suits. Have developed a reach device. Have collected suit reach data. Determined "reach mobility factor" of suits.

Joe McDaniel
(with Kennedy)
Wright Patterson A.F.B.

Has current project on body size and strength/endurance testing. Has suited data with SR 71 and U2 anti-G garments. Data base from various suited configurations. Data available thru simulator-computer programs. Also tests run for kinetic measurements plus fixed mode.

Dr. Don Sheffer and
Robert Herron
University of Akron
Institute for BioMedical
Engineering Research
(216) 375-3850

Have data on stereophotogrammetric body configurations. I.B.M. cards received by AML as sample of this program.

Dr. Herb Reynolds and
Dr. Howard Stoudt
Michigan State University
East Lansing, MI. 48824
(87) 375-4675
(87) 373-3200

Reynolds is currently collecting 3-D anthropometric data, using stereo X-ray technique. Cadaver use involves placement of metal pellets into joint cavities. Computer fortram program digitizes data. Also doing 3-D postural data on stewardesses.

John McConville

Anthropometric Research
Studies Inc.
503 Xenia Ave.
Yellow Springs, OH. 45387
(513) 767-7226

Has done early studies on volume and center of gravity of various body components. (using cadavers) Presently doing moments of inertia on body segments (cadavers). Has reference to W.P.A.F.B. large data bank, raw data, and various display programs for such data.

Lloyd Laubach

University of Dayton
P.E. Dept.
(513) 229-4225

Currently teaching only.
Has had important past involvement in anthropometrics studies.

John A. Roebuck

Space Division
Rockwell International Corp.
1224 Lakewood Blvd.
Downey CA. 90241
(87) (213) 594-3078 or 3311

Publication and familiarity with one and two camera approach on stereophotogrammetry. Has no data base on these techniques. Currently on space serve project at R.I.

Jaime Cuzzi

Institute for Rehabilitative
Research
Baylor University
1330 Moursund
Houston, TX 77030

Experienced with 3-D body configuration data collection techniques. Helped design program for data collection.

Dr. John Cooper

Indiana University at
Bloomington.
(812) 337-7302

Early work using single movie camera for determining moments of inertia, velocity, acceleration and angles. Currently using two camera (16mm) movies, with frame-by-frame analysis and digitization. Considerable experience with program writing.

Dr. Carol Widule

Purdue University at
West Lafayette, IN.
(317) 494-3675

Past work with Dr. John Cooper.
Currently working with 2-D cameras
only. Collecting kinematic information
for digitization from film frames.

Dr. Mary Dawson

Western Michigan University
Kalamazoo, MI.
(87) 383-1338

Using both 2 and 3-D 16 mm movie
data on motion.

Dr. Barry Bates

Biodynamics Inc.
Box 3157
Eugene, OR. 97403
(87) (503) 428-4118

Has three labs across country; Dallas
and Chapel Hill, N.C. Speciality in
software; data on sports medicine and
joint motion action with CYBEX.

Gideon Ariel

Goto Sports Research Cent.
(with Vic Braden)
2200Plano Trabuco Canyon Rd.
Trabuco Canyon Rd. CA 92678

"Sports training expert".

REFERENCES

- Kennedy, Kenneth W., (1978). Reach Capability of Men and Women: A Three Dimensional Analysis. Aerospace Medical Research Laboratory, Wright-Patterson A.F.B., Ohio.
- Lewis, James L., (1980). Computer Aided Crew Station Design for the NASA Space Shuttle. Paper presented to NATO Symposium on Anthropometry and Biomechanics. Cambridge, England.
- NASA (1978). Anthropometric Source Book; Vol. 1, Anthropometry For Designers. NASA Reference Publ. #1024. J.S.C. Houston.
- NASA (1978). Computer Aids For Operator Station Design. NASA Technical Report. J.S.C. Houston.
- Roebuck, John A., Kroemer, and Thompson, (1975). Engineering Anthropometry Methods. John Wiley and Son, N.Y.

D3
N82 23125

ANALYSIS OF I-V CHARACTERISTICS OF NEGATIVELY
BIASED PANELS IN A MAGNETO-PLASMA

Donald D. Miller, Ph.D.
Central Missouri State University
1981 NASA-ASEE Summer Faculty Fellow

Supervisor:

Andrei Konradi
Space Environment Office
Planetary and Earth Sciences Division

Abstract: Current-voltage characteristics of negatively biased panels placed in a plasma environment were analysed with respect to panel size, electron density, and superimposed magnetic field. This analysis indicates that the thickness of the surrounding sheath and its rate of growth with bias potential depends on all these parameters in a non-linear manner.

NATIONAL AERONAUTICS AND SPACE ADMINISTRATION
LYNDON B. JOHNSON SPACE CENTER
HOUSTON, TEXAS
AUGUST 13, 1981

ORIGINAL PAGE IS
OF POOR QUALITY

ANALYSIS OF I-V CHARACTERISTICS OF NEGATIVELY
BIASED PANELS IN A MAGNETO-PLASMA

Donald D. Miller, Ph.D.
Central Missouri State University
1981 NASA-ASEE Summer Faculty Fellow

Supervisor:

Andrei Konradi
Space Environment Office
Planetary and Earth Sciences Division

Abstract: Current-voltage characteristics of negatively biased panels placed in a plasma environment were analysed with respect to panel size, electron density, and superimposed magnetic field. This analysis indicates that the thickness of the surrounding sheath and its rate of growth with bias potential depends on all these parameters in a non-linear manner.

NATIONAL AERONAUTICS AND SPACE ADMINISTRATION
LYNDON B. JOHNSON SPACE CENTER
HOUSTON, TEXAS
AUGUST 13, 1981

Introduction and Statement of Problem

In order to ascertain the magnitude of the effect of power loss through the medium surrounding a large voltage-biased conducting object in Low Earth Orbit, experiments were conducted by Konradi, McIntyre and Potter in Chamber A at the Johnson Space Center.

This particular experiment involved measurements of current drain to rectangular metal panels maintained at negative bias potentials of up to 2400 volts. The ambient plasma was supplied by a Kaufman thruster using Argon gas.

These I-V data were obtained while varying the ambient plasma density (thruster parameters) and the externally applied magnetic field between runs, using three different panels.

It is desired to qualitatively codify the effects of different plasma densities and panel sizes as well as the relevance of magnetic fields on the I-V characteristics of these collectors.

Characterization of Raw Data

The three panels used as collectors were approximately .1m x 1m (Panel C), .32m x 3.16m (Panel B), and 1m x 10m (Panel A). They were suspended vertically in the center of the chamber.

The external magnetic field was supplied by coils surrounding Chamber A. Data was taken with three different values of magnetic field; ambient and with currents of 210 amp and 612 amp. This resulted in field magnitudes of .29 Gauss (small), .73 Gauss (medium), and 1.59 Gauss (large). These values were deduced from

current-field calibration experiments by A. Konradi utilizing an RF discharge technique. Using these magnitudes, the results of a magnetometer survey by J. McCoy, and the assumption that the only appreciable component of field produced by the external coils is axial, it was determined that the magnetic field is directed at angles of 27° (small field), 11° (medium field), and 5° (large field) with respect to the vertical.

Electron density determinations were made via a cylindrical Langmuir probe (suspended vertically near the center of the Chamber) for each I-V data run.

The computed electron densities for each run, indicating the attendant conditions, are given in Figure 1. A general observation is that the resulting density, for given thruster parameters, varied significantly with respect to the magnetic field present.

Additionally, instances occurred whereby spontaneous arcing or discharge limited the maximum applied bias potential. For any of the three possible magnetic fields this breakdown occurred at lower potentials for greater densities. This effect was more pronounced for the largest panel (A). This occurred as low as 500v for panel A with the large field. However it always happened for other panels and fields when at least 2400V was applied.

It was also observed that panel current was not linearly proportional to n_e and depended on bias potential and magnetic field. This facet complicated attempted comparisons of only one parameter at a time.

Density Scaling and Data Comparisons

In order to make panel, magnetic field, and bias potential comparisons it was necessary to somehow scale the data to some common electron density. From Figure 1 it can be seen that the overlapping region is about $3.5 (10^5)$ to $5(10^5) \text{ cm}^{-3}$, ergo $4.2 (10^5) \text{ cm}^{-3}$ was chosen as the reference value.

The first attempt involved a simple linear extrapolation to find a multiplicative factor to scale the panel current at each bias potential from the I-V run "nearest" in density. However, in most of the cases this resulted in values of panel current much smaller that was realized. This followed basically because this form of extrapolation assumes that the panel current goes to zero as n_e approaches zero. This is clearly not true for the range of densities exhibited by this data.

The second attempt involved examining the panel current at bias potentials sufficiently low so that non-linearities could be avoided. Since the average plasma potential was about -2V, bias potential of this value was chosen. The panel currents at negative 2V bias for each run are plotted vs. n_e in Figs. 2.1, 2.2, and 2.3 for small, medium and large fields respectively. Superimposed on these figures are the linear least square fits. At this point an attempt is also made to account for the non-uniformity of the density over the extent of the panels. Scaling according to a Gaussian Distribution over the chamber, the ratio of average densities of the panels is; k_C
 $: k_B : k_A = 1 : .94 : .86$. These straight line functions were then evaluated at $4.2 (10^5)/k_i \text{ cm}^{-3}$ ($i = A, B, \text{ or } C$), yielding the

scaled panel currents at negative 2V bias. These intercepts are indicated by the arrows on Figs. 2.1, 2.2, and 2.3. The ratio of this current to the actual panel current (at -2V bias) of the run "nearest" $4.2 (10^5) \text{ cm}^{-3}$ yielded the scale factor g . Such a scale factor was obtained for each panel-field combination and are listed in Table 1.

Table 1 Scale factors for each panel-field combination: Panels A, B, and C and small (S), medium (M) and large (L) fields.

Panel	Field	Scale Factor g
A	L	1.20
B	L	1.28
C	L	.97
A	M	1.29
B	M	1.14
C	M	1.09
A	S	1.00
B	S	1.00
C	S	1.00

The adjusted current for a given panel-field run is then obtained by multiplying the measured current of the "nearest" run by the corresponding scale factor. Plots of the adjusted current vs. bias potential for each panel field combination are given by Fig. 3a ($\ln I$ vs V), Fig. 3b (I vs. V), and Fig. 3c ($\ln I$ vs. $\ln V$).

In order to assess the relative rate of increase of the curves, the ratio of the adjusted current to its value at

negative 1V bias (Reference current) was computed for each combination. This ratio is plotted vs. bias potential for each panel on Figs. 4.1, 4.2, and 4.3 for small, medium, and large fields respectively.

In order to more readily perceive the effect of magnetic field on a given panel, this ratio (adjusted current/reference current) is plotted vs. bias potential for each field on Figs. 5.1, 5.2 and 5.3 for panel C, panel B, and Panel A respectively.

The computations required to generate the adjusted current and the ratios of adjusted current to reference current was facilitated by a FORTRAN program FILENT, a listing of which is provided in the appendix.

A general characterization being that the ratio increases more slowly for larger fields and larger panels, but that the reference current is larger for these cases, resulting in larger currents for larger fields and larger panels.

Further comparisons of the I-V run characteristics are made by examining the ratios of adjusted currents between panels for the same field and those values from the same panel for different fields. The computations required to generate these ratios at each bias potential for each run was facilitated by the FORTRAN program IVDMAS (I-V Data Massage), a listing of which is given in the Appendix.

Plots of the ratios of adjusted currents between panels vs. bias potential are given in Figs. 6.1, 6.2, and 6.3 for small, medium, and large fields respectively. In all cases, the ratios decrease with increasing bias. However this follows from the

fact that the current from the smaller panels increases faster with increasing bias.

Plots of the ratios of the adjusted currents between different fields vs. bias potential are given in Figs. 7.1, 7.2, and 7.3 for panel C, panel B, and panel A respectively. It can be noted that for panel A, this ratio increases sharply as the breakdown or arcing condition is approached. This is consistent with panel A current increasing at a greater rate.

Interpretation and Discussion

One possible additional phenomenon which is not capable of direct observation in this experiment is that of secondary electron emission. Those electrons which escaped through the sheath would simulate collected ions. Subsequent experiments (as yet not analyzed) observing identical gold and stainless steel collectors should provide considerable insight into this aspect.

The fact that the angle between the magnetic field and the axis of the panels varied with the magnitude of the field presents an additional complication which cannot be clarified from the data. It is to be expected that this orientation would be relevant in the sheath formation for these asymmetrical collectors.

Uncertainty also exists in the interpretation of the orbit-limited "regime" of Langmuir Probe theory in a magnetosheath. Theoretical investigations were undertaken by Szuszczewicz and Takacs¹ in order to account for Langmuir Probe data from a spinning scientific rocket payload. They observed that the electron density (through its control of sheath size) is

important in determining the effect of magnetic fields on electron-current collection. They chose the ratio of sheath thickness to the characteristic Debye length as a measure of the relevance of magnetic effects. They designated three characteristic regions: strong-magnetosheath (ratio $\ll 1$), transition-magnetosheath (ratio order of 1) and weak magnetosheath (ratio $\gg 1$). Because the sheath expands and contracts as plasma densities fall and rise, the ratio of gyroradius-to-sheath thickness varies and modifies the probe response in a non-linear way. They conclude that weak-magnetosheath conditions must be guaranteed before assuming $I_e = (\text{constant}) * n_e$ at constant bias. By monitoring the angular dependence of the probe response with the field, they observed a sharp decrease in the current at a fixed bias as the angle between the axis of the probe and the field decreased, causing a density dependent modulation. Quoting from Szuszczewicz and Takacs¹:

"We note the modulation increases with decreasing n_e , a parametric dependence not shown in current theories involving thick sheath conditions."

That reasonable levels of measurement integrity can still be maintained in weak magnetoplasmas has been indicated by Miller² and Laframboise and Rubinstein³. Their works indicate that accuracy is improved in cylindrical probe measurements when the angle between the probe and the magnetic field is large ($\geq 60^\circ$).

The analysis of the data from these rectangular plates seems to imply that sheath thickness variation and its

effect on I-V characteristics with respect to bias potential and density variations are present here in a manner analogous to that encountered by Szuszczewicz and Takacs¹. The uncertainty with the relevance of the angle between the axis of symmetry of the collector and the magnetic field could be circumvented by using spheres. Aspects concerning the dependence of sheath growth on collector shape could be assessed by using other shapes (e.g., cylinders). Both of these aspects should be clarified when analysis of later experiments which did use multisized spheres and cylinders of different materials are concluded.

The qualitative trends exhibited by the scaled I-V characteristics presented in this report should provide references or guidelines for evaluation of the validity of computer-aided simulations of sheath structure and growth being carried out by Parker⁴.

Acknowledgements

The author wishes to thank the JSC and contractor personnel of the Space Environment Office, Division of Planetary and Earth Sciences, particularly Drs. A. Konradi, A. Potter, E. Reyna and Mrs. Mary Petrovics for their cooperative attitude and his acceptance as a colleague while participating as a NASA/ASEE Summer Faculty Fellow.

References

1. Szuszczweicz, E.P. and Takacs, P.Z., "Magnetosheath Effects of Cylindrical Langmuir Probes". Phys. Fluids 22, 2424 (1979).
2. Miller, N.J., "Some Implications of Satellite Spin Effects in Cylindrical Probe Measurements", J. Geophys. Res., 77, 2851 (1972).
3. Laframboise, J. G. and Rubinstein, J., "Theory of a Cylindrical Probe in a Collisionless Magnetoplasma", Phys. FLuids, 19, 1900 (1976).
4. Parker, L. W., "Plasmasheath-Photosheath Theory for Large High-Voltage Space Structures", Space Systems and Their Interactions with Earth's Space Environment, ed. by Garrett and Pike, AIAA New York, NY 1980.

APPENDIX

Figures:

1. Indicated densities for each I-V run, grouped according to panel size (A-large, B-medium, and C-small) and magnetic field.
- 2.1 Current at 2V bias vs. density for small field with linear least square fit.
- 2.2 Current at 2V bias vs. density for medium field with linear least square fit.
- 2.3 Current at 2V bias vs. density for large field with linear least square fit.
- 3a. Adjusted current vs. bias potential for all panels and fields ($\ln(I)$ vs. V).
- 3b. Adjusted current vs. bias potential for all panels and fields (I vs. V).
- 3c. Adjusted current vs. bias potential for all panels and fields ($\ln(I)$ vs. $\ln(V)$).
- 4.1 Ratio of adjusted current to reference current at small field for all panels.
- 4.2 Ratio of adjusted current to reference current at medium field for all panels.
- 4.3 Ratio of adjusted current to reference current at large field for all panels.
- 5.1 Ratio of adjusted current to reference current for panel C at all fields.
- 5.2 Ratio of adjusted current to reference current for panel B at all fields.
- 5.3 Ratio of adjusted current to reference current for panel A at all fields.
- 6.1 Ratios of adjusted currents between panels vs. bias potential for small field.
- 6.2 Ratios of adjusted currents between panels vs. bias potential for medium field.
- 6.3 Ratios of adjusted currents between panels vs. bias potential for large field.

7.1 Ratios of adjusted currents from panel C vs. bias potential for all fields.

7.2 Ratios of adjusted currents from panel B vs. bias potential for all fields.

7.3 Ratios of adjusted currents from panel A vs. bias potential for all fields.

Program FILENT, listing and sample output.

Program IVDMAS, listing and sample output.

ORIGINAL PAGE IS
OF POOR QUALITY

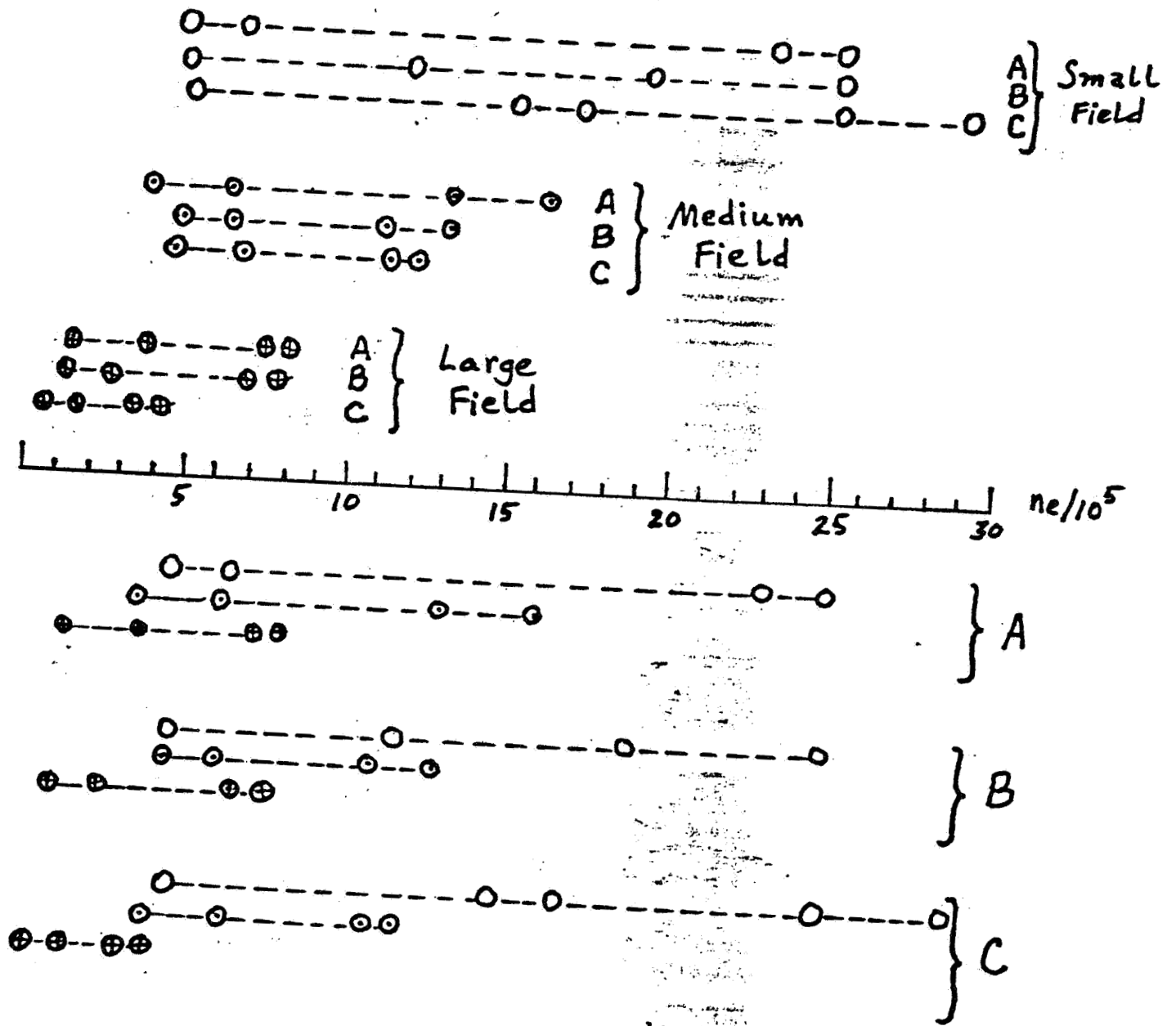


Fig. 1 Indicated densities for each I-V run, grouped according to panel size (A-large, B-medium, and C-small) and magnetic field.

ORIGINAL PAGE IS
OF POOR QUALITY.

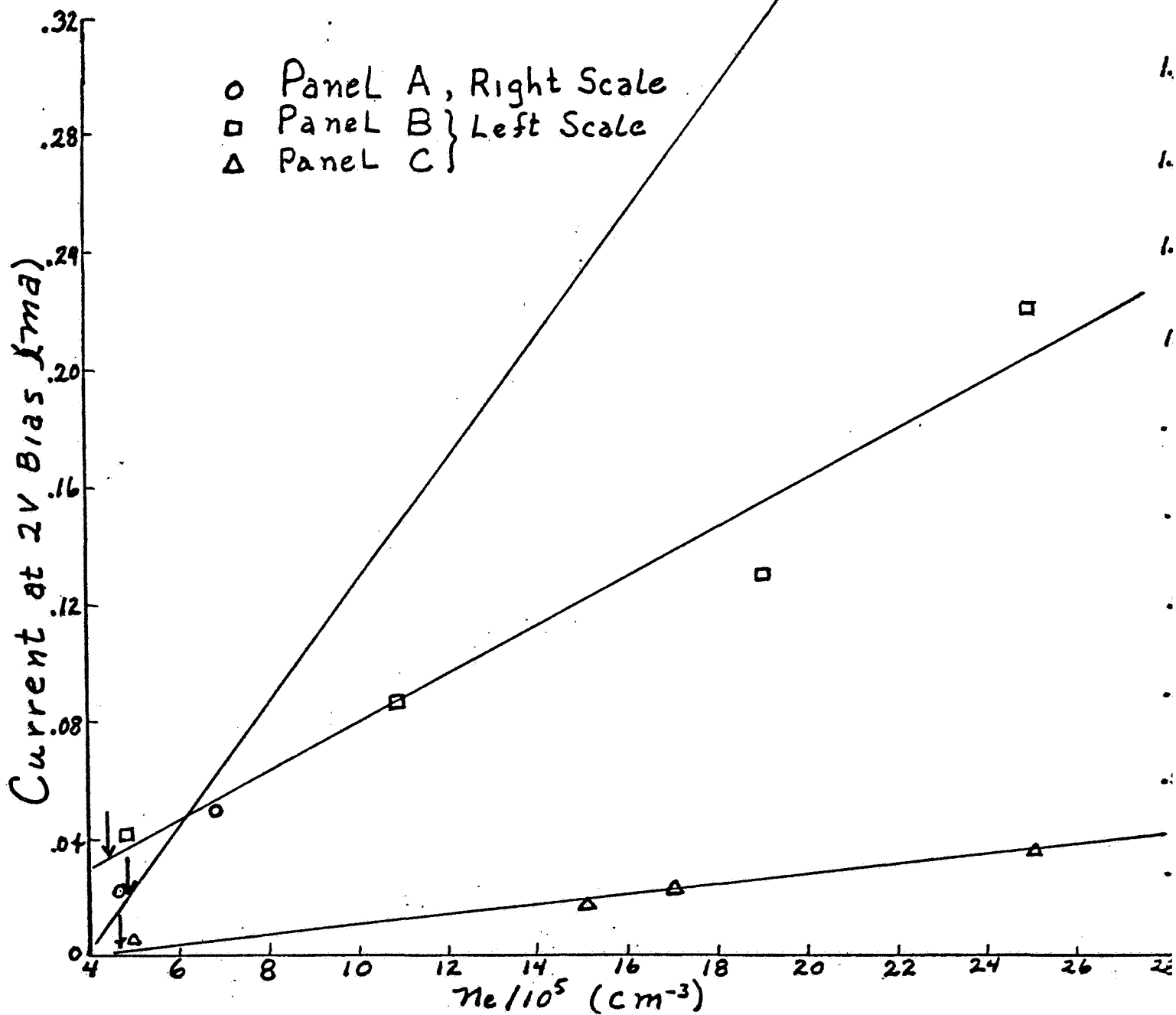


Fig. 2.1 Current at 2V bias vs. density for small field with linear least square fit.

ORIGINAL PAGE IS
OF POOR QUALITY

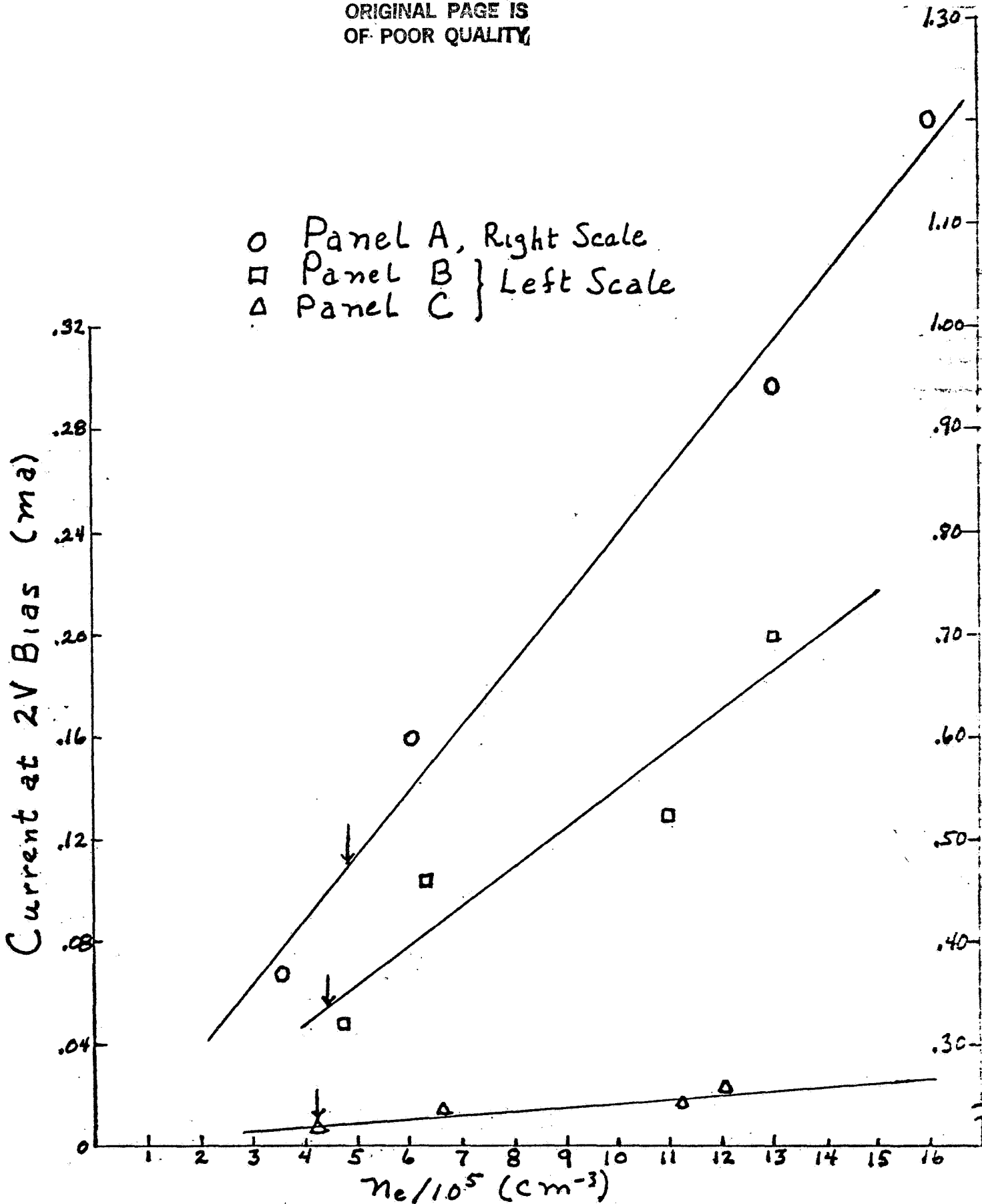


Fig. 2.2 Current at 2V bias vs. density for medium field with linear least square fit.

ORIGINAL PAGE IS
OF POOR QUALITY

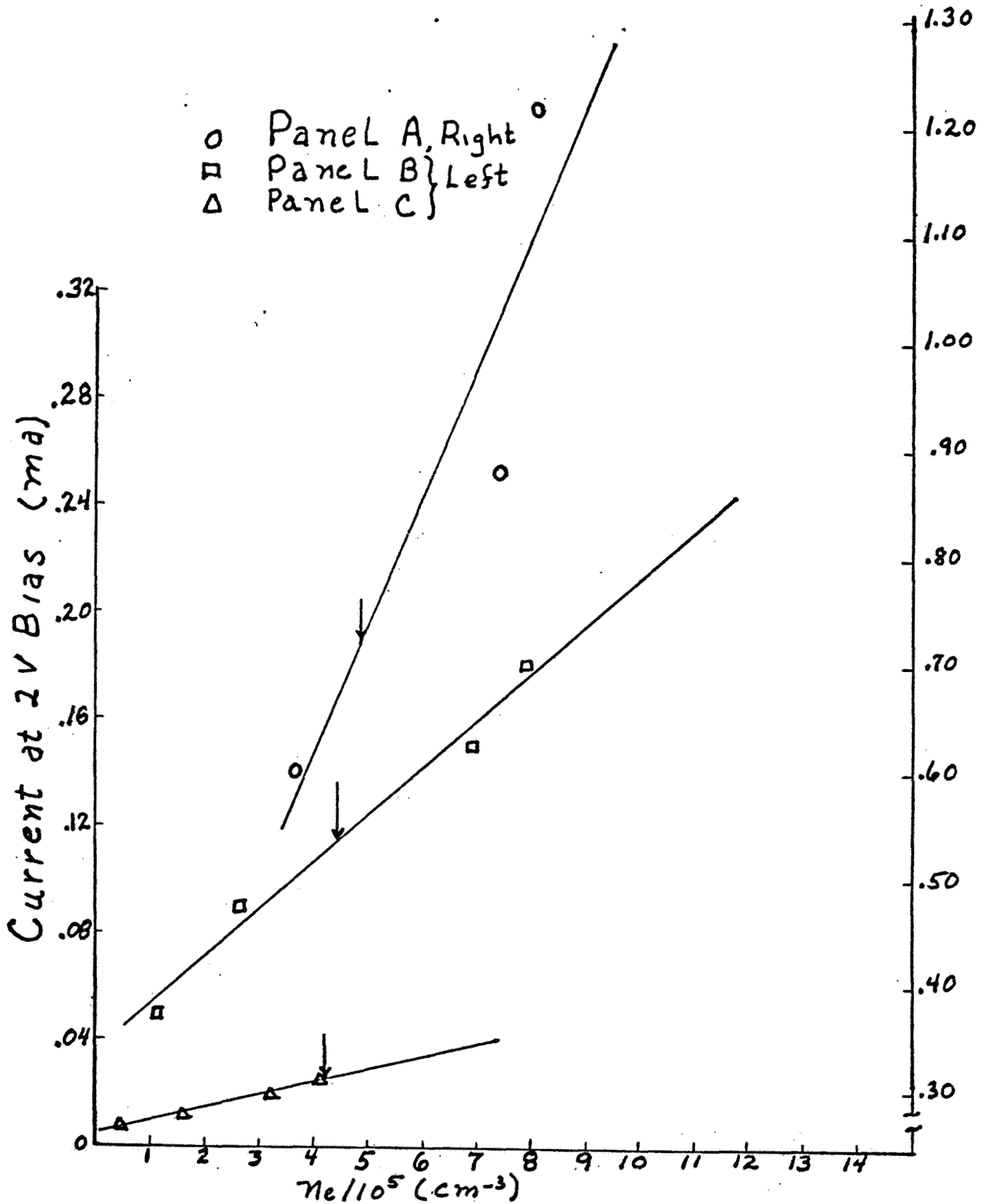


Fig. 2.3 Current at 2V bias vs. density for large field with linear least square fit.

ORIGINAL PAGE IS
OF POOR QUALITY

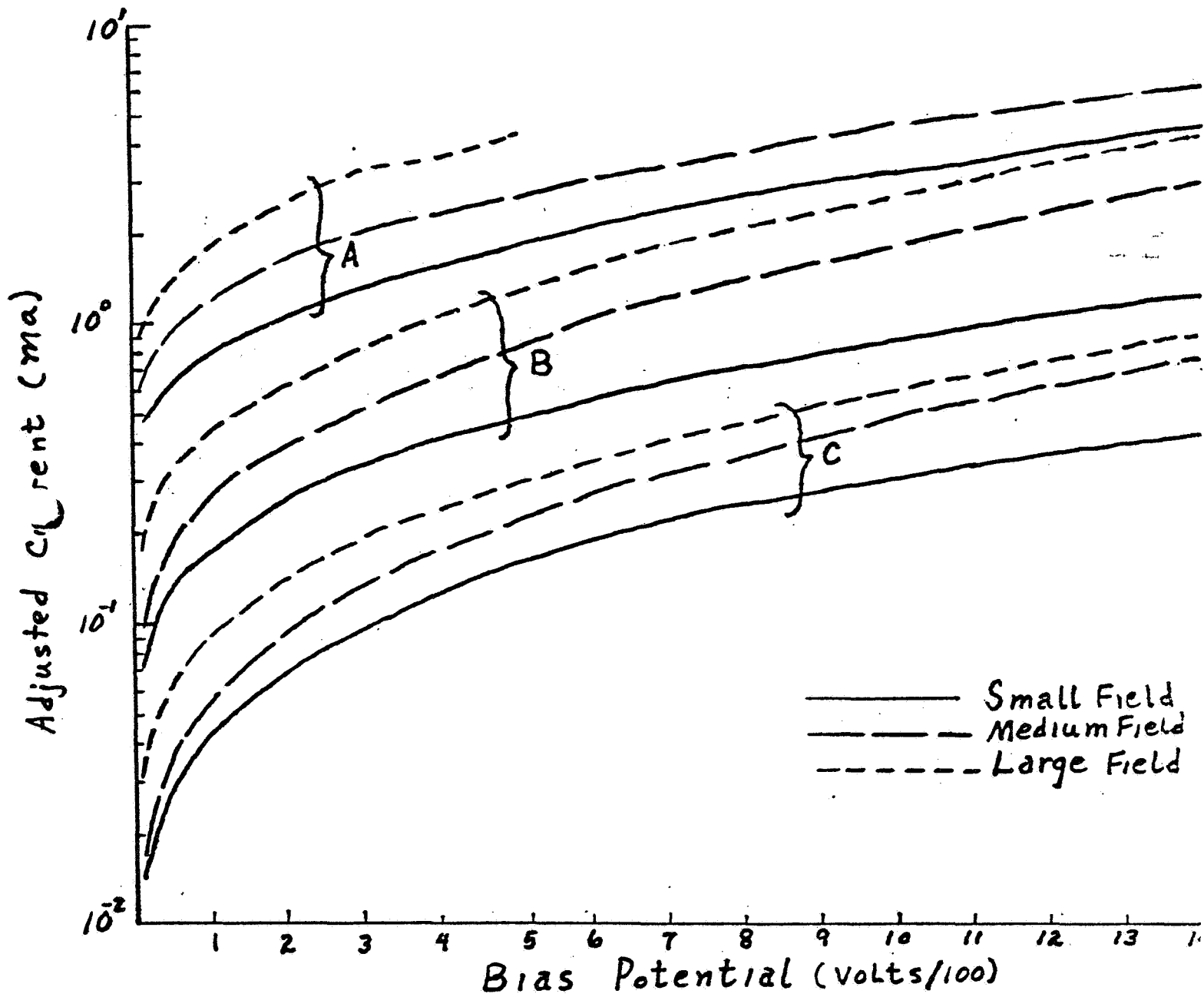


Fig. 3a. Adjusted current vs. bias potential for all panels and fields.

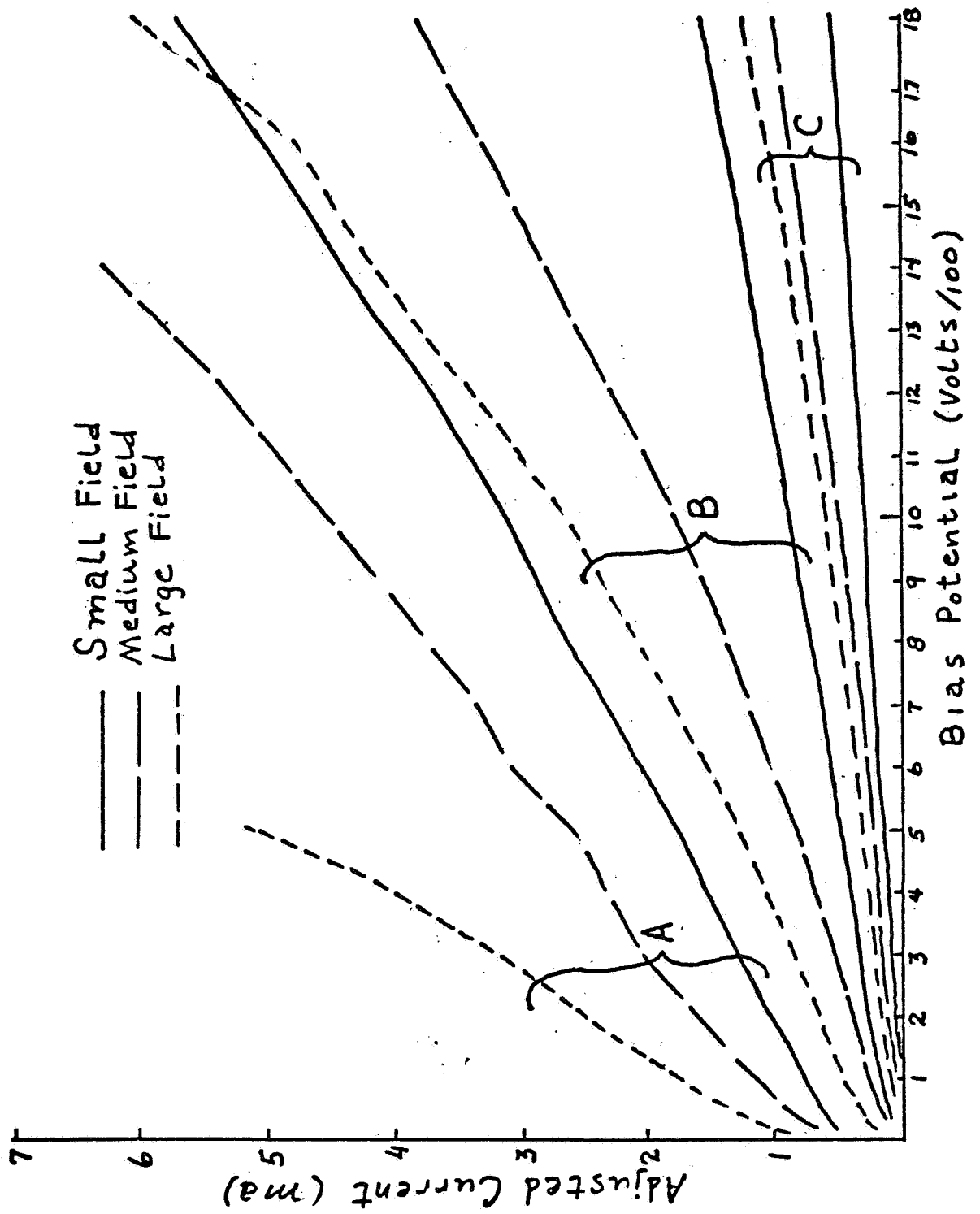


Fig. 3b. Adjusted current vs. bias potential for all panels and fields.

ORIGINAL PAGE IS
OF POOR QUALITY

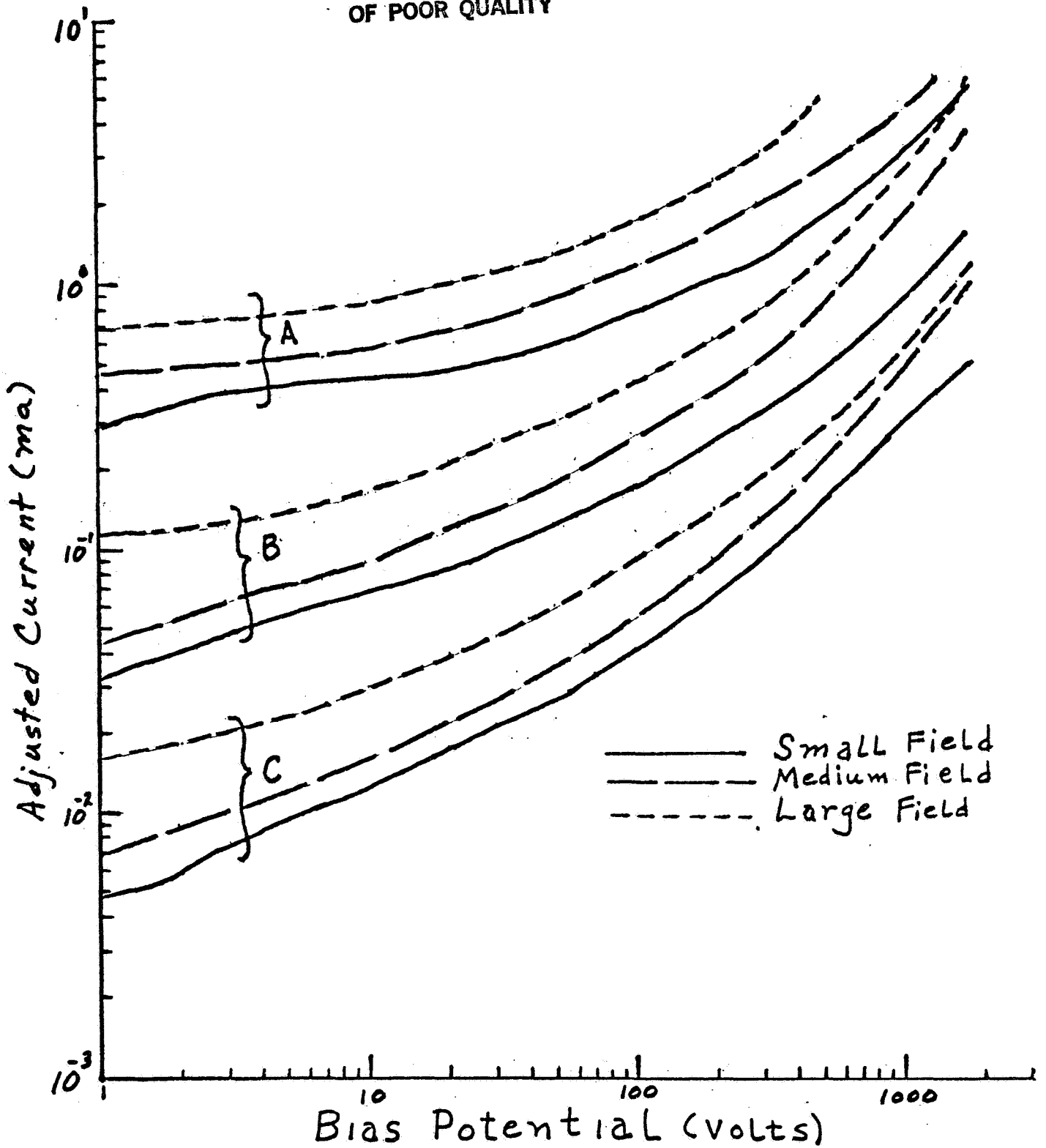


Fig. 3c. Adjusted current vs. bias potential for all panels and fields.

ORIGINAL PAGE IS
OF POOR QUALITY

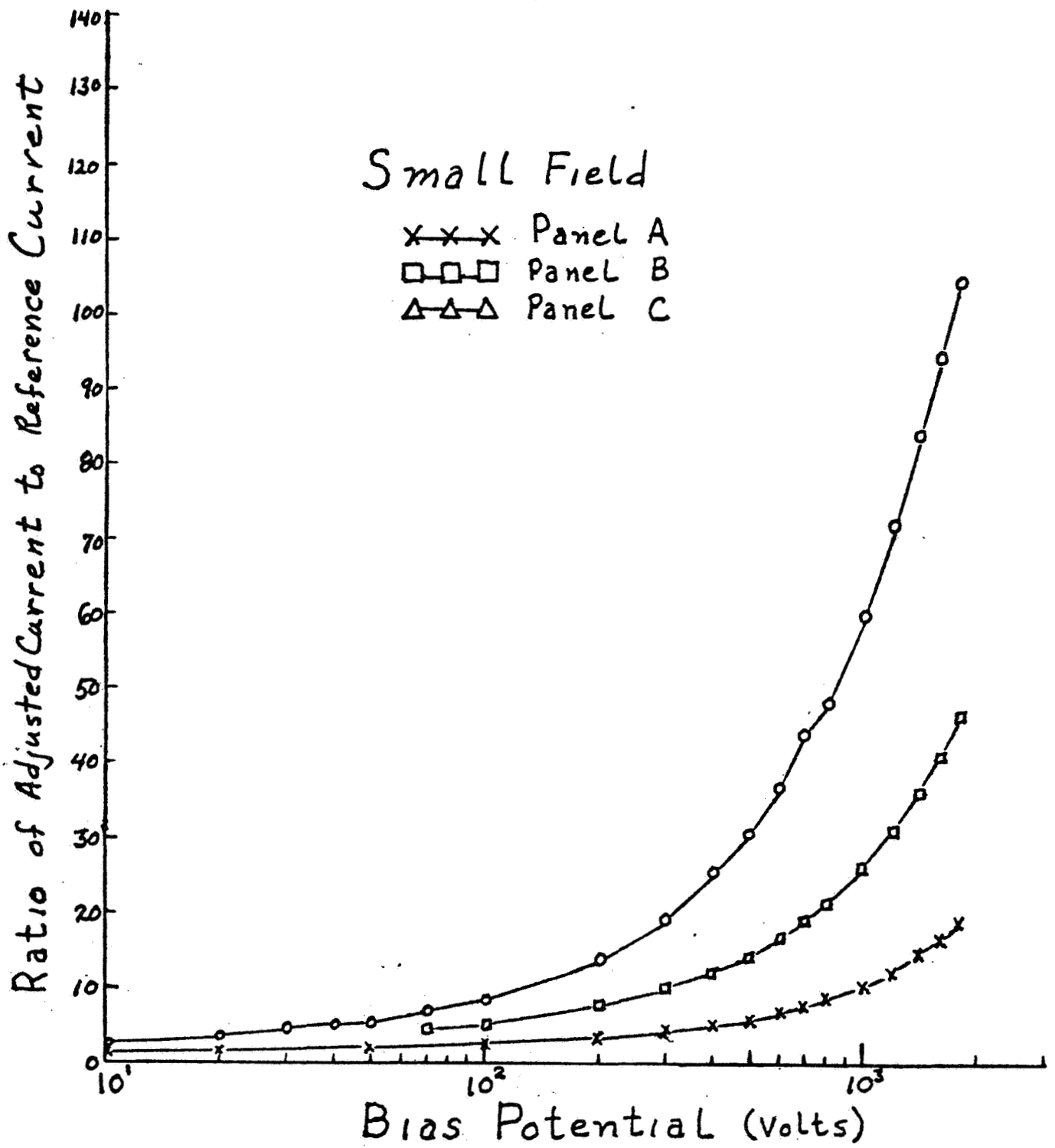


Fig. 4.1 Ratio of adjusted current to reference current at small field for all panels.

ORIGINAL PAGE IS
OF POOR QUALITY

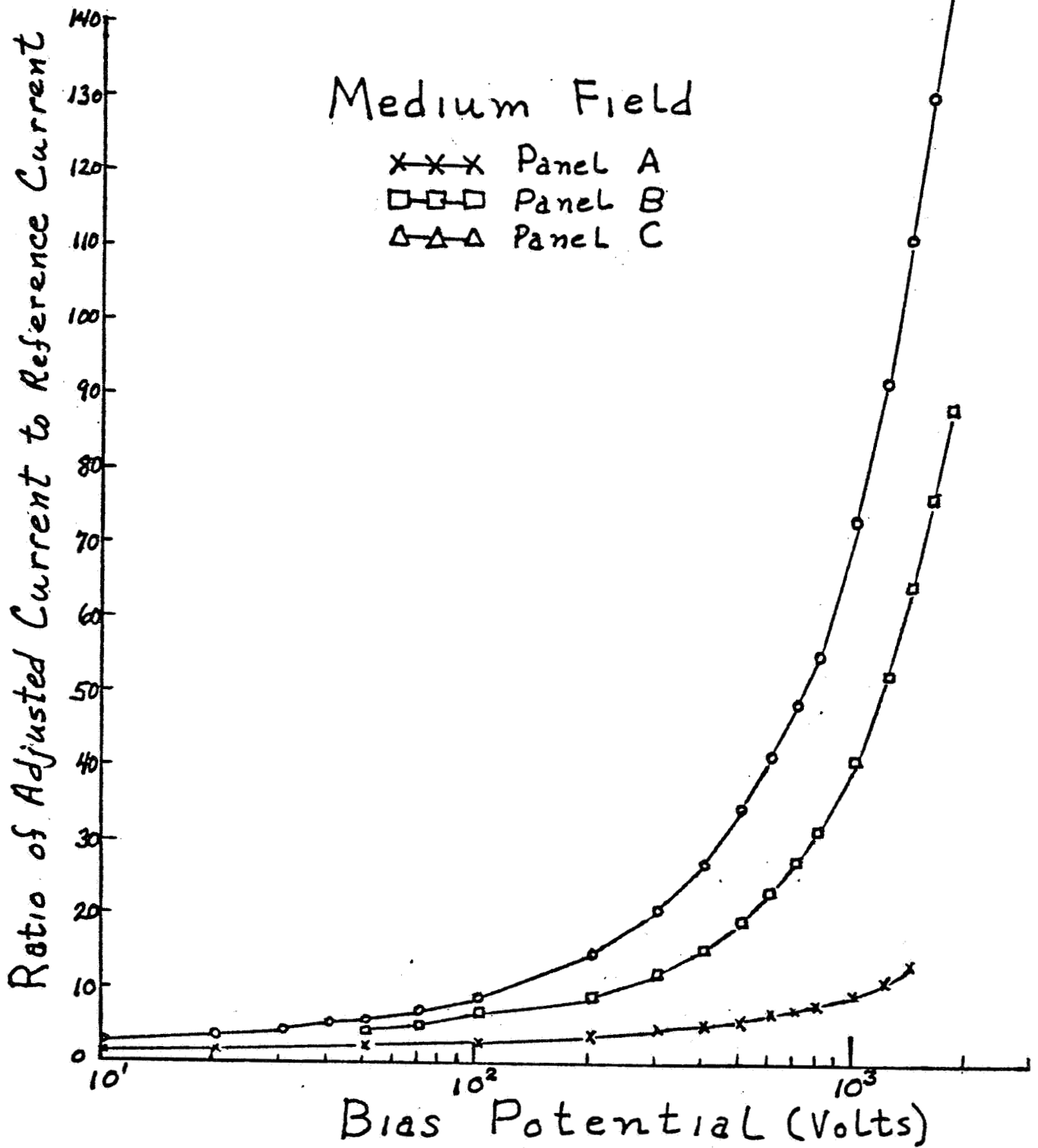


Fig. 4.2 Ratio of adjusted current to reference current at medium field for all panels.

ORIGINAL PAGE IS
OF POOR QUALITY.

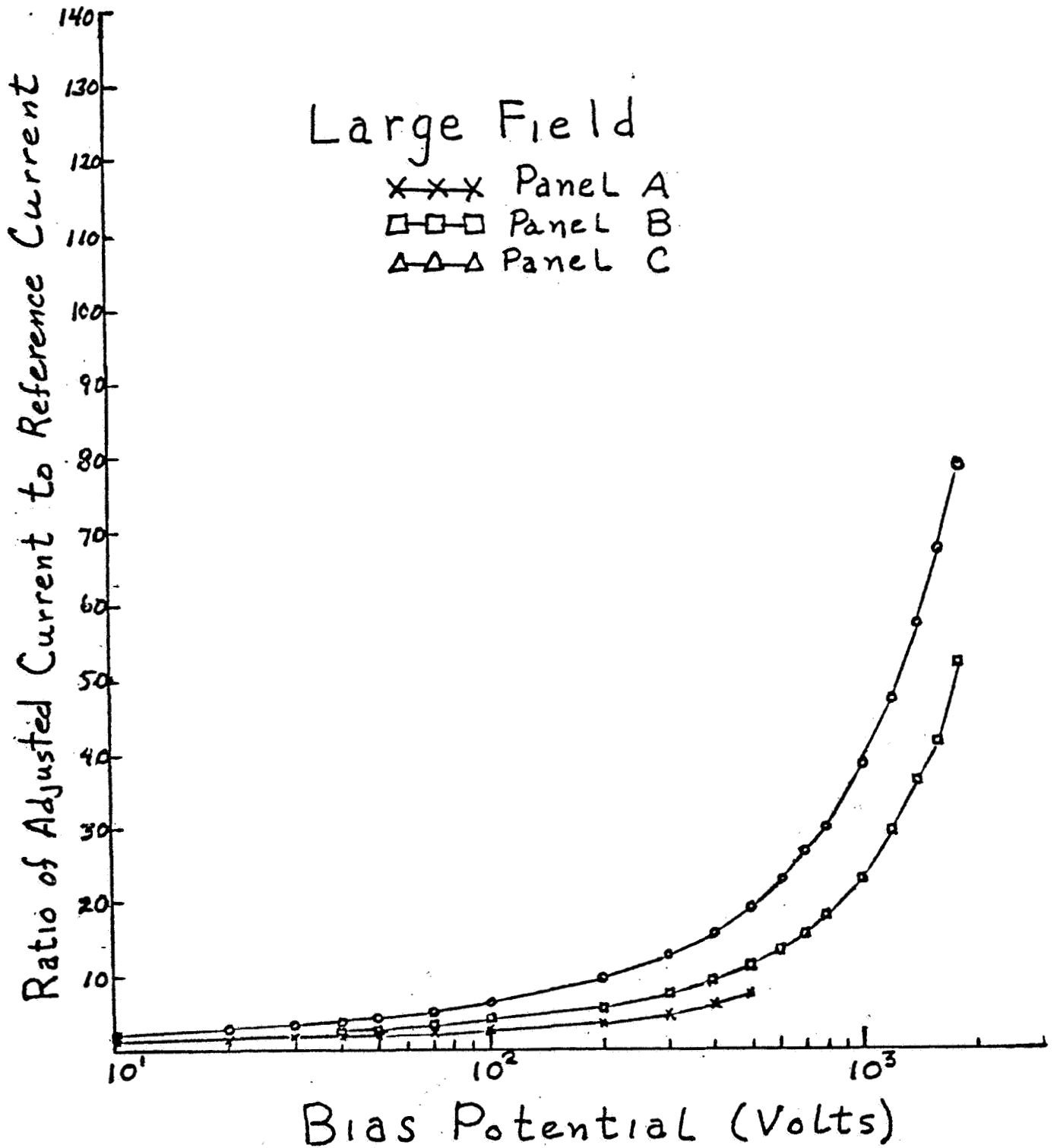


Fig. 4.3 Ratio of adjusted current to reference current at large field for all panels.

ORIGINAL PAGE IS
OF POOR QUALITY

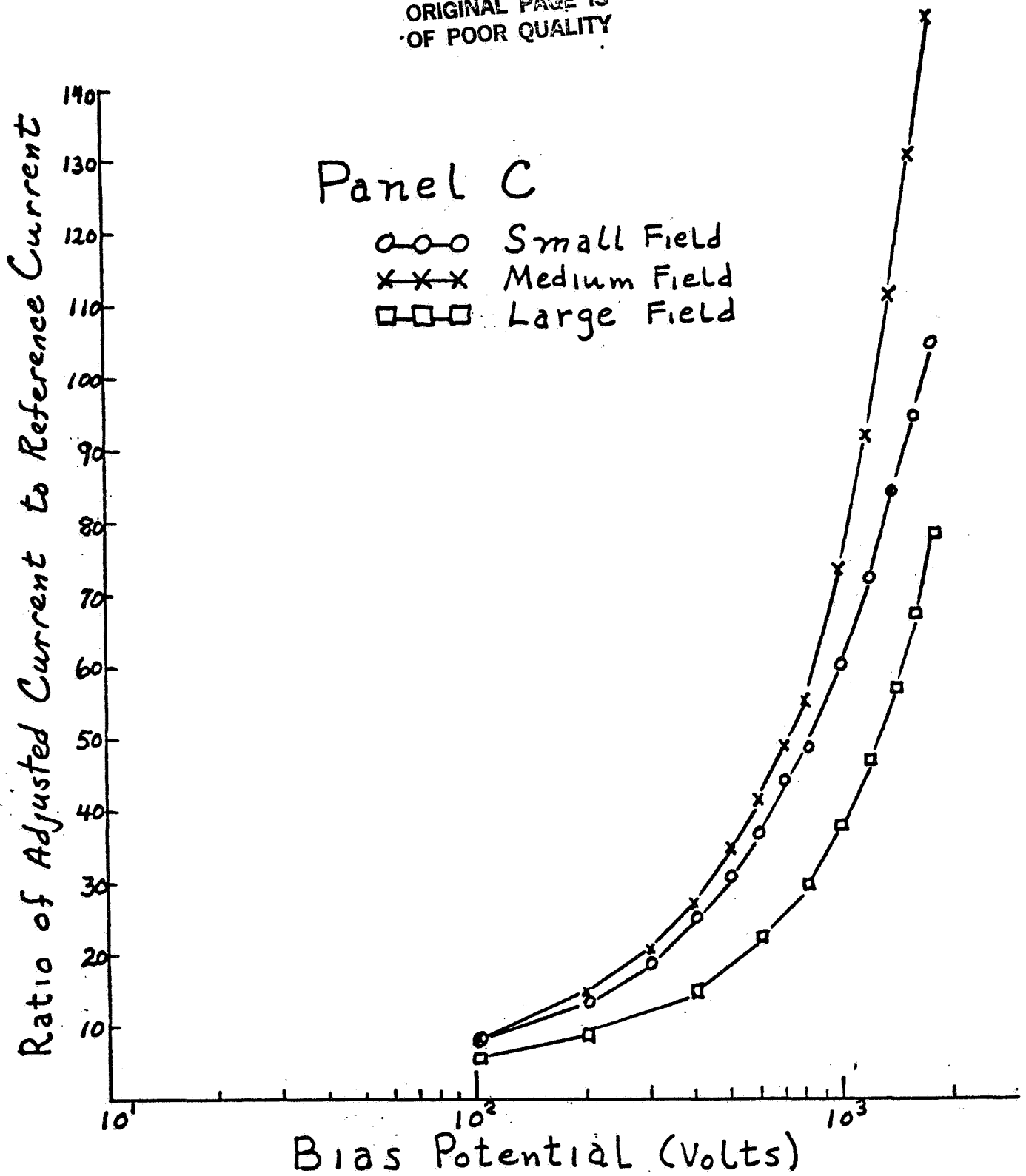


Fig. 5.1 Ratio of adjusted current to reference current for panel C at all fields.

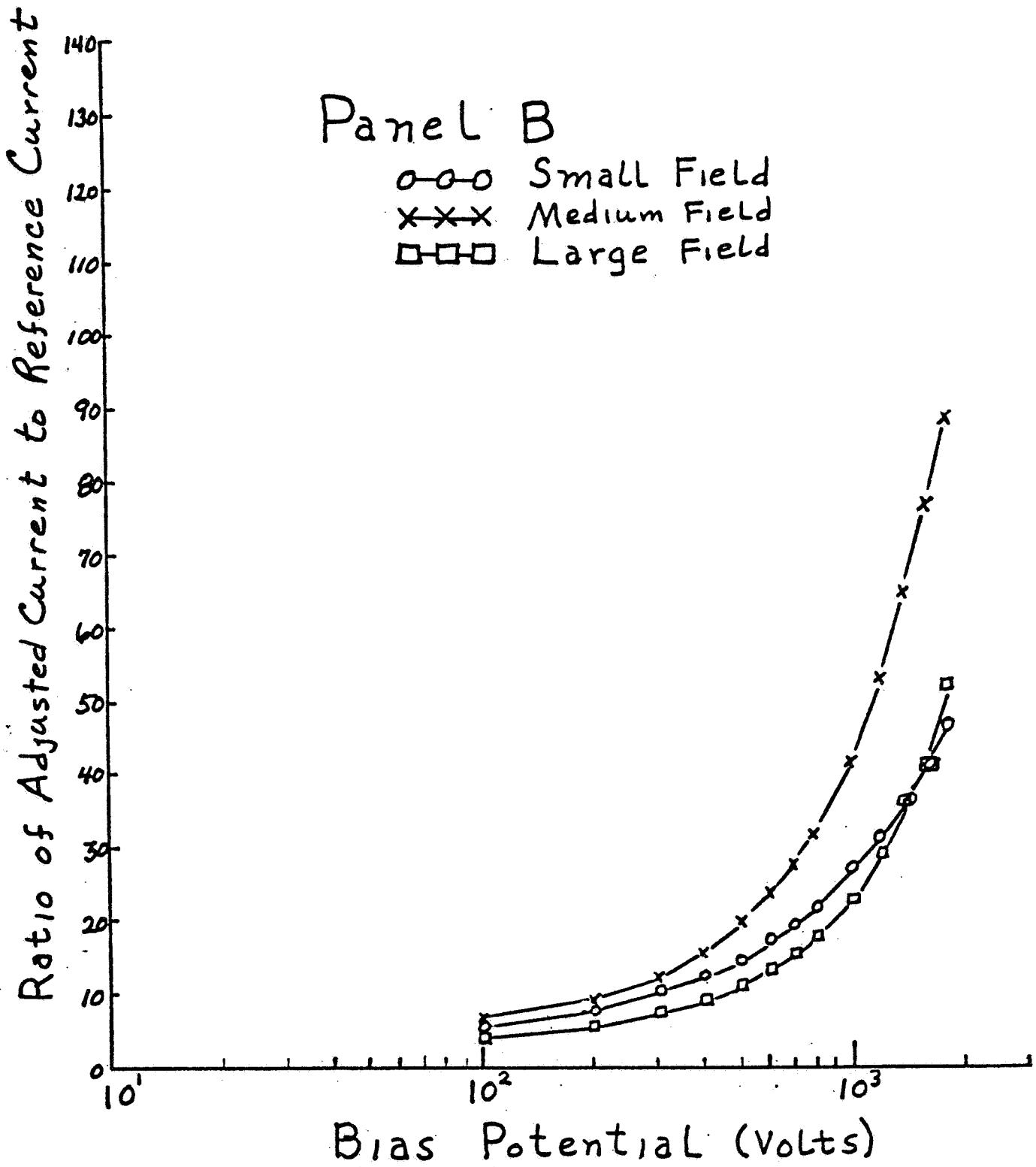


Fig. 5.2 Ratio of adjusted current to reference current for panel B at all fields.

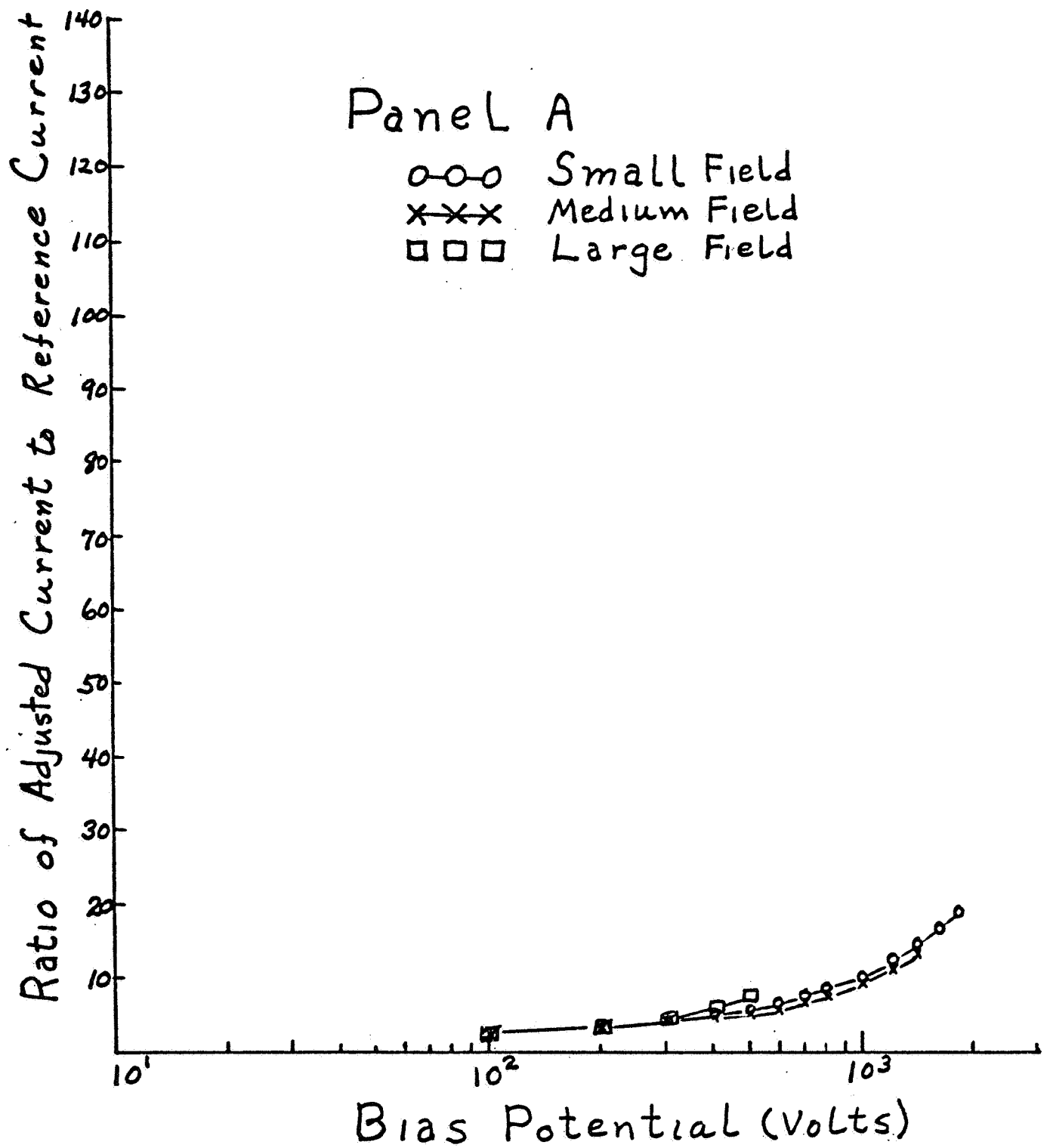


Fig. 5.3 Ratio of adjusted current to reference current for panel A at all fields.

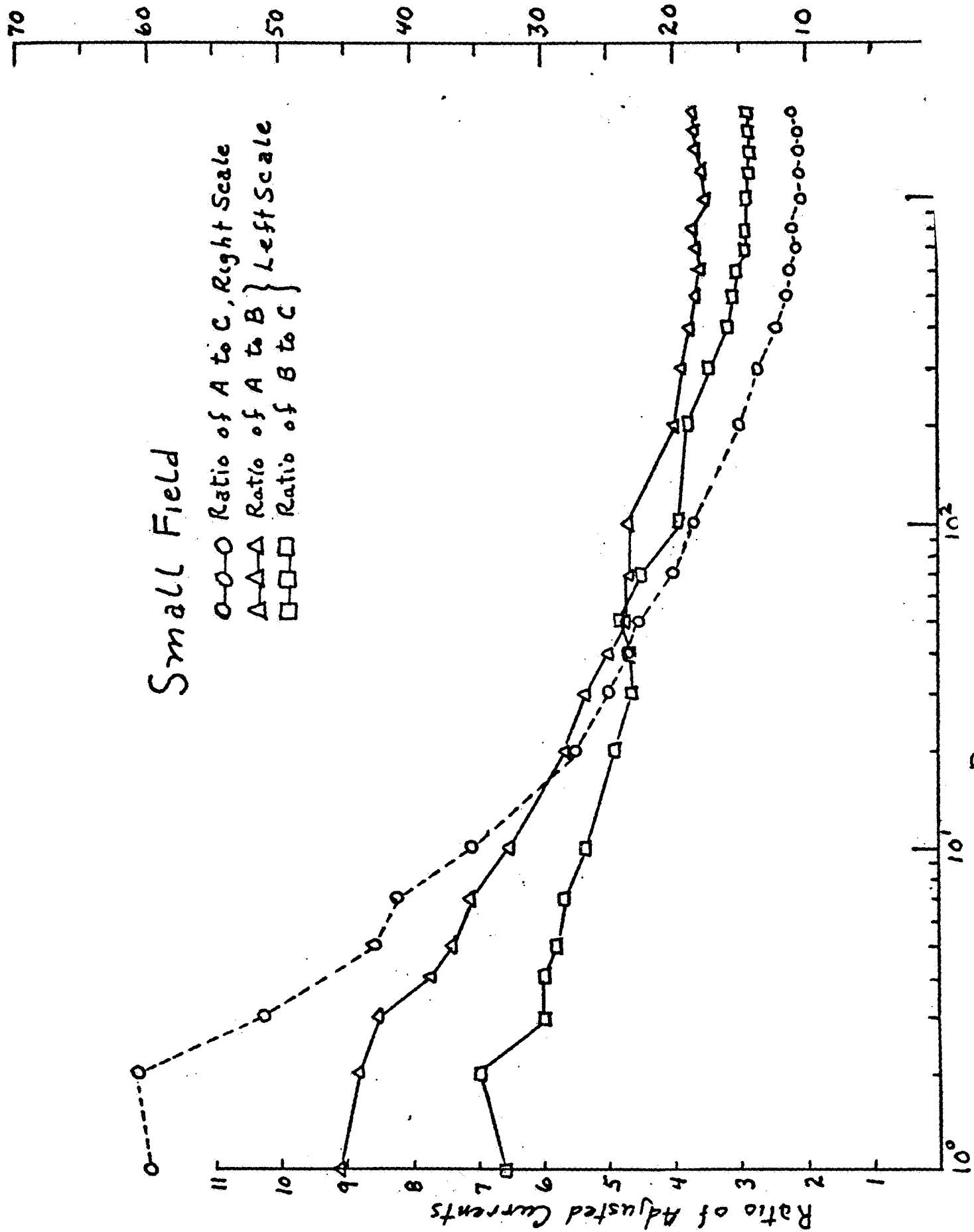


Fig. 6.1 Ratios of adjusted currents between panels vs bias potential for small field

ORIGINAL PAGE IS
OF POOR QUALITY

Medium Field

- Ratio of A to C, Right Scale
- △-△-△ Ratio of A to B } Left Scale
- Ratio of B to C }

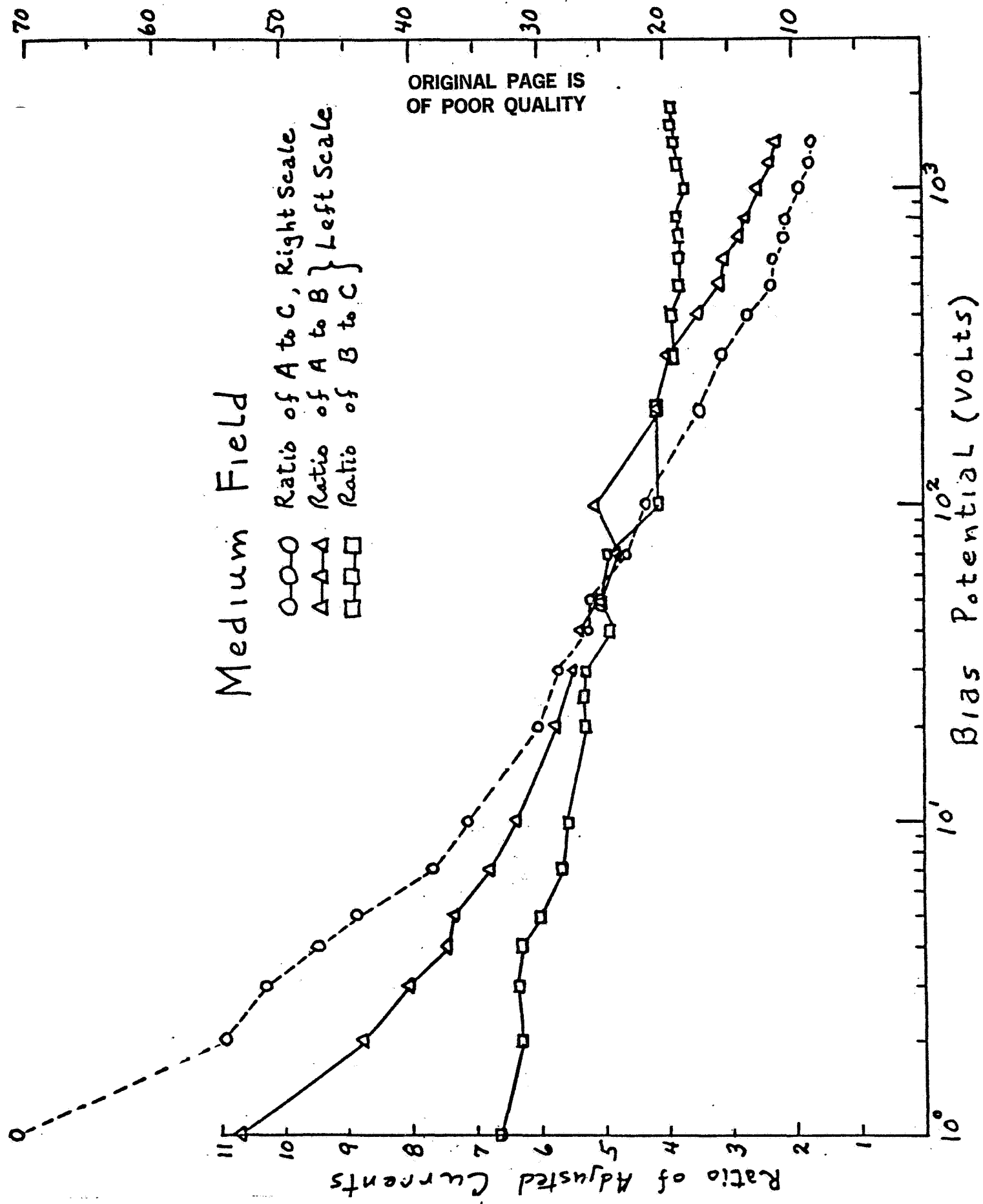


Fig. 6.2 Ratios of adjusted currents between panels vs. bias potential for medium field.

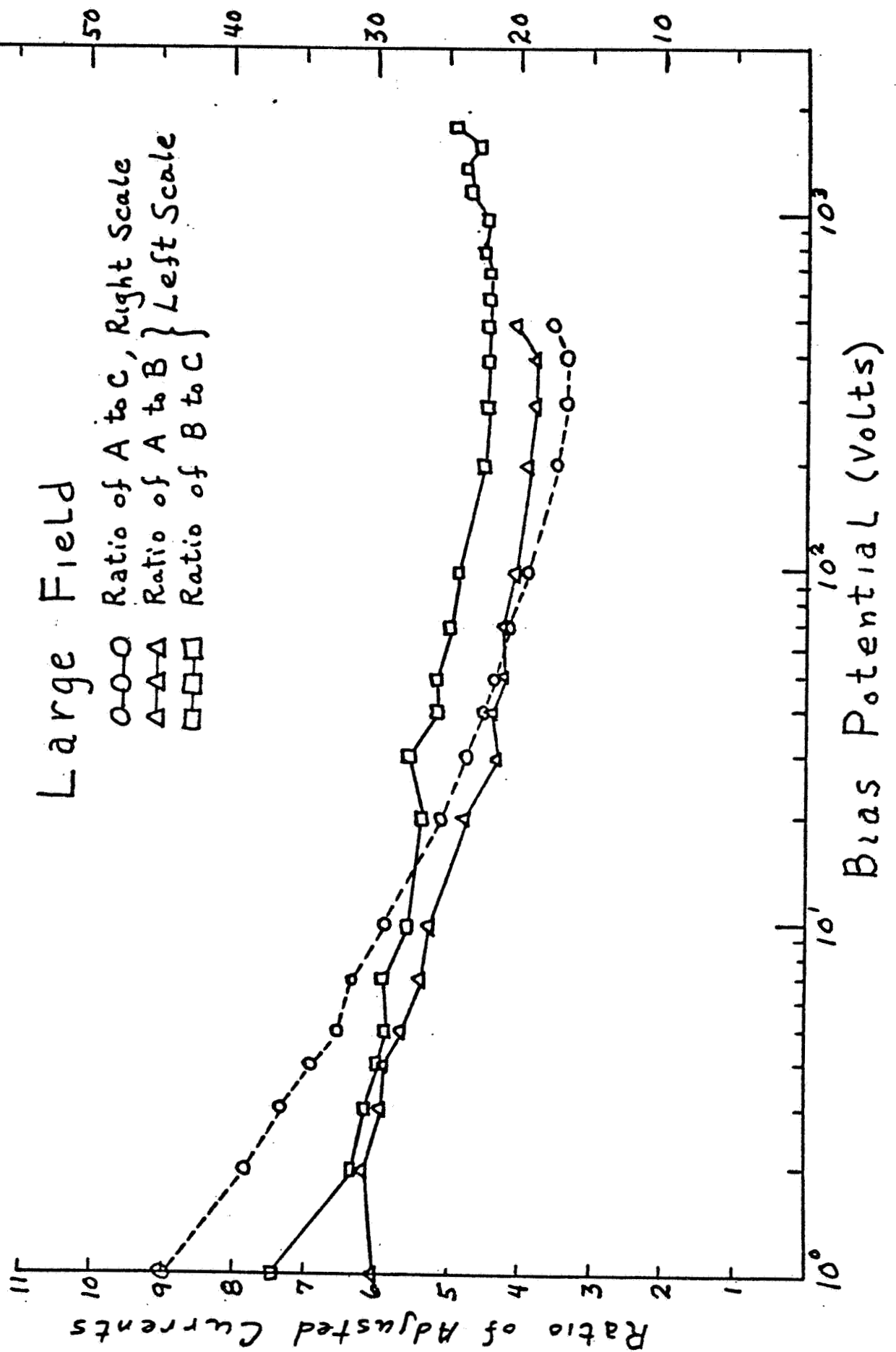


Fig. 6.3 Ratios of adjusted currents between panels vs. bias potential for large field.

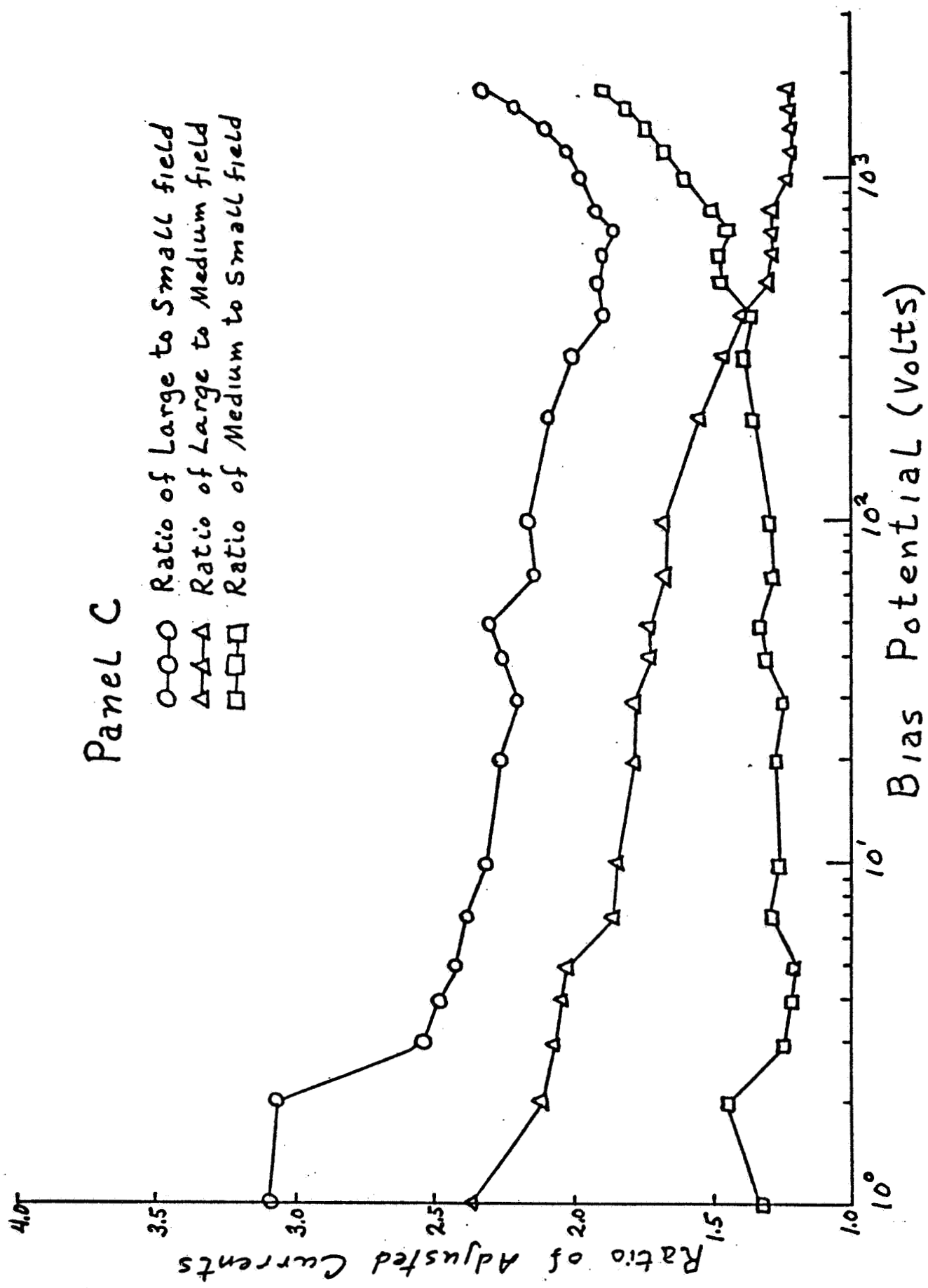


Fig. 7.1 Ratios of adjusted currents from panel C vs. bias potential for all fields.

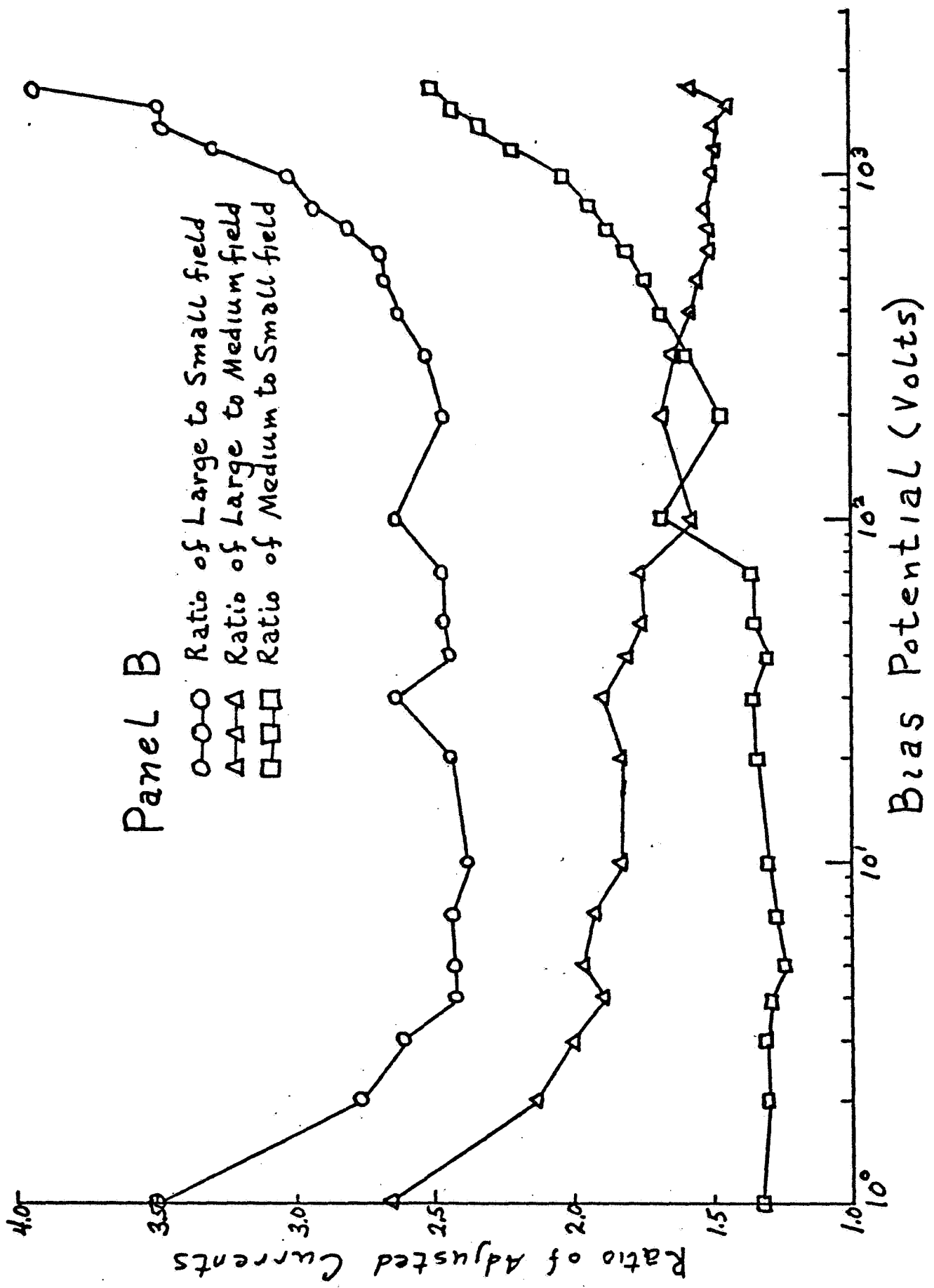
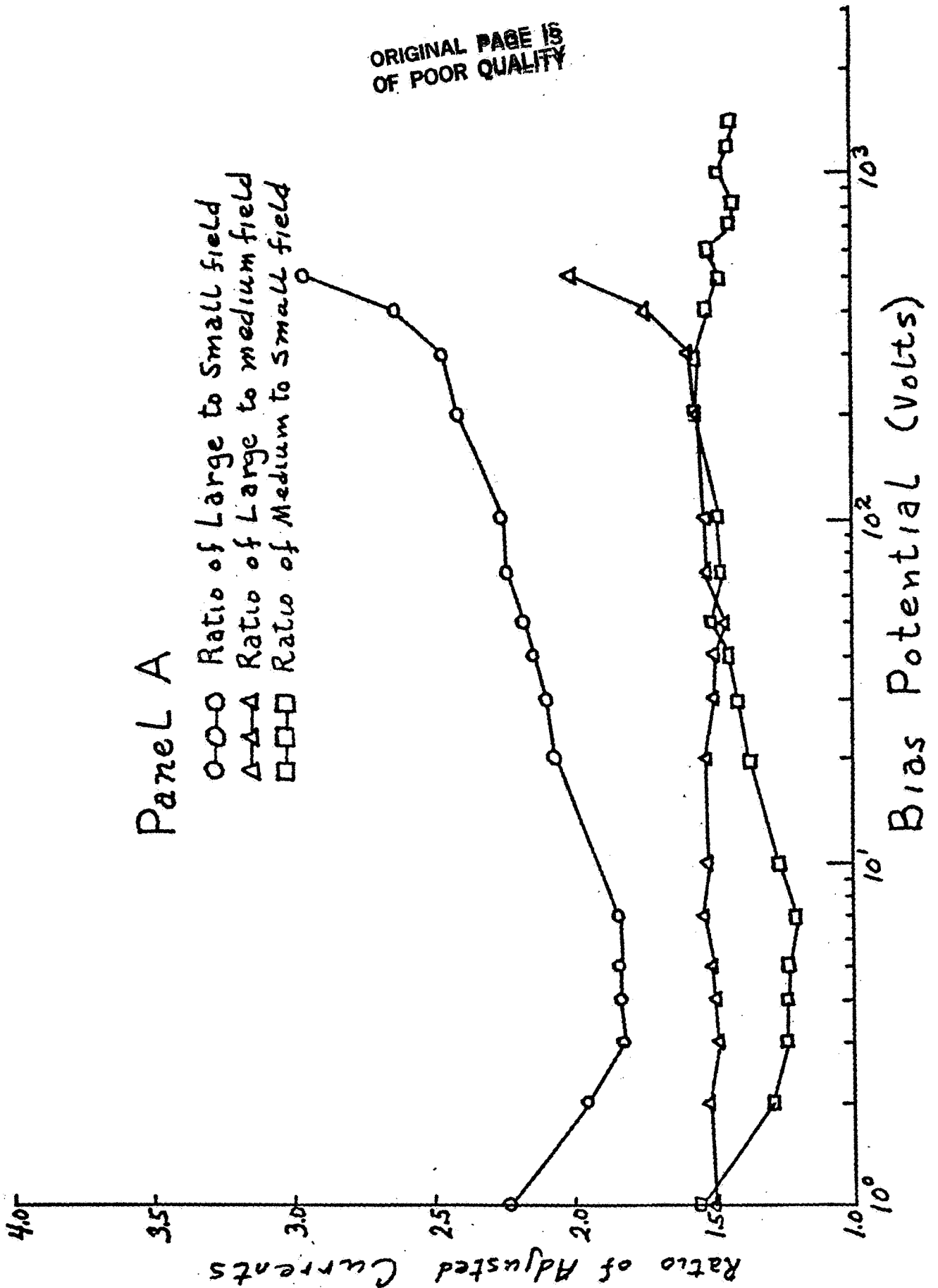


Fig. 7.2 Ratios of adjusted currents from panel B vs. bias potential for all fields.

ORIGINAL PAGE IS
OF POOR QUALITY



g. 7.3 Ratios of adjusted currents from panel A vs. bias potential

ORIGINAL PAGE IS
OF POOR QUALITY

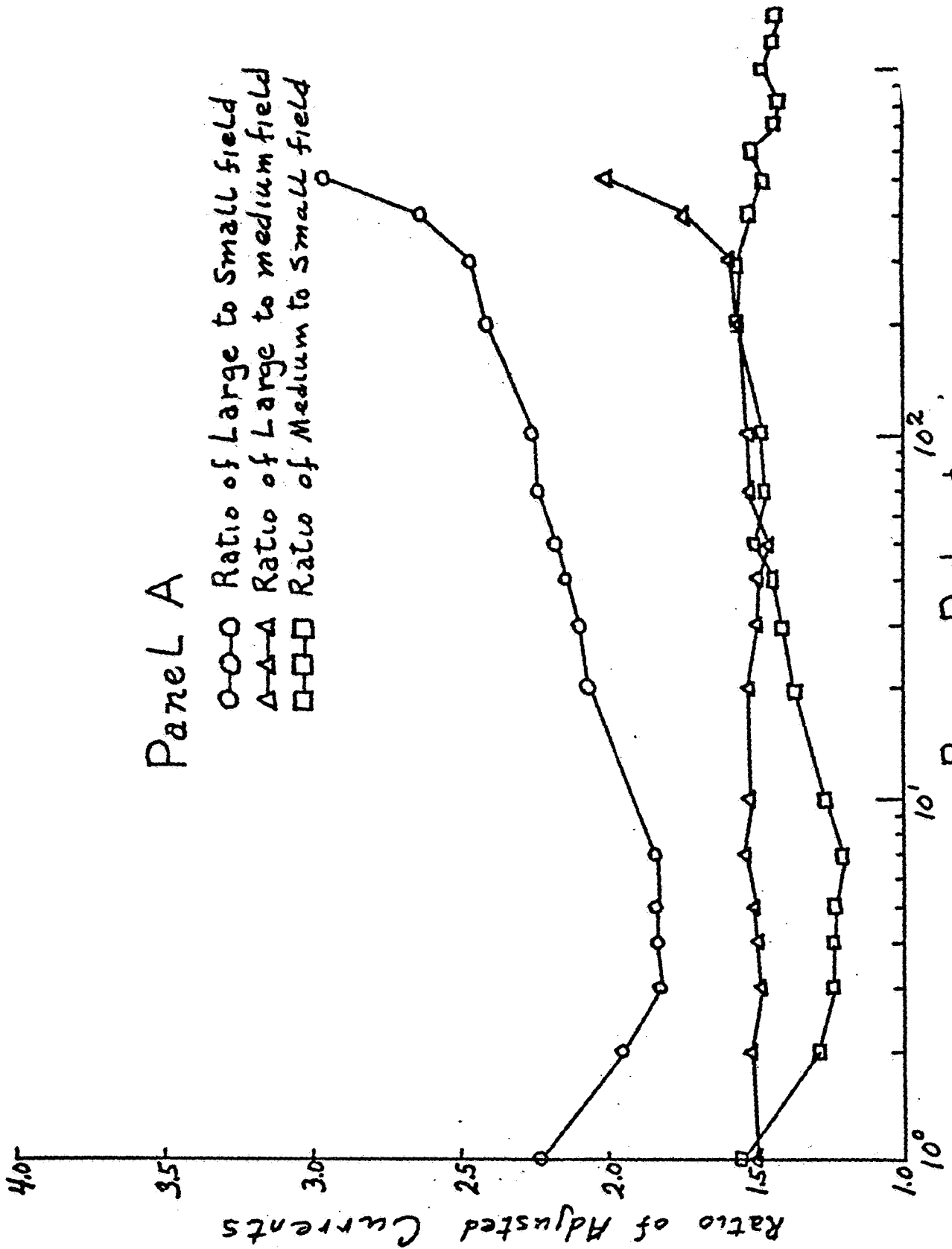


Fig. 7.3 Ratios of adjusted currents from panel A vs. bias pot.

-----STORE I-V DATA FILES**** D. D. MILLER JULY 1981

DIMENSION A(25),V(25),FNAME(6),H(20)
1 FORMAT('PROGRAM FILENT-MILLER JULY 1981')
TYPE 1

100 DO 2 I=1,6
FNAME(I)=0

2 CONTINUE
DO 17 I=1,20
H(I)=0

ORIGINAL PAGE IS
OF POOR QUALITY

17 CONTINUE
TYPE 3
3 FORMAT('SET FILE NAME? ')
ACCEPT 4,(FNAME(I),I=1,6)
4 FORMAT(6A4)
FNAME(6)=0

-----INPUT INFORMATION AND DATA FROM KEYBOARD-----

5 TYPE 5
FORMAT(' ENTER # OF ELEMENTS AND SCALE FACTOR')
ACCEPT *.N,G

6 TYPE 6
FORMAT(' ENTER VOLTAGE CURRENT PAIRS')
ACCEPT *. (V(I),A(I),I=1,N)
DO 7 I=1,N

A(I)=A(I)*G
7 CONTINUE
TYPE 16
16 FORMAT(' ENTER HEADER FOR PRINT OUT')
ACCEPT 8,(H(I),I=1,20)
8 FORMAT(20A4)
H(20)=0

-----MAKE HARDCOPY OF DATA AND HEADERS-----

9 WRITE(6,9) (FNAME(I),I=1,6),N,G,(H(I),I=1,20)
WRITE(6,10)
10 FORMAT('FILENAME ',(6A4),5X,'I2,' ELEMENTS',5X,'SCALE FACTOR',
1 F5.2,'/1X,(20A4)/')
11 FORMAT(4X,'BIAS(V)',3X,'CURRENT(MA)')
WRITE(6,11) (V(I),A(I),I=1,N)

-----STORE DATA ON A FILE-----

11 OPEN(UNIT=1,NAME=FNAME,TYPE='NEW',ERR=1000)
WRITE(1,*) N,G,(V(I),A(I),I=1,N)
FORMAT(2X,F5.0,7X,F7.3)
CLOSE(UNIT=1,DISPOSE='SAVE')
REF=A(1)

-----COMPUTE NORMALIZED CURRENT AND LIST-----

12 DO 12 I=1,N
A(I)=A(I)/REF
12 CONTINUE
WRITE(6,13)
13 FORMAT('/4X,'BIAS(V)',3X,'NORMALIZED CURRENT')
WRITE(6,14) (V(I),A(I),I=1,N)
14 FORMAT(2X,F5.0,6X,F7.2)
TYPE 15

```
NMAX=MAX0(N(1),N(2),N(3))
IF(NMAX .EQ. N(1)) MF=1
IF(NMAX .EQ. N(2)) MF=2
IF(NMAX .EQ. N(3)) MF=3
WRITE(6,13) (V(MF,T),R(1,T),P(2,T),R(3,T),A(1,T),A(2,T),
1  A(3,T),T=1,NMAX)
FORMAT(3X,F6.0,3X,F7.2,3X,F7.2,3X,F7.2,3X,F7.3,3X,F7.3,3X,F7.3)
TYPE=17
17 FORMAT(' DO YOU WANT TO PROCESS MORE FILES(YES OR NO)?')
ACCEPT R,F
IF(R .EQ. 'YES') GOTO 100
STOP
1000 STOP 'OPEN ERROR'
2000 STOP 'CLOSE ERROR'
END
```

ORIGINAL PAGE IS
OF POOR QUALITY

ORIGINAL PAGE IS
OF POOR QUALITY

PROGRAM TVDMAS**D D MILLER-JULY 1981

GROUP 4 COMPARISON: PANEL A, ALL FIELDS* 1ST=DATEAI, 2ND=DATEAM, 3RD=DATEAS

RTAS(V.)	1ST/3RD	2ND/3RD.	1ST/2ND	1ST	2ND	3RD
1.	2.32	1.55	1.50	0.696	0.464	0.300
2.	1.95	1.29	1.51	0.720	0.477	0.370
3.	1.81	1.23	1.48	0.744	0.503	0.410
4.	1.83	1.23	1.49	0.768	0.516	0.420
5.	1.84	1.23	1.50	0.792	0.529	0.430
7.	1.84	1.20	1.53	0.828	0.542	0.450
10.	1.90	1.26	1.51	0.876	0.580	0.460
20.	2.06	1.37	1.51	1.032	0.684	0.500
30.	2.09	1.41	1.49	1.152	0.774	0.550
40.	2.14	1.44	1.48	1.260	0.851	0.590
50.	2.17	1.50	1.45	1.344	0.929	0.620
70.	2.23	1.47	1.51	1.560	1.032	0.700
100.	2.25	1.48	1.52	1.800	1.187	0.800
200.	2.40	1.55	1.55	2.520	1.625	1.050
300.	2.45	1.56	1.57	3.240	2.064	1.320
400.	2.63	1.51	1.74	4.080	2.348	1.550
500.	2.95	1.47	2.00	5.160	2.580	1.750
600.	0.00	1.51	0.00	0.000	3.096	2.050
700.	0.00	1.43	0.00	0.000	3.354	2.350
800.	0.00	1.41	0.00	0.000	3.741	2.650
1000.	0.00	1.46	0.00	0.000	4.515	3.100
1200.	0.00	1.43	0.00	0.000	5.289	3.700
1400.	0.00	1.42	0.00	0.000	6.256	4.400
1600.	0.00	0.00	0.00	0.000	0.000	5.000
1800.	0.00	0.00	0.00	0.000	0.000	5.700

-----PROGRAM IVDMAS: I-V DATA MESSAGE-----

DIMENSION R(3,25),G(3),N(3),Y(3)
DIMENSION A(3,25),V(3,25),FNAME(6),H(20)
DATA X/' 1ST', ' 2ND', ' 3RD'
TYPE 1

1 FORMAT(' PROGRAM IVDMAS--MILLER JULY 1981')

DO 14 I=1,3

DO 15 I=1,25

R(I,I)=0

A(I,I)=0

V(I,I)=0

15 CONTINUE

14 CONTINUE

DO 2 I=1,20

H(I)=0

2 CONTINUE

DO 3 I=1,6

FNAME(I)=0

3 CONTINUE

ORIGINAL PAGE IS
OF POOR QUALITY

-----ASK FOR .GET. AND STORE THREE FILES-----

DO 4 I=1,3

TYPE 5,X(I)

5 FORMAT(' ENTER 1, A4, FILE NAME')

ACCEPT 6,(FNAME(I),I=1,6)

6 FORMAT(6A4)

FNAME(I)=0

OPEN(UNIT=1,NAME=FNAME,TYPE='OLD',ERR=1000)

READ(1,*) N(I),G(I),(V(I,I),A(I,I),I=1,N(I))

CLOSE(UNIT=1,DISPOSE='SAVE',ERR=2000)

4 CONTINUE

-----OBTAIN HEADER FOR PRINTOUT-----

TYPE 7

7 FORMAT(' ENTER HEADER FOR PRINTOUT')

ACCEPT 8,(H(I),I=1,20)

8 FORMAT(20A4)

H(20)=0

-----FORM ARRAYS OF RATIOS-----

NMTN=MTN/(N(1),N(3))

DO 9 I=1,NMTN

R(1,I)=A(1,I)/A(3,I)

9 CONTINUE

NMTN=MTN/(N(2),N(3))

DO 10 I=1,NMTN

R(2,I)=A(2,I)/A(3,I)

10 CONTINUE

NMTN=MTN/(N(1),N(2))

DO 11 I=1,NMTN

R(3,I)=A(1,I)/A(2,I)

11 CONTINUE

-----PRINT HEADINGS AND DATA RATIOS-----

WRITE(6,12) (H(I),I=1,20)

12 FORMAT(1H1,' PROGRAM IVDMAS**#D O MILLER-JULY 1981',/

1 1X,(20A4)///)

WRITE(6,16)

1000

IF (E .EQ. 'YES') GOTO 100
STOP
STOP 'ERROR'
END

ORIGINAL PAGE IS
OF POOR QUALITY

BIAS(V)	CURRENT(MA)
1.	0.043
2.	0.055
3.	0.063
4.	0.070
5.	0.072
7.	0.080
10.	0.091
20.	0.120
30.	0.142
40.	0.160
50.	0.182
70.	0.211
100.	0.285
200.	0.388
300.	0.524
400.	0.684
500.	0.832
600.	1.026
700.	1.197
800.	1.368
1000.	1.767
1200.	2.280
1400.	2.793
1600.	3.306
1800.	3.819

ORIGINAL PAGE IS
OF POOR QUALITY

BIAS(V)	NORMALIZED CURRENT
1.	1.00
2.	1.26
3.	1.45
4.	1.61
5.	1.66
7.	1.84
10.	2.11
20.	2.76
30.	3.29
40.	3.68
50.	4.21
70.	4.87
100.	6.58
200.	8.95
300.	12.11
400.	15.79
500.	19.21
600.	23.68
700.	27.63
800.	31.58
1000.	40.79
1200.	52.63
1400.	64.47
1600.	76.32
1800.	88.16

ORIGINAL PAGE IS
OF POOR QUALITY

N82 23126

Df

An Analytic Solution to the Classical
Two-Body Problem with Drag

Don Mittleman*

&

Don Jezewski**

Abstract:

An analytic solution to the two-body problem with a specific drag model is obtained. The model treats drag as a force proportional to the vector velocity and inversely proportional to the distance to the center of attraction. The solution is expressed in terms of known functions and is of a simple and compact form. The time-of-flight is expressed as a quadrature in the "true anomaly".

*Department of Mathematics, Oberlin College, Oberlin, Ohio 44074

**Mission Planning and Analysis Division, NASA Johnson Space Center,
Houston, Texas 77058

C-2

Introduction: There are few solutions, either analytic or in closed-form, to the classical two-body problem with drag. Brouwer and Hori [1] developed a closed-form solution in canonical variables of the motion of an artificial satellite in the gravitational field of an oblate earth including first-order corrections due to a spherical atmosphere and a velocity square law in drag acceleration.

Danby, [2] proposed an alternative drag model in which the resistance is proportional to the vector velocity and inversely proportional to the square of the distance to the center of the attracting mass. This model leads to a scalar inhomogeneous 2nd-order linear differential equation. He uses a perturbation technique to obtain the solution to the differential equation assuming that the constant of proportionality in the resisting force is small and that terms involving powers of this constant greater than one may be neglected.

Initially, we start with a general linear 2nd-order vector differential equation with arbitrary scalar coefficients. We then develop a 2nd-order vector differential equation in which the dependent variable is a unit vector in the direction of the radius and the independent variable is the "true anomaly". We show that this differential equation includes as special cases the classical Kepler solution and Danby's model.

By analyzing the coefficients in this vector differential equation, we are able to obtain an analytic solution to the model originally proposed by Danby. Our solution is shown to include his when the resistive coefficient goes to zero.

Using this analytic solution, the vector differential equation for this drag model reduces to the differential equation for the vector harmonic oscillator. The general solution to the problem is then expressed in a simple compact form.

We were not able to integrate the time-of-flight equation, the analogue

of Kepler's equation, in a finite number of terms of known functions.

The time-of flight, however, is readily expressed in terms of a quadrature.

Details of the computational procedure and characteristics of the functions used in the solution are included in appendices. Graphs illustrating the general characteristic of these functions and the solutions are also included.

Statement of the Problem

The two-body problem may be expressed by the vector differential equation

$$\ddot{\mathbf{R}} + \beta(\mathbf{R}, \dot{\mathbf{R}}) \dot{\mathbf{R}} + \gamma(\mathbf{R}) \mathbf{R} = 0 \quad (1)$$

where \mathbf{R} is the radius vector from the center of mass of the attracting body to the particle, $\beta(\mathbf{R}, \dot{\mathbf{R}})$ and $\gamma(\mathbf{R})$ are arbitrary scalar coefficients and dots denote differentiation with respect to the independent variable, time. To retain as much generality as possible, we refrain from specifying β and γ at this time.

We first transform equation (1) by introducing a polar angle, θ , which we shall refer to as the true anomaly, as the independent variable.

$$\dot{\mathbf{R}} = \mathbf{R}' \dot{\theta} \quad , \quad \ddot{\mathbf{R}} = \mathbf{R}'' \dot{\theta}^2 + \mathbf{R}' \ddot{\theta}$$

where the prime, denotes differentiation with respect the angle θ .

Equation (1) then becomes

$$\mathbf{R}'' \dot{\theta}^2 + \mathbf{R}' \ddot{\theta} + \beta \mathbf{R}' \dot{\theta} + \gamma \mathbf{R} = 0 \quad (2)$$

Classically, it has been found useful to introduce the unit vector $\xi = \frac{\mathbf{R}}{r}$. With this definition, equation (2) becomes:

$$r \dot{\theta}^2 \xi'' + (2r' \dot{\theta}^2 + r \ddot{\theta} + \beta r \dot{\theta}) \xi' + (r'' \dot{\theta}^2 + r' \ddot{\theta} + \beta r' \dot{\theta} + \gamma r) \xi = 0 \quad (3)$$

Paralleling the classical procedure, we let

$$r = \frac{1}{u} \quad , \quad r' = -\frac{u'}{u^2} \quad , \quad r'' = -\frac{u''}{u^2} + \frac{2(u')^2}{u^3}$$

and equation (3) becomes:

$$\xi'' + \left(\frac{\beta}{\dot{\theta}} + \frac{\ddot{\theta}}{\dot{\theta}^2} - \frac{2u'}{u} \right) \xi' + \left(\frac{2(u')^2 - uu''}{u^2} - \frac{\ddot{\theta}u'}{\dot{\theta}^2 u} - \frac{\beta u'}{\dot{\theta} u} + \frac{\gamma}{\dot{\theta}^2} \right) \xi = 0 \quad (4)$$

Equation (4) may be simplified if we let

$$\nu = \frac{\beta}{\dot{\theta}} + \frac{\ddot{\theta}}{\dot{\theta}^2} - \frac{2u'}{u} \quad (5)$$

$$\xi'' + \nu \xi' + \left(-\nu \frac{u'}{u} - \frac{u''}{u} + \frac{\gamma}{\dot{\theta}^2} \right) \xi = 0 \quad (6)$$

Particular Solution

We are motivated at this point by the solution to the classical Keplerian problem, $\beta = 0$ and $\gamma = \frac{\mu}{r^3}$, and where μ is the gravitational constant. For these values of β and γ , the conservation of angular momentum implies $\nu = 0$. We refrain from so specifying β and γ , but do explore the possibility that $\nu = 0$. Equation (5) becomes:

$$d(\dot{\theta}/u^2) + \beta \frac{d\theta}{u^2} = 0$$

and recalling that $u = \frac{1}{r}$,

$$d(r^2 \dot{\theta}) + \beta r^2 d\theta = 0 \quad (7)$$

(Note, if $\beta = 0$, the Keplerian angular momentum $r^2 \dot{\theta} = \text{constant}$.) Equation (7) readily admits another integral if $\beta = \frac{\alpha}{r^2}$ where α is a constant. This integral is

$$r^2 \dot{\theta} + \alpha \theta = h_0 \quad (8)$$

h_0 is a constant of integration.

With $\nu = 0$, equation (6) reduces to:

$$\xi'' + \left(\frac{\gamma}{\dot{\theta}^2} - \frac{u''}{u} \right) \xi = 0 \quad (9)$$

In retrospect, it is clear that ν is equal to zero in at least two cases, (1) when no drag is present and (2) when the drag is proportional to $1/r^2$.

It should be noted that any perturbation having an effect directed along the position vector can be reflected in our choice of γ . Thus, $\gamma = 0$ removes any coupling between the unit vectors in the direction of R and its derivative with respect to θ .

The simplest problem we can solve that includes a drag term is to choose $\gamma = \mu u^3$. For this choice, equation (9) becomes, using equation (8) to eliminate $\dot{\theta}$,

$$\xi'' + \left(\frac{\mu}{(h_0 + \alpha \theta)^2 u} - \frac{u''}{u} \right) \xi = 0 \quad (10)$$

Classically, when $\alpha = 0$, i.e. no drag present, the coefficient of ξ , when set equal to 1, produces the differential equation for the Keplerian conics. With drag present, i.e. $\alpha \neq 0$, setting the coefficient of ξ equal to 1, produces the differential equations

$$\xi'' + \xi = 0 \quad (11a)$$

and

$$u'' + u = \frac{\mu}{\alpha^2 \left(\frac{h_0}{\alpha} - \theta \right)^2} \quad (11b)$$

Equation (11b) is given by Danby, page 231.

Solution of equation (11b)

Danby, chapter 11, studied this equation with $\alpha \neq 0$. His method of solution assumes that $\frac{\alpha \theta}{h_0}$ is small compared to unity; he expands the right-hand side of (11b) in powers of α and neglects all but first order terms in α . The solution to this problem, however, for arbitrary α can be obtained in terms of known functions.

Knowing the solution of the homogeneous equation, $u'' + u = 0$, a particular solution can be obtained using the method of variation of parameters. We chose, however, to use the inverse Laplace transform [3]. Aside from simplifying the algebraic manipulations, this method demonstrates an alternate procedure for solving a class of differential equations. For convenience of notation, we temporarily change the independent variable by letting $z = \frac{h_0}{\alpha} - \theta$.

Equation (11b) is now rewritten as:

$$\frac{d^2 u}{d z^2} + u = \frac{\mu}{\alpha^2 z^2} \quad (12)$$

If u is the Laplace transform of U , then taking the inverse Laplace transform of equation (12), we obtain

$$z^2 U + U = \frac{\mu}{\alpha^2} z \quad (13)$$

so that,

$$U = \frac{\mu}{\alpha^2} \frac{z}{z^2 + 1}$$

The Laplace transform of this equation is

$$u(z) = \frac{\mu}{\alpha^2} \int_0^{\infty} \frac{z e^{-z\tau}}{\tau^2 + 1} d\tau$$

Using the standard notation [5, chapter 5],

$$g(z) = \int_0^{\infty} \frac{t e^{-zt}}{t^2 + 1} dt \quad (14)$$

For details concerning this function, see appendix (A).

The general solution for $u(\theta)$ is:

$$u(\theta) = e_0 \cos(\theta - \theta_0) + \frac{\mu}{\alpha^2} g\left(\frac{h_0}{\alpha} - \theta\right) \quad (15)$$

where e_0 and θ_0 are constants of integration. Hence, the equation for radius, r , is

$$r = \frac{p}{e \cos(\theta - \theta_0) + \left(\frac{h_0}{\alpha}\right)^2 g\left(\frac{h_0}{\alpha} - \theta\right)} \quad (16)$$

where $e = \frac{e_0 \mu}{h_0^2}$ and $p = \frac{h_0^2}{\mu}$

It can be shown (see Appendix A) that

$$\lim_{\alpha \rightarrow 0^+} \left(\frac{h_0}{\alpha} \right)^2 g \left(\frac{h_0}{\alpha} - \theta \right) = 1$$

and this is recognized as the solution to the classic Keplerian two-body problem.

The solution for the position vector R , as function of θ , is obtained from equation (11a),

$$R = r \left(A \sin \theta + B \cos \theta \right) \quad (17)$$

where A and B are arbitrary vector constants and r is given by equation (16).

Looking at the solution as given by equations (16) and (17), these are nine constants of integration, h_0 , e , θ_0 , and the vectors A and B . Since the original problem calls for the solution of a second-order vector differential equation, only six of these constants are independent. The relationship between them is developed in Appendix C.

The Time-of-Flight Equation

The only relationship involving time occurs in equation (8), which indicates how the magnitude of the angular momentum changes. Since r is expressible as function of θ by equation (16), the time-of-flight between two values $\theta = \theta_1$ and $\theta = \theta_2$ is given by the quadrature

$$\Delta t = \frac{1}{\alpha} \int_{\theta_1}^{\theta_2} \frac{(r(\theta))^2 d\theta}{\left(\frac{h_0}{\alpha} - \theta \right)} \quad (18)$$

Since we are dealing with a perturbed Keplerian problem, the standard transformation from true anomaly to eccentric anomaly does not yield an

integrand that is integrable in terms of elementary functions. Any standard quadrature formula, e.g. Romberg integration [4], may be used to evaluate the integral.

Graphical Illustrations^a

Figures (1a) and (1b) illustrate the effect of drag, α , on equation (16). The values of the constants h_0 and μ were chosen equal to 1 and the constant e was taken as 0.01. Comparing the two figures, it is apparent that the drag effect is more pronounced as α goes from 0.005 to 0.05.

Figures (2a) and (2b) are similar to (1a) and (1b) except that the constant e was increased to 0.5.

Conclusion

We have obtained a closed-form, analytic solution to the two-body problem including drag that generalized the classical Keplerian two-body problem and subsumes the Danby perturbation method.

Two serendipitous results are: 1) the development of a vector differential equation that permits the analysis of an infinite numbers of gravitational and drag models, and 2) the obtaining of the solution of a linear differential equation using the inverse, rather than the direct method of Laplace transforms.

^a We gratefully acknowledge the assistance of Eleta Malowitz and Jerry Yglesias of Barrios Technology Inc., for their aid in obtaining the graphical data.

ORIGINAL PAGE IS
OF POOR QUALITY

References

- [1] Brouwer, D., Hori, G., Theoretical Evaluation of Atmospheric Drag Effects in the Motion of an Artificial Satellite, The Astronomical Journal, Vol. 66, June 1961, page 193. (See also Brouwer, D. and Clemence, G., Methods of Celestial Mechanics, Academic Press, New York, 1961, Chapter 12)
- [2] Danby, J. M. A., Fundamentals of Celestial Mechanics, Macmillian Co., New York, 1962
- [3] Churchill, R. V., Operational Mathematics, 2nd Edition, McGraw-Hill, New York, 1958, page 183
- [4] Burden R. L., Faires, J. D., Reynolds, A. C., Numerical Analysis, Prindle, Wiber and Smidh, Boston, Mass., 1978, page 210
- [5] Abramowitz, M. Stegun, I. (Eds), Handbook of Mathematical Functions with Formulas, Graphs, and Mathematical Tables, National Bureau of Standards, U.S. Government Printing Office, Washington, D. C., 1964 (Eighth Dover printing)

Appendix A

The Function $g(z)$

The following is an amplification of material taken from [5].

A) In equation (14), the function $g(z)$ was given as

$$g(z) = \int_0^{\infty} \frac{z e^{-z\tau}}{\tau^2 + 1} d\tau \quad (A1)$$

This function may also be expressed in terms of sine and cosine integrals. If we denote

$$si(z) = - \int_z^{\infty} \frac{\sin \tau}{\tau} d\tau$$

and

$$Ci(z) = - \int_z^{\infty} \frac{\cos \tau}{\tau} d\tau$$

then,

$$g(z) = - Ci(z) \cos(z) - si(z) \sin(z) \quad (A2)$$

For $0 < z \leq 1$, the sine and cosine integrals may be expressed in terms of the following expansions.

$$si(z) = -\frac{\pi}{2} + \sum_{n=0}^{\infty} \frac{(-1)^n z^{2n+1}}{(2n+1)(2n+1)!}$$

$$Ci(z) = \gamma_0 + \ln z + \sum_{n=1}^{\infty} \frac{(-1)^n z^{2n}}{(2n)(2n)!}$$

γ_0 is the Euler constant: $\gamma_0 = 0.5772 \ 15664 \ 90153 \ 28606 \dots$

Clearly the two infinite series coverage rapidly for $|z| \leq 1$.

For $1 \leq z < \infty$, an asymptotic expansion is available.

$$g(z) \sim \frac{1}{z^2} \left(1 - \frac{3!}{z^2} + \frac{5!}{z^4} - \dots \right)$$

Also for this domain of z , rational approximation have been determined; e.g.

$$1 \leq x < \infty$$

$$g(x) = \frac{1}{x^2} \left(\frac{x^4 + a_1 x^3 + a_2 x^2 + a_3 x + a_4}{x^4 + b_1 x^3 + b_2 x^2 + b_3 x + b_4} \right) + \epsilon(x)$$

$$|\epsilon(x)| < 3 \times 10^{-7}$$

$$a_1 = 42.242855 \quad b_1 = 48.196927$$

$$a_2 = 302.757865 \quad b_2 = 482.485984$$

$$a_3 = 352.018498 \quad b_3 = 1114.978885$$

$$a_4 = 21.821899 \quad b_4 = 449.690326$$

The graph of $g(z)$ is given in Fig ().

B) It has been shown that $g(z)$ satisfies the differential equation:

$$g''(z) + g(z) = \frac{1}{z^2}$$

If we define

$$f(z) = \int_0^{\infty} \frac{e^{-zt}}{t^2 + 1} dt$$

then, $f(z)$ satisfies the differential equation

$$f''(z) + f(z) = \frac{1}{z}$$

Also,

$$g'(z) = -\frac{1}{z} + f(z)$$

$$f'(z) = -g(z)$$

Corresponding to (A2),

$$f(z) = \text{Ci}(z) \sin(z) - \text{si}(z) \cos(z)$$

An asymptotic formula for $f(z)$ is:

$$f(z) \sim \frac{1}{z} \left(1 - \frac{2!}{z^2} + \frac{4!}{z^4} - \dots \right)$$

For $1 \leq z < \infty$, rational approximation to $f(z)$ is given by:

$$1 \leq x < \infty$$

$$f(x) = \frac{1}{x} \frac{(x^6 + a_1 x^5 + a_2 x^4 + a_3 x^3 + a_4)}{(x^6 + b_1 x^5 + b_2 x^4 + b_3 x^3 + b_4)} + \epsilon(x)$$

$$|\epsilon(x)| < 5 \times 10^{-7}$$

$$a_1 = 38.027264 \quad b_1 = 40.021433$$

$$a_2 = 265.187033 \quad b_2 = 322.624911$$

$$a_3 = 335.677320 \quad b_3 = 570.236280$$

$$a_4 = 38.102495 \quad b_4 = 157.105423$$

The graph of $f(z)$ is given in Fig. ().

C) We asserted in the text that the

$$\lim_{\alpha \rightarrow 0^+} \left(\frac{h_0}{\alpha} \right)^2 g \left(\frac{h_0}{\alpha} - \theta \right) = 1$$

From the asymptotic expansion for $g(z)$,

$$g \left(\frac{h_0}{\alpha} - \theta \right) = \frac{1}{\left(\frac{h_0}{\alpha} - \theta \right)^2} - \frac{3!}{\left(\frac{h_0}{\alpha} - \theta \right)^4} + \frac{R_6}{\left(\frac{h_0}{\alpha} - \theta \right)^6}$$

where R_6 is bounded for small α . Thus,

$$\lim_{\alpha \rightarrow 0^+} \left(\frac{h_0}{\alpha} \right)^2 g \left(\frac{h_0}{\alpha} - \theta \right) = \lim_{\alpha \rightarrow 0^+} \left[\frac{\left(\frac{h_0}{\alpha} \right)^2}{\left(\frac{h_0}{\alpha} - \theta \right)^2} - \frac{3! \left(\frac{h_0}{\alpha} \right)^2}{\left(\frac{h_0}{\alpha} - \theta \right)^4} + \frac{\left(\frac{h_0}{\alpha} \right)^2 R_6}{\left(\frac{h_0}{\alpha} - \theta \right)^6} \right]$$

$$= 1$$

Appendix B

Computation of the constant α .

We propose three basic methods for computing α . In all cases, we assume that there exists a drag model given by $\mathcal{D}(R, \dot{R})\dot{R}$ where $\mathcal{D}(R, \dot{R})$ is a scalar function of the vectors R and \dot{R} .

- 1) The constant α may be computed from the initial conditions,

$$\alpha = r_0^2 \mathcal{D}(R, \dot{R}) \Big|_{R=R_0, \dot{R}=\dot{R}_0}$$

- 2) The second method uses an averaging technique.

$$\alpha = \frac{1}{\theta_2 - \theta_1} \int_{\theta_1}^{\theta_2} r^2 \mathcal{D}(R, \dot{R}) d\theta$$

where R , and \dot{R} are the position and velocity vectors determined from the Keplerian orbit having the same initial conditions.

- 3) A variation of (2) for longer flights would be an iteration on the trajectory. The first step is to calculate an α_1 , assuming a Keplerian orbit. Using α_1 in the drag model, a drag orbit is determined. The values of R and \dot{R} on this orbit are then used to calculate α_2 . The process is repeated.

- 4) A third possibility is to segment the total trajectory and compute an α for each segment using any of the above methods.

Appendix C

Computational sequence.

Given initial position and velocity vectors R_1 and $V_1 = \dot{R}_1$ at a given t_1 and a resistive constant α , what steps are necessary to compute R_2 and V_2 at a time t_2 ?

The initial value of the magnitude of the angular momentum is $|R_1 \times V_1|$. Thus, we may calculate $(r_1^2 \dot{\theta}_1) = |R_1 \times V_1|$. The angle θ_1 is computed from the initial position and velocity vectors using the Keplerian transformation to orbital elements. The constant h_0 is then determined from

$$h_0 = r_1^2 \dot{\theta}_1 + \alpha \theta_1 \quad (C1)$$

From equations (16) and its time derivative we may write:

$$\frac{e\mu}{h_0^2} \sin(\theta - \theta_0) = \frac{\dot{r}}{r^2 \dot{\theta}} - \frac{\mu}{\alpha^2} g'(\frac{h_0}{\alpha} - \theta)$$

$$\frac{e\mu}{h_0^2} \cos(\theta - \theta_0) = \frac{1}{r} - \frac{\mu}{\alpha^2} g(\frac{h_0}{\alpha} - \theta)$$

By squaring and adding we get

$$e^2 = \frac{h_0^4}{\mu^2} \left[\left(\frac{\dot{r}}{r^2 \dot{\theta}} - \frac{\mu}{\alpha^2} g'(\frac{h_0}{\alpha} - \theta) \right)^2 + \left(\frac{1}{r} - \frac{\mu}{\alpha^2} g(\frac{h_0}{\alpha} - \theta) \right)^2 \right]$$

By dividing,

$$\frac{\sin(\theta - \theta_0)}{\cos(\theta - \theta_0)} = \frac{\frac{\dot{r}}{r^2 \dot{\theta}} - \frac{\mu}{a^2} g'(\frac{h_0}{a} - \theta)}{\frac{1}{r} - \frac{\mu}{a^2} g(\frac{h_0}{a} - \theta)} \quad (C3)$$

where $\dot{r} = \frac{R \cdot \dot{R}}{r}$

From equations (C2) and (C3), evaluated at R_1 and R_1 , the constant A and θ_0 , $0 \leq \theta_0 < 2\pi$ are determined.

From equations (17) and its time derivative, we determine the vector constants A and B.

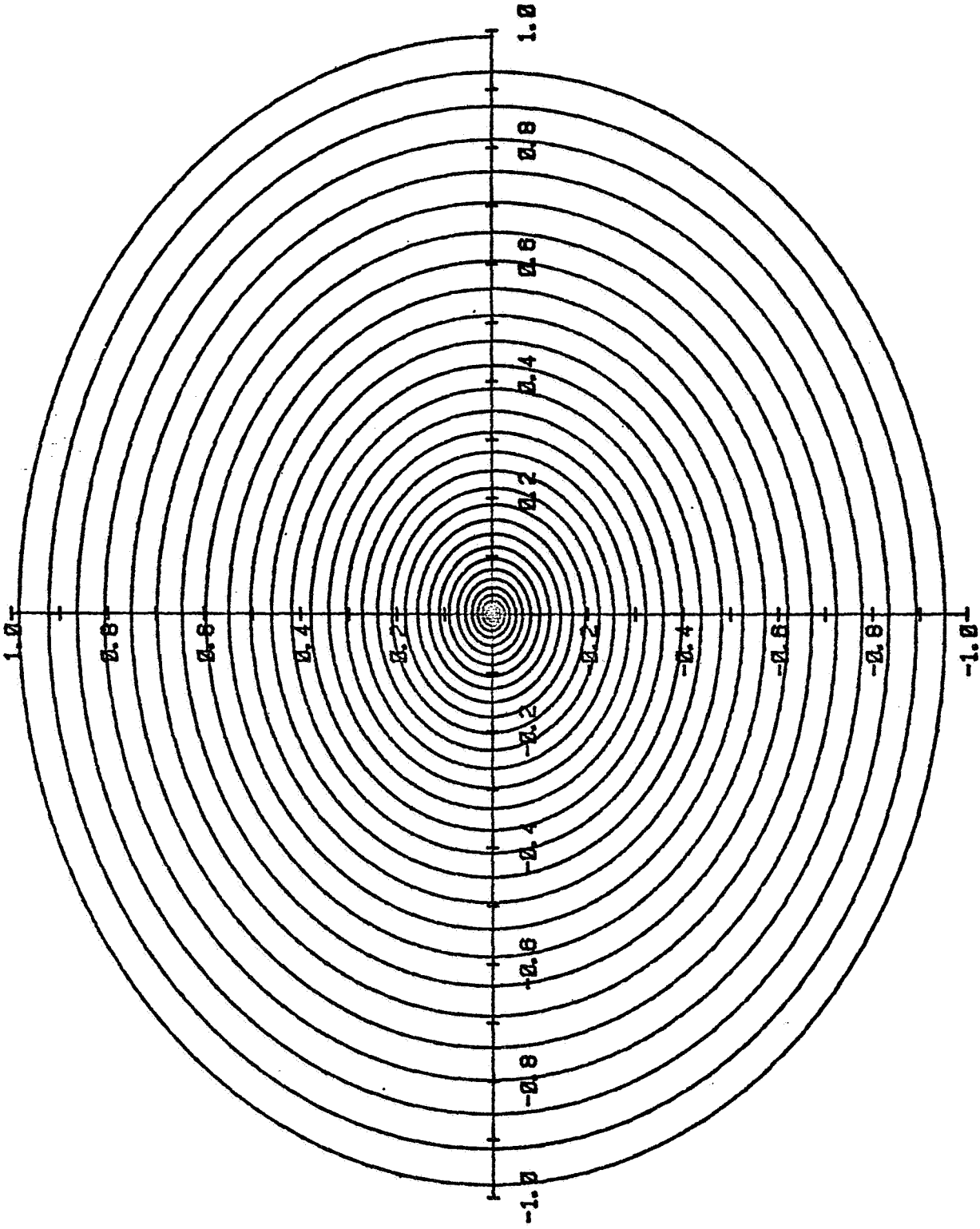
$$A = \frac{R_1}{r_1} \cos \theta_1 + \frac{R_1 \dot{r}_1 - r_1 \dot{R}_1}{(r_1^2 \dot{\theta}_1)} \sin \theta_1$$

$$B = - \left(\frac{R_1 \dot{r}_1 - r_1 \dot{R}_1}{r_1^2 \dot{\theta}_1} \right) \cos \theta_1 + \frac{R_1}{r_1} \sin \theta_1$$

It may readily be shown that A and B are orthogonal unit vectors.

ORIGINAL PAGE IS
OF POOR QUALITY

RADIUS AS A FUNCTION OF THETA



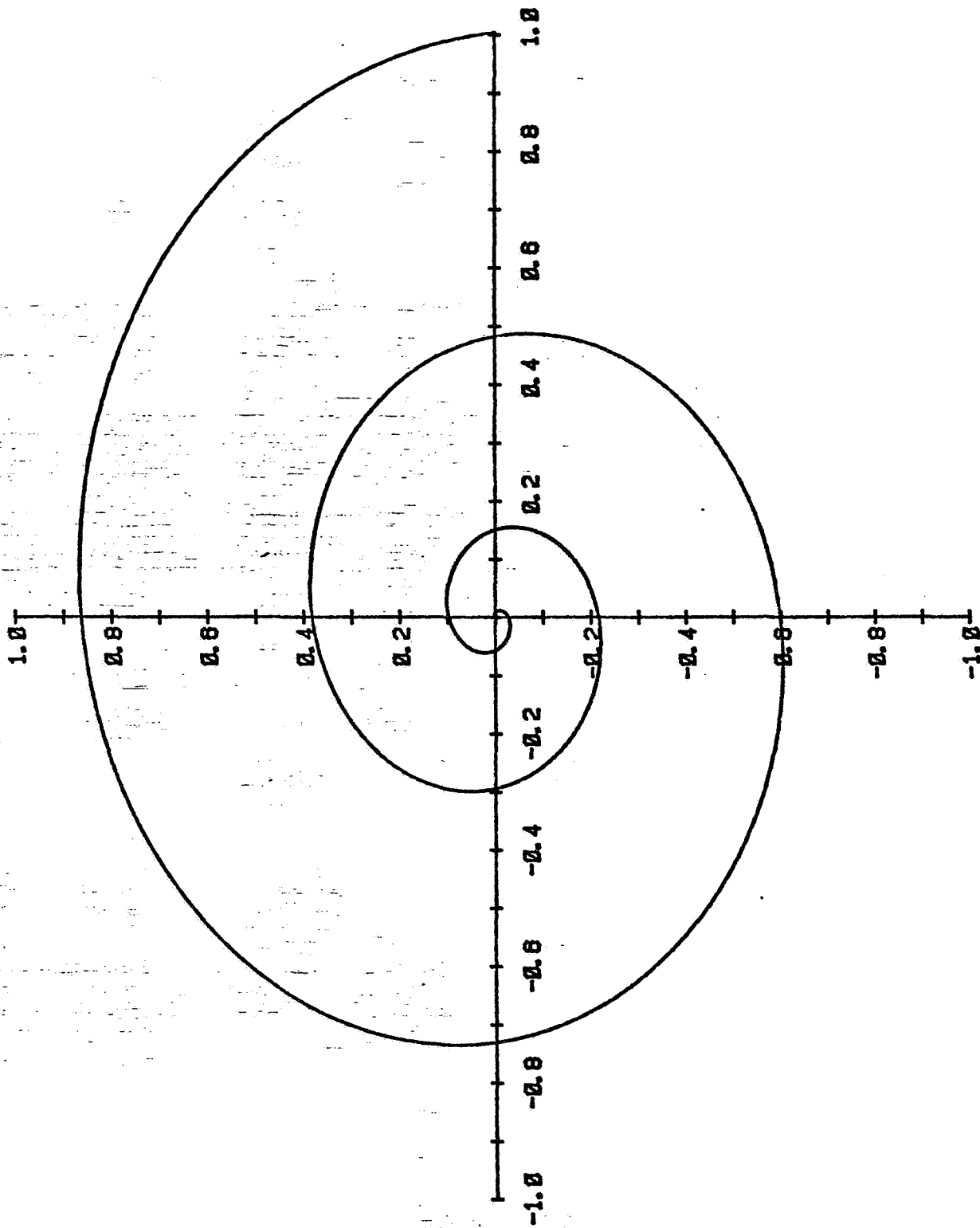
Alpha = 0.005

Eccentricity = 0.010

Fig 1A

ORIGINAL PAGE IS
OF POOR QUALITY

RADIUS AS A FUNCTION OF THETA

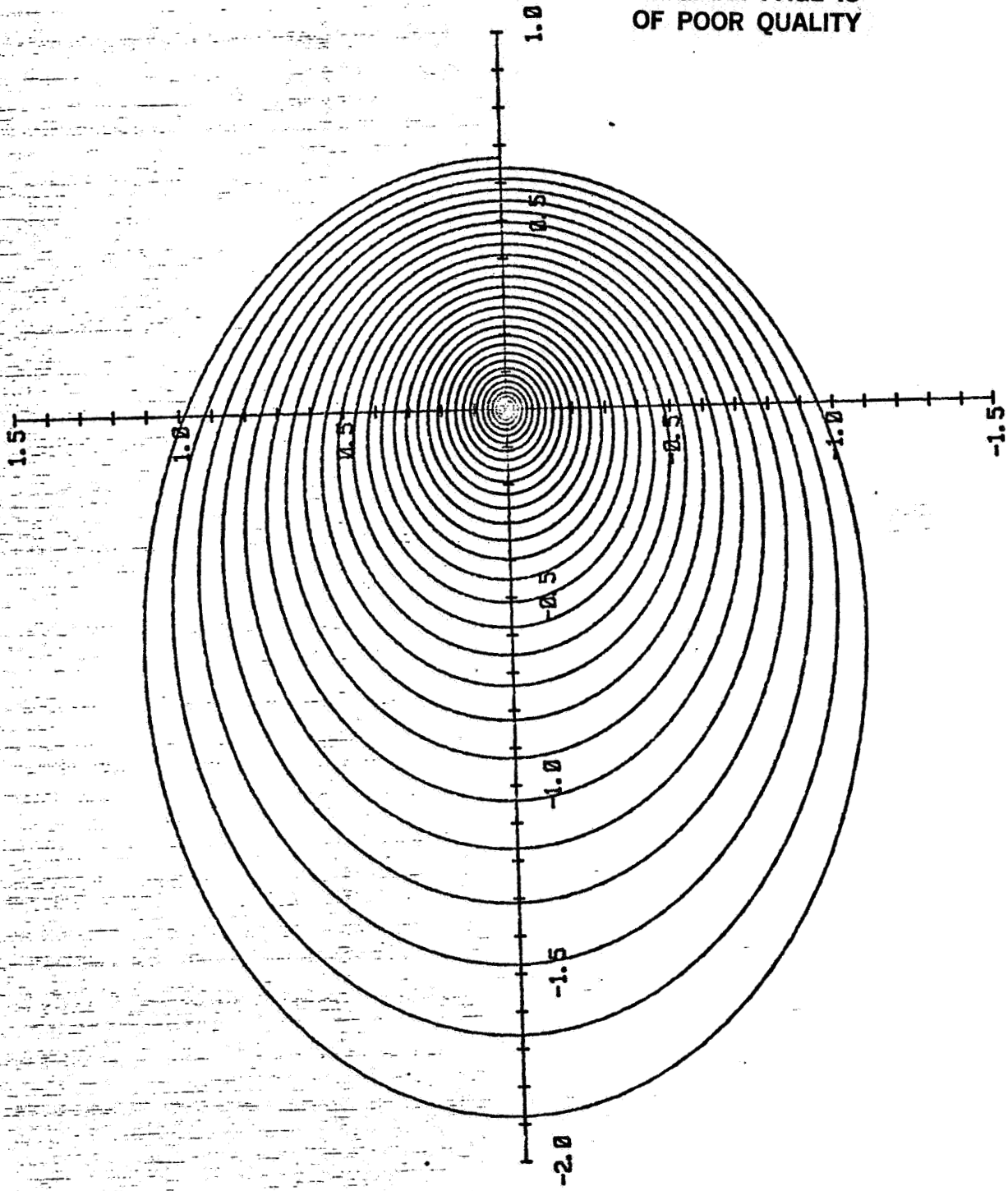


Alpha = 0.050

Eccentricity = 0.010

Fugib

RADIUS AS A FUNCTION OF THETA



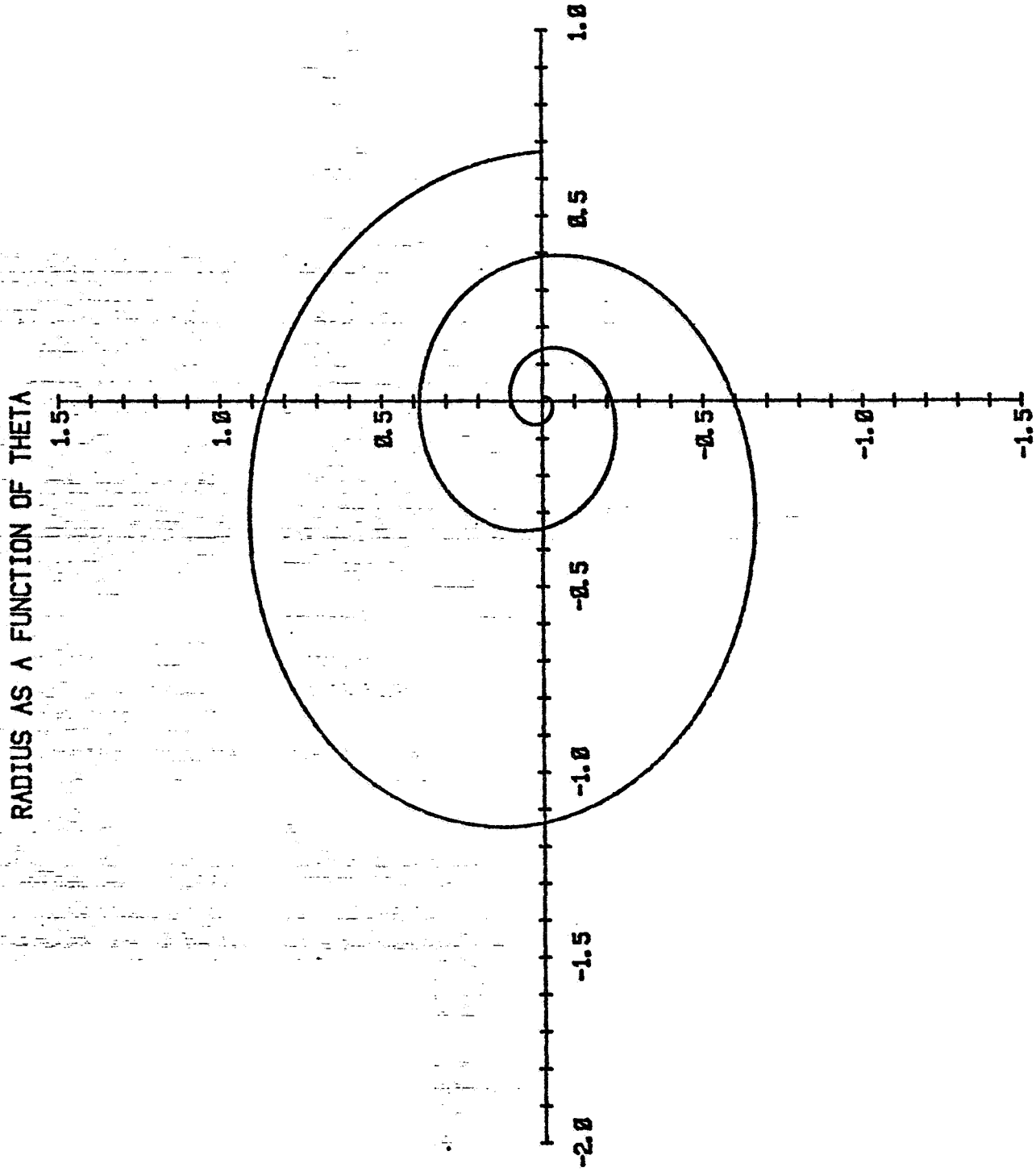
ORIGINAL PAGE IS
OF POOR QUALITY

Alpha = 0.005

Eccentricity = 0.500

Fig 2a

ORIGINAL PAGE IS
OF POOR QUALITY



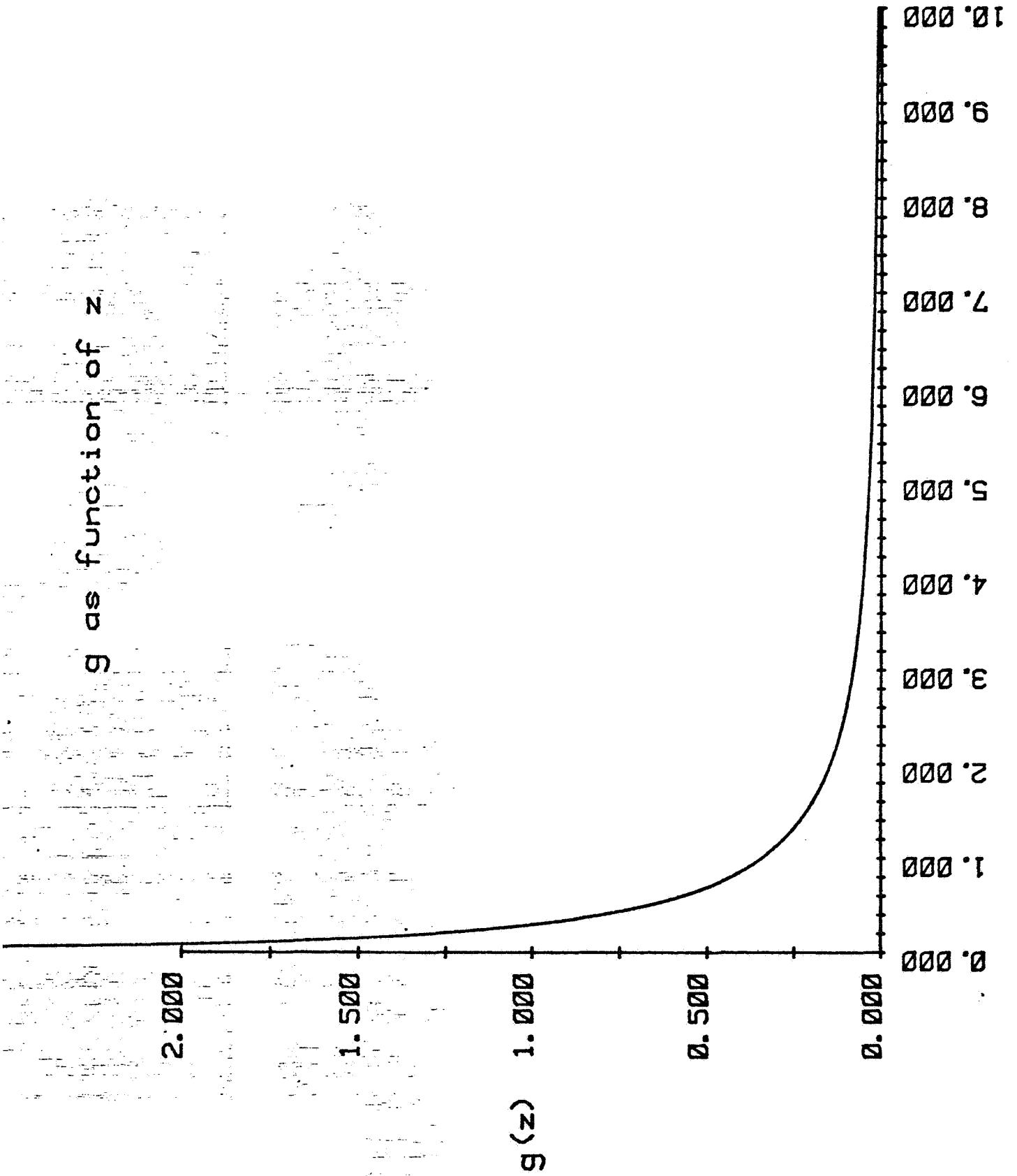
Alpha = 0.050

Eccentricity = 0.500

Fig 2b

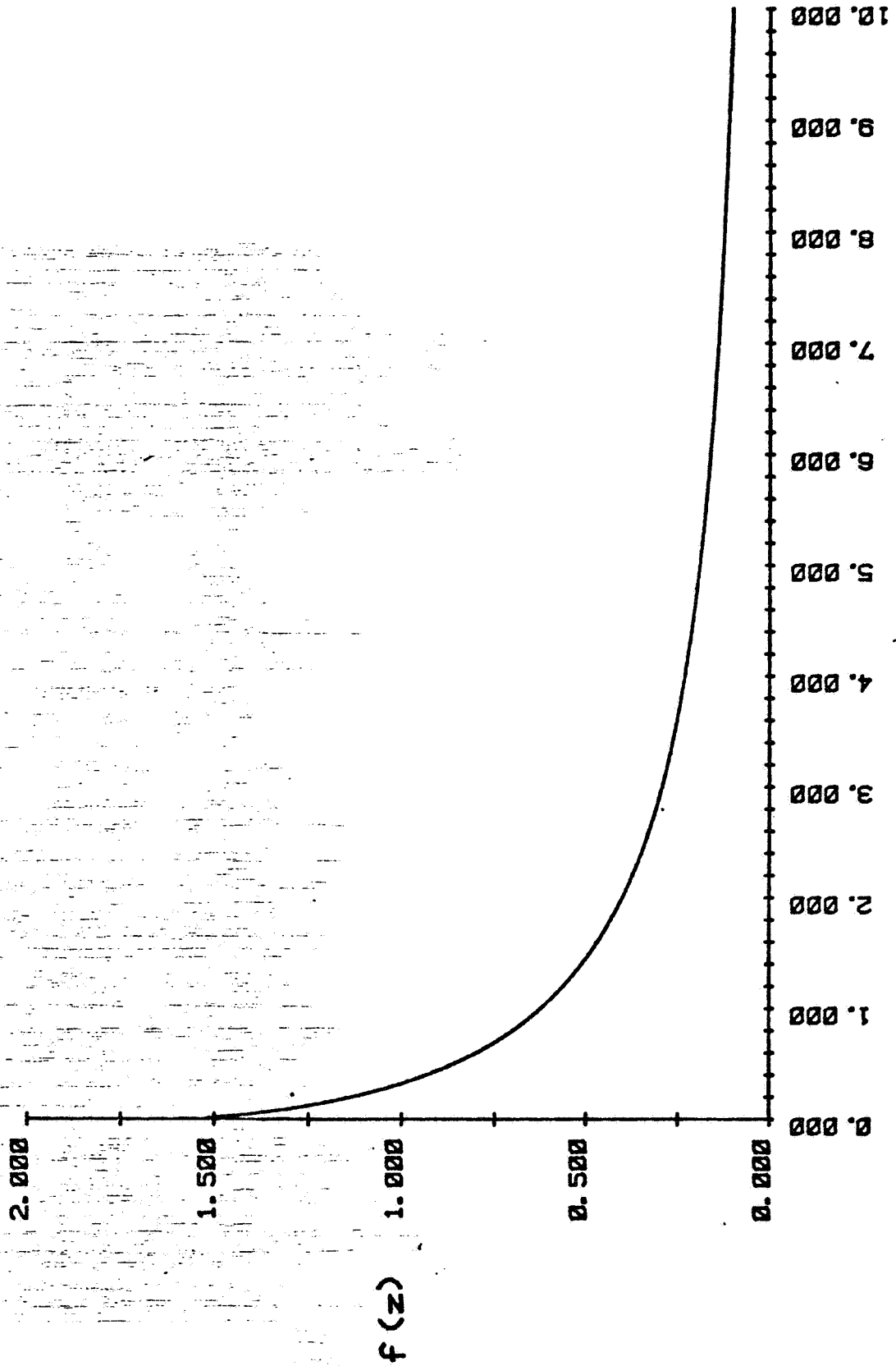
ORIGINAL PAGE IS
OF POOR QUALITY

g as function of z



ORIGINAL PAGE IS
OF POOR QUALITY

f as function of z



z (rad)

ORIGINAL PAGE IS
OF POOR QUALITY

N82' 23127

D5

A FAST VARIABLE STEP SIZE
INTEGRATION ALGORITHM
SUITABLE FOR COMPUTER SIMULATIONS
OF PHYSIOLOGICAL SYSTEMS

Larry Neal, Ph.D.

Tennessee Technological University

1981 NASA-ASEE Summer Faculty Fellow

Supervisor:

Wilber Boykin, Ph.D.

Data Systems Manager

Life Sciences Project Division

Abstract: A simple numerical algorithm has been developed for use in computer simulations of systems which are both stiff and stable. The method has been implemented in subroutine form and applied to the simulation of physiological systems.

NATIONAL AERONAUTICS AND SPACE ADMINISTRATION

LYNDON B. JOHNSON SPACE CENTER

HOUSTON, TEXAS

AUGUST 12, 1981

A Fast Variable Step Size Integration Algorithm
Suitable For Computer Simulations Of Physiological Systems

Due to physiological homeostasis, the maintenance of a constant or stable internal environment, mathematical models of physiological control systems are typically characterized by stability matrices. The matrix A is said to be a stability matrix if, and only if, each eigenvalue of A has a negative real part. Since physiological control is often complex, with some variables subject to control by more than one mechanism, mathematical models of physiological control usually result in stiff systems of differential equations. A system of differential equations is said to be stiff if the absolute values of its eigenvalues differ by orders of magnitude. Mathematical models in physiology frequently result in non-linear systems of differential equations, due in part to the complex interaction between various control systems. Thus, the mathematical modeling of complex physiological control often leads to a stiff system of non-linear differential equations characterized by a stability matrix.

Because it is usually very difficult to solve non-linear systems of differential equations by analytic techniques, mathematical models of complex physiological control systems are usually solved using numerical integration techniques and high speed computers. The numerical solution of a stiff differential system poses an interesting dilemma. How does one achieve both accuracy and computational efficiency when solving stiff differential systems using numerical integration techniques? Shampine and Gear [1] discuss the problem at length. They point out that explicit numerical methods fail on

**ORIGINAL PAGE IS
OF POOR QUALITY**

stiff problems because of the severely restricted step size. When very small step sizes are used throughout a computer simulation, efficiency suffers due to the large number of computations required and accuracy may be limited due to roundoff error resulting from many computations. Implicit numerical methods permit larger step sizes, but usually require many computations per step to either invert a matrix or to iterate in order to find a suitable solution at each step. Again, efficiency and accuracy may be sacrificed.

In the modeling of many physiological control systems, high order accuracy is not required since the values of many of the parameters are not known with great precision. It is, therefore, desirable to have an efficient numerical integration method for use in physiological simulations. The order of accuracy of the method is not of primary importance. The method should be easy to implement in a computer simulation; hence, a subroutine to do the numerical integration is desirable. The method should be capable of recognizing and following rapidly changing transients wherever they occur and should be capable of using a large step size when the system is at, or very near steady state. Efficiency precludes iteration and/or matrix inversion at each step.

A simple variable step size method based upon Euler integration which possesses all of the above traits has been devised for use in a large class of simulations of physiological control. This method is developed in the remainder of this report.

Consider the initial value problem

$$\dot{y} = Ay, \quad y(0) = c,$$

where A is a stability matrix. The case where elements of A vary with time is not excluded in this consideration.

Let $A = A - dI + dI$ where d is a scalar. Then $\dot{y} = (A - dI + dI) \cdot y$.

Define a hybrid Euler method which has both explicit and implicit parts by

$$y_{n+1} = y_n + h(A - dI)y_n + hdIy_{n+1}$$

The implicit part is confined to the main diagonal. Since d is a scalar, iteration is not necessary to solve for y_{n+1} .

$$(I - hdI) y_{n+1} = (I + hA - hdI) y_n$$

$$y_{n+1} = (I + (1/(1 - hd)) hA) y_n$$

$$y_{n+1} = y_n + (1/(1 - hd)) h\dot{y}_n \tag{1}$$

Let $r = 1/(1 - hd)$. Solving equation (1) for r , we obtain

$$r = ((y_{n+1} - y_n)/h)/\dot{y}_n \approx \dot{y}_{n+1}/\dot{y}_n$$

ORIGINAL PAGE IS
OF POOR QUALITY

If $r = \dot{y}_{n+1}/\dot{y}_n$, then (1) becomes the implicit Euler method which permits large step sizes, but is not very accurate during transients. We seek to improve upon this choice of r .

Consider a single variable y for a moment, rather than a large system. Let us say that y is approaching stability when the graph of y is either decreasing and concave up or increasing and concave down. Similarly, say that y is approaching instability when the graph of y is increasing and concave up or decreasing and concave down. If y is approaching stability, then r must be between 0 and 1 for accuracy. If y is approaching instability, then r must be greater than 1 for accuracy. When y is not changing, r should be 1. The diagrams on the next page illustrate how r should be chosen. Let $r = (z\dot{y}_n + (1-z)\dot{y}_{n+1})/\dot{y}_n$ ($0 \leq z \leq .5$) Then

$$y_{n+1} = y_n + h(z\dot{y}_n + (1-z)\dot{y}_{n+1}) \quad (2)$$

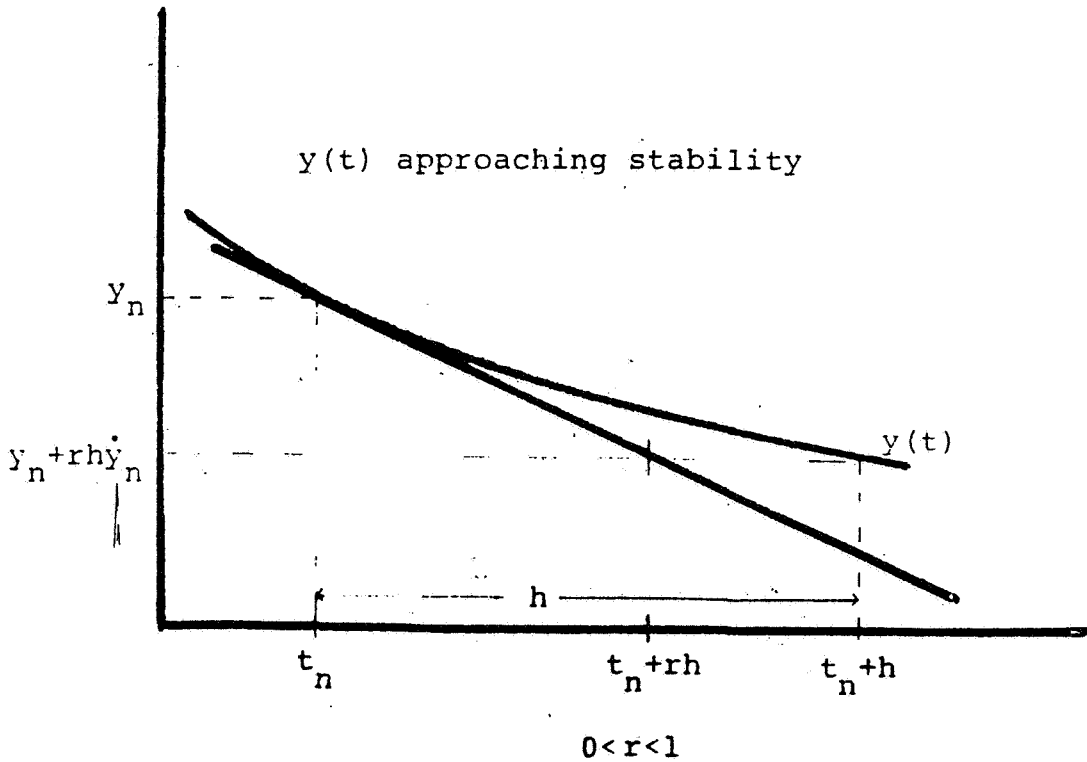
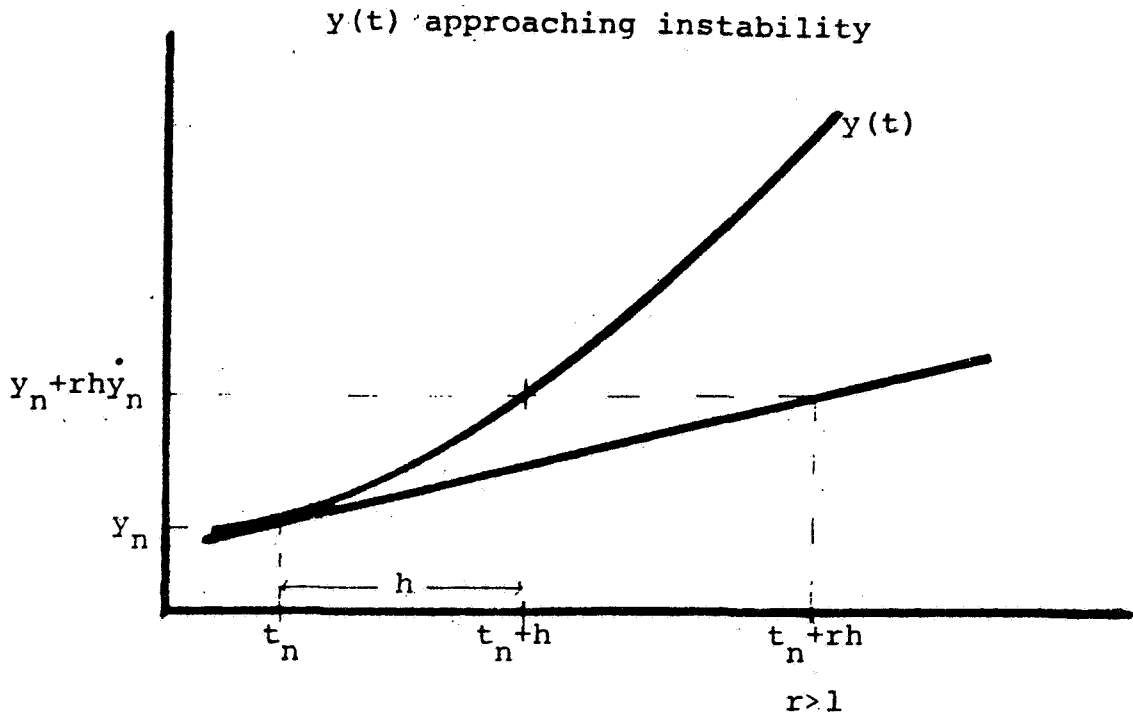
At any point in time, \dot{y} can be expressed as a linear function of y . That is,

$$\dot{y} = a + by, \quad (3)$$

where a and b might vary with time, but a is independent of y .

So $\dot{y}_n = a + by_n$ and $\dot{y}_{n+1} \approx a + by_{n+1}$. At steady state, a and b should not change with time. Thus (2) becomes

$$y_{n+1} = y_n + zh(a + by_n) + (1-z)h(a + by_{n+1})$$



Solving for y_{n+1} ,

$$y_{n+1} = (y_n + h(a + zby_n)) / (1 - (1 - z)hb) \quad (4)$$

which becomes our integrator equation. It is interesting to note that when $z = 0$, (4) reduces to $y_{n+1} = y_n + (1/(1 - hb))hy_n$

So d in equation (1) is the same as b in equation (3) when $z = 0$.

If $z = .5$, the method is the familiar trapezoidal rule. If $z = 0$, the method is the implicit Euler method. It seems that we have traded the problem of selecting r for the problem of selecting z . The fact that z remains unknown should be viewed as our opportunity rather than a problem. We should choose z in order to optimize accuracy during transients and efficiency at or near steady state. That is, z should be $.5$ when y is changing rapidly and z should be zero near steady state to permit large step sizes. Thus, z depends on h , which depends on the magnitude of \dot{y} . If $z = .5\exp(kh)$ for some $k < 0$, then z behaves as desired. We must now select k .

If one examines a typical solution equation in a stiff system, one finds that it is usually composed of two or more terms, one of which soon ceases to contribute to the overall solution. Bui (?) provides the following simple example.

Let $\dot{y} = Ay$ with $y(0) = [2, 0, -1]^T$ where

$$A = \begin{bmatrix} -21 & 19 & -20 \\ 19 & -21 & 20 \\ 40 & -40 & -40 \end{bmatrix}$$

with analytic solution

$$y_1(t) = \exp(-2t) + \exp(-40t) \cdot (\cos 40t + \sin 40t)$$

$$y_2(t) = \exp(-2t) - \exp(-40t) \cdot (\cos 40t + \sin 40t)$$

$$y_3(t) = -\exp(-40t) \cdot (\cos 40t - \sin 40t)$$

Note that $\exp(-40t)$ is a factor in a term in at least one of the solution equations. This is typical of stiff differential systems. After t has increased sufficiently, $\exp(-40t)$ is negligible, yet the presence of that term continues to restrict the step size in explicit methods. When a step of size h is taken starting at $t = t_n$, then $\exp(-40(t_n + h)) = \exp(-40t_n) \cdot \exp(-40h)$.

Near steady state, h should be large and $\exp(-40(t_n + h))$ should be zero. If k is chosen to be equal to the most negative real part of any eigenvalue of the system, the integrator equation defined in (4) with $z = \exp(-kt)$ gives good results. Furthermore, it is only necessary to estimate the most negative eigenvalue. Its exact value is not required. A subroutine TSTEP has been written to determine h at each step. The size of h is inversely proportional to the maximum magnitude of the derivatives at each step. SUBROUTINE INTGRL and SUBROUTINE TSTEP appear in the appendix of

this report. Also in the appendix, the proper calling sequence in a simulation is illustrated as is the proper arrangement of arguments for SUBROUTINE INTGRL. SUBROUTINE INTGRL has three arguments, a, b, and y, where y is the variable to be integrated, a is that portion of \dot{y} which is contributed by off-diagonal elements of the matrix A which defines $\dot{y} = Ay$, and b is the diagonal element of A which represents the coefficient of y in the calculation of \dot{y} .

There is a pitfall to be avoided when using this hybrid Euler method.

With

$$y_{n+1} = (y_n + h(a + zby_n)) / (1 - (1 - z)hb), \quad 0 \leq z \leq .5, \quad \text{and } h > 0,$$

there is a possibility for division by zero if b is positive. If the diagonal elements of the matrix A are all negative, there is no problem with division by zero. If one or more of the diagonal elements of A are non-negative, the step size h is limited. Some stability matrices possess non-negative diagonal elements. If a non-negative element appears on the main diagonal of matrix A, one should first seek to interchange equations to obtain only negative diagonal elements. This is not always possible. Work continues to find a suitable method of solving this problem.

References

- [1] Shampine, L.F. and C.W. Gear, "A User's View of Solving Stiff Differential Equation," SIAM Review, 21 (1979), pp. 1-17.
- [2] Bui, T.D., "Solving Stiff Differential Equations in the Simulation of Physical Systems," Simulation, 37 (1981), pp. 37-46.

**ORIGINAL PAGE IS
OF POOR QUALITY.**

APPENDIX

ORIGINAL PAGE IS
OF POOR QUALITY

```
00100 C BUJ'S 2X3 STIFF EXAMPLE
00200 C
00300 COMMON /HZ/ H,Z,YOOTHX
00350 COMMON /TIME/ T
00400 C
00500 C I N I T I A L I Z E
00600 C
00700 T = 0
00800 Y1 = 2
00900 Y2 = 9
01000 Y3 = -1
01100 C
01200 C CONTINUE
01300 C
01400 CALL TSTEP
01500 CALL INTEGR(19, *Y2 - 20, *Y3, -21, Y1)
01600 CALL INTEGR(19, *Y1 + 20, *Y3, -21, Y2)
01700 CALL INTEGR(40, *Y1 - 40, *Y2, -40, Y3)
01800 C
01900 C E X A C T V A L U E S
02000 C
02100 EY1 = EXP(-2.*T) + EXP(-40.*T)*(COS(40.*T) + SIN(40.*T))
02200 EY2 = EXP(-2.*T) - EXP(-40.*T)*(COS(40.*T) + SIN(40.*T))
02300 EY3 = - EXP(-40.*T)*(COS(40.*T) - SIN(40.*T))
02400 C
02500 WRITE(6,20) T, Y1, EY1, Y2, EY2, Y3, EY3, H, Z
02600 FORMAT(1X, F10.5, 3(2X, 2F7.3), 1X, F8.5, 1X, F5.3)
02700 IF(T .LT. 100.) GO TO 1
02800 STOP
02900 END
```

```

00100 SUBROUTINE TSTEP
00200 COMMON /HZ/ H,Z,YDOTMX
00300 COMMON /TIME/ T
00400
00500 GET YDOTMX FROM SUBROUTINE INTGRL
00550
00600 IF(T LE.0.) THEN
00700   WRITE(6,1)
00800   FORMAT(' ENTER MOST NEGATIVE EIGENVALUE ')
00900   READ(5,2) EIGEN
01000   FORMAT(F10.0)
01100   IF(EIGEN.GT.0.) EIGEN = - EIGEN
01200   YDOTMX = 0
01300   H = -.005/EIGEN
01400   Z = .5
01500   T = T + H
01600   RETURN
01700   ENDIF
01800
02400 HNEW = 1.05*H
02500 H = 01/(YDOTMX + 1E-10)
02550 IF(H.GT. HNEW) H = HNEW
02600
02700 IF(EIGEN*H.GT.-50.) THEN
02800   Z = .5*EXP(EIGEN*H)
02900 ELSE
03000   Z = 0.
03100   ENDIF
03200
03400 T = T + H
03500 YDOTMX = 0.
03600 RETURN
03700 END

```

C

C

C

C

1

2

C

C

C

```
00100 SUBROUTINE INTGRL(A,B,Y)
00200
00300 GET H AND Z FROM SUBROUTINE TSTEP
00400
00500 COMMON /HZ/ H,Z,YDOTMX
00600
00700 YDOT = A + B*Y
00800
00900 IF ( YDOT .GT. YDOTMX ) YDOTMX = YDOT
01000 IF ( -YDOT .GT. YDOTMX ) YDOTMX = -YDOT
01100
01200 I N T E G R A T E
01300
01400 Y = (Y + H*(A + Z*B*Y))/(1. - (1. - Z)*H*B)
01500
01600 A N T I C I P A T E YDOT AT N E X T S T E P
01700
01800 YDOT = A + B*Y
01900 IF( YDOT .GT. YDOTMX ) YDOTMX = YDOT
02000 IF( -YDOT .GT. YDOTMX ) YDOTMX = -YDOT
02100
02200 RETURN
02300 END
```

ORIGINAL PAGE IS
OF POOR QUALITY

N82 23128

A SPECTROSCOPIC EXPERIMENTAL AND COMPUTER-ASSISTED EMPIRICAL
MODEL FOR THE PRODUCTION AND ENERGETICS OF EXCITED OXYGEN MOL-
ECULES FORMED BY ATOM RECOMBINATION ON SHUTTLE TILE SURFACES

David Allan Owen, Ph. D.

Murray State University

1981 NASA-ASEE Summer Faculty Fellow

Supervisor:

Carl D. Scott, Ph. D. ES3

Aerothermodynamics Section

Thermal Technology Branch

Structures & Mechanics Division

Abstract:

A visible emission spectroscopic method has been developed in which the amounts of excited singlet and triplet oxygen molecules produced by recombination on the NASA Space Shuttle Orbiter thermal protective tiles at elevated temperatures have been determined. Rate constants and energetics of the extremely exothermic reaction have then been evaluated in terms of a chemical and mathematical model, and conclusions and implications for their potential contribution to Shuttle surface reentry heating fluxes have been drawn.

NATIONAL AERONAUTICAL AND SPACE ADMINISTRATION

LYNDON B. JOHNSON SPACE CENTER

HOUSTON, TEXAS

ORIGINAL PAGE IS
OF POOR QUALITY

Table of Contents:

I. Introduction	1
II. Model Assumptions & Reaction Mechanism	3
III. Surface Model, Adsorption Phenomena, and Energy and Entropy Consideration for Oxy- gen Recombination and Deexcitation	8
IV. Apparatus & Procedures	13
V. Results & Discussion	17
VI. Model Predictions & Conclusions	24
VII. Acknowledgments	26
VIII. References	26
Figures 1 - 16	30
Tables I - VI	46

I. Introduction:

The mode of generation and the fate of the energy released in oxygen-atom recombination reactions are of crucial importance in the operation of NASA's JSC-Houston's arc-jet tunnel facility, and are of paramount concern in the continuing, mission-by-mission performance of the Space Shuttle Orbiter during its upper atmosphere reentry.¹ Oxygen atoms generated by high frequency shock wave vibration behind bow shock of the Orbiter recombine on the reaction cured glass (RCG) surface of the low-density, 96% silica, 4% boron silicide-coated thermal protective tiles, whose surface atoms catalyze, in an apparent first order reaction, the recombination of these atoms into diatomic molecules. In so doing, these "critical" tiles absorb a fraction of the recombination energy, resulting in extreme Orbiter tile surface heating, with temperatures of about 2500°F and heat fluxes of 2-10 BTU/ft² on certain key areas of the spacecraft underside. Although these temperatures and heat fluxes have been mapped, simulated and predicted by complex, state-of-the-art engineering and computer-solved models or "codes", which now include contributions from energy lost through grey-body radiative emission, substantial arc-jet tunnel data and recent limited actual flight data suggest that the heat flux to the tiles still falls short of the amount predicted by the current heat flux models.^{2,3,4} The resulting lower accommodation of energy observed for these Tile TPS species may be more adequately explained by the release of a significant portion of the product molecules in the form of electronically excited species or "excitons", which, for oxygen, include $^3\Sigma_u^- O_2$, $^1\Delta_g O_2$ and $^1\Sigma_g^- O_2$. These excitons are all higher lying energetic forms of molecular oxygen, capable, in theory, of carrying away 20% or more of the total recombination energy.^{5,6} Some of their characteristics are enumerated in Table I. Furthermore, at the low pressures (.1-10 torr) and high temperatures (1500°K) encountered by the tile surfaces during the reentry stage, one of these species, $^1\Delta_g O_2$ or singlet delta oxygen, has a considerable radiative

lifetime of around a second. That oxygen atoms recombine on siliceous and other surfaces to produce excited species has already been established, both $^3\Sigma_u^- O_2$ and $^1\Delta_g O_2$ have been generated in this fashion.⁷ These species, among others, have been identified in upper-atmosphere phenomena such as aurora and nightglows, which are found in the regions that the Orbiter has been found to experience its greatest thermal stress during reentry.^{8,9} Apparently, emission from these excitons and those of nitrogen has actually been observed by STS-1 Shuttle pilots beginning at 63 Km. altitude.¹⁰ Recently, $^3\Sigma_u^- O_2$, one of the most energetic excitons, has been identified in glows in the upper atmosphere and also found to be a 4% recombination product of (3P) oxygen atoms.¹¹

In this report, I propose a mechanism and model for the surface-catalyzed oxygen-atom recombination reaction sequence which is consistent with data obtained through computer-assisted, band-specific emission spectroscopy of excited oxygen molecules and pressure-differential analysis of oxygen-atom concentration, at a variety of temperatures (25-300°C) and pressures (.1-2.3 torr), conditions similar to those experienced by the Shuttle during its crucial reentry phase. The mechanism proposed includes analysis of kinetics, energetics, reaction orders and recombination or deexcitation coefficients for each of the three important surface-assisted phenomena, including atom adsorption and recombination leading to desorption of oxygen molecules of all types, atom recombination and desorption leading to the major excited species produced, $^1\Delta_g O_2$, and the surface catalyzed deexcitation of $^1\Delta_g O_2$ and $^3\Sigma_u^- O_2$. Since $^1\Sigma_g^- O_2$ is formed in a steady state, energy pooling reaction from $^1\Delta_g O_2$, its characteristics could not be determined at this time.¹² In addition, we present a reevaluated picture of the surface-adsorbate profile, and from it, and previous arc-jet tunnel data, have attempted to more closely quantify the energies and entropies of activation for oxygen atom recombination and $^1\Delta_g O_2$ and $^3\Sigma_u^- O_2$ deactivation on the tile surface.^{2,3,11} In addition, we have deter-

mined what we believe are only the second set of $^1\Delta_g$ molecule-deexcitation coefficients, γ'_w and γ'_t , for this particular exciton.¹³ The numbers obtained both experimentally and through interpretation offer conclusions about the oxygen-recombination and deexcitation phenomena on RCG-coated tile surfaces, and has allowed us to formulate initial ideas about the analogous atom and exciton phenomena involving nitrogen, which we hope to be able to study.

II. Model Assumptions and Reaction Mechanism:

Previous data published on oxygen-atom recombination reactions in tile-like, siliceous surfaces, are all consistent with the model assumptions that we have adopted and enumerated below.

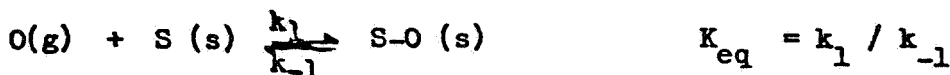
- 1) Oxygen-atom recombination reactions are apparently first order in oxygen concentration at low pressures, but develop a second order component at higher gas pressures or flow velocities, indicative of a marked change in surface site populations. We have observed this effect in certain of our experiments.¹⁴
- 2) Oxygen atoms recombine on siliceous surfaces to form a predominance of ground state molecules, but a fraction of excited species have been produced as well.^{11,15,16}
- 3) Oxygen-atom recombination is very rapid when compared with surface catalyzed exciton deexcitation, leading to the expected result that a significant amount of recombination energy may be carried away in the form of excited species.
- 4) Oxygen atom recombination is extremely fast when compared with oxygen-exchange with glass surface B-O or Si-O units.
- 5) Calculated low energies of activation indicate that no strong bonds are broken in the rate determining reaction steps, but the rather large and negative calculated entropies of activation indicate that surface orientation is important in the rate-determining steps.^{2,17}
- 6) The surface modelled is a uniform, typical, silicate-like medium with 10^{15} to 10^{16} Si-O-Si "sites"/cm², and is rather sparsely occupied by adsorbate atoms and molecules under the conditions of low pressure and high temperature characteristic of Shuttle reentry. No multilayer adsorption exists.¹⁷
- 7) The RCG sites are behaving in the Polyani sense as a repulsive surface, i.e., ground state and excited state O₂ molecules are leaving with high recoil energy, and hence, imparts the RCG surface material with a relatively low value of the energy accommodation coefficient, β .¹⁸

ORIGINAL PAGE IS
OF POOR QUALITY

The following reaction mechanism is consistent with all previous oxygen atom recombination data and with our initial excited species determination data.^{2,3} We hope to supplement it with microcalorimetric recombination data in the near future.

I. Atom Adsorption:

In a rapid, equilibrium-controlled adsorption step, oxygen atoms are weakly chemisorbed ($\Delta H = 6-10$ Kcal/mol.) onto surface sites, which are oxygen atoms in Si-O-Si linkages, and electron-rich. At lower temperatures, and hence at slower recombination rates, an appreciable fraction of all possible surface sites are so occupied, or are occupied by other product molecules. This condition is also met under conditions of higher gas pressures:



In such a process, since $\Delta n_g = -1$, and $\Delta H_{ads} = (-)$, we would expect a moderate and negative entropy contribution to the reaction kinetics.

During shuttle reentry conditions, as well as under early flow conditions in our experimental apparatus, and especially at the lower temperatures where surface coverages are higher and effective recombination rates are lower, atom recombination can be appreciably slowed by competitive site occupancy by product molecule species:

$$K_{eq} = k_1/k_{-1} = \frac{[S-O]}{[S_o][O_o]} = \frac{[S-O]}{([S_o]-[S-O])[O_o]}, \text{ when } [O_o] \gg [S_o].$$

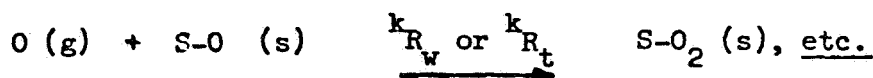
As such, $K_{eq}(\text{early}) = k''/[O_o]$, or the reaction rate is held up or depends on $1/[O_o]$, and the reaction has a second order component. At later flow conditions in our experimental apparatus, or at very high temperatures and/or low pressures, when $[O_o] \ll [S_o]$, there are more free sites than occupied ones, and the rate is not controlled or held up by site occupancy. The experiments of Scott and Myerson are consistent with this behavior.^{2,13} When $[S_o] \gg [O_o]$, then $[S_o] = [S_o] - [S-O]$,

and $K_{eq} = \frac{[S-O]}{[S_o]([O_o]-[S-O])}$. At this point the rate of reaction ceases to depend on $1/[O_o]$, but follows the typical first order, logarithmic behavior. Certain of our

data is consistent with this apparent order change with coverage change, for as $3\tau_u$ oxygen exciton concentration as measured by intensity of emission drops, the second order dependence on concentration is replaced, at a surface-glutted transition point, by a first order dependence. We believe that the apparent low recombination and deexcitation coefficients observed for oxygen on siliceous surfaces are consistent with an inability of the "glutted" surface to rapidly catalyze recombination of atoms, and hence, an inability to accept a relatively large portion of the potential recombination energy carried to it by oxygen atoms and excitons.

II(a). Direct, Rate-determining Reaction of Gas-phase Atoms with Surface-fixed Adsorbate Atoms:

In a slower, rate-determining reaction, it is possible that gas-phase oxygen atoms next strike the atom-occupied surface sites, and recombination occurs immediately with formation of surface-bound adsorbed ground state molecules and excitons; depending on the surface site distribution:



In such a process, since $\Delta n_g = -1$, and $\Delta H = (-)$, we would expect a large and negative entropy contribution. This process would also be favored under the conditions of high temperature and low pressure, where recombination rates would be high and surface occupancy by adsorbed products and other molecules would be small. A suitable rate expression for this reaction is:

$$\text{rate} = d[O]/dt = k_{R_t} [O_x][S-O]$$

At high $[O]$ concentrations, or under our apparatus conditions, at early reaction, since $[S-O] = K_{eq} [O_x][S_o] - [S-O]$, the rate = $k_{R_t} K_{eq} [O_x]^2 [[S_o] - [S-O]]$ or $\propto [O_x]^2$.

But, at lower $[O]$ concentrations, since $[S-O] = K_{eq} [S_o][O_x] - [S-O]$, the rate expression becomes $k_{R_t} K_{eq} [O_x][S_o][O_x] - [S-O]$, or $\propto [O]^1$. Our experimental results are in accord with the order change predicted for a surface of varying occupancy.

II(b). Rate Determining Surface Migration of Adsorbate O-Atoms:

Another reasonable recombination step involves on-surface recombination of oxygen atoms by migration:



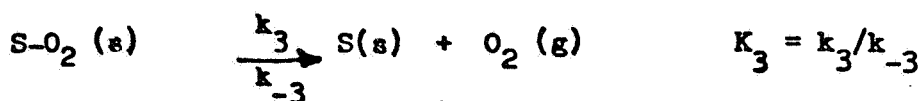
In such a process, since $\Delta n_g = 0$ and $\Delta H = (-)$, but less negative, since half of the adsorption energy is lost, the entropy change would be expected to be relatively modest, or even positive, since there has been no decrease in the number of moles of gas nor no increase in surface ordering. Since $[S-O] = K_{eq} [S_o] [[O_o] - [S-O]]$, the rate of the process might be expected to follow the law:

$$\text{rate} = k_{R_s} [S-O]^2 = k_{R_s} [S_o]^2 (K_{eq})^2 [[O_o] - [S-O]]^2$$

and hence, would be independent of $[O]$ concentration. Since our data does not, at this time, support this rate phenomena, and the data of Scott and Myerson is also not consistent with it, we tentatively propose that step II(b) is much less important than the gas surface alternative II(a). Migration of atoms bonded to metallic surfaces has been reported, but involved rather large activation energies.^{19,20,21} Such processes were followed using field ion microscope measurements. Energetic for such surface-adsorbate atom jumps are on the order of 3-22 Kcal/mole, comparable with the oxygen atom energies of activation found by Scott.² It is possible that both surface-surface and surface-gas recombination phenomena are occurring simultaneously.

III. Rapid, Equilibrium-controlled Desorption of Recombined Molecules:

In the final step, product ground state and excited molecules are desorbed in an equilibrium reaction from the surface. At higher temperatures and low gas concentrations, this process should approach an equilibrium, and should not control the rate of formation of products in any fashion:



In our experiments, where $^1\Delta_g O_2$ and $^3\Sigma_g O_2$ (ground state) are approximately constant at any tube position, and $^1\Sigma_g O_2$ is generated in steady-state fashion, we can estimate values of K_3 for each of these species, as:

$$K_3 = \frac{[O_2]([S_0] - [S-O_2] - [S-O])}{[S-O_2]}$$

At early apparatus conditions, or under the conditions of low temperature and/or high gas pressure, the k_{-3} reverse reaction will tend to impede the forward recombination reaction, but at late apparatus conditions, or under typical Shuttle flight conditions of low oxygen concentration, high temperature, and lower pressure, there will be no rate retardation, and recombination should follow typical first order kinetics. Our work is consistent with this model, and Scott's data on arc-jet recombination can be interpreted in this fashion. Following this behavior, Scott, Melin and Madix, noted that γ_o values increase with an increase in temperature, consistent with more rapid desorption rates for product oxygen molecules, leaving more surface area available for recombination at higher temperatures and hence a larger expected recombination efficiency and energy accommodation.^{2,15} The reaction path vs. energy profile pictured in Figure 1. is consistent with the observed energetics and entropies and our proposed mechanism. With a rate-determining step like II(a) above involved, it is likely that the surface can accept up to one-half of the available recombination energy, resulting in a β -value of less than, or at most equal to, 0.5. This premise is based on similar conclusions drawn by Melin & Madix in their studies of oxygen-atom recombination on metal surfaces.¹⁵ We have not, as of August 1981, quantified the energy accommodation by the surface for excitons, but in a continuing series of calorimetric experiments, due for completion this coming year, will determine a β -value for the energy accommodation for deexcitation of $^1\Delta_g O_2$.

III. Surface Model, Adsorption Phenomena, and Energy and Entropy Considerations

For Oxygen Recombination and Deexcitation:

One of the major problems for a person in developing a mechanism for atom recombination on Shuttle TPS RCG tile materials involves the nonuniform, irreproducible nature of the tile surface itself. The species' surface has been heretofore assumed to have many of the characteristics of quartz and other siliceous materials, as extrapolated from its physical properties and from its 96% silica, 4% boron silicide composition, although, contrary to quartz and many other glasses, it has been shown by electron diffraction and scanning electron micrography that the tile surface undergoes alteration (through apparent oxidation), when exposed to oxygen at elevated temperatures for extended periods of time. To suggest that it is a uniformly catalytic substance over all regions is more than a gross assumption, but one that we were forced to make. From previous calculations, we can be sure there are, on the average, about 10^{15} to 10^{16} surface active "sites" per cm^2 , and the surface, in general, resembles other silicates.²³ Interaction of O-atoms with quartz and other silicate surfaces such as RCG are presumed to occur through rather weakly chemisorption interactions, on the order of 6-20 Kcal/mole, while adsorption of ground state oxygen or its higher-lying excitons are presumed to occur through even weaker, physisorption interactions, on the order of the enthalpy of adsorption, of 2-6 Kcal/mole. These result in widely spaced adsorbate interactions. It has been estimated that only 10^{-2} to 10^{-4} of the potential site area is covered at any time, with available mole site spacings of $\Gamma = 10^{-10}$ to 10^{-9} moles/ cm^2 .²¹⁵ In any case, exchange of adsorbed O-atoms or O_2 molecules with oxygen bound in surface Si-O-Si units proceeds prohibitively slowly when compared with atom recombination or exciton deexcitation. That recombination or deexcitation takes place at only a fraction of the possible or potential surface sites aids in explaining the low values observed for γ , γ' , and β for these systems. These low reaction and energy recombination and energy accommodation coefficients contrast

ORIGINAL PAGE IS
OF POOR QUALITY.

strongly with those previously determined for platinum; silver, copper, nickel, and the other transition metals.^{15,16} There it is assumed that nearly all of the surface atoms may serve as a template for recombination or for exciton-specific deexcitation, with concomitantly higher γ, γ' , and β values.^{13,14,15} These metal surfaces have also been shown to be readily poisoned or deactivated catalytically by introduction of foreign atom layers, which usually adopt well-ordered surface positions atop the regular metal lattice, and as such, can be rather precisely located using low energy electron diffraction techniques (LEED Spectroscopy).^{27,28} One might a priori expect that introduction of the boron silicide $B_{12}Si_3$ subgroups into the RCG surface region to cause the surface to have a considerably lower catalytic recombination coefficient than quartz or other siliceous materials, but in fact, the reverse has been shown to be true. 2

It was beyond the capabilities of our research team to closely define, elucidate, or even approximate the average nature of the RCG surface. Thus, any deexcitation or recombination data must be discussed in terms of an imaginary average surface with approximate kinetic, energetic, and entropic parameters. In theory, when a reaction such as recombination takes place on a nonuniform surface, in which there is a variation in site-types, both the resultant site adsorbate populations and their energies of activation for a particular reaction are different.¹⁷ It is even conceivable that the sites differ in enough respects that different products may be preferred from them. Assuming that all of the different site types are more or less equally but sparsely (10^{-2} to 10^{-4}) occupied, then the kinetics and energetics may be averaged, and the reaction rate expressed as:

$$\text{rate} = \frac{\Gamma_0 k T}{\Gamma_T h} (e^{-E_{a1}/RT} \cdot c_1 + e^{-E_{a2}/RT} \cdot c_2 + e^{-E_{a3}/RT} \cdot c_3 + \dots)$$

$$\text{or rate} = \frac{\Gamma_0 k T}{\Gamma_T h} \sum_{i=0}^{\infty} c_i e^{-E_{a_i}/RT}$$

In our flow apparatus experiments, we made the very simplistic assumption that there were only two types of sites, v , or pyrex, and t , or RCG tile. Our later deexcitation k values showed that the tile sites are nearly chemically indistinguishable from the glass sites. In the flow experiments, with the tiles absent, $c_1 = c_v = 1.0$, and when the tiles were present, $c_1 = c_v = .663$ and $c_2 = c_t = .337$. We analyzed each of these arbitrary site types as uniform, with the full understanding that they could each be further subdivided, and with the knowledge that the RCG tile sites, at least, were constantly being modified by oxygen atoms at the elevated temperatures of our experiments.

Adsorption Times and Equilibria:

For the first and last steps of the proposed recombination process, we assume that these reactions are governed by typical, physisorption phenomena. If there were no attractive forces at all between oxygen atoms or molecules to surface sites, the residence time τ would be expected to be on the order of a single molecular vibration, which, for O_2 , would be $\tau_{O_2} = 10^{-12}$ seconds. The interaction energy Q and energy accommodation coefficient β would both be essentially zero for this "hot" atom and cold surface and the particle would strike the "cold" surface and rebound with all of its energy, with none transferred to the surface, and no chemical reaction there would have time to occur. However, since coulombic or electrostatic or electronic attractive forces are present, a nonzero energy of interaction results. This value of Q is on the order of the enthalpy of adsorption, and results in a measurable accommodation coefficient β , since more chemical energy is thus transferred to the surface. The time of surface residence is expressed as:

$$\tau_w = \tau_o e^{Q/RT} \quad T = \text{Kelvin}, R = .001987 \text{ Kcal/mole}$$

As expected, the residence time of adsorption decreases with an increase in temperature. As adsorbate species gain the needed activation energy (E_{aI} or E_{aIII} in

Figure 1.), they are able to escape their surface sites and free them for other species. It is safe to assume that when τ_x is as large as several vibrational periods, that rather strong chemisorption has occurred, and a considerable amount of energy is accommodated by the surface. In our study of deexcitation of delta oxygen by surface sites, it has been calculated that only about 1 of 40,000 surface-exciton collisions possesses a long enough residence time for deexcitation to occur.^{15,38}

Langmuir developed relationships that connect the process of chemisorption to ordinary kinetic parameters, expressing the rates of adsorption and desorption in terms of molecular properties. The rate constant for desorption, important in steps I and III of our mechanism, is related to the adsorption time τ_0 as:²⁸

$$k_{-1}(\text{O-atoms}) = 1/\tau_0 \cdot e^{-Q_0/RT} \quad \text{and} \quad k_3(\text{O}_2 \text{ molecules}) = 1/\tau_{\text{O}_2} \cdot e^{-Q_{\text{O}_2}/RT}$$

Assuming τ_0 and τ_{O_2} to be 10^{-12} sec, and Q_0 to be 10 Kcal/mole and Q_{O_2} to be 6 Kcal/mole, k_{-1} and k_3 may be obtained, assuming a temperature of 300°K. These results are:

$$\begin{array}{ll} k_{-1} = 5.2 \times 10^4 / \text{sec} & \tau_0 = 1.9 \times 10^{-5} \text{ sec} \\ k_3 = 4.3 \times 10^6 / \text{sec} & \tau_{\text{O}_2} = 2.35 \times 10^{-7} \text{ sec} \end{array}$$

The rate constants for adsorption, or the reverse reaction, may be expressed as a function of the number of particles striking the catalyst surface, which is considered to be a 2-dimensional box of site area σ_0 , which follows the relationship:²⁸

$$k_a = N_0 / (2\pi MRT)^{1/2}, \text{ in cm}^2 / \text{mole} \cdot \text{sec}$$

Solving this expression at 300°K and assuming values of $\sigma_0 = 10^{15}$ sites/cm² for O-atoms and 5×10^{16} sites/cm² for O₂ molecules, gives rise to the adsorption constants, assuming 1 torr total pressure, 27% O atoms, 73% O₂ molecules:

$$\begin{array}{ll} k_1(\text{O-atoms}) = 3.3 \times 10^{18} \frac{\text{atoms} \cdot \text{sec}}{\text{cm} \cdot \text{cm}^2} & K_{\text{eq}} = 6.1 \times 10^{13} \frac{\text{atoms} \cdot \text{sec}^2}{\text{cm}^2} \\ k_{-3}(\text{O}_2 \text{ molecules}) = 3.2 \times 10^{18} \frac{\text{molecules} \cdot \text{sec}}{\text{cm}^2} & K_3 = 7.4 \times 10^{11} \frac{\text{molecules} \cdot \text{sec}^2}{\text{cm}^2} \end{array}$$

should be strongly pointed out that changes in σ_0 area, by occupancy of the limited

number of surface sites, can strongly alter the values of K_{eq} and K_3 , and disturb the equilibria in these steps. Such predictions find support in our early-reaction tube, high-pressure, low temperature second order effects noted for both deexcitation reactions.

Energy and Entropy of Activation, Oxygen Recombination:

Previous work by Scott² and Melin and Madix¹⁵ showed that oxygen atom and nitrogen atom recombination coefficients at elevated temperatures exhibited temperature dependencies indicative of small energies of activation for the recombination processes. In addition, each term contained a small preexponential term which could be factored into a temperature dependent collision frequency parameter and an entropy of activation, S_a , or surface orientation parameter. In general, the various contributors to a given reaction kinetic expression are:¹⁷

$$k_w = Z e^{S_a/R} e^{-E_a/RT} = \frac{kT}{h} e^{S_a/R} e^{-E_a/RT}$$

Scott's data fit the recombination expression:²

$$\gamma'_0 = 16 e^{-10271/T_w}, \text{ where the value of } T_w \text{ was about } 1525^\circ\text{K.}$$

From the well-known expression relating the forward reaction velocity to γ'_0 :

$$k_w = (kT/2\pi m)^{1/2} \gamma'_0 = (kT/2\pi m)^{1/2} \cdot 16 e^{-10271/T_w}$$

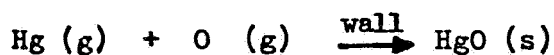
Now, using the value of k_w assumed by Scott, 1040 cm/sec for Shuttle flight reentry, and assuming that the enthalpic term has unity coefficient, $E_a = +20.4$ Kcal/mole and $S_a = -41.4$ cal/ $^\circ\text{K}$ at 1525 $^\circ\text{K}$. Working from a different direction, assuming no specific value for k_w , by equating the two expressions for k_w , and then substituting into the well known expression for γ'_0 , with constant E_a at 1525 $^\circ\text{K}$, S_a values of about -45.3 cal/ $^\circ\text{K}$ are obtained. These large and negative values for S_a are all consistent with the proposed surface-catalyzed mechanism, with a rate-determining step in which there is either a decline in the number of moles of gas, and/or in which a gaseous species is adsorbed on the surface on limited sites. Table III summarizes energies and entropies of activation for recombination and deexcitation reactions for oxygen and nitrogen.

IV. Apparatus & Procedures:

Determination of the identities of, concentrations of, rates of formation of, and rates of deexcitation or quenching of $^3\Sigma_u^- O_2$, $^1\Sigma_g^- O_2$, and $^1\Delta_g O_2$ excitons in the presence of one another and in the presence of ground state oxygen and 3P oxygen atoms, over a temperature range of 25° to $550^\circ C$ and a pressure range of 0.1 to 2.28 torr, is a ticklish procedure, and required construction and constant modification of a complex apparatus.^{7,12,29,30,31} Through generous support of NASA, under contract #NAS-9-16254, and through Murray State University's Committee on Institutional Studies & Research, under grant #CISR-777, along with other needed equipment and microcomputer hardware and software furnished by our Collegiate Dean and Vice President for University Services, we fabricated and/or assembled the components of the discharge-flow, band-specific emission spectroscopic, computer assisted reactor-detector apparatus for excited oxygen species, pictured in Figure 3. Pure, ground state oxygen was first precooled to remove condensable impurities such as water vapor, which were known to "quench" or deexcite oxygen excitons.^{11,32,33} The gas was then pressure pumped and vacuum pulled through a gas-flowmeter into the discharge region, at pressures of 0.1 to 3.0 torr, and using flow rates of 2 to $20 \text{ cm}^3/\text{sec}$ (at STP). The gas stream so developed had average forward velocities of 100 to 600 cm/sec. Some of the typical gas flow parameters are listed in Table II. In the 12 mm quartz discharge tube region, the oxygen flow stream was excited and partially dissociated into atoms. Conversions were in the 15-40% range, although 26-27% dissociation, as determined by pressure drop measurements, were common. Dissociation was accomplished using 2450 MHz microwave radiation from a Raytheon power source and microwave generator, operating at power ratios of 70 to 120 watts.^{29,31} The radiation was carefully tuned using an air-cooled teflon tuning bar, was monitored with a jackmeter, and shielded from operating personnel in an aluminum housing.

ORIGINAL PAGE IS
OF POOR QUALITY

After passage through the discharge system, the gas stream was passed through a series of light traps to cut down any visible light from the discharge region from reaching the detector. The gas stream could be partially saturated with mercury vapor, which could cause recombination of oxygen atoms when their presence in the detector was unwanted. In order to remove the products of this reaction, a condenser was also placed in the line, in which mercuric oxide, HgO, occasionally formed:



The gas stream was then passed by a stopcock that led to a nitrogen dioxide gas reservoir, whose contents could be used to "titrate" the amount of atomic oxygen present in the mixture, by the reaction:^{24,25}



The pressure was monitored at this point, and at several other convenient places, by use of a Varian vacuum gauge, as an alternate measure of O-atom concentration. The gas stream was then passed into a 4.61 cm i.d. pyrex reactor/detector tube set firmly in an insulated, circulating oven, of which a 1 cm viewing slit was open to the photomultiplier detection system. The photomultiplier tube was powered by a variable high-voltage power source operating at typical voltages of 1400 to 1800 volts. It was necessary to use narrow band filters with each photodetector, in order that the radiation detected be in a relatively narrow range, of about 100 angstroms. In this way it was possible to detect the presence of a particular exciton by measuring the intensity of its most intense radiative band. We used the 6340 angstrom emission for $^1\Delta_g \text{O}_2$, and the 2800-4000 complex for $^3\Sigma_u \text{O}_2$. Although $^1\Sigma_g \text{O}_2$ could be detected using a near infrared photodetector at 7619 angstroms, since it was constantly being replenished in the gas phase from $^1\Delta_g \text{O}_2$ in an energy pooling reaction, it was not measured, for it was generated in steady state.

The complete visible emission spectrum for diatomic oxygen is presented in Figure 4. The photomultiplier tubes were mounted on a "car" driven by a gear chain and a stepping motor, and could be driven in either direction along the 43" or 109.2 cm of the viewing slot of the detector tube so that a radiation profile with a distance parameter, in cm., could be obtained. By multiplying the distance parameter by the gas flow rate, a reaction time vs. tube position could be obtained. Assumptions made in this extrapolation included laminar flow by the gas, constant tube diameter, and an average gas flow rate calculated by the expression:

$$\bar{u} = V/.5\pi R^2 \quad \text{or} \quad \bar{u} = .12V, \text{ in cm/sec}$$

where \bar{u} was the average gas flow velocity corrected for temperature and pressure, V was the average gas flow volume, corrected for temperature and pressure, and R was the constant radius of the tube, 2.305 cm. The flow profile was assumed to follow the laminar pattern pictured in Figure 5a.³⁴ The detector could be driven either manually or by a computer. Typical scan rates used .58 cm/step and 250 steps/minute. Chart speed variation allowed spreading or attenuating a spectrum or any part of one, in order to obtain more accurate slopes for analysis. As data was taken at each point, it was also plotted on a cathod ray screen through operation with our 48K Apple II Plus microcomputer and peripherals. A modified Applab[®] plotting program was utilized. Gas pressure and temperature were monitored at three points within the reactor profile, at 0, 25 and 75 cm, and another pressure reading was available after the gas passed out of the reactor tube.

After detection and nearly total recombination and/or deexcitation, the often hot gas stream was pumped through a flw-limiting final stopcock. Experience showed us that the oxygen released from the reactor had to be cooled before it was passed into the Duoseal filled vacuum pump. A Dewar flask filled with dry ice/acetone was used for this purpose. One of the major early problems encountered

in the project was getting the number of molecules or mass of oxygen passed through in order to get good visible emission from these excited species. This was finally accomplished by using a pump of 500 liters/minute pumping capacity, and constantly changing the oil in the pump. One of the easiest measurements to obtain was the gas flow volume per unit time, for during a run, all exit gases pumped from the reactor could be collected by displacement at a given temperature, and using the ideal gas relationship, the amount of material could be very accurately determined.

Runs were obtained at different pressures and temperatures, with or without tiles present in the apparatus. It was found that eight 1.6" x 6" tiles, cut to a hemicylindrical shape, could be placed contiguously in the chamber, in such a fashion that they filled slightly less than one-half of the tube and had an effective surface fraction in the tube of 0.337. The modified D-shape of the tube was then normalized to a slightly smaller cylinder, and the gas flow average velocities were calculated from the relationship $\bar{u} = .179V$ cm/sec. Particular excitons could be attenuated by the use of Co or Ag metal coils, and mercury vapor could be used to remove oxygen atoms, although it tended to reduce the amount of ${}^3\Sigma_u^- O_2$ as well. These different experiments allowed collection of enough data to obtain rather good kinetic parameters for two of the exciton species, as well as a temperature dependence of rate constants for deexcitation, and calculation of energies of activation. In addition, we found that, at late tube conditions, reaction rates were proportional to gas velocity as well. Estimates of deexcitation coefficients, γ'_w , were also obtained.

ORIGINAL PAGE IS
OF POOR QUALITY

V. Results & Discussion:

The filtered radiation detected by the photomultiplier tube was expressed in terms of a current, and was measured at each tube position(x, cm) and recorded. It was assumed that the radiation intensity was exactly proportional to the number of atoms undergoing radiative decay, and that the decay process was at least 10^3 times slower(guesses of 10^4 have been made^{16,38}) than the wall or tile deactivation process. The further assumption made was that the relationship between intensity and particle number was everywhere linear, and followed Beer's Law in the fashion:

$$I_x = [^1\Delta_g O_2]_x \cdot a, \text{ where } a \text{ was a proportionality constant } \frac{I_1}{I_2} = \frac{[^1\Delta_g O_2]_1}{[^1\Delta_g O_2]_2}$$

In order that intensity always reflect a given number of delta particles, the photomultiplier shutter opening and the photomultiplier voltage were kept constant throughout a series of runs, averaging 5mm and 1600 volts for the $^1\Delta_g O_2$ determinations and 5 mm and 1400 volts for the $^3\Sigma_u$ "green glow" determinations, respectively. All spectra were recorded over the entire 43" or 109.2 cm tube opening distance. It was assumed that time-distance steady-state reaction conditions were in force soon after the emission had begun.

Typical decay profiles of intensity vs. tube position, cm., are shown in Figures 6 and 7. More data of this type are available upon request, since over 40 runs have been made to date (August 17, 1981). The results indicated that $^1\Delta_g O_2$ is deactivated or quenched on pyrex or tile surfaces only about 1/5 as quickly as $^3\Sigma_u O_2$. Plotting the intensity data on semilogarithmic paper indicated, that at tube positions of 50 cm or greater, in a "downstream" sense, that good first order kinetic plots were obtained for the decay of each exciton. Examples of these are given in Figures 8 and 9. These plots were corrected for reproducible "equipment variations", such as the enhanced(vs. apparent decay) tube regions shown in Figures 6 and 7 at about 35-50 cm. The regions where the discrepancies occurred coincided with entry ports used for pressure measurements and other operations. The plots of distance vs. \log_{10} intensity were analyzed in typical fashion

to give first order position rate constants, κ , /cm. These were temperature and velocity dependent, but more or less independent of pressure. They were reminiscent of the types of rate constants determined by Winer and Bayes by a different, chemical, assay method.³⁸ Values for $^1\Delta_g O_2$ were .004 to .008/cm, while values for the more reactive $^3\Sigma_g O_2$ were .017 to .042. It was found that each position rate constant κ could be multiplied by the average gas velocity \bar{u} , in cm/sec, to give a more universally useful time-dependent rate constant, k , /cm. The rate constants obtained by this method for both excitons are enumerated in Tables V. and VI.

Each plot had an interesting region in which the reaction rate law was rapidly changing. It averaged out to an order of about $[I]_x^{1.4}$, and the "early" part of the tube regime for each exciton displayed a region in which a second order reaction was occurring. This region was in the first 25 cm of the tube. The next 25 cm was one of mixed rate, and by the time 50 cm had been reached, the regular, first order rate law was observed. Figure 10 shows a plot of early tube position vs $1/[I]_x$.

The second order behavior was clear. These "early" tube effects were consistent with several possible causes:

- (1) Laminar flow had not yet fully developed, so that surface-normal velocities were rapidly changing and eddying caused by entrance effects was enhancing the rate. That an exact second order effect should result was puzzling.
- (2) There were significant gas-gas deactivation reactions occurring in this regime of the flow apparatus, where the species density was higher and enhancement of a two-body reaction was expected, as might be a second order behavior for it.
- (3) In this region of higher concentrations of undeexcited excitons, there was a preponderance of atom- or exciton-filled surface sites, leading to surface "glutting", and causing an expected $1/[I]_x$ rate dependence, as discussed on pp. 4-6.

This second order effect could be attenuated and even apparently removed by three techniques:

- (1) by increasing the temperature of the gas stream
- (2) by decreasing the gas flow rate to near or below $100 \text{ cm}^3/\text{min}(\text{STP})$
- (3) by a combination of (1) and (2)

The second order effect was more or less independent of pressure. This effect is mentioned by Bayes and Winer³⁸, who evaluated it in terms of gas-gas phase recombination. In order to test their hypothesis, we performed a series of experiments. First, in order to determine if any special entry effects were responsible for the behavior, we decided to see if the "early part" of the apparatus was in any flow-sense unique. We calculated at what length \underline{l} , surface or eddying effects should have been minimized, that is, when the boundary layer position for laminar flow had reached the midpoint of the reaction tube. Since our Reynolds diameter numbers for different flows were in the range of 20 to 300, there was no doubt that a rather early laminar flow would be obtained. We used the formula for boundary thickness, as determined by Blasius and Schlichting³⁴:

$$\delta \text{ (boundary layer thickness, ft.)} = 5(\nu \underline{l} / \bar{u})^{1/2}$$

where \bar{u} was the average velocity and ν was the kinematic viscosity. It was assumed that the viscosity of the excitons was similar to that of ground state O_2 . The length of tube \underline{l} , that corresponds to the midpoint, was set at the tube inner radius $R = 2.305$ cm, and this equation was partially solved and rearranged to give:

$$\underline{l} = \frac{(2.305)^2 \bar{u}}{25 \cdot (30.48)^2 \nu} \quad \text{or} \quad \frac{.0000287 \bar{u}}{\nu}$$

By changing the pressure (density) and flow rate, a series of values of \underline{l} were obtained. These are displayed in Table IV. The results indicated that while there was a small prelamina regime in which the boundary layer was less than the tube radius, the values obtained for \underline{l} were much smaller than the break point of 25-50 cm., being more on the order of 0.2 to 2.55 cm. Laminar effects were essentially constant throughout the tube regime.

Since the second order or "early tube" effect was diminished by both an increase in temperature and a decrease in flow rate, we assumed that it was due to a site-filling or adsorption change in that region. Melin and Madix have discussed site

coverage as an explanation for low energy accommodation during recombination and excitation of oxygen, and their explanation is applicable here.¹⁵ Ogryzlo¹⁶ and Elias, and Winer and Bayes³⁸, and Vallance-Jones and Harrison³⁹ have all shown gas-gas deactivation to be much too slow at exciton concentrations much below 3×10^{15} molecules/cm³, and we were operating on the edge of this concentration regime.

Enhancement Effect:

When mercury vapor was not present in the system, and O-atoms were allowed to pass into the detector tube, enhanced and non-first(or second) order intensity was observed for both $^1\Delta_g O_2$ and $^3\Sigma_u O_2$ emission. The rate of appearance of additional intensity showed a poor first order factor, and gave an approximate value of $k_{w\Delta}$ of about 0.14. However, no adequate curve fitting expression could arrive at a profile similar to the intensity pattern observed, since much of the change was taking place in the "early" part of the reaction apparatus. In any case, the rate of conversion of O-atoms to excitons was at least five times faster than the $^3\Sigma_u O_2$ deactivation and 25 times faster than the $^1\Delta_g O_2$ deactivation. We are continuing to study this O-atom enhancement effect.

Calculation of Reaction Deactivation Coefficients, γ'_Δ and γ'_Σ :

Following the analysis of Winer and Bayes, we calculated γ'_Δ and γ'_Σ values for the two excitons on glass surfaces. Since the reaction rates for tile surfaces were usually about 90% of those of the pyrex system, they were assumed to give similar deactivation coefficients. Each showed a temperature dependence similar to that displayed by O-atom recombination coefficients on glass and metal surfaces(Figure 2.) The results are displayed, when plotted as $\log_{10} \gamma'$ vs. $1/T$, in Figures 11 and 12, and were calculated from the time-dependent first order rate constants, k , /sec, by converting these into the reaction rate velocity by multiplying them times a tube-characteristic dimension, C , characteristic of the tube dimension unit area:

Since k_v (cm/sec) = $(kT/2\pi m)^{1/2} \cdot \gamma'$, and k_v (cm/sec) = $k / \text{sec} \cdot C$ (cm²/cm), then :

$$\gamma_{\Delta}^{\prime} = \frac{k_{\Delta} C}{\sqrt{\frac{kT}{2\pi m}}} \quad \text{and} \quad \gamma_{\Sigma}^{\prime} = \frac{k_{\Sigma} C}{\sqrt{\frac{kT}{2\pi m}}}$$

These recombination values, were, as expected, about 10 times larger than the energy accomodation and deexcitation values reported by Winer and Bayes.³⁸ We must await refinement of our technique and determination of β , the accomodation coefficient, from our soon to be performed microcalorimetry measurements. These independent measured values of β will allow us to predict, with confidence, the γ , catalytic energy deexcitation coefficients for each of the two excitons, and hence be able to predict their contributions to tile (and shuttle) heating. Values of the two reaction deexcitation coefficients, are given in Tables V. and VI., and plotted with $1/T$ °K x 10³ in Figures 11 and 12.

Variation of κ_{Δ} , κ_{Σ} , k_{Δ} , and k_{Σ} with Temperature:

As might be expected from their great difference in electronic energy and structure, the two excitons gave quite different temperature rate constant behavior. When the temperature of the ¹ Δ_g O₂ stream was increased, only a small rate enhancement was observed for κ_{Δ} /cm, and a small, but larger, as expected increase for k_{Δ} /sec ascribed to an increase in gas velocity. The small change in activation energy was calculated over a rather wide temperature range, 25 to 280 °C, and was calculated using the Arrhenius Law:

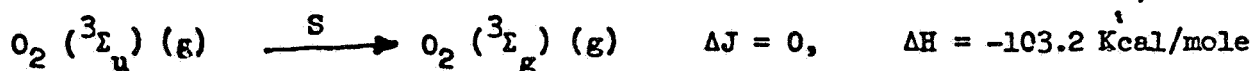
$$\log_{10} \frac{k_{\Delta 2}}{k_{\Delta 1}} = \frac{E_{a\Delta} (1000)(T_2 - T_1)}{4.57(T_2)(T_1)} \quad \text{or} \quad E_{a\Delta} = \frac{(4.57)(T_2)(T_1) \cdot \log_{10}(k_{\Delta 2}/k_{\Delta 1})}{1000(T_2 - T_1)}$$

The result was a very low energy for ¹ Δ_g O₂ deactivation of 0.34 to 1.1 Kcal/mole, which indicates that the reaction mechanism is not enhanced by kinetic energy, but is probably dominated by an electronic parameter in the spin-forbidden reaction:



Evidently the surface is not able to provide spin crossing for the system.

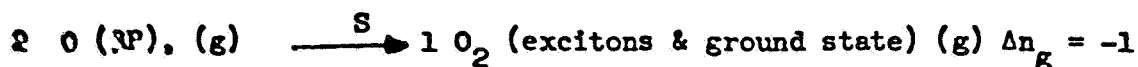
As expected for the spin-allowed conversion of ${}^3\Sigma_u O_2$ to ground state, ${}^3\Sigma_g O_2$, we noted a much greater temperature dependence for this process, with an energy of activation in the 6.7 to 8.6 Kcal/mole range. The reaction was so facile that the ${}^3\Sigma_g O_2$ intensity would fall to near zero at very short tube position when the temperature is raised only 100°C. In this deactivation process, which proceeds without spin change, the tile or pyrex surface need not interact electronically with the exciton, which can release its energy in a quite exothermic and spin-allowed reaction:



We predict that when energy accommodation coefficients for each exciton are obtained, that the ${}^1\Delta_g O_2$ state will have a very low value when compared with ${}^3\Sigma_u O_2$. Plots of \log_{10} (deactivation position-dependent or time-dependent rate constants) for the two excitons with change in temperature as $1/T \text{ } ^\circ K \times 10^3$ are displayed in Figures 13, 14, 15 and 16, and the data is arranged in Tables V and VI.

Attempted Evaluation of Oxygen Atom Recombination Rates by Pressure Difference:

It was noted early on that the total gas pressure, when measured at the pump end of the reaction tube, or at a port 75 cm or about 3/4 of the way down the tube, was about 13-15% lower than the value measured prior to gas entry into the reaction tube. It was suspected that this pressure drop was not a flow property, dealing with surface shear, and calculations showed that this shear could amount to no more than 1% of the observed pressure drop. The pressure drop was then believed to be derived from recombination of oxygen atoms into excitons and/or ground state O_2 over the distance of the tube. As expected, when O-atoms were "scavenged" by the use of mercury vapor, no detectable pressure change was observed in the entire tube regime. The drop in pressure, then was due to the loss of one mole of gas by the reaction(s):



The following pressure differential method and attendant rate law was worked out to test on the pressure drop data:

Let the change in pressure of the recombined oxygen at pos. $x = -2p_x$, where p_x is the difference in pressure between the oxygen atoms before recombination and their products, which are all O_2 molecules, ground state or excitons. $P_{O_0} - p_x = P_{O_x}$ (1)

At tube position 0, let the pressure of oxygen atoms be P_{O_0} , at position x , P_{O_x} , and at the end of the tube, when all recombination has occurred, $P_{O_\infty} = 0$.

Let P_T = the total pressure at any time or position; P_{T_0} , initial total measured pressure; P_{T_x} , the pressure at any tube distance x , cm; and P_{T_∞} , the pressure measured at the end of the tube after all oxygen recombination has occurred.

For a second-order recombination reaction: k_R = recombination rate constant

$$\frac{p_x}{P_{O_0}(P_{O_0} - 2p_x)} = k_R \cdot x \quad \text{or} \quad k_R = \frac{p_x}{x(P_{O_0})(P_{O_0} - 2p_x)} \quad (2)$$

Since all production of recombination from O-atoms results in a drop of pressure equal to $1/2 P_{O_0}$:

$$P_{T_\infty} = P_{T_0} - 1/2 P_{O_0} \quad (3) \quad \text{or} \quad P_{O_0} = 2(P_{T_0} - P_{T_\infty}) \quad (4)$$

Substituting (1) into (2):

$$\frac{p_x}{x(2(P_{T_0} - P_{T_\infty}))(2P_{T_0} - 2P_{T_\infty} - 2p_x)} = k_R \quad (5) \quad \text{or} \quad k_R = \frac{p_x}{4x(P_{T_0} - P_{T_\infty})(P_{T_0} - P_{T_\infty} - p_x)} \quad (6)$$

Now, substituting $p_x = P_{T_0} - P_{T_x}$ into (6) affords the final expression:

$$\frac{(P_{T_0} - P_{T_x})}{4x(P_{T_0} - P_{T_\infty})(P_{T_x} - P_{T_\infty})} = k_R \quad (7)$$

It is clear that the pressure need only be measured at three positions to give a value for k_R , at the tube entrance, exit, and at some measured point x . The curve generated from the various values which k_R may assume is asymptotic with the vertical axis. Although we do not have a good value for k_R at this time, we believe we can obtain one soon.

VI. Model Predictions: & Conclusions:

The RCG thermal protective tile system coatings catalyze oxygen atom recombination through equilibrium, fast formation of a chemisorbed, site-specific, non-contiguous atom coating, with gas surface energies in the range of 6-20 Kcal/mole., and an activation energy for recombination of about 20 Kcal/mole at typical shuttle conditions, low pressures and about 1500°K. The entropies of activation for the process are large and negative, indicative of a strongly adsorbed surface-catalyzed recombination reaction. Product molecules are released in an equilibrium controlled process, independent of the reaction rate, and give rise to ground state oxygen as the major product. At least one experiment was consistent with the formation of $^3\Sigma_u O_2$ on the tile-glass surface, and the intensity measurements indicated that a growth of 4% of the concentration of this exciton was consistent with at least 12% conversion of O-atoms to it. This particular exciton, $^3\Sigma_u O_2$, was found to rather rapidly deexcite on tile surfaces, with a first-order rate constant of about .017-.042 /cm at gas velocities in the 300-400 cm/sec range. The energy of activation for this process was found to be about 7-8 Kcal/mole. The other exciton, $^1\Delta_g O_2$, was not deexcited as rapidly by the tiles, with a first-order rate decay constant of about .006 /cm at gas velocities in the 100-600 cm/sec range at near room temperature. There was only a small activation energy for the process, of about 0.34 to 1.0 Kcal/mole, indicating that the glass or surface tile deexcitation reaction does not involve strong ordering or bond formation. That $^1\Delta_g O_2$ is only slowly deactivated on the tiles is consistent with the fact that any reaction involving a change in spin, as from $^1\Delta_g O_2$ to $^3\Sigma_g O_2$, in the ground state, must transfer spin to a third body. Evidently the tile- $^1\Delta_g O_2$ interaction is one in which such a spin transfer does not take place readily.

The most interesting result obtained was the change in order for each of the deexcitation reactions, from second order to first order. Since the process was

found to be diminished at low pressure, higher temperature, and lower flow rate, it was assumed to be due to a site-coverage effect discussed in the mechanism. But other postulates, including non-laminar flow in the early reactor tube, gas-gas recombination or deexcitation, and an unusual tube regime in the first or early part of the tube could also explain this result.

It is yet too early to predict what fraction of the deexcitation energy or recombination energy leading to excitons is actually accepted by the tile surface and results in heating. These evaluations must await our soon-to-be-performed calorimetric studies. But, following Ogryzlo's observation that oxygen atoms recombine to produce about 4-12% $\frac{3}{2} \text{u } \text{O}_2$ and a comparable amount of $\frac{1}{2} \text{g } \text{O}_2$, obviously only a small fraction of the total recombination energy is converted into exciton electronic energy. However, with the low deexcitation rates on glass and the RCG tile surface, coupled with the very modest rate enhancements expected for processes of such low energy of activation, there is good evidence, that once formed, oxygen excitons can carry a fraction of recombination energy away from the tile surface. In addition, at the higher temperatures characteristic of Shuttle reentry conditions, it is expected that the higher lying electronic states might be initially be more highly populated, and will also include significant contributions from vibrational and rotational states. One intriguing possibility remaining to be explored is the possibility of defining the populations of higher lying vibrationally, rotationally, and electronically excited oxygen states. Even more importantly, a study of the energy partition of excited species produced from nitrogen, the major component of the atmosphere, and with the larger share of the recombination energy to be accommodated, could give fruitful results. Nitrogen excitons in higher lying electronic and vibrationally excited states have been detected, and have been found to have significant radiative lifetimes.^{35,36,37} We had proposed future experiments addressing these problems in an unsolicited proposal to NASA, and hope to be able to study them. These new experiments, coupled with our on-

going excited oxygen work, including our upcoming calorimetric studies, will expand our growing recombination model, and will allow us to more closely define the heat flux impact of excited species, which are produced by or deexcited by surface reactions on the Orbiter TPS tile materials.

VII. Acknowledgments:

The author gratefully acknowledges the NASA-ASEE Summer Faculty Fellowship Program for its support of this work over the last two years, and NASA through contract #NAS-9-16254. In addition, we acknowledge Murray State University's Committee on Institutional Studies and Research, for its support under grant #CISR-777. Special thanks are given to Dean Gary Boggess and Vice President for University Services Dr. Marshall Gordon for supplying equipment for the experiments, and to Dr. Fred Senftleber of M.S.U. for his glassblowing expertise. Others who have significantly aided in the development of our technique have included Dr. Ruford Anderson, Dr. Grady Cantrell, Mr. Bill Call, and r. Joe Callais of M.S.U. Much of the routine, yet sensitive data-gathering and systems modification work was performed by Mr. Alan Bradbury, the NASA research assistant for whom the data collected in these experiments will serve as a M.S. Thesis. We also thank Dr. Winston Goodrich of NASA JSC-Houston for stimulating discussions about the systems and data interpretation, and Dr. Carl Scott, whose timely suggestions and great support behind the scenes are greatly appreciated.

VIII. References:

1. M. Faget, Astronautics Aeronautics, 52 (1970).
 2. C. D. Scott, AIAA J. 18, 1477(1980).
 3. C. D. Scott, AIAA Paper #81-1144, 16th Thermophysics Conference, Palo Alto, California, June 23-25, 1981.
 4. D. A. Stewart and J. V. Rakich, AIAA Paper #81-1143, 16th Thermophysics Conference, Palo Alto, California, June 23-25, 1981.
- H. P. Broida and A. G. Gaydon, Proc. Roy. Soc. (London), Ser. A., 222, 181 (1954).

6. J. F. Noxon, Canad. J. Phys., 39, 1110 (1961).
7. F. S. Klein and J. T. Herron, J. Chem. Phys., 41, 1285 (1964).
8. F. Furukawa, E. W. Gray and E. A. Ogryzlo, Ann. New York Acad. Sci., 171, 175 (1970).
9. R. H. Kummler and M. H. Bortner, Ann. New York Acad. Sci., 171, 273 (1970).
10. "STS-1 Technical Crew Debriefing", NASA Report JSC-17306, April, 1981, p. 6-22.
11. R. D. Kenner and E. A. Ogryzlo, Int. J. Chem. Kin., 12, 501 (1980).
12. R. J. O'Brien and G. H. Myers, J. Chem. Phys., 55, 3832 (1972).
13. A. L. Myerson, J. Chem. Phys., 50, 1228 (1969).
14. J. C. Greaves and J. W. Linnett, Trans. Faraday Soc., 55, 1346, 1355 (1959).
15. G. A. Melin and R. J. Madix, Trans. Faraday Soc., 67, 198 (1971).
16. L. Elias, E. A. Ogryzlo, and H. I. Schiff, Canad. J. Chem., 37, 1680 (1959).
17. K. J. Laidler, "Chemical Kinetics", McGraw-Hill, Inc., New York, New York, 1950, pp. 365-387.
18. J. C. Polyani, Accounts Chemical Res., 5, 161 (1972).
19. G. Erlich, Physics Today, 34, 6, 44 (1981).
20. G. Erlich, J. Vac. Sci. Technol., 17, 9 (1980).
21. G. Erlich and K. Stolt, Ann. Rev. Phys. Chem., 31, 603 (1980).
22. G. Manella and P. Harteck, J. Chem. Phys., 34, 2177, (1961).
23. R. B. Sosman, "The Phases of Silica", Rutgers University Press, New Brunswick, New Jersey, 1965, pp. 278-315.
24. F. Kaufman, J. Chem. Phys., 28, 352 (1958).
25. F. Kaufman, Progress in Reaction Kinetics, 1, 1-39 (1961).
26. S. J. Arnold, N. Finlayson, and E. A. Ogryzlo, J. Chem. Phys., 44, 2529 (1966).
27. G. A. Somerjai, Accounts Chem. Res., 9, 333 (1976).
28. E. K. Ridcal, "Concepts in Catalysis", Academic Press, New York, New York, 1968, pp. 38-82.
29. P. Harteck and R. R. R. Reeves, Jr., Trans. Faraday Soc., 37, 82 (1964).

30. F. C. Fehrendfeld, K. M. Evenson, and H. P. Broida, Rev. Sci. Instrum., 36, 294 (1965).
31. E. A. Ogryzlo and C. W. Tang, J. Am. Chem. Soc., 95, 3381 (1970).
32. J. A. Davidson and E. A. Ogryzlo, in "Chemiluminescence and Bioluminescence", (M. J. Cormier, D. M. Hercules and J. Lee, eds.), Plenum Publishing Co., New York, New York, 1973, pp. 111-116.
33. M. Yaron, A. von Engel, and P. H. Vidaud, Chem. Phys. Lett., 37, 159 (1976).
34. H. Schlichting, "Boundary Layer Theory", 6th Ed., McGraw Hill, Inc., New York, New York, 1968, pp. 11-26.
35. H. P. Broida, in "The Threshold of Space" (M. Zelikoff, Ed.), Pergamon Press, Oxford, England, 1962, p. 194.
36. J. Berkowitz, W. A. Chupka, and G. B. Kistiakowski, J. Chem. Phys., 23, 729 (1955).
37. K. D. Bayes and G. B. Kistiakowski, J. Chem. Phys., 32, 992 (1960).
38. A. M. Winer and K. D. Bayes, J. Phys. Chem., 70, 302 (1966).
39. A. Vallance-Jones and A. W. Harrison, J. Atmospheric Terrest. Phys., 40, 1769 (1968).

IX. Nomenclature:

c	area-dependent proportionality constant
E _a	energy of activation, Kcal/mole
h	Planck's constant
ΔH	enthalpy of reaction, Kcal/mole
I	emission intensity, arbitrary units
k _B	Boltzmann's constant
k	first order reaction rate constant
K	equilibrium constant, surface adsorption-desorption
Δn	change in number of moles
O	oxygen atoms
P	Pressure, atm.
Q	Energy difference between ground state and exciton state, Kcal/ mole
R	radius of reaction tube, cm.
RCG	reaction cured glass.
Re	Reynolds number, diameter

ORIGINAL PAGE IS
OF POOR QUALITY

Nomenclature: (cont.)

S	silicate surface site
Sa	entropy of activation, cal./deg.
T	Temperature, °K
TPS	Thermal Protective System
\bar{u}	bulk-average linear gas flow rate, cm/sec
\bar{v}	root mean square gas molecular velocity, cm/sec
V	gas volume flow rate, cm ³ /sec
[]	concentration, moles/cm ³
β	energy accommodation coefficient
γ'	recombination coefficient
Γ	molar site surface coverage, moles/cm ²
Δ	delta oxygen electronic state
κ	first order rate constant, /sec
ν	kinematic viscosity, lb _m /ft-sec
ρ	density, g/cm ³
τ	adsorption "sticking" time, sec

Subscripts:

1,2,3....	characteristic of reaction 1,2,3....
a	adsorption
b	Boltzmann
D	deactivation
eq	equilibrium
g	gas state
0	zero (initial) tube position
O	oxygen atom
O ₂	oxygen molecule
R	recombination

ORIGINAL PAGE IS
OF POOR QUALITYSubscripts:(cont.)

- s surface species
 T total
 t tile(reaction cured glass coated)
 w wall(pyrex tube)
 x tube position, cm.
 †
 ∞ end(infinity) tube position

Figure 1. Reaction Profile vs. Energy Consistent with Observed Energetics for Oxygen Atom Recombination.

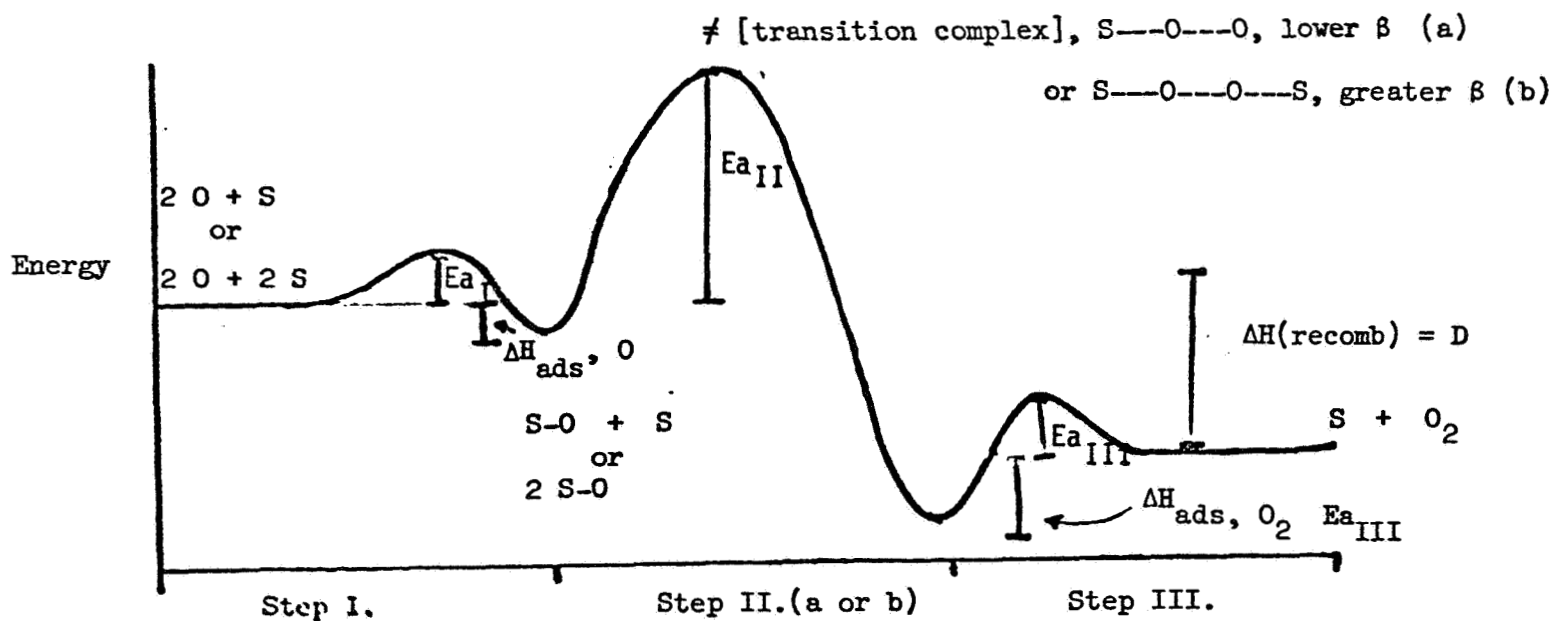
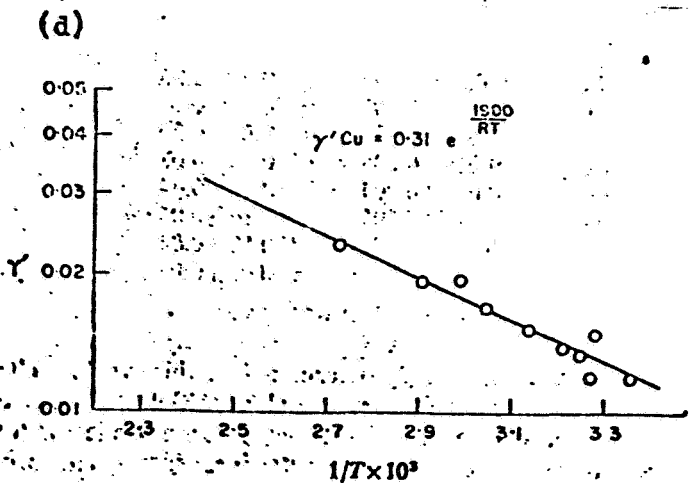
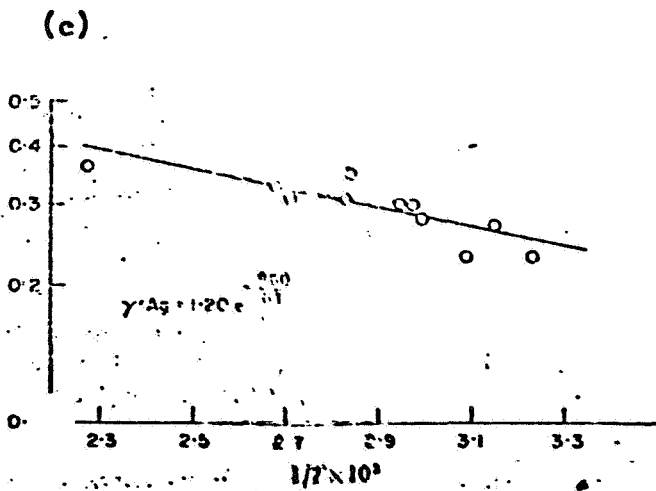
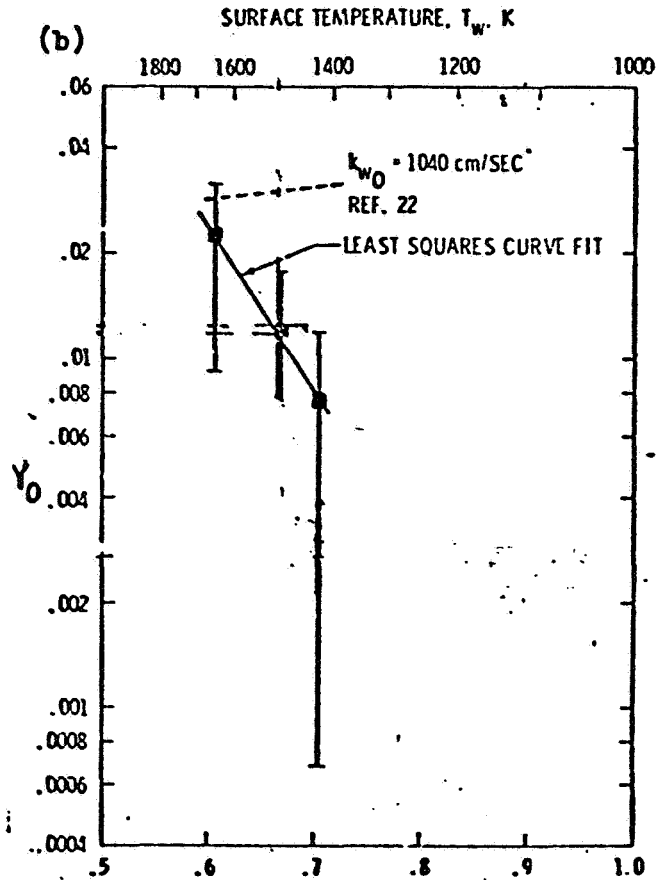
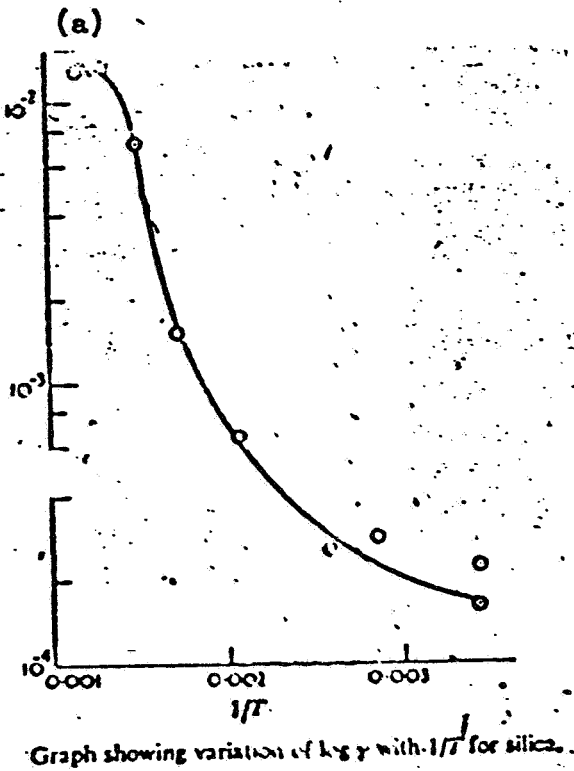


Figure 2: Variation in the Recombination Coefficient, γ , of Oxygen Atoms ^{2,14,15} on (a), silica; (b), HRSI; (c), silver metal; and (d) copper metal. Note the similarity in form to Figure 12.

ORIGINAL PAGE IS
OF POOR QUALITY



ORIGINAL PAGE IS
OF POOR QUALITY

Figure 3. Apparatus for Production and Detection of Excited Oxygen Species.

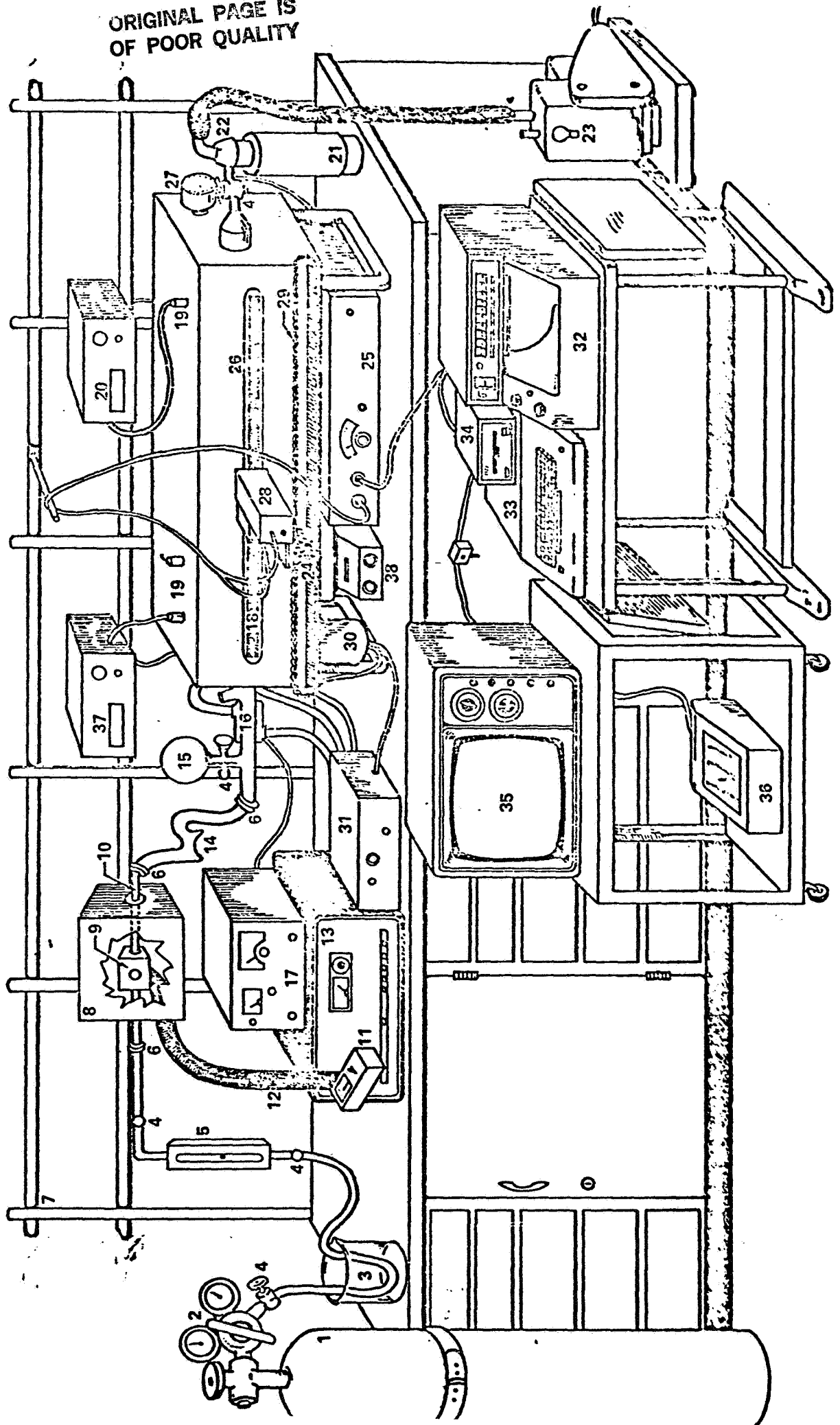
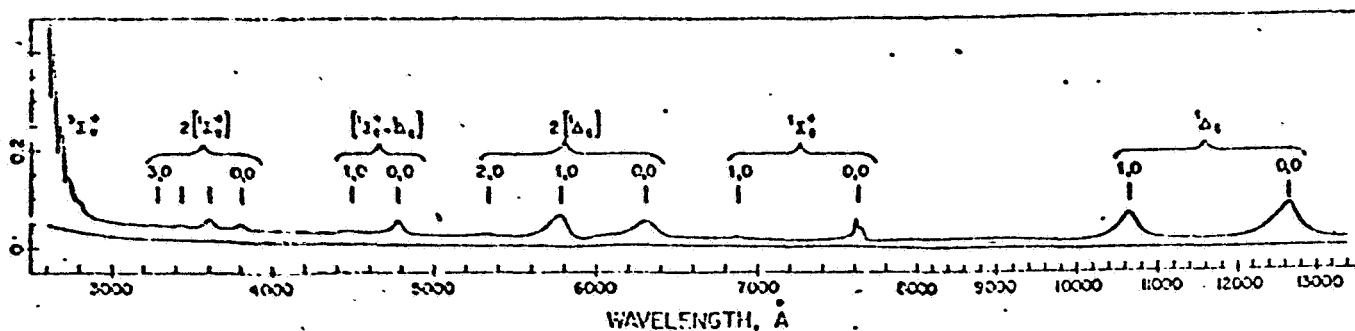


Figure 3. Legend.

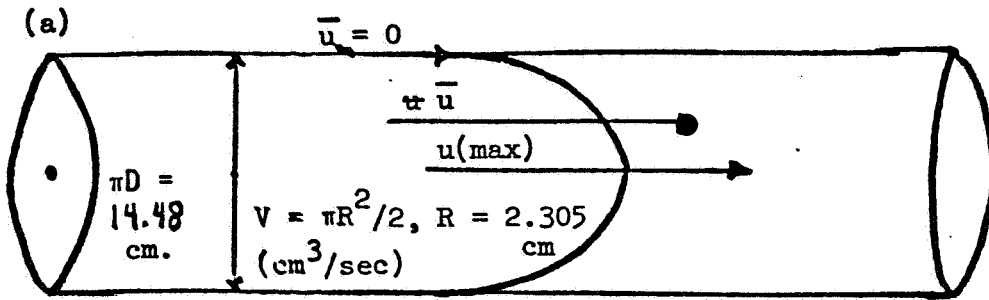
- | | |
|-------------------------------|---|
| 1. Oxygen Cylinder | 20. Pressure/Vacuum Gauge |
| 2. Oxygen Regulator | 21. Dewar Flask |
| 3. Precooling Bath | 22. Post-cooling Trap |
| 4. Flow Stopcock | 23. Vacuum Pump of Capacity 500 liters/min. |
| 5. Gas Flowmeter | 24. Photomultiplier Tube Car or Carriage |
| 6. SJ Clamps | 25. Photomultiplier Tube Power Supply |
| 7. Utility Rack | 26. Oven for Reactor/Detector |
| 8. Microwave Discharge Region | 27. Oven Circulating Fan Motor |
| 9. Microwave Tuning Cavity | 28. Photomultiplier Tubes & Filters |
| 10. Quartz Discharge Tube | 29. Stepped Chain Track |
| 11. Microwave Backmeter | 30. Stepping Motor |
| 12. Coaxial Cable | 31. Stepping Motor Control Box |
| 13. Microwave Power Source | 32. Stripchart Recorder |
| 14. Light Traps | 33. Apple II Plus 48K Microcomputer |
| 15. NO ₂ Reservoir | 34. Disk Drive & Diskette |
| 16. In-line Condenser | 35. CRT (color) |
| 17. Oven Power Control | 36. Printer |
| 18. Reactor/Detector Tube | 37. Digital Thermal Analyzer |
| 19. Pressure/Detector Ports | 38. Oven Thermoregulator |

Figure 4. Complete Assigned Visible and Near-visible Oxygen Emission Spectrum.



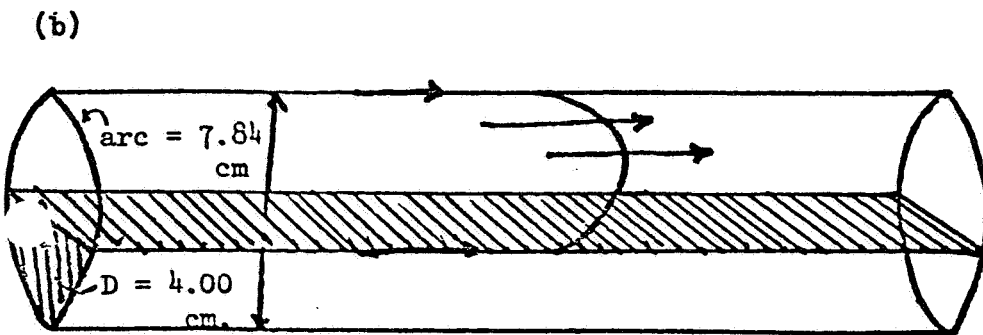
ORIGINAL PAGE IS
OF POOR QUALITY.

Figure 5. Laminar Flow Profile Assumed for Empty Reaction Tube(a); Tile-Filled Tube(b); and Normalized Tile Filled Tube(c).



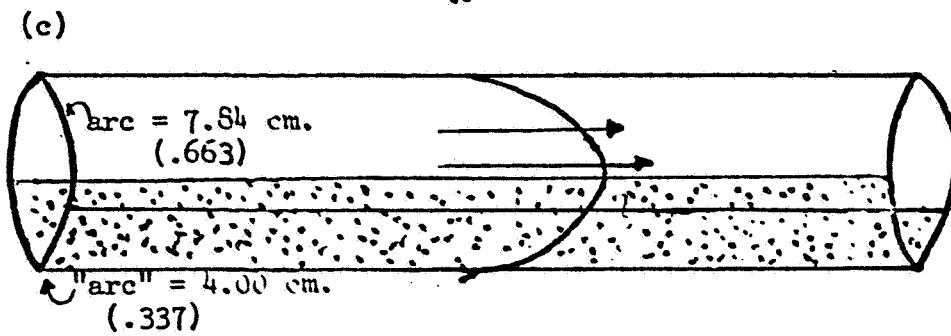
cylindrical flow path

or \bar{u} , cm/sec =
.12V / cm²



hemicylindrical
flow path norm-
alized to

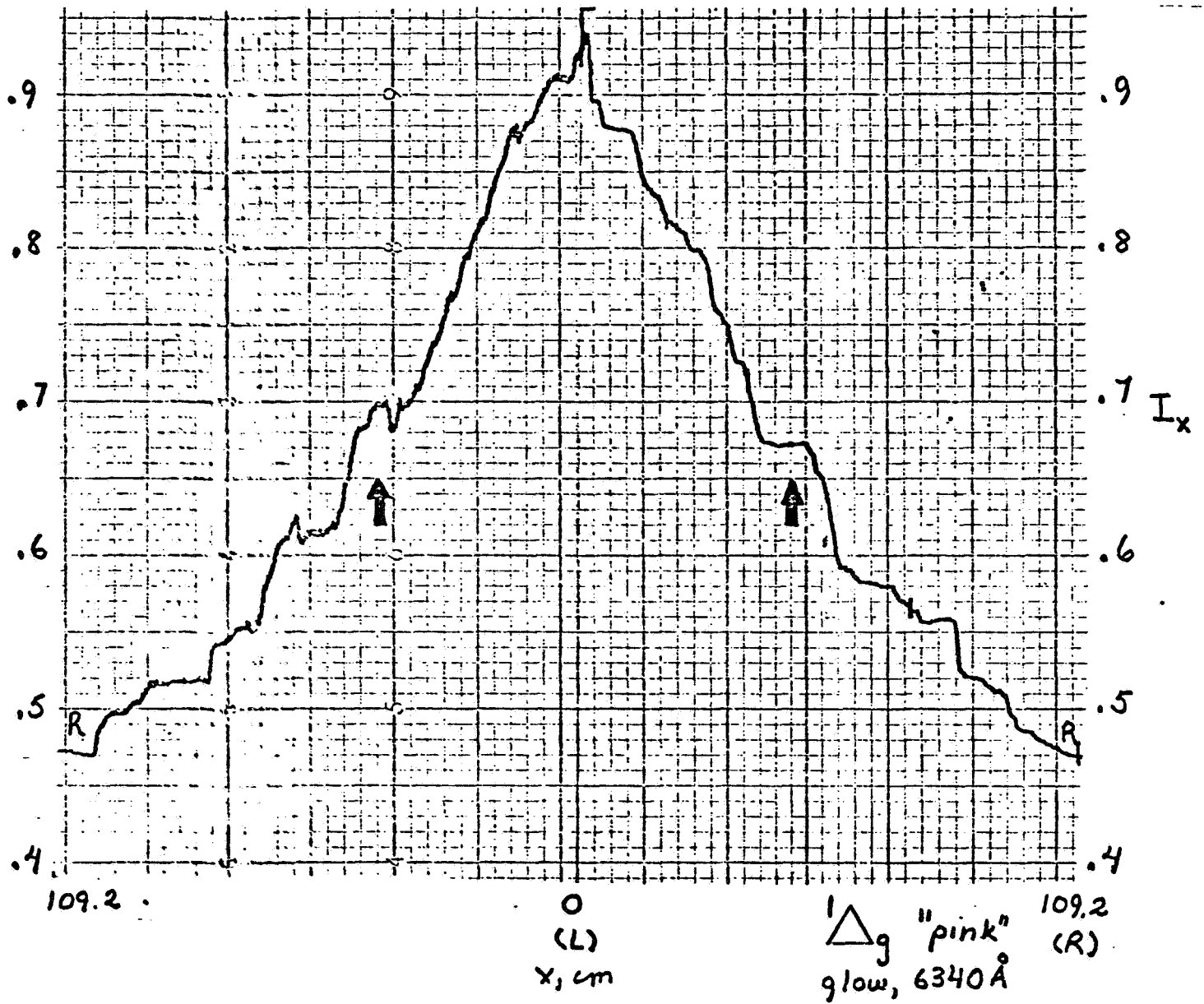
||



cylindrical
flow path.

$\bar{u} = .179V$
"D" = 3.778 cm.

Figure 6. Typical Double Tube Scan at 6340 Angstroms, for $^1\Delta$ O_2 Intensity with Tube Position, x. Double Large Arrows Indicate Tube Irregularities.



ORIGINAL PAGE IS
OF POOR QUALITY

Figure 7. Typical Single Tube Scan, $^3\Sigma_u$ "Green Glow". Large Arrow Indicates Reproducible Tube Irregularity.

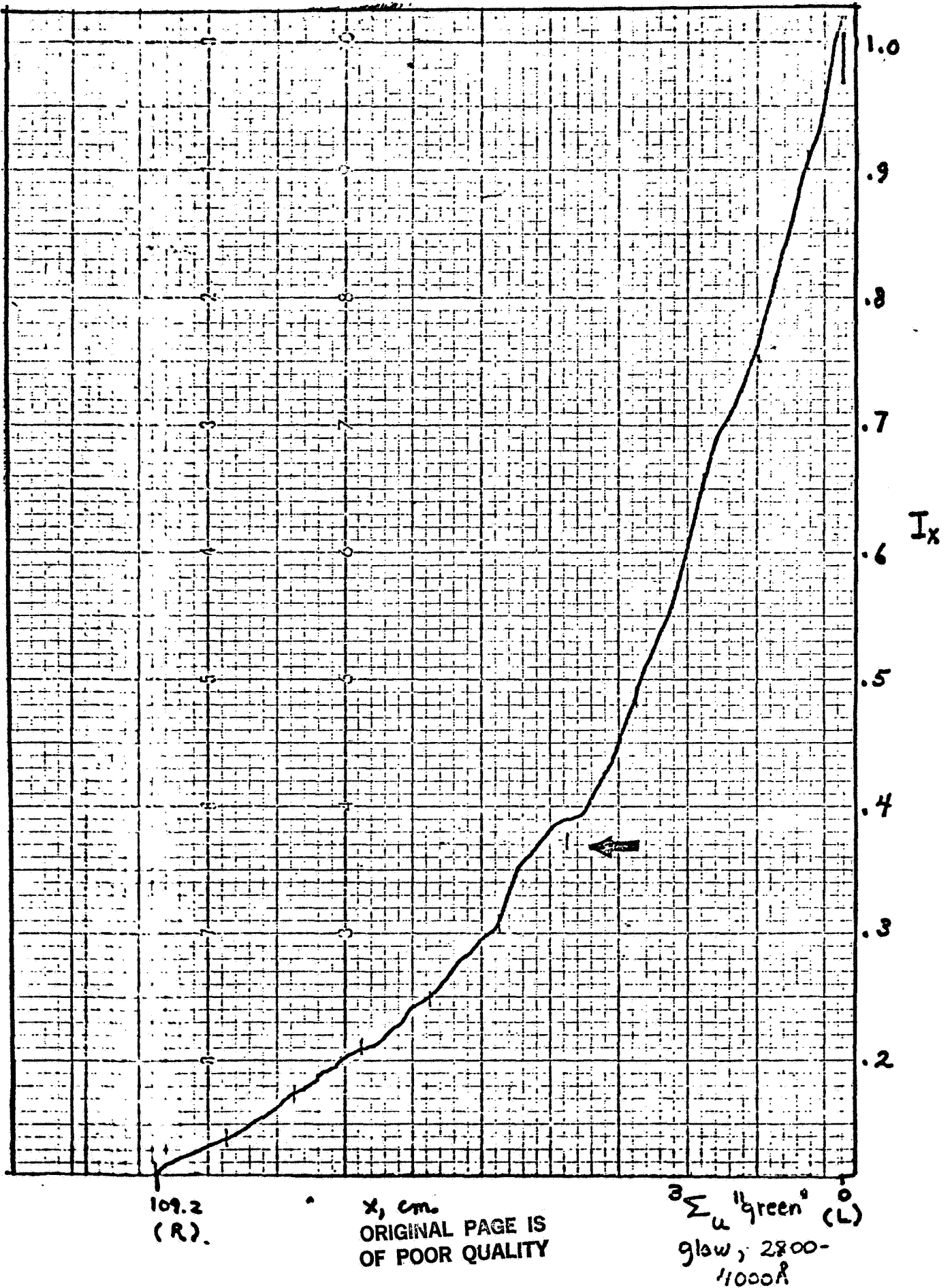
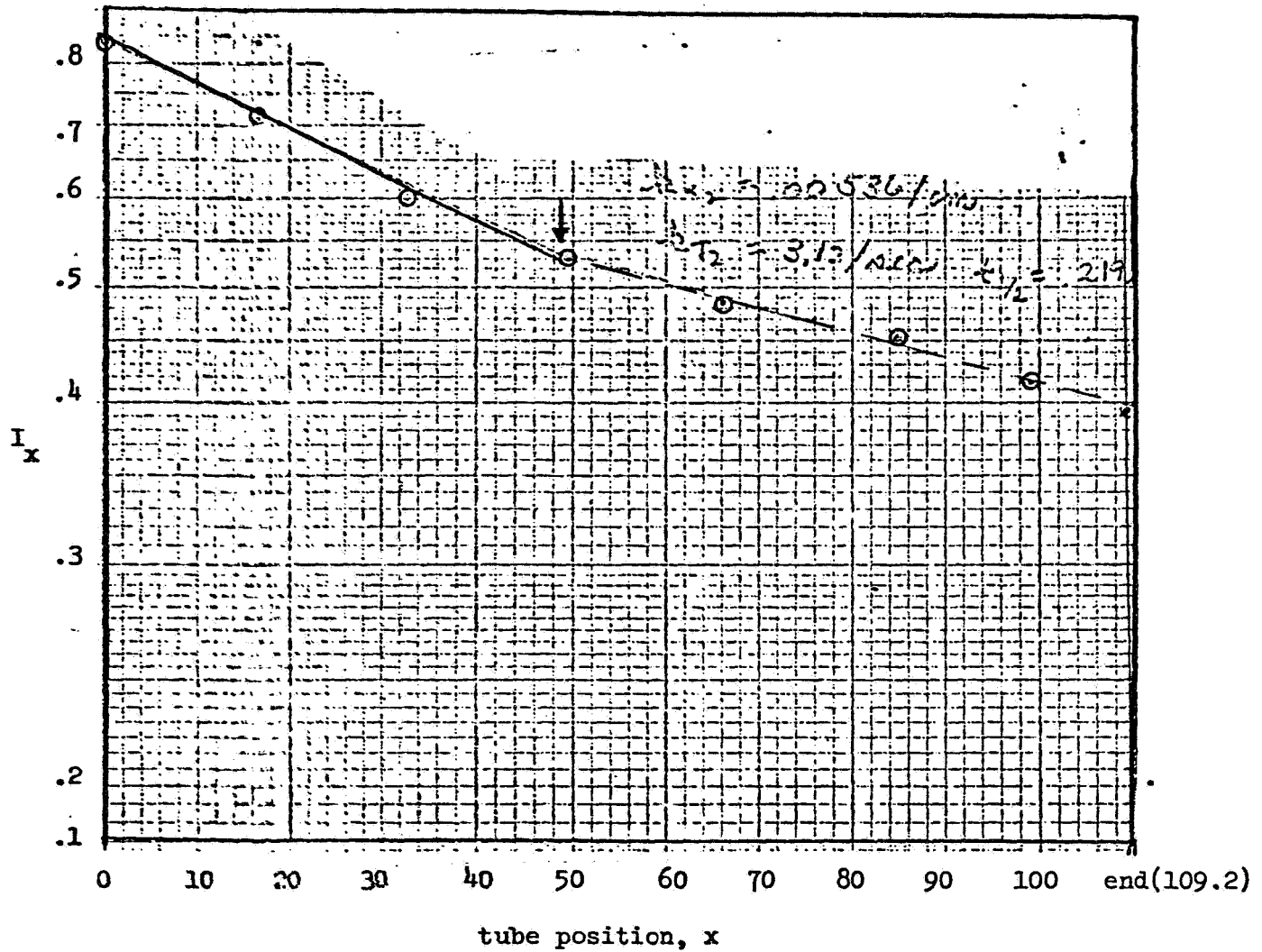


Figure 8. Variation in $\log_{10} I_x$ with Tube Position, x , cm. Note Data Break Point near 50 cm. Measurement for 6340 angstrom $^1\Delta_g O_2$ "pink glow".



ORIGINAL PAGE IS
OF POOR QUALITY

Figure 9. Variation in $\log_{10} I_x$ with Tube Position, x cm. Note Data Break Point in 40-50 cm. Range. \times Measurement for $^3\Sigma_g^-$ "green glow".

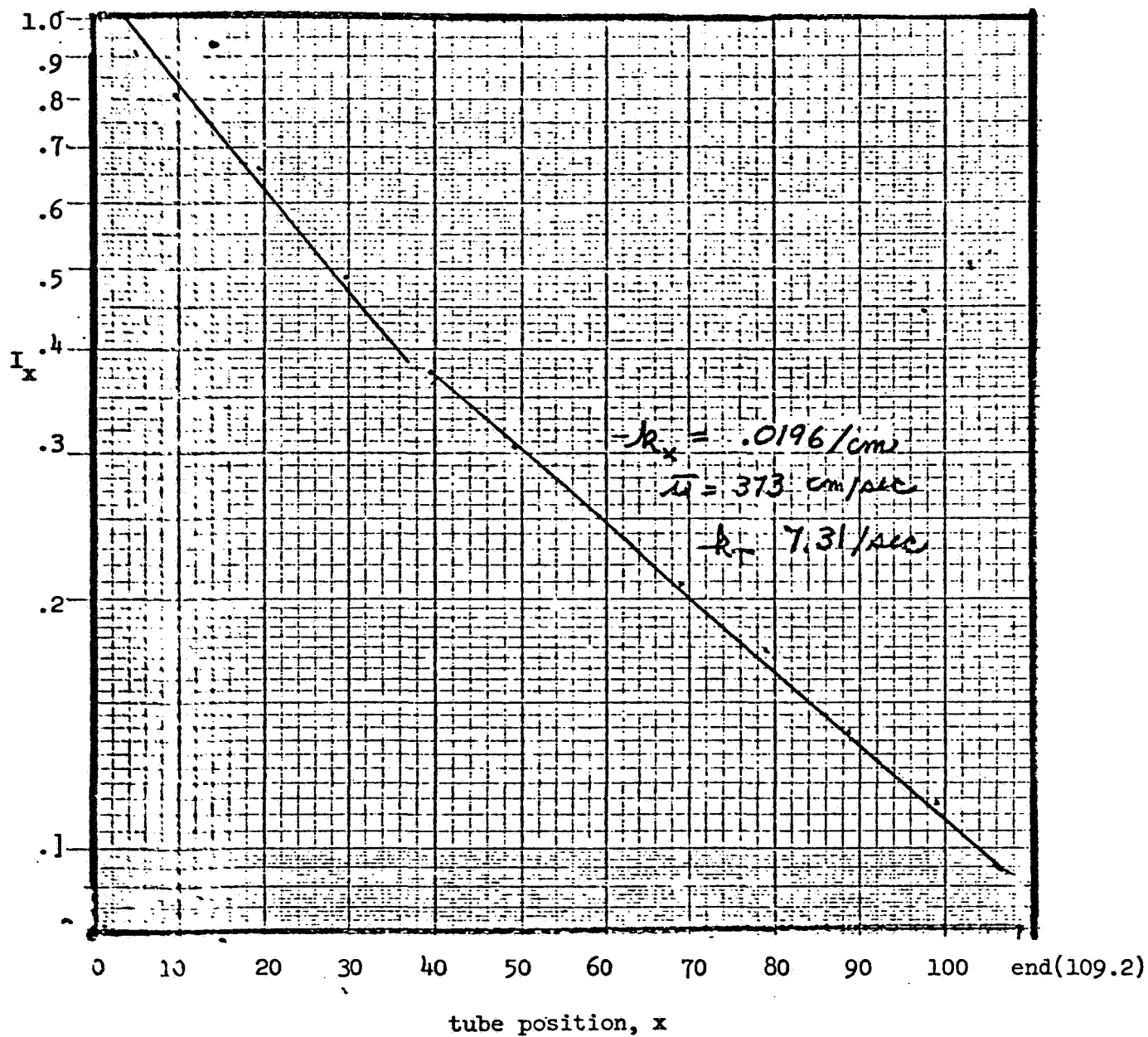


Figure 10. Variation of ${}^3\Sigma_u$ "green glow" Intensity, $1/I_x$, with Early Tube Position x .

ORIGINAL PAGE IS
OF POOR QUALITY

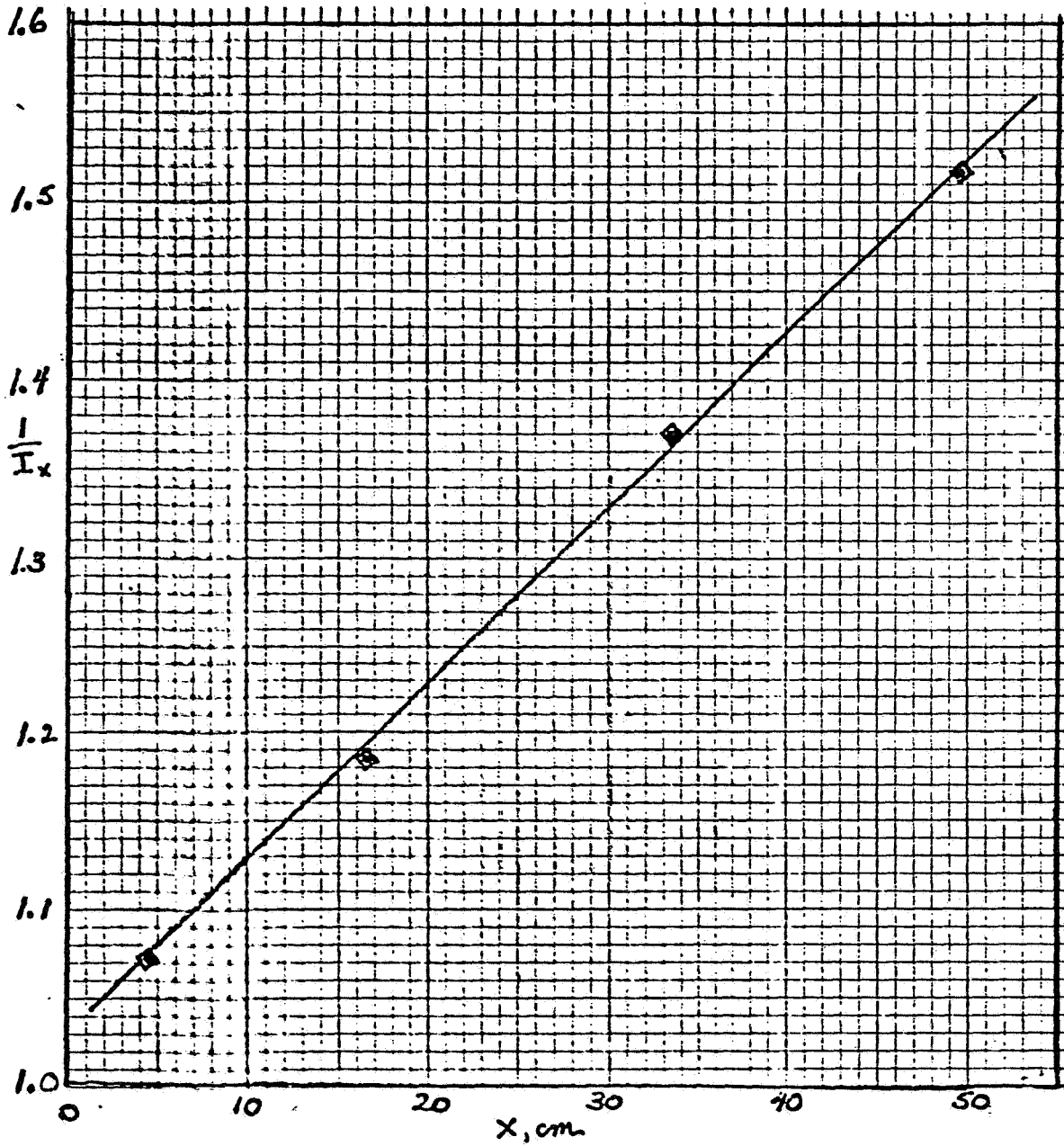


Figure 11. Variation in $\log_{10} \gamma'_\Delta$ with $1/T$, Temperature in $^\circ\text{Kelvin}$.

ORIGINAL PAGE IS
OF POOR QUALITY

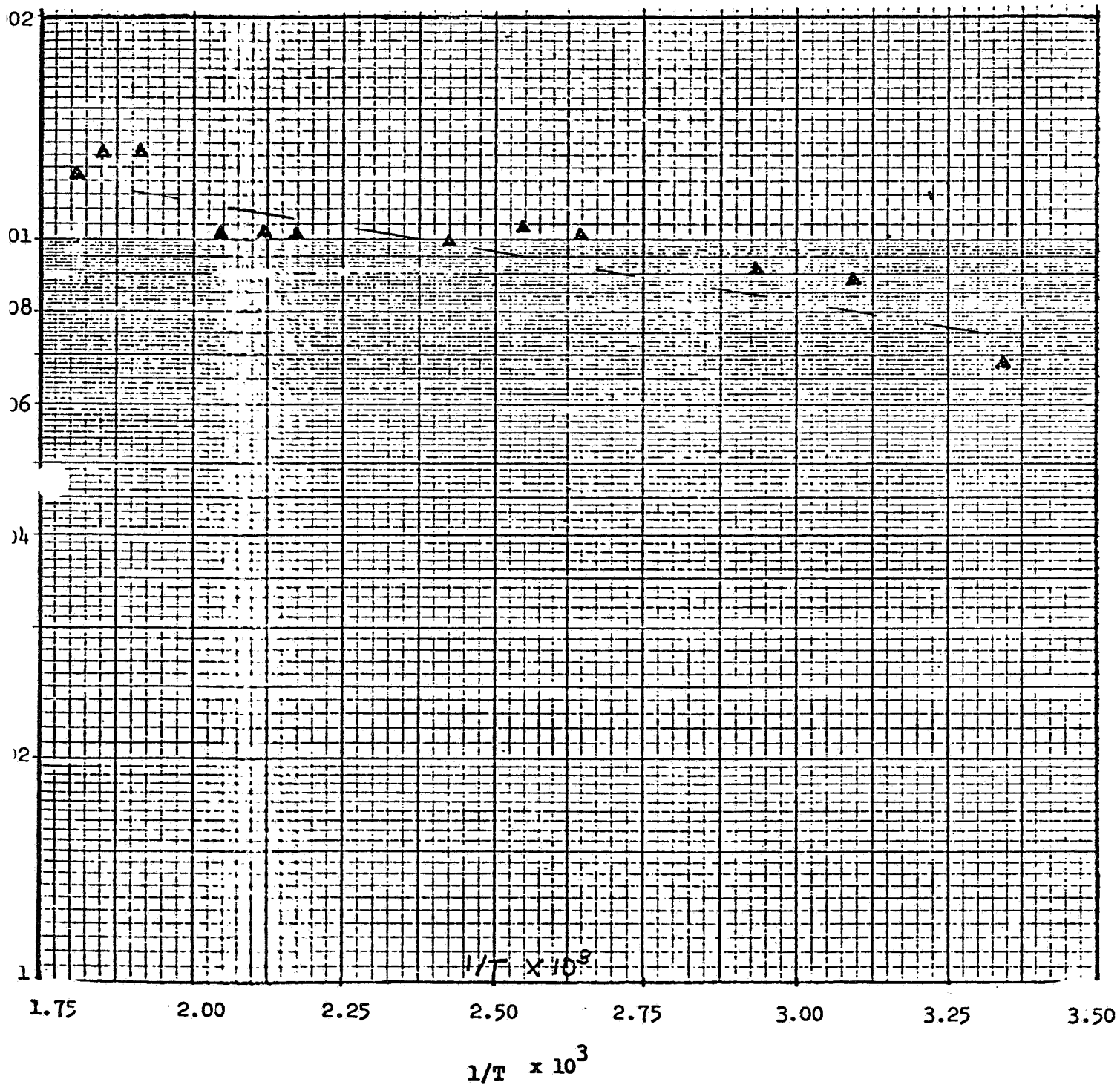


Figure 12. Variation in $\log_{10} \gamma_{\Sigma}$ with $1/T$, Temperature in $^{\circ}$ Kelvin.

ORIGINAL PAGE IS
OF POOR QUALITY.

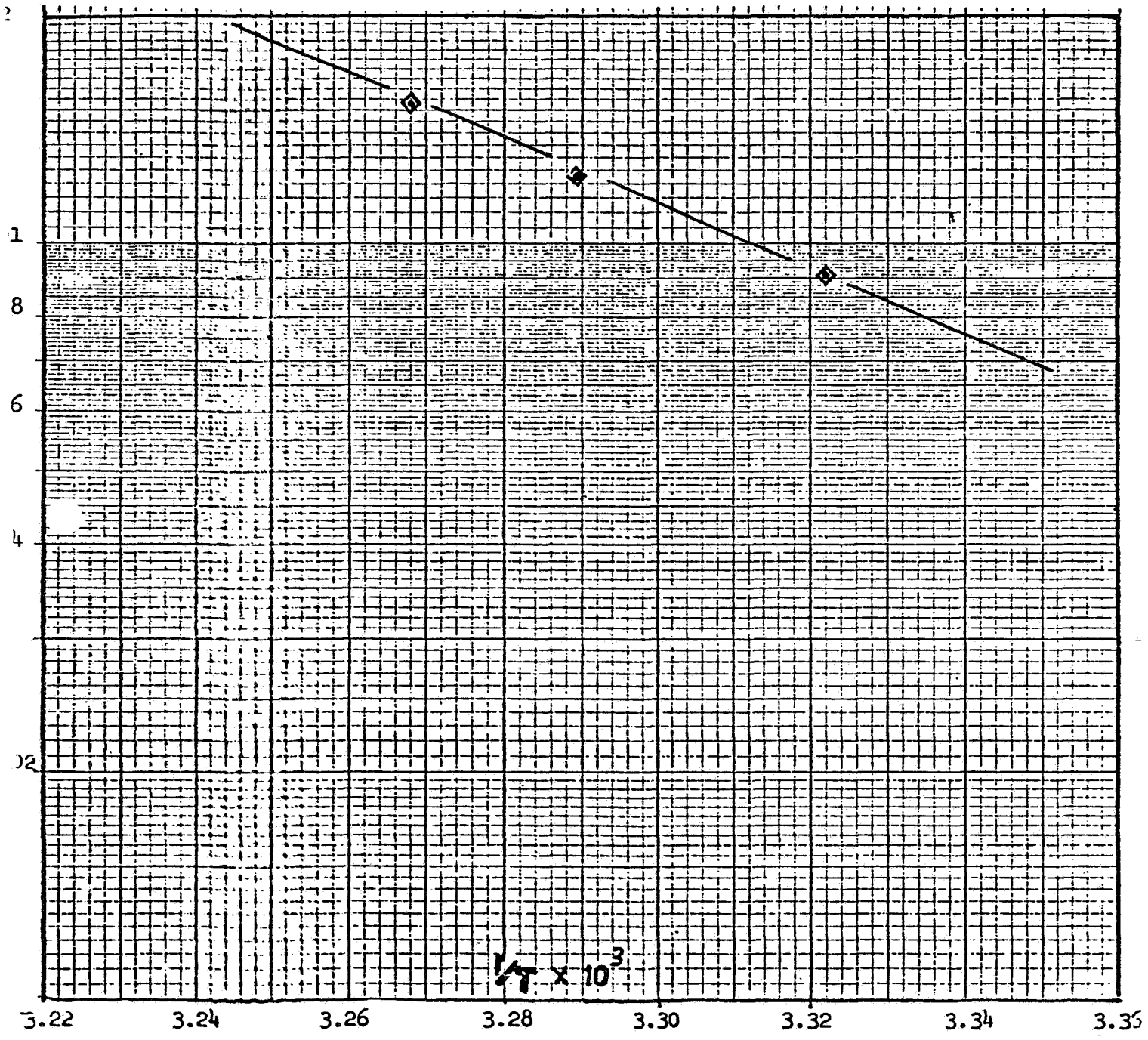


Figure 13. Variation in κ , /cm, $^1\Delta_g O_2$, (pink glow), with $1/T$, $^{\circ}\text{Kelvin}$.

ORIGINAL PAGE IS
OF POOR QUALITY

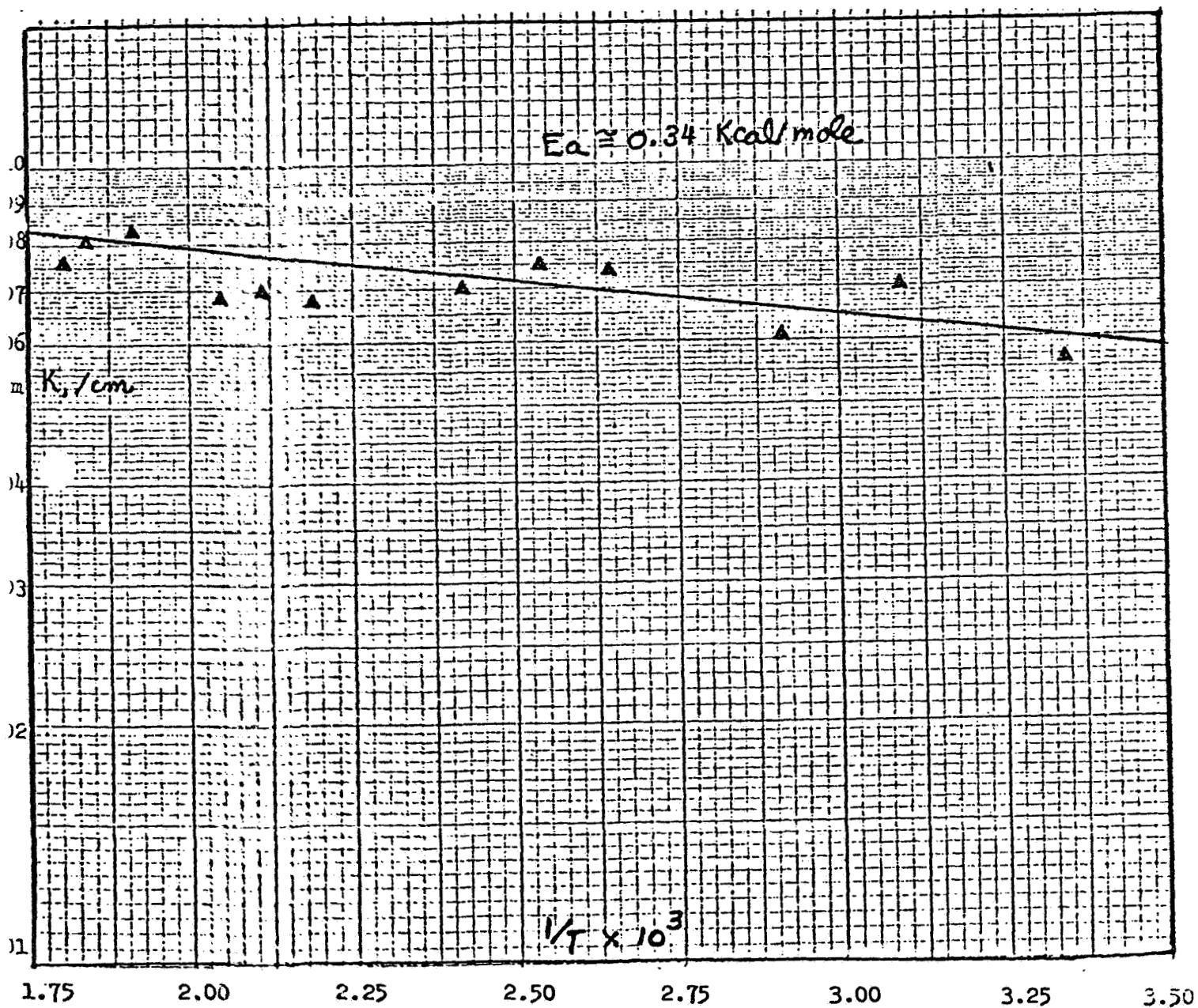


Figure 14. Variation in $k, \text{/sec}, ^1\Delta_g \text{O}_2(\text{pink glow}),$ with $1/T, \text{ }^\circ\text{Kelvin}.$

ORIGINAL PAGE IS
OF POOR QUALITY

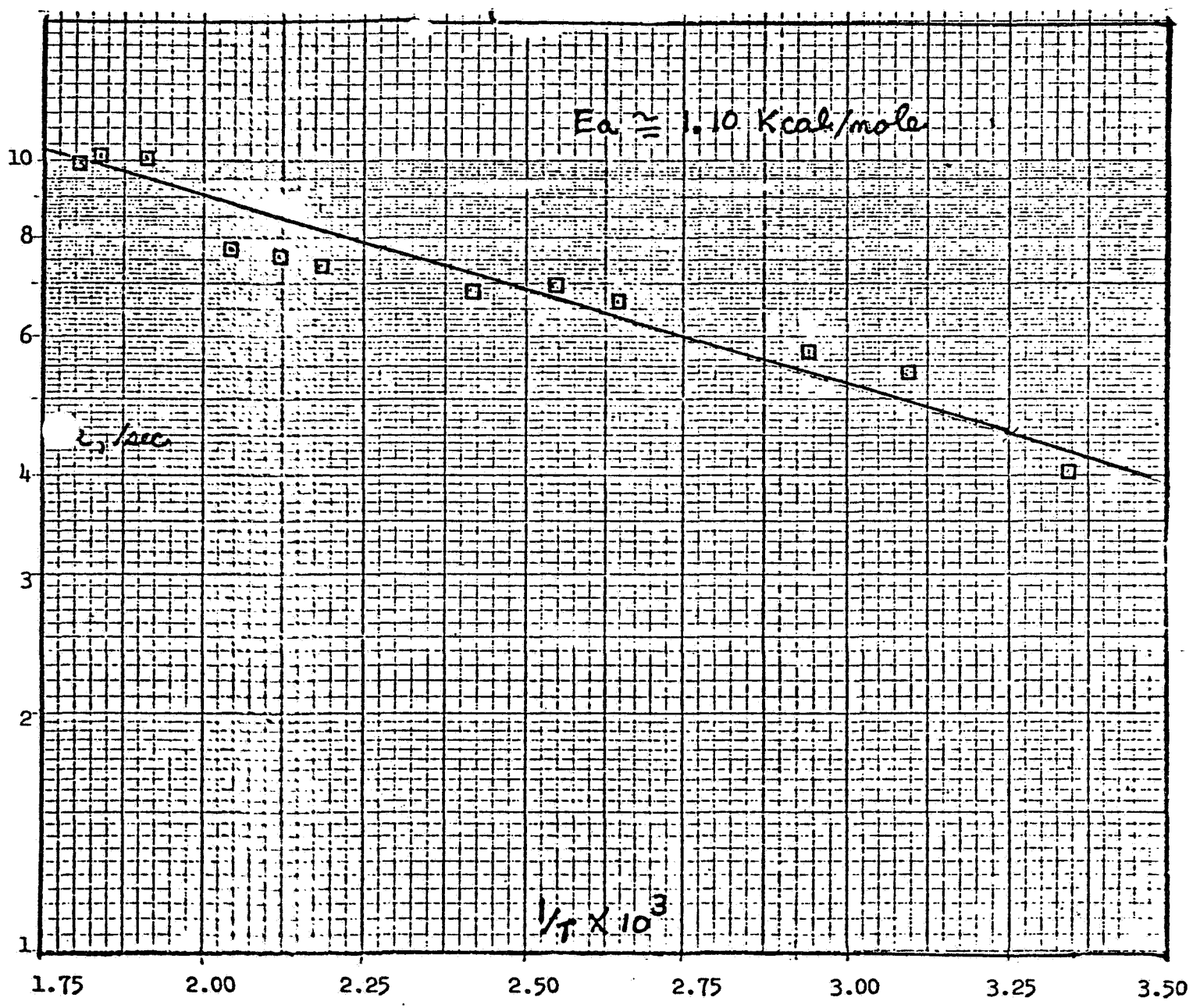


Figure 15. Variation in κ , /cm, (green glow), with $1/T$, °Kelvin:

ORIGINAL PAGE IS
OF POOR QUALITY

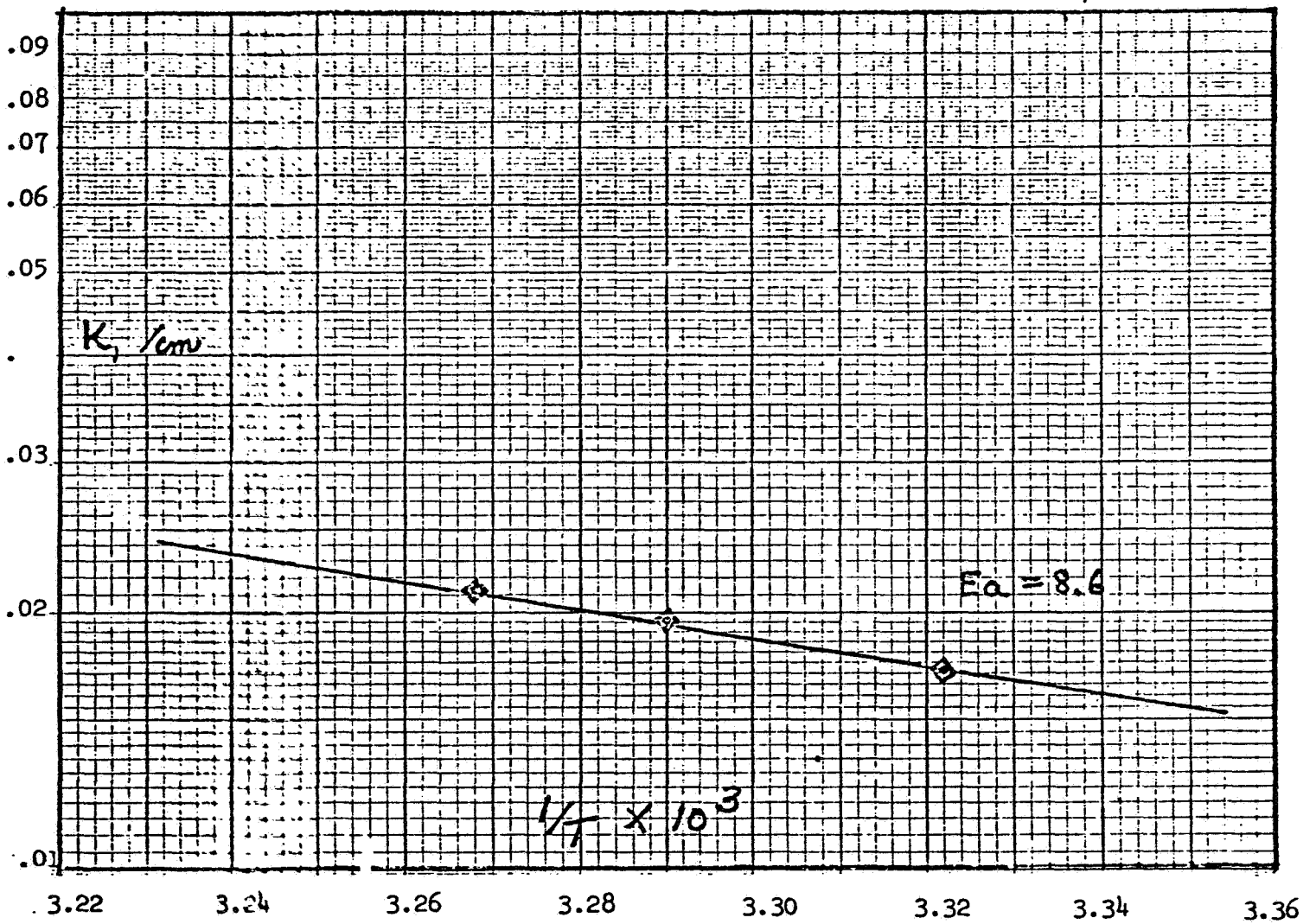


Figure 16. Variation in k ,/sec, (green glow), with $1/T$, °Kelvin.

ORIGINAL PAGE IS
OF POOR QUALITY

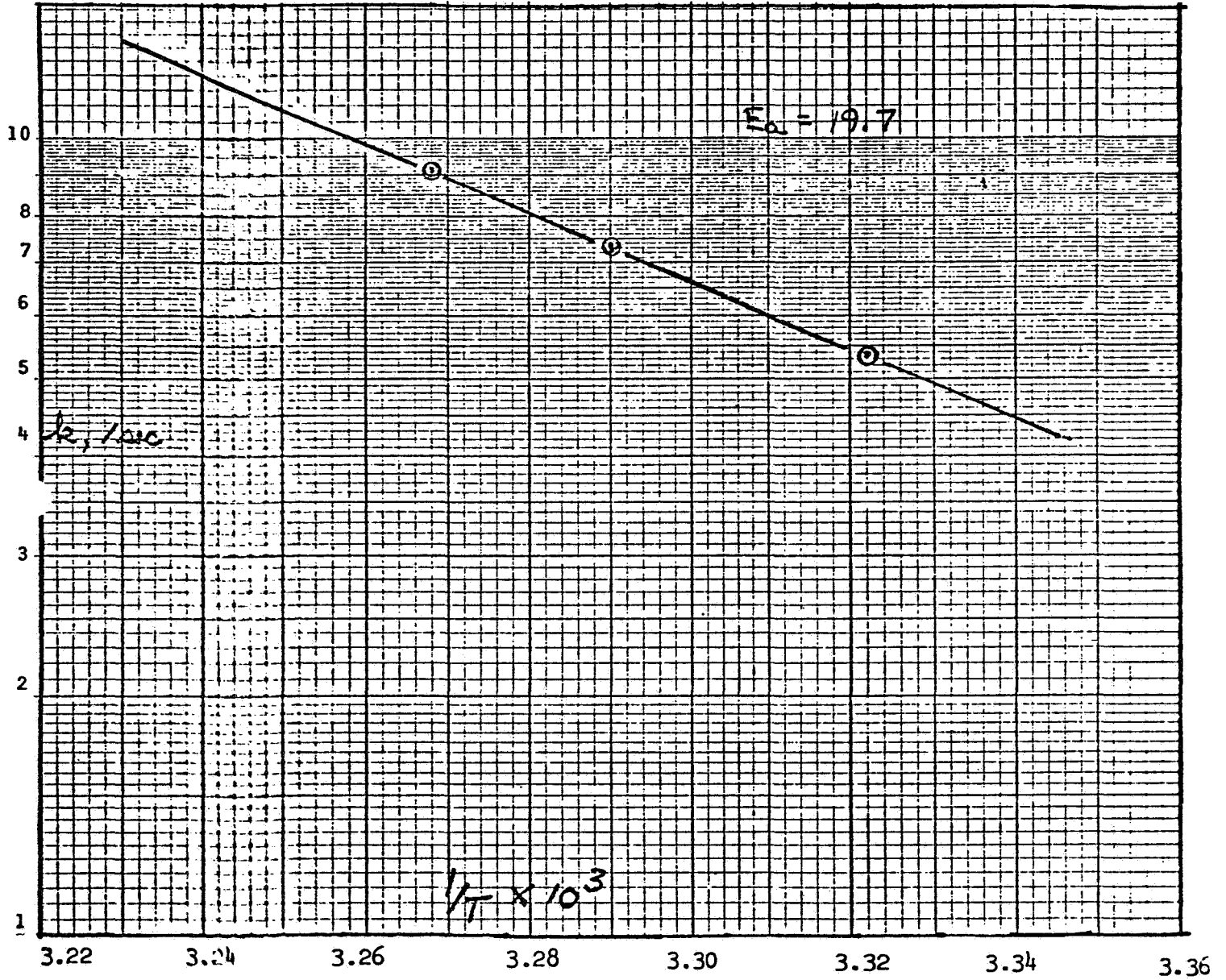


Table I. Some Properties of Excited Oxygen Molecules & Atoms.				
State Symbol:	Energy above G.S., Kcal/mol O ₂ , O(θ)	O(θ)/O(θ):	Diameter, Ang.	
O ₂ , 3-SIGMA g (-)	0.0 (G.S.)	0.0	1.207	
O ₂ , 1-DELTA g (-)	22.6	0.192	1.216	
O ₂ , 1-SIGMA g (+)	37.7	0.320	1.227	
O ₂ , 3-SIGMA u (+)	103.2	0.875	1.420	
O ₂ , 3-SIGMA u (-)	142.4	1.207	1.600	
3-P O-ATOMS	59.0 x 2	1.000	-----	

Table II. Typical Experimental Oxygen Flow Stream Parameters.			
Volume, cm ³ /min.	868	142	163
Pressure, Atm.	.00333	.00200	.00100
Pressure, O-atoms	.00089	.00053	.00027
Pressure, Delta:	.00023	.00014	.00007
Tube Diameter, ft.	.151	.151	.151
Kinem. Visc.	.00502	.00864	.01670
Reynolds No. (Dia.)	348	39.8	55
Gas Velocity, cm/s.	530.0	142	224
/cm ³ of Pressure Delta Molecules,	8.0 x 10 ⁽¹⁵⁾	4.8 x 10 ⁽¹⁵⁾	2.4 x 10 ⁽¹⁵⁾

Table III. Entropies and Energies of Activation.

Gas Species	Temp., Deg. K.	E ₀ , Kcal/mole	S ₀ , cal./deg. K
4-S N-Atoms	1000-1700	1.0-4.4	-----
3-P O-Atoms	1400-1650	19.6-20.4	-41 10 -45
O ₂ , 3-Sigma u (+)	301-306	6.90-8.60	-----
O ₂ , 1-Delta g (-)	298-553	0.34-1.10	-----

ORIGINAL PAGE IS
OF POOR QUALITY

Table IV. Variation in End Position of Tube Entrance Effects					
P, Atm.	\bar{U} , ft/sec	Visc., ft ² /sec	Lam. Pos., ft	Lam. Pos., cm	
.001	3	.171	.004	0.12	
.002	3	.086	.008	0.24	
.003	3	.057	.012	0.37	
.001	10	.171	.013	0.40	
.002	10	.086	.026	0.80	
.003	10	.057	.040	1.20	
.001	17	.171	.028	0.85	
.002	17	.086	.055	1.75	
.003	17	.057	.084	2.55	

Table V. Variation in k , k' , and δ' with Temperature.

T, DEG. C.	$1/T \times 1000$	$k, /cm. \times 1000$	$k, /sec.$	$\delta', (w + t)$
26	3.344	5.66	4.02	.00068
50	3.296	7.03	5.40	.00088
70	2.915	6.07	5.73	.00091
105	2.646	7.38	6.63	.00100
120	2.546	7.00	6.97	.00103
140	2.421	7.45	6.87	.00099
185	2.183	6.90	7.34	.00101
200	2.114	6.82	7.59	.00102
215	2.049	8.29	7.75	.00102
250	1.912	6.76	10.3	.00132
270	1.842	8.06	10.4	.00131
280	1.808	7.55	9.92	.00123

Table VI. Variation in K , k , and γ'_w with Temperature:

T, Deg. C.	$1/T \times 10^3$	$K, \text{ cm.} \times 10^3$	$k, /\text{sec.}$	γ'_w
28	3.322	1.72	9.11	.00091
31	3.289	1.96	7.31	.00123
33	3.268	2.11	5.38	.00153

CAPILLARY PRIMING CHARACTERISTICS OF A DUAL PASSAGE
HEAT PIPE IN ZERO-G

George P. Peterson, Asst. Prof.
Texas A&M University
1981 NASA-ASEE Summer Faculty Fellow

Supervisor

D. William Morris, Head
Environmental and Thermal Systems
Systems Engineering Branch
Crew Systems Division

ABSTRACT - A mathematical model is formulated and a computer program developed which describes the transient priming characteristics of a dual passage heat pipe. In addition, an experimental test package is described for flight in the KC-135 Zero-g Aircraft, to be used to verify the modeling predictions.

NATIONAL AERONAUTICS AND SPACE ADMINISTRATION
LYNDON B. JOHNSON SPACE CENTER
HOUSTON, TEXAS
August 12, 1981

ORIGINAL PAGE IS
OF POOR QUALITY

1. INTRODUCTION
2. STATEMENT OF OBJECTIVES
3. ANALYSIS
 - 3.1 BACKGROUND
 - 3.2 MINIMIZATION OF FREE SURFACE ENERGY
 - 3.3 CALCULATION OF PRIMING TIME
 - 3.3.1 METHOD I
 - 3.3.2 METHOD II
4. TEST PROGRAM
 - 4.1 OBJECTIVES
 - 4.2 TEST DESCRIPTION
 - 4.3 TEST SET-UP
 - 4.4 ANTICIPATED RESULTS
5. SUMMARY
6. APPENDICES
 - A. NOMENCLATURE
 - B. COMPUTER CODE FOR METHOD I
 - C. COMPUTER CODE FOR METHOD II
 - D. JSC REDUCED GRAVITY AIRCRAFT USER'S GUIDE

1. INTRODUCTION

At present the primary means for rejecting heat from orbiting spacecraft is through a space radiator system composed of fluid loops which circulate fluid through radiator panels rejecting heat to the space environment. The current system uses a mechanically pumped coolant circuit to transfer heat throughout the radiating surface. This results in a system whose long mission reliability is low and which is vulnerable to complete failure due to penetration by a single meteoroid. Reliability can be increased through the use of redundant plumbing, pumping, and valving hardware. However, this causes a large increase in system weight. There is a need for significant technical improvements in the development of a long life heat-rejection system, suitable for long duration high power missions, that can be constructed and deployed on orbit.

One solution to this problem is the development of a large modular radiator system that can be assembled on orbit from a number of standard components. This space-constructable radiator system would fulfill the needs and demands of large long-lived heat rejection systems and would allow systems to be built up to any desired heat load capability.

The key component of this concept is an innovative, high-capacity, dual-passage heat pipe design. This heat pipe with radiator fins attached would be "plugged in" to contact heat exchangers providing heat removal from a centralized heat transport loop. This type of system would be insensitive to complete failure due to micrometeoroid puncture, with the puncture of any single heat pipe resulting in only the loss of that module's 2-kilowatt capacity. The damaged segments could be removed by the Orbiter and replaced or repaired as necessary.

The basic design of this improved high-performance dual-passage, heat-pipe consists of two large axial channels, one for vapor flow and another for liquid flow (see figure 1). These two channels are separated by a small "monogroove" slot which creates a high capillary pressure difference and causes liquid to be pumped from the liquid channel to the circumferential grooves in the vapor channel. This configuration permits the axial transport and radial heat-transfer phases to be handled independently resulting in high axial heat-transport capability.

The initial effort in the development of this heat pipe has been concentrated on a feasibility demonstration of the dual-passage concept. Presently, a limited amount of investigation is being done on the priming capabilities and behavioral characteristics of the liquid-vapor interface configuration during subjection to a zero-g environment. Knowledge of the static and dynamic behavior of this liquid vapor interface is necessary to answer questions involving time to prime both initially and after dryout and the effects of sudden accelerations on fluid configuration and liquid vapor interfaces.

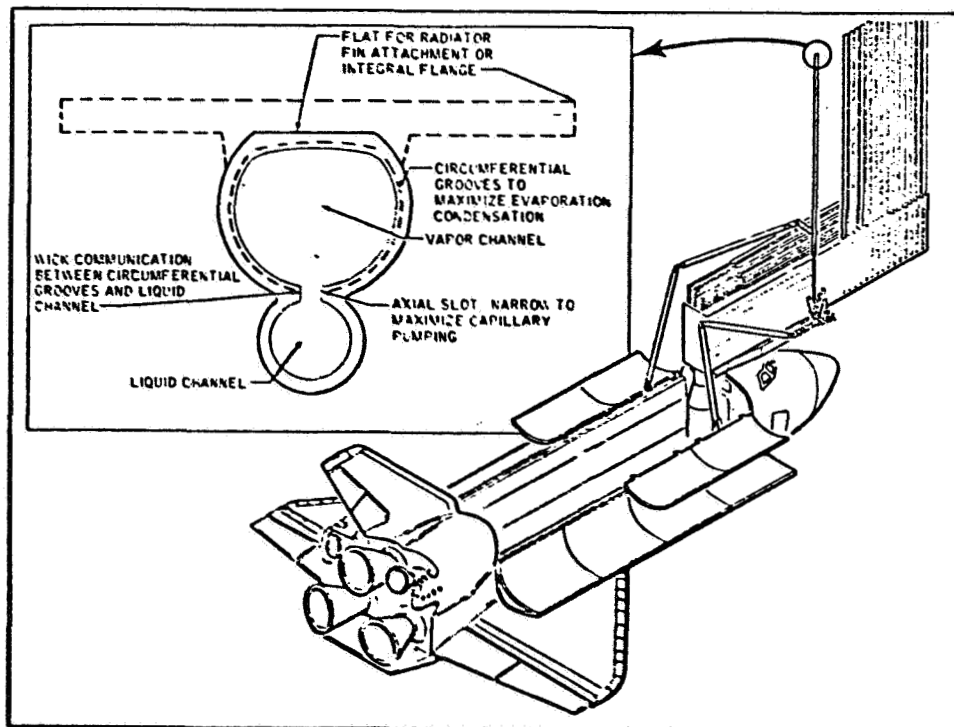


Figure 1

ORIGINAL PAGE IS
OF POOR QUALITY

2. OBJECTIVES

The specific objectives of the Summer Research Program as discussed at the outset were:

1. Determine if the Grumman monogroove heat pipe design would in fact prime as required for proper operation in a zero-g environment regardless of its initial orientation with the gravitational field encountered prior to entrance into zero-g.
2. Develop a mathematical model to determine the time necessary for priming in zero-g.
3. Design an experiment to demonstrate proper priming in a zero-g environment.

These objectives are fairly independent and as such are addressed individually in the following text.

C-3

3. ANALYSIS

3.1 Background

The capillary head in a saturated heat pipe wick arises as a dynamic phenomenon. It is due to the existence of a pressure difference across a curved liquid-vapor interface.

Capillary pressure can be defined as

$$(3.1) P_c = P_v - P_l$$

or from the Laplace and Young equation

$$(3.2) P_c = \sigma \left(\frac{1}{R_1} + \frac{1}{R_2} \right)$$

where R_1 and R_2 are the principle radii of curvature of the meniscus and σ is the surface tension of the liquid.

This pressure difference, which for concave menisci results in a depression of the liquid pressure with respect to the vapor, exists all along the heat pipe wick. In order to obtain a net capillary head, it is necessary for it to be greater at the evaporator than at the condenser. In a heat pipe under load, this is exactly what occurs due to changes in the interface curvatures. Vaporization of the liquid in the evaporator causes the menisci to recede into the wick resulting in a decrease in radii of curvature while condensation in the condenser has the opposite effect. Therefore, the capillary pressure is not constant. Capillary pumping is a passive phenomenon which automatically adjusts to meet the flow requirements.

For a hemispherical surface the forces acting around the surface $F_c = 2\pi R\sigma$ must balance the pressure acting across the surface $F_p = \pi R^2 \Delta P$.

This yields

$$\Delta P = \frac{2\pi R\sigma}{\pi R^2} = 2\sigma/R$$



For capillary rise in a tube of circular cross-section (see figure 2).

$$R_1 = R_2 = R = \frac{r}{\cos\theta}$$

$$\Delta P_c = \rho gh = 2\sigma \cos\theta \frac{1}{r}$$

or in a zero-g environment

for a single cylinder of radius r with surface tension σ

$$(3.3) \quad \Delta P_c = 2\sigma \cos\theta \frac{1}{r}$$

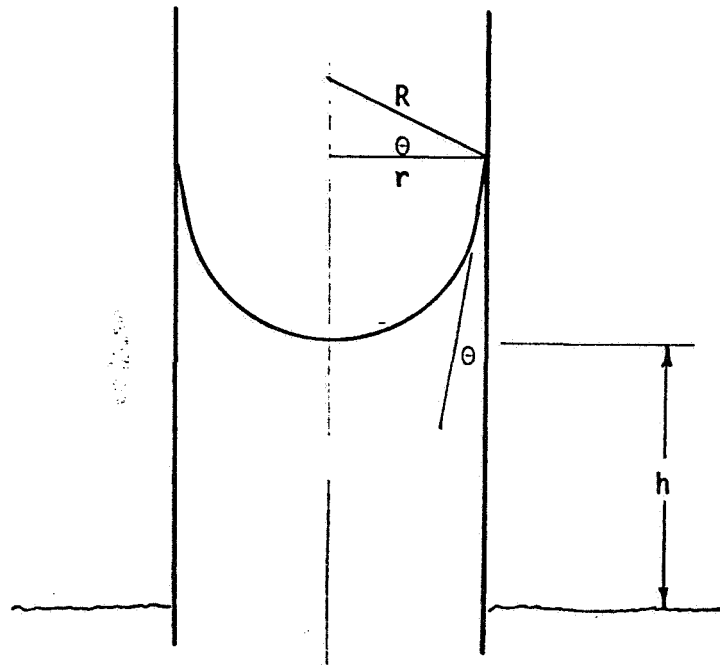


Figure 2

3.2 Minimization of Free Surface Energy

Investigations of capillary and zero-g behavior have suggested that the solid-liquid-vapor system will tend to assume a condition of minimum free surface energy when removed from a gravitational field. Experiments involving drop tower zero-g simulations have attempted to confirm this. In all cases the liquid-vapor surface tended toward a configuration in which the total energy of the system was at a minimum. If the Grumman monogroove heat pipe is analyzed by minimizing the free surface energy in the liquid and vapor channels we can arrive at the theoretical geometric configuration that the liquid-vapor interface would assume in a zero-g environment.

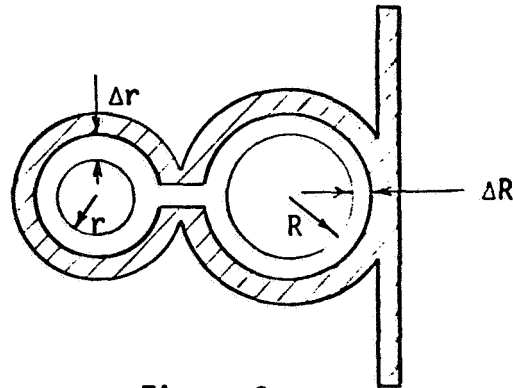


Figure 3

The free surface energy can be equated as

$$\Delta S = (\text{Force}) (\Delta \text{Distance})$$

or

$$(3.4) \Delta S = 2 \cos\theta \frac{1}{r + \Delta r} (2\pi) (r + \Delta r) (L) (\Delta r)$$

Since an increase in Δs results in a decrease in ΔS

$$(3.5) \Delta S = -2 \cos\theta \frac{1}{R + \Delta R} (2\pi) (R + \Delta R) (L) (\Delta R)$$

Equating $\Delta v = \Delta V$ yields

$$(3.6) \quad r^2 - (r + \Delta r)^2 = (R + \Delta R)^2 - R^2$$

or

$$(3.7) \quad \Delta R = \frac{r + \Delta R}{R}$$

Adding equations (3.4) and (3.5) and substituting (3.7)

$$(3.8) \quad \Delta s + \Delta S = -4\sigma\pi L \cos\theta \left(\Delta r - \frac{r + \Delta r}{R} \right)$$

(3.9) or

$$\Delta s + \Delta S = -4\sigma\pi L \cos\theta (1 - r/R)$$

where Δs and ΔS represent the free surface energy of the liquid and vapor channels respectively.

The premise that the liquid-vapor system will seek a configuration of minimum total surface energy requires that the sum of the energy changes $\Delta s + \Delta S$, be negative or zero. This condition will be met with the above equation (3.9) if the product of $(L, \sigma, \cos\theta$ and $(1-r/R)$ is positive. Thus, for a wetting fluid ($\cos\theta$ is positive) the liquid will move into the liquid channel if $r < R$ and move out of the channel when $r > R$. When $r = R$ the fluid will be at an equilibrium state.

3.3 Calculation of Priming Time

Presented herein are two mathematical models which describe the priming phenomenon of the Grumman monogroove heat pipe design. Both methods are accompanied by a computer run, comparing the height of the fluid in both the liquid and vapor passages vs. time.

The first method is a simplified approach which equates the system with two parallel capillary tubes of different diameters drawing fluid from a common reservoir. The second method presented, which is similar to work done by Grumman, is a more complex approach and reflects the decreasing cross-sectional area in the monogroove through which the fluid passes from the vapor to the liquid passage.

Although the two methods differ in some ways they both assume fully developed flow and the principle of minimization of free surface energy.

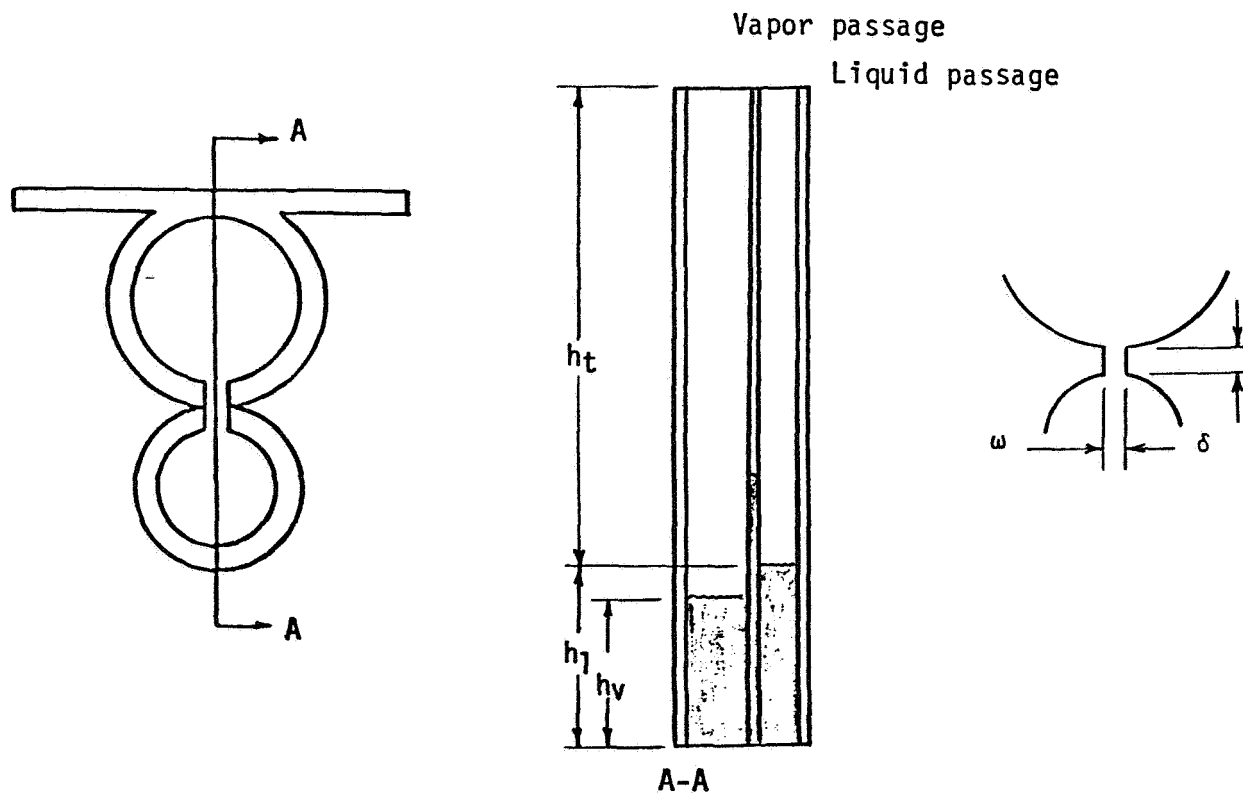


Figure 4

3.3.1 Method I

Initially, the fluid levels are not the same but vary directly with the diameter (see figure 4).

in one-g

$$\Delta P_V = \rho g h_V = 2\sigma \cos\theta \frac{1}{r_V} \quad \Delta P_I = \rho g h_I = 2\sigma \cos\theta \frac{1}{r_I}$$

and the net capillary height difference

$$(1) \quad \Delta h_C = h_I - h_V = \frac{2\sigma}{\rho g} \left(\frac{1}{r_I} - \frac{1}{r_V} \right)$$

in zero-g

$$\Delta P_V = 2\sigma \cos\theta \frac{1}{r_V} \quad \Delta P_I = 2\sigma \cos\theta \frac{1}{r_I}$$

and the net capillary pressure difference

$$(2) \quad \Delta P_C = 2\sigma \cos\theta \left(\frac{1}{r_I} - \frac{1}{r_V} \right)$$

Calculation of Initial Charge

$$\begin{aligned} \text{Initial charge} = & (\text{Liquid in Liquid Channel}) + (\text{Liquid in Monogroove}) \\ & + (\text{Liquid to Fill Wall Groove}) \end{aligned}$$

$$M_{IC} = A_t h_t + A_m h_t + A_{wg} (\# \text{ Threads per inch}) h_t$$

Rearranging and taking into account % charge

$$(3) \quad M_{IC} = C h_t (A_I + A_m + (A_{wg})(TPI)(2\pi r_V))$$

ORIGINAL PAGE IS
OF POOR QUALITY

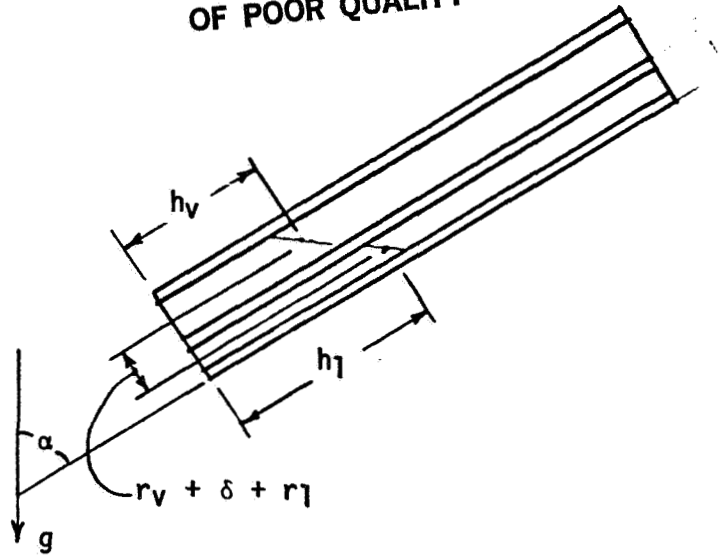


Figure 5

Computation of initial height of liquid in both the liquid and vapor channel.

$\Delta h = \text{funct.}$ (angle the longitudinal axis makes with the gravitational field (α); and difference in capillary height Δh_c)

Δh due to tilt

$$(4) (h_l - h_v)_{\text{tilt}} = (r_v + \delta + r_l) \tan \alpha$$

Δh_c due to capillary head

$$\text{from (1)} (h_l - h_v)_c = \frac{2\sigma}{g} \left(\frac{1}{r_l} - \frac{1}{r_v} \right)$$

$$\Delta h_{\text{total}} = \Delta h_{\text{tilt}} + \Delta h_c$$

$$(5) \Delta h_{\text{total}} = (r_v + \delta + r_l) \tan \alpha + \frac{2\sigma}{g} \left(\frac{1}{r_l} - \frac{1}{r_v} \right)$$

$$(5a) \text{ or } h_v = h_l - (r_v + \delta + r_l) \tan \alpha + \frac{2\sigma}{g} \left(\frac{1}{r_l} - \frac{1}{r_v} \right)$$

$$(6) M_{IC} = (h_l (\pi r_l^2) + h_v (\pi r_v^2))$$

combining (5) and (6) and rearranging

$$(7) \quad h_1 = \left(\frac{M_{IC}}{\pi} + \Delta h_{total} r_v^2 \right) \frac{1}{r_1^2 + r_v^2}$$

$$(8) \quad h_r = h_t - h_1$$

Assuming viscous flow pressure drop and fully developed flow in the liquid channel.

From the Poiseuille equation for pipe flow

$$\text{From (2)} \quad v = \frac{dh}{dt} = \frac{r^2}{8\mu} \frac{\Delta p}{h}$$

$$(9) \quad v = \frac{dh}{dt} = \frac{r_1^2}{8\mu h} 2\sigma \cos\theta \left(\frac{1}{r_1} - \frac{1}{r_v} \right)$$

rearranging and integrating

$$\int 8\mu h dh = \int r_1^2 2\sigma \cos\theta \left(\frac{1}{r_1} - \frac{1}{r_v} \right) dt$$

$$(10) \quad \frac{r_1 \mu h^2}{r_1^2} = 2\sigma \cos\theta \left(\frac{1}{r_1} - \frac{1}{r_v} \right) t$$

or

$$(11) \quad t = \frac{2\mu h r^2}{r_1^2 \sigma \cos\theta} \left(\frac{1}{r_1} - \frac{1}{r_v} \right)$$

$$(11a) \quad t = \frac{2\mu h r^2 r_v}{r_1 \sigma \cos\theta (r_v - r_1)}$$

ORIGINAL PAGE IS
OF POOR QUALITY

3.3.2 Method II

The liquid must flow from the vapor passage to the liquid passage through the monogroove slot at a rate

$$\frac{dm}{dt} = v \rho$$

$$\Delta P \propto \frac{1}{2} \rho v^2 \quad v = \sqrt{\frac{2}{\rho} \Delta P}$$

$$(1) \quad \frac{dm}{dt} = \rho w \sqrt{\frac{2}{\rho} \sqrt{P_{1V}(h) - P_{1L}(h)}}$$

Assume fully developed flow in the liquid channel

$$(2) \quad P_{1L}(h_V) - P_{1L}(h_L) = \frac{\pi}{2} (f N_R) \frac{\mu}{\rho A_1^2} (h_L - h_V) \dot{m}$$

from the Laplace and Young equation

$$\Delta P = \sigma \left(\frac{1}{r_L} - \frac{1}{r_V} \right)$$

$$(3) \quad P_{1V}(h_V) - P_{1L}(h_L) = 2 \sigma \left(\frac{1}{r_L} - \frac{1}{r_V} \right)$$

combining (3) - (2)

$$(4) \quad P_{1V}(h_V) - P_{1L}(h_V) = 2 \sigma \left(\frac{1}{r_L} - \frac{1}{r_V} \right) - \frac{\pi}{2} (f N_R) \frac{\mu}{\rho A_1^2} (h_L - h_V) \dot{m}$$

if the pressure difference between the liquid and vapor passages varies linearly from 0 to h_V

$$(5) \quad P_{1V}(h) - P_{1L}(h) = [P_{1V}(h_V) - P_{1L}(h_V)] \left(\frac{h}{h_V} \right)$$

integrate [1] over $0 \leq h \leq h_V$

$$(6) \quad \dot{m} = \frac{2}{3} h_V \rho w \sqrt{\frac{2}{\rho} \sqrt{P_{1V}(h) - P_{1L}(h)}}$$

or

$$(7) \quad P_{1V}(h_V) - P_{1L}(h_V) = \frac{\dot{m}^2}{\frac{8}{9} \rho w^2 (h_V)^2}$$

Now equating (7) and (4) and rearranging

$$(8) \quad 0 = \dot{m}^2 + \underbrace{\frac{4}{9} \pi (fN_r) \mu \frac{w^2}{A_1^2} v^2 (h_1 - h_v)}_{2b} \dot{m} - \underbrace{\frac{32}{9} \sigma w^2 \left(\frac{1}{D_1} - \frac{1}{D_v} \right) (h_v)^2}_c$$

Eq (8) can be regarded as a quadratic equation in \dot{m} (with instantaneous quasi-steady flow) and

$$(9) \quad \dot{m} = -b + \sqrt{b^2 - c}$$

In a fully charged pipe with $C = \% \text{ overcharge}$ and approximating full charge as that amount needed to fill the liquid channel.

$$(10) \quad CM = A_1 h_t \quad C = A_1 h_1 + A_v h_v$$

which rearranges to

$$(11) \quad h_v = \frac{Ch_t - (h_1 - h_v)}{A_t/A_1} \quad \text{where } A_t = A_1 + A_v$$

since

$$(12) \quad \dot{m} = -\rho A_v \frac{dh_v}{dt}$$

$$(13) \quad \dot{m} = \rho \frac{A_v A_1}{A_t} \frac{d(h_1 - h_v)}{dt} = \gamma \frac{d\beta}{dt}$$

where

$$\beta = \frac{h_t A_1}{h_t} \quad : \quad \gamma = \rho \frac{A_v A_1}{A_t} h_t$$

then

$$h_v = \frac{h_t A_1}{A_t} (C - \beta)$$

$$h_1 - h_v = h_t \beta$$

$$(14) \quad b = - \left[\frac{2}{9} \pi (fN_r) \mu w^2 \frac{h_t^3}{A_t^2} \right] \quad \beta (C - \beta)^2 = \alpha \beta (f - \beta)^2$$

$$c = \left[\frac{32}{9} \sigma \rho \left(\frac{wh_t A_1}{A_t} \right)^2 \left(\frac{1}{D_1} - \frac{1}{D_v} \right) \right] (C - \beta)^2 = \delta (C - \beta)^2$$

Equation (9) becomes

$$\gamma \frac{d\beta}{dt} = -\alpha \beta (C - \beta)^2 + [\alpha^2 \beta^2 (C - \beta)^4 + \delta (C - \beta)^2]^{\frac{1}{2}}$$

$$(15) \quad \frac{\gamma}{\alpha} \frac{d\beta}{dt} = -\beta (C - \beta)^2 + (C - \beta) [\beta^2 (C - \beta)^2 + (\frac{\delta}{\alpha^2})]^{\frac{1}{2}}$$

with an overcharge of zero or $C = 1$

$$\frac{d\beta}{dt} \rightarrow 0 \text{ as } \beta \rightarrow 1$$

Computer programs for both Method I and Method II have been developed. Program listings are shown in Appendix B and Appendix C, respectively. These programs compute the time to prime and plot the liquid height in both the liquid and vapor passages vs. the time.

Test runs of both models were made using the following input parameters:

Length of Pipe	60"
Diameter of Vapor Passage	0.5270"
Diameter of Liquid Passage	0.3050"
Width of Monogroove	0.0100"
Depth of Monogroove	0.0500"
Initial Charge	120%
Angle with Respect to Gravity	0.0 degrees
Surface Tension	1.43×10^{-3} lb/ft
Density	1.1810 sl/ft ³
Viscosity	2.87×10^{-6} sl/ft-s.

A five-foot test length was selected since that is the length originally selected for the zero-g flight test described in Section 4.

Figure 6 shows a comparison of heights of the liquid and the vapor passages at various times as calculated by the two methods. These values show a close correlation for total priming time but vary significantly at intermediate points. This discrepancy can be attributed to the difference in the two methods. The second method considers the decrease in cross sectional flow area between the liquid and vapor passages. Naturally as the fluid level in the vapor passage falls this area or liquid interface decreases causing an increased flow velocity through a decreasing area. The first method does not consider this but takes into account the positive pressure rise in the vapor channel and monogroove which decreases the overall pressure rise in the liquid channel.

ORIGINAL PAGE IS
OF POOR QUALITY

The anticipated results of the actual flight test are discussed in Section 4.4. Briefly however, it is anticipated that the models are accurate in their overall time to prime prediction with the intermediate times occurring at some point within the region resulting from the lack of coincidence of the paths plotted by the two methods (see figure 6). Tables 1 and 2 list the intermediate values of h_1 and h_2 .

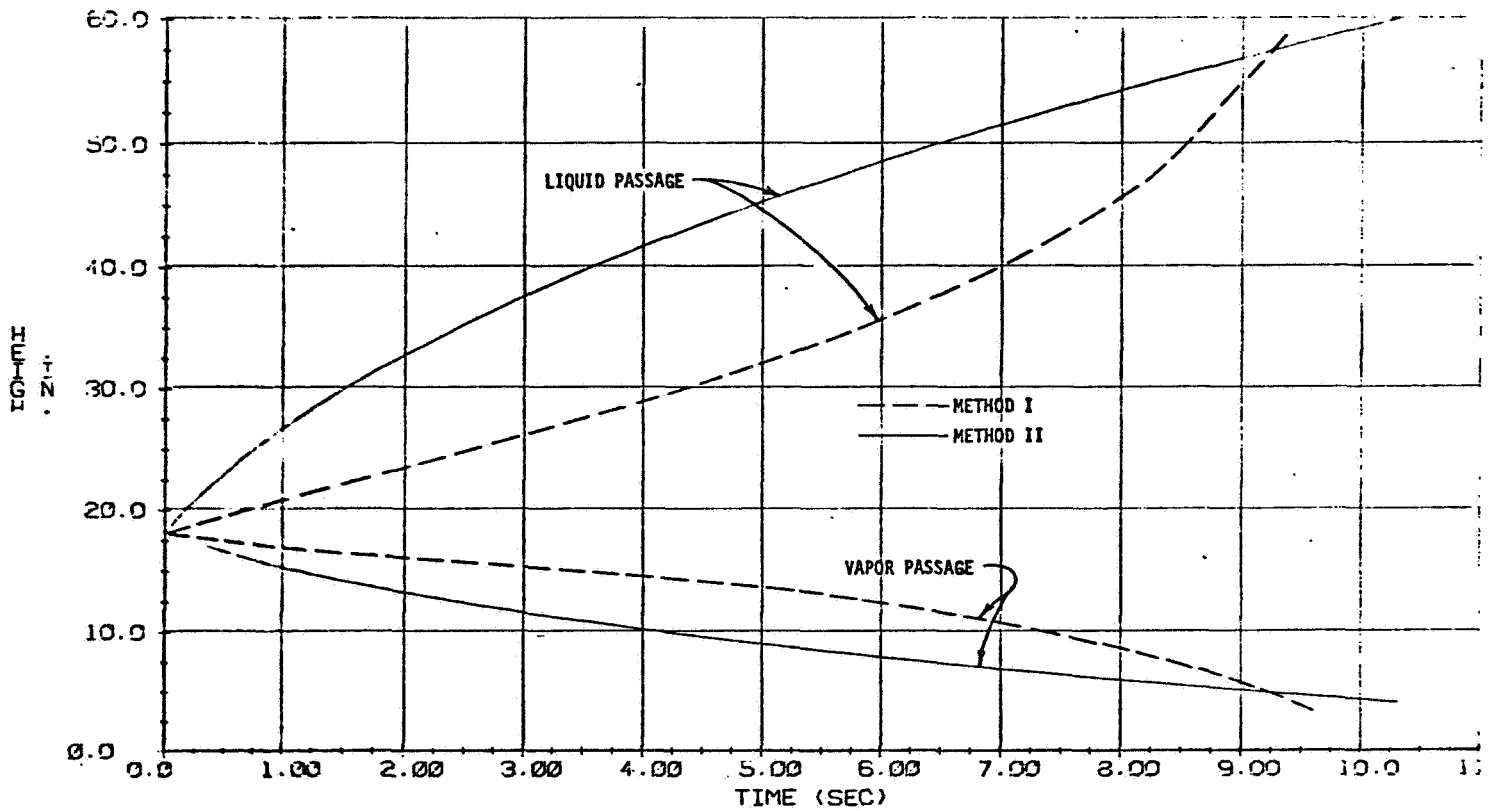


Figure 6 - Comparative Results of
Method I and Method II

DIAMETER OF VAPOR PASSAGE = 0.5270"
 DEPTH OF VAPOR PASSAGE = 0.3090"
 INITIAL CHARGE = 1.20

DIAMETER OF LIQUID PASSAGE = 0.5270"
 DEPTH OF LIQUID PASSAGE = 0.3090"
 INITIAL CHARGE = 1.20

DIAMETER OF VAPOR PASSAGE = 0.5270"
 DEPTH OF VAPOR PASSAGE = 0.3090"
 INITIAL CHARGE = 1.20

DIAMETER OF LIQUID PASSAGE = 0.5270"
 DEPTH OF LIQUID PASSAGE = 0.3090"
 INITIAL CHARGE = 1.20

TIME (SEC)	HEIGHT OF VAPOR (IN)	HEIGHT OF LIQUID (IN)	TIME (SEC)	HEIGHT OF VAPOR (IN)	HEIGHT OF LIQUID (IN)
0.00	18.2118	18.2114	4.14	14.1142	30.4509
0.04	18.1447	18.4289	4.09	14.0147	30.7479
0.08	18.0747	18.5414	4.70	13.9147	31.0480
0.12	17.9997	18.6540	4.81	13.8147	31.3481
0.16	17.9247	18.7665	4.91	13.7101	31.6475
0.20	17.8497	18.8790	5.00	13.6084	31.9473
0.24	17.7747	18.9915	5.09	13.5014	32.2480
0.28	17.6997	19.1040	5.18	13.3983	32.5479
0.32	17.6247	19.2165	5.27	13.2979	32.8478
0.36	17.5497	19.3290	5.36	13.1993	33.1472
0.40	17.4747	19.4415	5.45	13.0993	33.4470
0.44	17.3997	19.5540	5.54	12.9980	33.7480
0.48	17.3247	19.6665	5.63	12.8982	34.0487
0.52	17.2497	19.7790	5.72	12.7989	34.3493
0.56	17.1747	19.8915	5.81	12.6980	34.6498
0.60	17.0997	20.0040	5.91	12.5976	34.9475
0.64	17.0247	20.1165	6.00	12.4984	35.2482
0.68	16.9497	20.2290	6.09	12.3984	35.5492
0.72	16.8747	20.3415	6.18	12.2987	35.8497
0.76	16.7997	20.4540	6.27	12.1947	36.1490
0.80	16.7247	20.5665	6.36	12.0900	36.4481
0.84	16.6497	20.6790	6.45	11.9853	36.7481
0.88	16.5747	20.7915	6.54	11.8803	37.0475
0.92	16.4997	20.9040	6.63	11.7759	37.3480
0.96	16.4247	21.0165	6.72	11.6729	37.6487
1.00	16.3497	21.1290	6.81	11.5703	37.9493
1.04	16.2747	21.2415	6.91	11.4683	38.2498
1.08	16.1997	21.3540	7.00	10.3656	38.5498
1.12	16.1247	21.4665	7.09	10.2630	40.8494
1.16	16.0497	21.5790	7.18	10.1611	40.7480
1.20	15.9747	21.6915	7.27	10.0600	41.3115
1.24	15.8997	21.8040	7.36	9.9587	41.7847
1.28	15.8247	21.9165	7.45	9.8579	42.2705
1.32	15.7497	22.0290	7.54	9.7576	42.7701
1.36	15.6747	22.1415	7.63	9.6578	43.2845
1.40	15.5997	22.2540	7.72	9.5583	43.8153
1.44	15.5247	22.3665	7.81	9.4590	44.3641
1.48	15.4497	22.4790	7.91	9.3605	44.9329
1.52	15.3747	22.5915	8.00	9.2635	45.5240
1.56	15.2997	22.7040	8.09	9.1680	46.1402
1.60	15.2247	22.8165	8.18	9.0739	46.7852
1.64	15.1497	22.9290	8.27	8.9813	47.4634
1.68	15.0747	23.0415	8.36	8.8903	48.1803
1.72	14.9997	23.1540	8.45	8.8007	48.9437
1.76	14.9247	23.2665	8.54	8.7125	49.7639
1.80	14.8497	23.3790	8.63	8.6254	50.6557
1.84	14.7747	23.4915	8.72	8.5403	51.6222
1.88	14.6997	23.6040	8.81	8.4571	52.7630
1.92	14.6247	23.7165	8.91	8.3756	54.0901
1.96	14.5497	23.8290	9.00	8.2956	55.6211

ORIGINAL PAGE IS OF POOR QUALITY

TABLE 1. PIPE ANALYSES

ORIGINAL PAGE IS
OF POOR QUALITY

REFRACT INDEX = 1.4750
DENSITY = 1.3000 G/CC
VISCOSITY = 0.0000 G/CM-SEC

WIDTH = 0.0100"
DEPTH = 0.0000"
INITIAL CHARGE = 1.00

DIAMETER OF VAPOR PASSAGE = 0.5270"
DIAMETER OF LIQUID PASSAGE = 0.3840"
HEIGHT OF PIPE = 40.000"
ANGLE WITH HORIZONTAL TO GRAVITY FIELD = 0.00 DEG

TIME (SEC)	HEIGHT OF VAPOR (IN)	HEIGHT OF LIQUID (IN)	TIME (SEC)	HEIGHT OF VAPOR (IN)	HEIGHT OF LIQUID (IN)
0.00	16.0654	16.0654	5.20	8.6077	46.0045
0.10	17.0754	19.1927	5.30	8.5709	46.4132
0.20	17.4481	20.0047	5.41	8.4554	46.7727
0.31	17.6836	21.1808	5.51	8.3409	47.0977
0.41	17.7804	22.1114	5.62	8.2277	47.4078
0.52	17.8406	22.8049	5.72	8.1146	47.7004
0.62	17.8754	23.3044	5.82	8.0046	48.1018
0.72	17.8956	23.6687	5.91	7.8947	48.4039
0.83	17.9112	24.0416	6.03	7.7858	48.7049
0.93	17.9236	24.2060	6.14	7.6780	49.0769
1.04	17.9347	24.3042	6.24	7.5717	49.3988
1.14	17.9436	24.3480	6.34	7.4659	49.7118
1.24	17.9504	24.3384	6.45	7.3604	50.0050
1.35	17.9557	24.3067	6.55	7.2555	50.3053
1.45	17.9594	24.2629	6.66	7.1516	50.6049
1.56	17.9615	24.2054	6.76	7.0514	50.9048
1.66	17.9794	24.0869	6.87	6.9501	51.2000
1.76	17.9894	24.0450	6.97	6.8497	51.5047
1.87	17.9962	24.0047	7.07	6.7482	51.8048
1.97	17.9965	24.0011	7.18	6.6515	52.1015
2.08	17.9911	24.0000	7.28	6.5586	52.4037
2.18	17.9896	24.0000	7.39	6.4646	52.7025
2.29	17.9819	24.0000	7.49	6.3668	53.0110
2.39	17.9778	24.0000	7.59	6.2647	53.3062
2.49	17.9707	24.0000	7.70	6.1700	53.5998
2.60	17.9656	24.0000	7.80	6.0760	54.1000
2.70	17.9622	24.0000	7.91	5.9827	54.4047
2.81	17.9597	24.0000	8.01	5.8901	54.6089
2.91	17.9550	24.0000	8.11	5.7983	54.9071
3.01	17.9499	24.0000	8.22	5.7071	55.2013
3.12	17.9455	24.0000	8.32	5.6166	55.4994
3.22	17.9444	24.0000	8.43	5.5268	55.7655
3.33	17.9458	24.0000	8.53	5.4377	56.0297
3.43	17.9493	24.0000	8.63	5.3482	56.2920
3.53	17.9551	24.0000	8.74	5.2613	56.5524
3.64	17.9612	24.0000	8.84	5.1741	56.8109
3.74	17.9678	24.0000	8.95	5.0875	57.0676
3.85	17.9746	24.0000	9.05	5.0015	57.3225
3.95	17.9812	24.0000	9.16	4.9161	57.5756
4.05	17.9857	24.0000	9.26	4.8314	57.8269
4.16	17.9899	24.0000	9.36	4.7472	58.0766
4.26	17.9938	24.0000	9.47	4.6636	58.3245
4.37	17.9974	24.0000	9.57	4.5805	58.5707
4.47	17.9994	24.0000	9.68	4.4981	58.8152
4.58	17.9994	24.0000	9.78	4.4162	59.0581
4.68	17.9994	24.0000	9.88	4.3348	59.2994
4.78	17.9994	24.0000	9.99	4.2540	59.5391
4.89	17.9994	24.0000	10.09	4.1737	59.7772
4.99	17.9994	24.0000	10.20	4.0940	60.0137
5.10	17.9994	24.0000	10.30	4.0147	

TARII ATD RESIII TS (METHOD II)

4. TEST PROGRAM

4.1 Test Objectives

- I. Demonstrate that priming will occur in a zero-g environment.
 - a) Determine the effect of various initial liquid orientations on priming capability.
 - b) Confirm expectations of proper priming of the liquid passage.
- II. Provide data for correlation of the mathematical model.

4.2 Test Description

Three heat pipe elements will be tested in a zero-g environment representative of that experienced in low earth orbit. Various initial test positions will be evaluated to determine the effect of liquid location in the heat pipe upon entry to a zero-g environment. In addition, data on the reprime characteristics in the event localized dryout does occur can be obtained.

The basic heat pipe design dimensions are a function of the type of fluid and amount of heat to be transported. In this particular test since the primary investigation involves capillary pumping and priming actions both static and dynamic, there are no plans for any data involving heat transport or heat rejection capabilities.

4.3 Test Setup

Three separate test articles will be prepared; Test Article #1 and Test Article #2 will both be two-foot sections of the Grumman monogroove heat pipe design. TA1 will be machined lengthwise (see figure 7) maintaining the monogroove width of 0.0100".

TA2 will also be machined lengthwise but in this case only enough material will be removed so that a gap approximately 1/2" in width and running the full length of the test article vapor passage will be achieved (see figure 8). The machined surfaces on both TA1 and TA2 will be covered with a plexiglass sheet which will enclose the liquid and vapor channels. The pipes should then be charged and capped.

TA3 will consist of a two inch long section of the Grumman monogroove heat pipe charged and capped on both ends with plexiglass. It may prove necessary to use a coloring agent on the fluid in the heat pipes in order that the fluid will be more easily distinguished from the vapor space.

ORIGINAL PAGE IS
OF POOR QUALITY

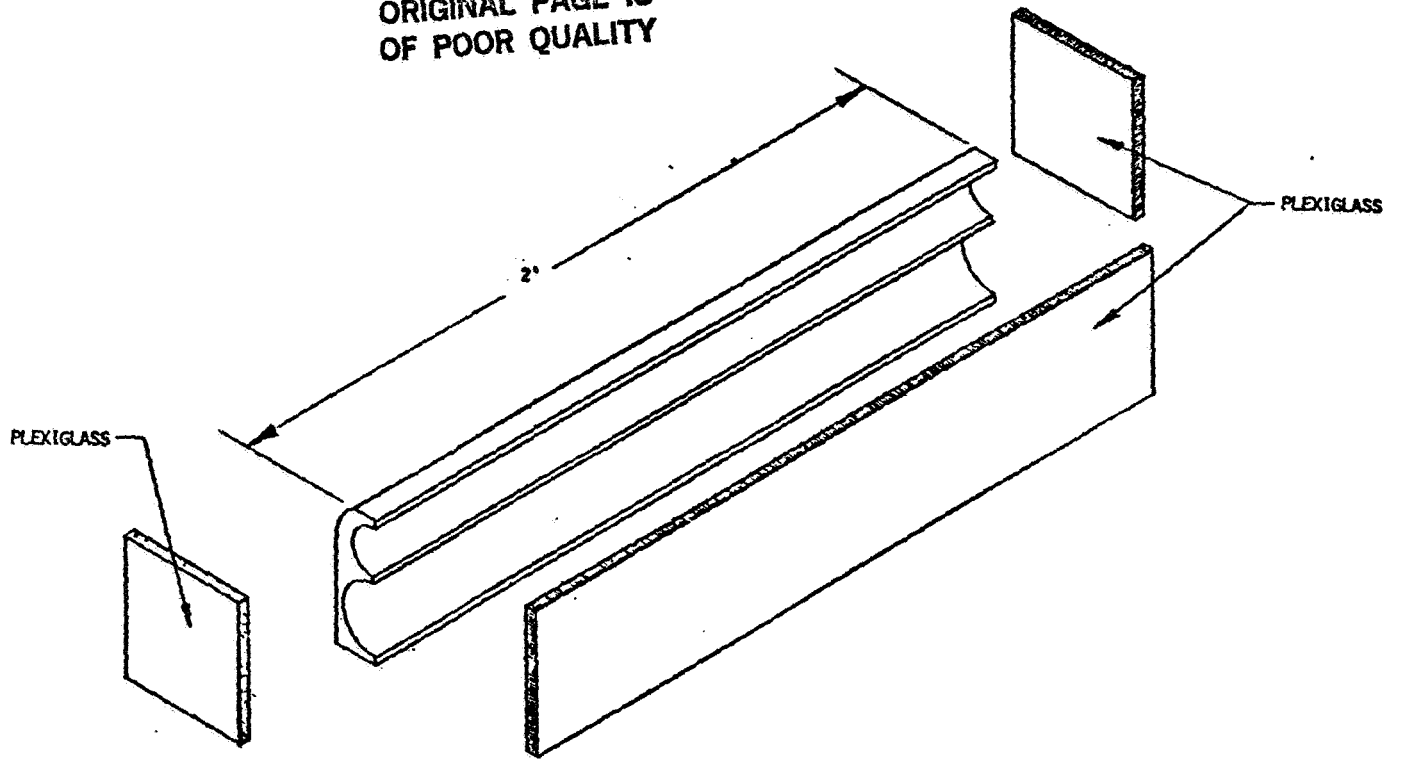


Figure 7 - Test Article #1 (TA1)

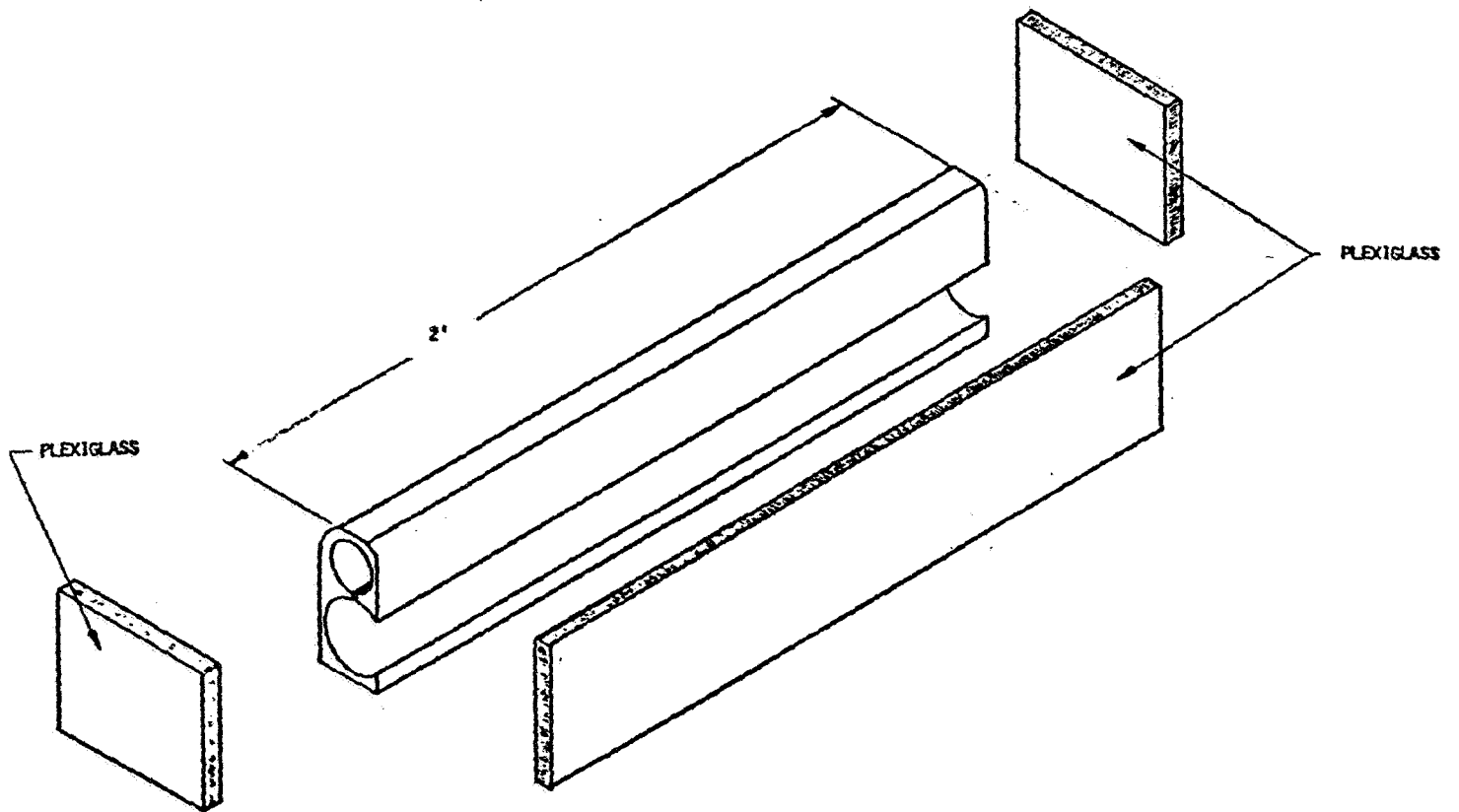


Figure 8 - Test Article #2 (TA2)

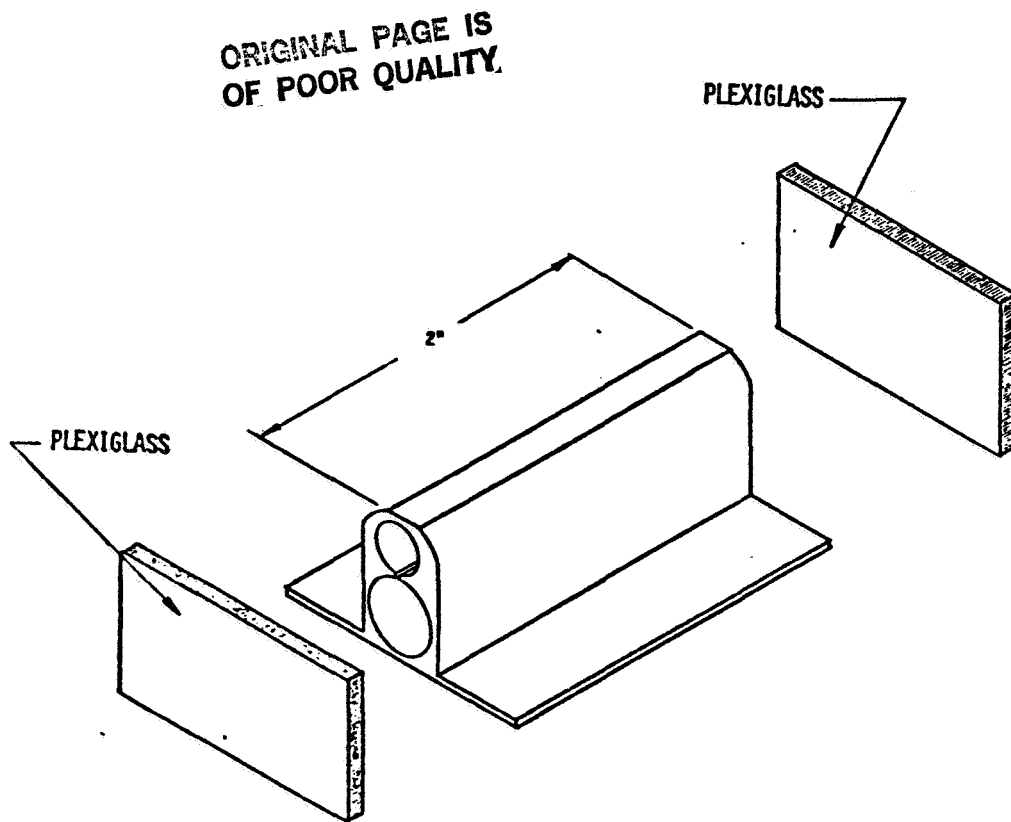


Figure 9 - Test Article # 3 (TA3)

Figure 11 shows the method for providing a seal between the heat pipes and the plexiglass covers for all three test articles. It should be noted that the groove in which the heat pipes rest should be ≈ 0.005 " less than the heat pipe itself in order to provide a positive seal. A brief stress analysis was run using the configuration shown and a deflection of approximately 0.008" will occur in the vicinity of the monogroove. This small additional width of the monogroove should prove insignificant when determining the priming tendency but may affect the time to prime characteristics.

ORIGINAL PAGE IS
OF POOR QUALITY

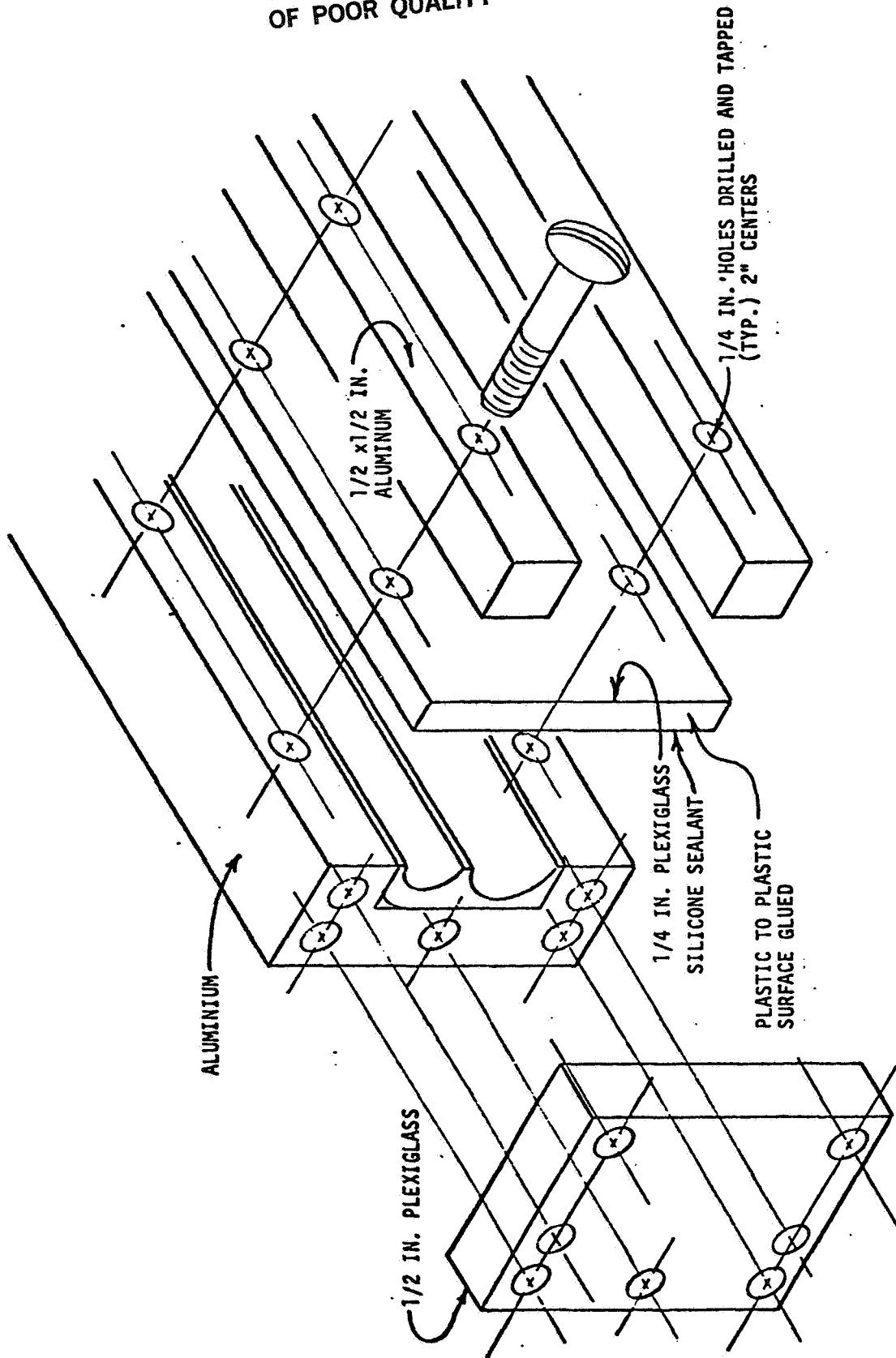


FIGURE 11

ORIGINAL PAGE IS
OF POOR QUALITY.

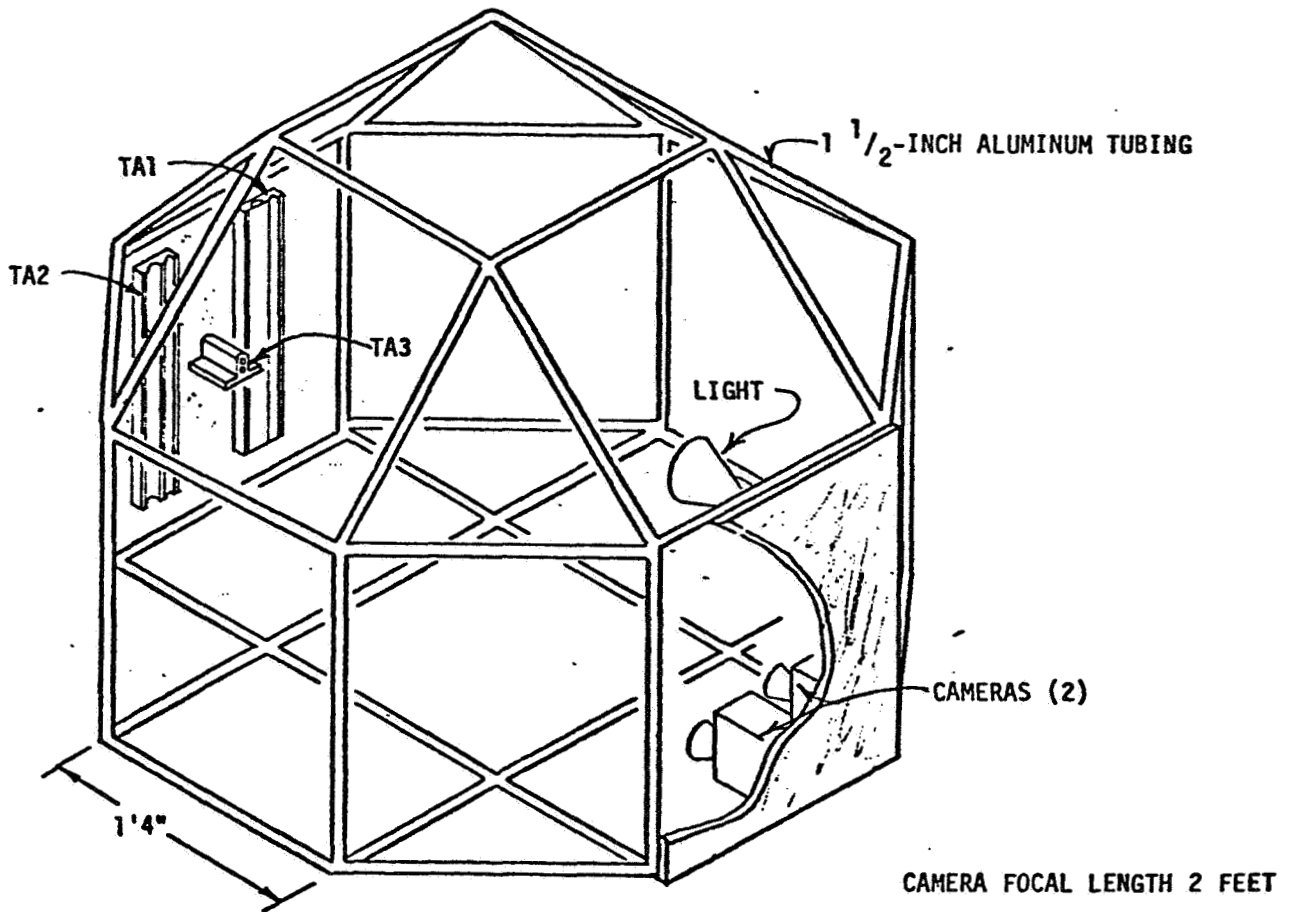


FIGURE 12 TEST APPARATUS

APPENDIX A

NOMENCLATURE

	<u>SYMBOLS</u>		<u>SUBSCRIPTS</u>
A	AREA	c	CAPILLARY
C	% OF CHARGE	l _c	INITIAL CHARGE
F	FORCE	l	LIQUID
g	ACCELERATION OF GRAVITY	m	MONOGROOVE
h	HEIGHT	r	RISE
\dot{m}	MASS FLOW RATE	t	TOTAL
M	MASS OF CHARGE	v	VAPOR
P	PRESSURE		
Q	HEAT TRANSFER		
r	RADIUS		
R	RADIUS OF CURVATURE		
V	VELOCITY		
α	ANGLE BETWEEN LONGITUDINAL AXIS AND GRAVITY FIELD		
δ	DEPTH OF MONOGROOVE		
ω	WIDTH OF MONOGROOVE		
	DENSITY		
σ	SURFACE TENSION		
μ	VISCOSITY		
θ	WETTING ANGLE		

```

10 REM ----- HEAT PIPE ANALYSIS PROGRAM
20 DIM
30 REM ----- VARIABLE LIST ;
40 REM ----- D1=Dv          R1=Rv          A1=Av
                   D2=Dl          R2=rl          A2=Aj
                   P=pi=atan(1.0)          g=32.179
                   S=sigma          M=mu          K=rho
50 REM D=depth of menogroove          W=width of menogroove
                   A=alpha (ANGLE W/R TO g)          C=charge.
                   H1=del Htotal          H2=del Hc          H3=del Htilt
                   H4=Hr          H5=Hl          H6=Hv
60 REM T=t          T0=tmax          M1=Mic
                   T1=threads/in          A3=Awg

```

```

70 DIM H5(200), H6(200), T(200)
80 G = 32.179 : SELECT R : P = 4.0*ATAN(1.0) : SELECT D :
90 PRINT HEX(03) : PRINT USING 100: PRINT : RETURN
100 Z-----

```

HEAT PIPE ANALYSIS

```

110 GOSUB 90 : PRINT "ENTER THE FOLLOWING INFORMATION PLEASE:"
120 INPUT "DIAMETER OF VAPOR CHANNEL, INCHES", D1 : R1=D1/2
130 INPUT "DIAMETER OF LIQUID CHANNEL, INCHES", D2 : R2=D2/2
140 A1=PI*RI^2 : A2=PI*RL^2
150 INPUT "TOTAL PIPE HEIGHT, INCHES", H0 : H0=H0/12
160 INPUT "WIDTH OF MENOGROOVE, INCHES", W
170 INPUT "DEPTH OF MENOGROOVE, INCHES", D
180 A4=W*D
190 INPUT "ANGLE WITH RESPECT TO GRAVITY FIELD, DEG", A
200 INPUT "INITIAL CHARGE", C : GOSUB 90
210 INPUT "WALL GROSS CROSS-SECTIONAL AREA, SQ IN", A3
220 INPUT "LIQUID CHANNEL THREADS PER INCH", T1
230 PRINT : PRINT "LIQUID PROPERTIES : "
240 INPUT "SURFACE TENSION (LIQUID VAPOR)", S
250 INPUT "VISCOSITY", M
260 INPUT "DENSITY", R

```

```

270 GOSUB 90 : REM ----- START COMPUTATIONS

```

```

280 REM ----- COMPUTE DEL HCAPILARY
290 H2=(2*S/(R2*(P*(1/R2-1/R1))^2)
300 REM ----- COMPUTE DEL HTILT
310 H3=(R1+R2)*TAN(A)^2
320 REM ----- COMPUTE DEL HTOTAL
330 H1=H2+H3
340 REM ----- MASS OF INITIAL CHARGE
350 M1=C*PI*(A3+A4+A5)^2*(P*(R1))^2/144
360 REM ----- HEIGHT OF LIQUID (MIN HL)
370 H5(1)=(M1/(R2*(H1+R1)^2*(P/144))^2)^.44*(1/(R1^2+R2^2))
380 REM ----- HEIGHT OF VAPOR (MAX HV)
390 H5(1)=H5(1)-(R1+R2)*TAN(A)+(2*S/(R2*(P*(1/R2-1/R1)))
400 REM ----- CALCULATE TIME (MAX T)
410 H4=H0-H5(1)
420 T0=(.775*H4^2*(R1))/(R2*S*(R1-R2)/12) : T(1)=T0
430 LN 1=2 TO 100
440 REM ----- DECREMENT TIME AND ITERATE

```

```

10  REM ----- HEAT PIPE ANALYSIS PROGRAM
20  REM
30  REM ----- VARIABLE LIST ;
40  REM -----  D1=D1V      R1=R1V      A1=A1V
                   D2=D1L      R2=R1L      A2=A1L
                   P=PI*4*ARCTAN(1.0)      G=32.179
                   S=SIGMA      M=MU      R=RHO
50  REM      D=depth of menogroove      W=width of menogroove
                   A=alpha (ANGLE W/RT TO G)      C=charge
                   H1=del Htotal      H2=del Hc      H3=del Htilt
                   H4=Hr      H5=Hl      H6=Hv
60  REM      T=t      TO=tmax      M1=Mic
                   T1=threads/in      AB=Avg

```

```

70  DIM H(200), HC(200), T(200)
80  G = 32.179 : S=PI*4 : R : P = 4.0*ARCTAN(1.0) : SELECT D :
90  PRINT HEX(03) : PRINT USING 100: PRINT : RETURN
100  X-----

```

HEAT PIPE ANALYSIS

```

110  GOSUB 90 : PRINT "ENTER THE FOLLOWING INFORMATION PLEASE:"
120  PRINT

```

```

130  INPUT "DIAMETER OF VAPOR CHANNEL, INCHES",D1 : R1=D1/2
140  INPUT "DIAMETER OF LIQUID CHANNEL, INCHES",D2 : R2=D2/2
150  A1=PI*R1^2 : A2=PI*R2^2
160  INPUT "TOTAL PIPE LENGTH, INCHES",H0 : H0=H0/12
170  INPUT "WIDTH OF MENOGROOVE, INCHES",W
180  INPUT "DEPTH OF MENOGROOVE, INCHES",D
190  A4=W*D
200  INPUT "ANGLE WITH RESPECT TO GRAVITY FIELD, DEG",A
210  INPUT "INITIAL CHARGE",C : GOSUB 90
220  INPUT "WALL CRUISE CROSS-SECTIONAL AREA, SQ IN",A3
230  INPUT "LIQUID CHANNEL THREADS PER INCH",T1
240  PRINT : PRINT "LIQUID PROPERTIES :"
250  INPUT "SURFACE TENSION (LIQUID VAPOR)",S
260  INPUT "VISCOSITY",M
270  INPUT "DENSITY",R

```

```

270  GOSUB 90 : REM ----- START COMPUTATIONS

```

```

280  REM ----- COMPUTE DEL HCAPILARY
290  H2=(2*S/(R*G))*(1/R2-1/R1)*12
300  REM ----- COMPUTE DEL HTILT
310  H3=(R1+D)*R2*TAN(A)*12
320  REM ----- COMPUTE DEL HTOTAL
330  H1=H2+H3
340  REM ----- MASS OF INITIAL CHARGE
350  M1=C*(PI*H0*(A3+A4+A1+T1)*PI*R1)*1/144
360  REM ----- HEIGHT OF LIQUID (MIN HL)
370  H5(1)=(M1/(R*PI*H0*T1)*PI/144)*144*(1/(R1^2+R2^2))
380  REM ----- HEIGHT OF VAPOR (MAX HV)
390  H5(1)=H5(1)-(R1+R2)*TAN(A)+(2*S/(R*G))*(1/R2-1/R1)
400  REM ----- CALCULATE LINE (MAX T)
410  H4=H0-H5(1)
420  TO=(M1*M1*(H4+2*R1))/(R2*S*(R1-R2)/12) : T(1)=TO

```

```

43  LN 1=2 TO 100
44  REM ----- DECREMENT LINE AND ITERATE

```

ORIGINAL PAGE IS
OF POOR QUALITY

```

10 REM ----- HEAT PIPE ANALYSIS PROGRAM
20 REM ----- JULY 1981
30 REM ----- VARIABLE LIST ;
40 REM ----- D1=Dv          R1=Rv          A1=Av
          D2=Dl          R2=RL          A2=Al
          P=PI=4*PI*ATAN(1.0)          G=32.179
          S=sigma          M=mu          R=rho
50 REM ----- D=depth of monogroove          W=width of monogroove
          A=alpha (ANGLE W/RT TO G)          C=charge
          H1=del Htotal          H2=del Hc          H3=del Htilt
          H4=Hr          H5=Hl          H6=Hv
60 REM ----- T=t          TO=tmax          M1=Mic
          T1=threads/in          A3=Awg

70 DIM H5(200), HC(200), T(200)
80 G = 32.179 : SELECT R : P = 4.0*PI*ATAN(1.0) : SELECT D :
      GO TO 110
90 PRINT HEX(03) : PRINT USING 100: PRINT : RETURN
100 Z-----
          HEAT PIPE ANALYSIS
-----
110 GOSUB 90 : PRINT "ENTER THE FOLLOWING INFORMATION PLEASE:"
      PRINT
120 INPUT "DIAMETER OF VAPOR CHANNEL, INCHES",D1 : R1=D1/2
130 INPUT "DIAMETER OF LIQUID CHANNEL, INCHES",D2 : R2=D2/2
140 A1=PI*R1**2 : A2=PI*R2**2
150 INPUT "TOTAL PIPE HEIGHT, INCHES",H0 : H0=H0/12
160 INPUT "WIDTH OF MONGROOVE, INCHES",W
17 INPUT "DEPTH OF MONGROOVE, INCHES",D
18 A4=W*D
19 INPUT "ANGLE WITH RESPECT TO GRAVITY FIELD, DEG",A
200 INPUT "INITIAL CHARGE",C : GOSUB 90
210 INPUT "WALL GROOVE CROSS-SECTIONAL AREA, SQ IN",A3
220 INPUT "LIQUID CHANNEL THREADS PER INCH",T1
230 PRINT : PRINT "LIQUID QUALITIES :"
240 INPUT "SURFACE TENSION (LIQUID VAPOR)",S
250 INPUT "VISCOSITY",M
260 INPUT "DENSITY",R

270 GOSUB 90 : REM ----- START COMPUTATIONS
280 REM ----- COMPUTE DEL HCAPILARY
290 H2=(2*S/(R*R*G))*(1/R2-1/R1)**2
300 REM ----- COMPUTE DEL H TILT
310 H3=(R1+D)*R2*TAN(A)**2
320 REM ----- COMPUTE DEL HTOTAL
330 H1=H+H2
340 REM ----- MASS OF INITIAL CHARGE
350 M1=C*PI*H0*(A4+A3*T1)**2*PI*R1**2/144
360 REM ----- HEIGHT OF LIQUID (MIN HL)
370 H5(1)=(M1/(R*R*PI*H1*R1)**2*PI/144)**.5*(1/(R1**2+R2**2))
380 REM ----- HEIGHT OF VAPOR (MAX HV)
390 H5(1)=H5(1)-(R1*H1+R2)*TAN(A)+(2*S/(R*G))*(1/R2-1/R1)
400 REM ----- CALCULATE TIME (MAX T)
410 H6=H0-H5(1)
420 T0=(T1*M1*H4+2*R)/(R2*S*(R1-R2)/12) : T(1)=T0

43 FOR J=2 TO 100
44 REM ----- DECREMENT TIME AND ITERATE

```

ORIGINAL PAGE IS
OF POOR QUALITY

```

70 T(1)=1(1-1)-T0/100
80 H4=SQRT(1(1)*R2**2*(R1-R2)/12*(1/(2*M*R1)))
90 H5(1)=H0-H4
420 H5(1)=H5(1-1)-(H5(1)-H5(1-1))*(R2+2/R1+2)
430 NEXT I

500 REM ----- CONVERT TIME REMAINING TO ELAPSED TIME
510 FOR I=1 TO 100
520 T(1)=10-T(1)
530 NEXT I

540 REM ----- PRINT OUT RESULTS
550 SELECT PRINT ON(132) : PRINT HEX(OE), "
HEAT PIPE ANALYSIS" : PRINT
560 PRINT USING 570, D1,W,S : PRINT USING 580, D2,D,R :
PRINT USING 590, H0*12,C,M,A
570 Z DIAMETER OF VAPOR PASSAGE = #.####" WIDTH
OF MINOR DOME = #.####" SURFACE TENSION = #.##+### LB/FT
580 Z DIAMETER OF LIQUID PASSAGE = #.####" DEPTH
OF MINOR DOME = #.####" DENSITY = #.#### SL/CU.FT.
590 Z HEIGHT OF PIPE = ###.##" INITIAL
L CHARGE = ##.## VISCOSITY = #.##+### SL/FT-S
ANGLE WITH RESPECT TO GRAVITY FIELD = ###.##
DEG
600 FOR J = 1 TO 100 : H5(1)=H5(1)*12 : H6(1)=H6(1)*12 :
NEXT J
610 PRINT : PRINT USING 620 : PRINT USING 630 : FOR J=1 TO 50 :
PRINT USING 640, T(1),H5(1),H6(1),T(1+50),H6(1+50),H5(1+50)
: NEXT I
620 Z TIME HEIGHT OF VAPOR HEIGHT OF LIQUID
TIME HEIGHT OF VAPOR HEIGHT OF LIQUID
(IN) (IN) (IN)
630 Z (SEC) (IN) (IN)
640 Z -----
###.## ###.#### ###.####
###.## ###.#### ###.####
650 SELECT PRINT ON(64) : GOSUB 90 : SELECT PY : PRINT :
PRINT "BEGIN PLOTTING SEQUENCE....." : FOR I=1 TO 5
660 PRINT : NEXT I : PRINT "START DRUMPLD) PACKAGE...." :
PRINT : SELECT P
700 REM ----- "DRUMPLD)"
710 REM ----- MIKE CARTER EC 3 22 JULY 81
SURPRISING TO DO GENERAL PLOTTING IN SUPPORT
OF THE PROGRAM "HEATPIPE"
720 DIM X(500), Y(500), G(2), X1(40), X2(40), Y1(40), Y2(40), A(10),
R(20), K(40), T1(500), T2(500), H(4), J(4)
730 SELECT PRINT ON(4) : GOTO 740 : GOTO 760
740 PRINT HEX(OE) : PRINT USING 750 : PRINT : RETURN
750 Z -----
DRUMPLD)
-----
760 PRINT "TURN IN PLOTTER AND SET HOME POSITION" : PRINT
770 INPUT "Hit RETURN TO BEGIN",C : C=1
780 L=100 : FOR I=1 TO 100
790 IF C=1 THEN Y(I)=H5(I) : IF C=2 THEN Y(I)=H6(I) :
X(I)=T(I) : NEXT I
80 REM ----- SENT DATA POINTS IN INCREASING X ORDER AND

```

ORIGINAL PAGE IS
OF POOR QUALITY

DETERMINE THE LARGEST X AND Y VALUES.

270 GOSUB 740 : PRINT "SORTING...." : GOSUB 1690 : GOSUB 740

280 IF C > 1 THEN 290

290 G1=1

300 LN G1 GOTO 250,260,270 : GOTO 280

350 PLOT <,,1+X(C,1)> : GOTO 280

360 PLOT <,,1+X(C,2)> : GOTO 280

370 PLOT <,,1+X(C,3)> : GOTO 280

380 GOSUB 1070

390 G=2

400 X1#="TIME" : X2#="(SEC)"

410 Y1#="HEIGHT" : Y2#=".IN."

420 FOR I = 1 TO L

430 I1(I)=(X(I)-S1)*200/S2 : I1(I)=ROUND(I1(I)+0.5,0)

440 I2(I)=(Y(I)-S3)*200/S4 : I2(I)=ROUND(I2(I)+0.5,0)

450 NEXT I

460 G=C+1

470 GOSUB 740 : PRINT "DATA BEING PROCESSED , HEAT PIPE ANALYSIS

" : PRINT "WORKING....."

480 IF C > 1 THEN 490

490 REM ----- DRAW AXES, TICK MARKS AND UNIT LABELS

1000 X1 = D1*200 : X2 = D2*200

1010 PLOT<,,R> : PLOT D1<200,0,U>

1020 PLOT<0,-10,U>,<0,20,D>,<0,-10,U>

1030 FOR I = 1 TO D1 : FOR J = 1 TO 3 : PLOT<-50,-5,U>,<0,10,D>,<0,-5,U> : NEXT J : PLOT<-50,-10,U>,<0,20,D>,<0,-10,U> :

NEXT I

1040 PLOT<,,R> : PLOT D2<0,200,U>

1050 PLOT<-10,0,U>,<20,0,D>,<-10,0,U>

1060 FOR I = 1 TO D2 : FOR J = 1 TO 3 : PLOT<-5,-50,U>,<10,0,D>,<-5,0,U> : NEXT J : PLOT<-10,-50,U>,<20,0,D>,<-10,0,U> :

NEXT I

1070 PLOT<,,R>

1080 PLOT<-50,-30,U> : A=S1

1090 FOR I=1 TO D1+1

1100 IF ABS(A) >= 1000. THEN 1130 : IF ABS(A) >= 100. THEN 1140

: IF ABS(A) >= 10. THEN 1150 : IF ABS(A) >= 1 THEN 1160 :

IF A = 0. THEN 1110

1110 CONVERT A TO AC, (##) : GOTO 1170

1120 CONVERT A TO AC, (-.###) : GOTO 1170

1130 CONVERT A TO AC, (-####) : GOTO 1170

1140 CONVERT A TO AC, (-##.) : GOTO 1170

1150 CONVERT A TO AC, (-##.#) : GOTO 1170

1160 CONVERT A TO AC, (-#.##) : GOTO 1170

1170 PLOT<I,,C> : PLOT<I3,,S> : PLOT<,,A#> :

PLOT<-IEN(AC)*20,0,U> : A = A + S2 : PLOT<200,0,U>

1180 NEXT I : PLOT<,,R>

1190 PLOT<,,R>

1200 PLOT<-150,0,U> : A=S3

1210 FOR I=1 TO D2+1

1220 IF ABS(A) >= 1000. THEN 1250 : IF ABS(A) >= 100. THEN 1260

: IF ABS(A) >= 10. THEN 1270 : IF ABS(A) >= 1 THEN 1280 :

IF A = 0. THEN 1230

1230 CONVERT A TO AC, (##) : GOTO 1290

1240 CONVERT A TO AC, (-.###) : GOTO 1290

1250 CONVERT A TO AC, (-####) : GOTO 1290

1260 CONVERT A TO AC, (-##.) : GOTO 1290

1270 CONVERT A TO AC, (-##.#) : GOTO 1290

1280 CONVERT A TO AC, (-#.##) : GOTO 1290

ORIGINAL PAGE IS
OF POOR QUALITY

```

1000 CONVERT A TO A*, (-##.##) : GOTO 1290
1100 CONVERT A TO A*, (-#.##) : GOTO 1290
1200 PLOT<1,,C>,<13,,S>,<,,A* >,<-LEN(A*)*26,0,U> : A = A + S4 :
      PLOT<0,200,U>
1300 NEXT I : PLOT<0,200,U>,<,,R>

1310 LN G GOTO 1340, 1320, 1330, 1340
1320 IF G=2 THEN G=1 : IF G=3 THEN G=2 : S=1 :
      FOR J=1 TO D1*G : PLOT<200/G,,U>,<D2<S*200,D> : S=-S :
      NEXT J : PLOT<,,R>
1330 S=1 : FOR J=1 TO D2*G : PLOT<,200/G,U>,<D1<S*200,,D> :
      S=-S : NEXT J : PLOT<,,R>

1340 LN G2 GOTO 1350,1360,1370
1350 PLOT<,,HEX(C1)> : GOTO 1380
1360 PLOT<,,HEX(C2)> : GOTO 1380
1370 PLOT<,,HEX(C3)>
1380 REM ----- JOIN POINTS BY A LINE
1390 PLOT<,,R>
1400 IF Z = 1 THEN 1450
1410 FOR I = 1 TO L
1420 IF I>1 THEN 1430 : PLOT<I(1)/D1,,U> : PLOT<I2(I)/D2,U>
      : GOTO 1440
1430 PLOT<I(1)-I(I-1),I2(I)-I2(I-1),D>
1440 NEXT I : PLOT<,,R>

1450 REM ----- ADD AXIS LABELS

1460 IF C > 1 THEN 1500
1470 LN O1 GOTO 1480,1490,1500
1480 PLOT<,,HEX(C1)> : GOTO 1510
1490 PLOT<,,HEX(C2)> : GOTO 1510
1500 PLOT<,,HEX(C3)> : GOTO 1510
1510 L3=LEN(X1$) : L4=LEN(X2$) : L5=LEN(Y1$) : L6=LEN(Y2$)
1520 PLOT<I(1)*200/D1-L3*13/D1,,U>,<,-80,X1$> : PLOT<,,R>
1530 PLOT<I(1)*200/D1-L4*13/D1,,U>,<,-120,X2$> : PLOT<,,R>
1540 PLOT<1,,C>,<,,-15,S>,<D2<(D2*200/2+L5*15)/D2,U>,<-250,,Y1$>
      <,,R>
1550 PLOT<D2<(D2*200/2+L6*15)/D2,U>,<-200,,Y2$>,<,,R>,<13,,S>

1560 REM ----- ADD A KEY

1570 IF C=1 THEN K$="LIQUID HEIGHT" :
      IF C=2 THEN K$="VAPOR HEIGHT"
1580 G$ = " "
1590 K1$ = G$ & " " & " " & K$
1600 PLOT<200,0,U>
1610 PLOT<0,200,U>
1620 LN O2 GOTO 1630,1640,1650
1630 PLOT<,,HEX(C1)> : GOTO 1660
1640 PLOT<,,HEX(C2)> : GOTO 1660
1650 PLOT<,,HEX(C3)> : GOTO 1660
1660 PLOT<20,-100-(C-1)*100,K1$> : PLOT<,,R>

1670 C=C+1 : IF C=2 THEN 780
1680 GOSUB 50 : PRINT "HEAT PIPE ANALYSIS COMPLETE" : END
1690 REM ----- SUBROUTINE TO SORT X VALUES IN INCREASING
      ORDER AND FIND THE MAX X AND Y VALUES

1700 REM ----- SORT IN INCREASING X

```

ORIGINAL PAGE IS
OF POOR QUALITY

```
10 M=L-1
20 FOR J = 1 TO M
1730 I1 = J + 1
1740 FOR I = J1 TO L
1750 IF X(J) < X(I) THEN 1790
1760 I1 = X(J) : I2 = Y(J)
1770 X(J) = X(I) : Y(J) = Y(I)
1780 X(I) = I1 : Y(I) = I2
1790 NEXT I
1800 NEXT J

1810 REM ----- (FIND THE MAX AND MIN VALUE OF X AND Y

1820 IF C > 1 THEN 1850
1830 L1 = MAX(X()) : S1 = X(1)
1840 L2 = MAX(Y()) : S3 = MAX(Y())
1850 FOR I = 1 TO L : IF Y(I) < S3 THEN S3 = Y(I) : NEXT I
1860 RETURN

1870 REM ----- SUBROUTINE TO LOAD AXIS LIMITS AND PLOT SIZE

1880 GOSUB 740 : PRINTING 1890, S1, L1, S3, L2
1890 ZMIN X VALUE=####.### MAX X VALUE=-####.###
MIN Y VALUE=-####.### MAX Y VALUE=-####.###
1900 PRINT "NOTE: MAXIMUM X AXIS HORIZONTAL LENGTH IS 12IN,
STANDARD LENGTH IS 10IN."
1910 INPUT "X AXIS LENGTH (WHOLE INCHES)",D1 :
INPUT "Y AXIS LENGTH (WHOLE INCHES)",D2
1920 INPUT "ENTER MIN X AXIS VALUE DESIRED",S5 :
INPUT "ENTER MAX X AXIS VALUE DESIRED",L5 :
) INPUT "ENTER MIN Y AXIS VALUE DESIRED",S6 :
INPUT "ENTER MAX Y AXIS VALUE DESIRED",L6
1940 S2=ABS((S5-L5)/D1) : S4=ABS((S6-L6)/D2)
1950 PRINT USING 1960, S2,S4
1960 YOUR X AXIS UNITS/INCH ARE ####.##
YOUR Y AXIS UNITS/INCH ARE ####.##
1970 INPUT "TYPE 1 TO CONTINUE WITH PROGRAM ,
TYPE 2 TO CHANGE ABOVE VALUES",Q :
UN G GOTO 1980, 1980 : GOTO 1970
1980 S1=S5 : L1=L5 : S3=S6 : L3=L6
1990 S2=ABS((S1-L1)/D1) : S4=ABS((S3-L3)/D2)
2000 RETURN
```

APPENDIX C

ORIGINAL PAGE IS
OF POOR QUALITY

```

1  REM ----- "HT PIPE-H"
2  REM ----- HEAT PIPE ANALYSIS PROGRAM
3  REM ----- JULY 1981
4  REM ----- VARIABLE LIST ;
5  REM ----- D1=DIAMETER      R1=RVAPOR      A1=AVAPOR
6  REM ----- D2=DIAMETER      R2=RLIQUID     A2=ALIIQUID
7  REM ----- P=PRARCTAN(1.0)  G=32.174
8  REM ----- S=SIGMA          M=MU           R=RHO
9  REM ----- D=DEPTH OF MANGROOVE  W=WIDTH OF MANGROOVE
10 REM ----- A=ALPHA (ANGLE W/R 10 G)  C=CHARGE
11 REM ----- H5=HLIQUID      H6=HVAPOR
12 REM ----- I=I             J=JMAX        A5=Atotal
13 REM ----- Z1=ALPHA        Z2=gamma      Z3=delta
14 REM ----- F=FN           C(t)=time integral
15 REM H(200), HS(200), T(200)
16 G = 32.174 : SELECT M : P = 4.0*PRARCTAN(1.0) : SELECT D :
17 GOTO 140
18 PRINT REPORT : PRINT USING 120 : PRINT : RETURN
19 -----
20 HEAT PIPE ANALYSIS
21 -----
22 GOTO 110 : PRINT "ENTER THE FOLLOWING INFORMATION PLEASE" :
23 PRINT
24 INPUT "DIAMETER OF VAPOR CHANNEL, INCHES", D1 : D1=D1/12 :
25 R1=D1/2
26 INPUT "DIAMETER OF LIQUID CHANNEL, INCHES", D2 : D2=D2/12 :
27 R2=D2/2
28 A1=3.14159 : A2=3.14159
29 INPUT "INITIAL PIPE HEIGHT, INCHES", H0 : H0=H0/12
30 INPUT "WIDTH OF MANGROOVE, INCHES", W : W=W/12
31 INPUT "DEPTH OF MANGROOVE, INCHES", D : D=D/12
32 A5=5.0
33 INPUT "ANGLE WITH RESPECT TO GRAVITY FIELD, DEG", A
34 GOTO 110 : INPUT "INITIAL CHARGE", C
35 INPUT "INITIAL PRIME (UPPER LIMIT OF SIMPSON'S RULE)", L2
36 PRINT : PRINT "LIQUID QUALITIES : "
37 INPUT "SURFACE TENSION (LIQUID VAPOR)", S
38 INPUT "VISCOSITY", M
39 INPUT "DENSITY", R
40 GOTO 110 : REM ----- START COMPUTATIONS
41 REM ----- CALCULATE TIME (MAX 1)
42 A5=3.14159 : F=16
43 Z1=1.0 : Z2=1.0 : Z3=1.0 : Z4=1.0 : Z5=1.0
44 Z6=1.0 : Z7=1.0 : Z8=1.0 : Z9=1.0 : Z10=1.0
45 Z11=1.0 : Z12=1.0 : Z13=1.0 : Z14=1.0 : Z15=1.0
46 I=0 : REM ----- LIMITS OF INTEGRAL
47 REM ----- BY SIMPSON'S RULE
48 DEF FN F(X)=1/(C-R1*(Z1/Z2)+(S/R*(R*(C-B)+2*Z3/Z1+2) -
49 B*(C-B)))
50 GOTO 500
51 B=0 : I(1)=0
52 REM I=1 TO 100
53 REM ----- INCREMENT TIME AND ITERATE
54 I(I+1)=I(I)+10/100
55 R1 = 1/M*(R) * 10/100

```

ORIGINAL PAGE IS
OF POOR QUALITY

```

410 REM ----- CALCULATE HEIGHT OF LIQUID AND VAPOR
420 H5(1) = H*H0*(D**2)*R**2/AS
430 H5(1)=A2*((C*H)-H5(1))/A1
440 H5(1)=H5(1)
450 NEXT I

460 REM ----- CONVERT TIME REMAINING TO ELAPSED TIME
470 FOR I=1 TO 100
480 T(I)=10-T(I)
490 NEXT I

500 REM ----- PRINT OUT RESULTS
510 SELECT PRINT (P) (C=2) : PRINT HEX(OH), "
HEAT PIPE ANALYSIS" : PRINT
520 PRINTING 500, I*12, W*12, S : PRINT USING 540, D*12, D*12, R
: PRINTING 570, H*12, C, M, A
530 Z DIAMETER OF VAPOR PASSAGE = #.####" WIDTH
OF MEANFLOW = #.####" SURFACE TENSION = #.#### LB/FT
540 Z DIAMETER OF LIQUID PASSAGE = #.####" DEPTH
OF MEANFLOW = #.####" DENSITY = #.#### SG/CU.FT.
550 Z HEIGHT OF PIPE = ###.##" INITIA
L CHARGE = ##.## VISCOSITY = #.#### SL/FT-S
ANGLE WITH RESPECT TO GRAVITY FIELD = ##.##
IFG
560 FOR I = 1 TO 100 : H5(I)=H5(I)*12 : H6(I)=H5(I)*12 :
NEXT I
570 PRINT : PRINTING 600 : PRINTING 610 : FOR I=1 TO 50 :
PRINTING 620, T(I), H5(I), H6(I), T(I+50), H5(I+50), H6(I+50)
: NEXT I
580 Z TIME HEIGHT OF VAPOR HEIGHT OF LIQUID
TIME HEIGHT OF VAPOR HEIGHT OF LIQUID
(IN) (IN) (IN)
590 Z -----
600 Z -----
610 Z -----
620 Z -----
630 SELECT PRINT (C) (C=4) : GOSUB 110 : SELECT P9 : PRINT :
PRINT "BEGIN PLOTTING SEQUENCE....." : FOR I=1 TO 5
640 PRINT : NEXT I : PRINT "START DRUMPLUI PACKAGE...." :
PRINT : SELECT P
700 REM ----- "DRUMPLUI"
710 REM ----- WIRE CARTER EC 3 22 JULY 81
SERPPROGRAM TO DO GENERAL PLOTTING IN SUPPORT
OF THE PROGRAM "HEATPIPE"
720 DIM X(500), Y(500), C(2), X1(40), X2(40), Y1(40), Y2(40), A(10),
A(50), K1(50), I(500), I2(500), H(64), I(64)
730 SELECT PRINT (C) : GOSUB 740 : GOTO 760
740 PRINT HEX(OH) : PRINTING 750 : PRINT : RETURN
750 Z -----
DRUMPLUI
-----
760 PRINT "WIRE CARTER AND SET HOME POSITION" : PRINT
770 INP(0) "BT) RETURN TO BEGIN", (C : C=1
780 I=100 : FOR I=1 TO 100
790 IF C=1 THEN Y(I)=H5(I) : IF C=2 THEN Y(I)=H6(I) :
X(I)=T(I) : NEXT I
800 REM ----- SORT DATA POINTS IN INCREASING X ORDER AND

```

ORIGINAL PAGE IS
OF POOR QUALITY

DETERMINE THE LARGEST X AND Y VALUES.

2000 GOTO 740 : PRINT "WORKING...." : GOSUB 1700 : GOTO 740

2010 IF C > 1 THEN 2000

2020 GOTO 740

2030 LET X1 = G111 * S2 / S4 : G111 = X1

2040 LET X2 = X1 + S2 / S4 : G111 = X2

2050 LET X3 = X2 + S2 / S4 : G111 = X3

2060 LET X4 = X3 + S2 / S4 : G111 = X4

2070 GOTO 1000

2080 GOTO 740

2090 LET TIME = TIME (SEC) : LET M = "METHOD B"

2100 LET V1 = "FEET/SEC" : LET V2 = ". IN."

2110 LET I = 1 TO 4

2120 LET Y1 = (Y(I) - 1) * 200 / S2 : Y2(I) = ROUND(Y1 + 0.5, 0)

2130 LET Y3(I) = (Y(I) - 1) * 200 / S4 : Y4(I) = ROUND(Y3(I) + 0.5, 0)

2140 NEXT I

2150 GOTO 740

2160 GOTO 740 : PRINT "DATA BEING PROCESSED , HEAT PIPE ANALYSIS

2170 : PRINT "WORKING"

2180 IF C > 1 THEN 1700

2190 REM ----- DRAW AXES, TICK MARKS AND UNIT LABELS

1000 LET X1 = 0 * 200 : X2 = 0 * 200

1010 PLOT(X1, R) : PLOT(X2, 0, U)

1020 PLOT(X1, -10, U), (X2, 0, U), (X1, 0, U)

1030 FOR I = 1 TO 4 : FOR J = 1 TO 3 : PLOT(-50, -5, U), (0, 10, U),

(0, -5, U) : NEXT J : PLOT(-50, -10, U), (0, 20, U), (0, -10, U) :

NEXT I

1040 PLOT(X1, R) : PLOT(X2, 0, U)

1050 PLOT(-10, 0, U), (20, 0, U), (-10, 0, U)

1060 FOR I = 1 TO 4 : FOR J = 1 TO 3 : PLOT(-5, -50, U), (10, 0, U),

(-5, 0, U) : NEXT J : PLOT(-10, -50, U), (20, 0, U), (-10, 0, U) :

NEXT I

1070 PLOT(X1, R)

1080 PLOT(-50, -30, U) : A = S1

1090 FOR I = 1 TO 100

1100 IF ABS(A) >= 1000. THEN 1130 : IF ABS(A) >= 100. THEN 1140

1110 IF ABS(A) >= 10. THEN 1150 : IF ABS(A) >= 1 THEN 1160 :

1120 IF A = 0. THEN 1110

1130 GOSUB 91 A 10 27 (.,#) : GOTO 1170

1140 GOSUB 91 A 10 27 (.,###) : GOTO 1170

1150 GOSUB 91 A 10 27 (-####) : GOTO 1170

1160 GOSUB 91 A 10 27 (-###.) : GOTO 1170

1170 GOSUB 91 A 10 27 (-##.#) : GOTO 1170

1180 GOSUB 91 A 10 27 (-#.##) : GOTO 1170

1190 PLOT(X1, C) : PLOT(X2, S) : PLOT(X1, A) :

PLOT(-LEN(A) * S, 0, U) : A = A + S2 : PLOT(200, 0, U)

1200 NEXT I : PLOT(X1, R)

1210 PLOT(X1, R)

1220 PLOT(-150, 0, U) : A = S3

1230 FOR I = 1 TO 100

1240 IF ABS(A) >= 1000. THEN 1260 : IF ABS(A) >= 100. THEN 1260

1250 IF ABS(A) >= 10. THEN 1270 : IF ABS(A) >= 1 THEN 1280 :

1260 IF A = 0. THEN 1250

1270 GOSUB 91 A 10 27 (.,#) : GOTO 1290

1280 GOSUB 91 A 10 27 (.,###) : GOTO 1290

1290 GOSUB 91 A 10 27 (-####) : GOTO 1290

1300 GOSUB 91 A 10 27 (-###.) : GOTO 1290

ORIGINAL PAGE IS
OF POOR QUALITY

```
1200 GOVERN A TO AT (I=I, #) : GOTO 1290
1210 GOVERN B TO AT (I=I, #) : GOTO 1290
1220 PLU1<X1, Y1, X2, Y2, AT> : <-LEN(AT)*20, 0, U> : A = A + S4 :
    PLU1<0, 200, U>
1230 NEXT I : PLU1<0, 200, U>, <I, R>

1240 DO GO GOTO 1300, 1320, 1320
1250 PLU1<I, 10, 20>
1260 IF G=1 THEN G=1 : IF G=2 THEN G=2 : S=1 :
    FOR I=1 TO 100 : PLU1<200/G, U>, D1<S*200, U> : S=S :
    NEXT I : PLU1<I, R>
1270 S=1 : FOR I=1 TO 100 : PLU1<I, 200/G, U>, D1<S*200, U> :
    S=S : NEXT I : PLU1<I, R>

1280 DO GO GOTO 1300, 1370, 1380
1290 PLU1<I, H1(I)> : GOTO 1390
1300 PLU1<I, H2(I)> : GOTO 1390
1310 PLU1<I, H3(I)>
1320 REM ----- JUMP POINTS BY A LINE
1330 PLU1<I, R>
1340 IF I = 1 THEN 1430
1350 FOR I = 1 TO 1
1360 IF I = 1 THEN 1430 : PLU1D1<H1(I)/D1, U> : PLU1D2<H2(I)/D2, U> :
    GOTO 1430
1370 PLU1<H1(I)-H1(I-1), H2(I)-H2(I-1), U>
1380 NEXT I : PLU1<I, R>

1390 REM ----- ADD AXIS LABELS

1400 IF C > 1 THEN 1570
1410 DO GO GOTO 1480, 1500, 1510
1420 PLU1<I, H1(I)> : GOTO 1520
1430 PLU1<I, H2(I)> : GOTO 1520
1440 PLU1<I, H3(I)> : GOTO 1570
1450 L5=LEN(X1) : L6=LEN(X2) : L5=LEN(Y1) : L6=LEN(Y2)
1460 PLU1<D1*(X1+L5)/D1, U>, <I, X1> : PLU1<I, R>
1470 PLU1<D1*(X2+L6)/D1, U>, <I, X2> : PLU1<I, R>
1480 PLU1<D1*(Y1+L5)/D1, U>, D2< (D2*200/2+L5*15)/D2, U>, <-250, Y1> :
    PLU1<I, R>
1490 PLU1<D1*(Y2+L6)/D2, U>, <-200, Y2>, <I, R>, <13, S>

1500 REM ----- ADD A KEY

1510 IF G=1 THEN KEY="LIQUID HEIGHT" :
    IF G=2 THEN KEY="VAPOR HEIGHT"
1520 G=1
1530 KEY = G$ * " " * R$
1540 PLU1<200, U, U>
1550 PLU1<0, 200, U>
1560 DO GO GOTO 1640, 1650, 1650
1570 PLU1<I, H1(I)> : GOTO 1670
1580 PLU1<I, H2(I)> : GOTO 1670
1590 PLU1<I, H3(I)> : GOTO 1670
1600 PLU1<0, -100, U> : PLU1<I, R>

1610 GOTO : IF G=1 THEN 780
1620 GOTO 110 : PRINT "HEAT PIPE ANALYSIS COMPLETE" : END
1630 REM ----- MAXIMIZING TO SORT X VALUES IN INCREASING
    ORDER AND FIND THE MAX X AND Y VALUES
```

```

1100 FOR J = 1 TO M
1110 FOR I = J + 1
1120 FOR L = J TO L
1130 IF X(J) < X(I) THEN 1100
1140 X(I) = X(J) : Y(I) = Y(J)
1150 X(J) = X(I) : Y(J) = Y(I)
1160 NEXT I
1170 NEXT L
1180 NEXT J

1200 MAIN ----- FIND THE MAX AND MIN VALUE OF X AND Y

1210 IF C > 1 THEN 1270
1220 L1 = MAX(X()) : S1 = X(1)
1230 L2 = MAX(Y()) : S2 = Y(1)
1240 FOR I = 1 TO L : IF Y(I) < S2 THEN S2 = Y(I) : NEXT I
1250 RETURN

1300 MAIN ----- SUBROUTINE TO LOAD AXIS LIMITS AND PLUT SIZE

1310 GOTO 140 : PRINT USING 1300, S1, L1, S2, L2
1320 ZONE X VALUE=-----,### MAX X VALUE=-----,###
      MIN Y VALUE=-----,### MAX Y VALUE=-----,###
1330 PRINT "NOTE: MAXIMUM X AXIS HORIZONTAL LENGTH IS 12IN,
      STANDARD LENGTH IS 10IN."
1340 INPUT "X AXIS LENGTH (WHOLE INCHES)",D1 :
      INPUT "Y AXIS LENGTH (WHOLE INCHES)",D2
1350 INPUT "ENTER MIN X AXIS VALUE DESIRED",S5 :
      INPUT "ENTER MAX X AXIS VALUE DESIRED",L5
1360 INPUT "ENTER MIN Y AXIS VALUE DESIRED",S6 :
      INPUT "ENTER MAX Y AXIS VALUE DESIRED",L6
1370 S2=ABS((S5-L5)/D1) : S4=ABS((S6-L6)/D2)
1380 PRINT USING 1370, S2,S4
1390 ZONE X AXIS UNITS/INCH ARE ####,##
      Y AXIS UNITS/INCH ARE ####,##
1400 INPUT "TYPE 1 TO CONTINUE WITH PROGRAM ,
      TYPE 2 TO CHANGE ABOVE VALUES",Q :
      IF Q GOTO 1300,1300 : GOTO 1300
1410 S = S2 : L1=L5 : S3=S6 : L2=L6
1420 S2=ABS((S1-L1)/D1) : S4=ABS((S3-L2)/D2)
1430 RETURN

1500 MAIN ----- SUBROUTINE TO DETERMINE THE VALUE OF AN
      INTEGRAL BY USING SIMPSON'S RULE

1510 S1=10 : D9=(L2-L1)/100
1520 Y1=NO(L1)
1530 Y2=NO(L2)
1540 FOR I=1 TO (L2-L1)/D9-0.5
1550 Y=NO(L1+I*D9)
1560 IF I/2=INT(I/2) THEN 1590
1570 S1=S1+Y
1580 GOTO 1510
1590 S1=I+Y
1600 NEXT I
1610 I=(L2-L1)/D9
1620 I2=I/3*(Y1+4*S1+Y2)
1630 RETURN

```

JSC Reduced Gravity Aircraft Users' Guide

Flight Operations Directorate
Aircraft Operations Division

May 1981

NASA

National Aeronautics and
Space Administration

Lyndon B. Johnson Space Center
Houston, Texas

1.0 PROGRAM DESCRIPTION

The Reduced Gravity Program, operated by the National Aeronautics and Space Administration (NASA) Lyndon B. Johnson Space Center (JSC) in Houston, Texas, provides a "weightless" environment similar to the environment of spaceflight for test and training purposes on a cost reimbursable basis. The program will operate in accordance with NASA's established safety procedures (NASA Safety Series 1700.1, Volumes 1 and 3, JSC Safety Manual, 1700B), including the requirements of this document, to assure safe and efficient flight test operations.

2.0 SIMULATION DESCRIPTION

The reduced gravity environment is obtained with a specially modified KC-135A jet transport flown over a parabolic arc to produce short periods of less than one "g" acceleration force. This parabolic maneuver is initiated and terminated with a pull-up and pull-out of 1.8 to 2.0 g's (figure 1). The length of these reduced-gravity periods depends on the g level required for the specific test. Below are listed typical lengths of various maneuvers:

Negative g	(-.1 g)	15 seconds
Zero g	(0 g)	23 seconds
Lunar g	(1/6 g)	30 seconds
Martian g	(1/3 g)	40 seconds

These maneuvers may be flown consecutively, roller-coaster fashion, or separated by enough time to alter the test setup. A normal mission is as follows:

- a. 2 to 3 hours' duration.
- b. 30 to 40 maneuvers.
- c. Flights originate and terminate at Ellington Air Force Base, Houston, Texas.

Changes to the normal mission can be made to insure more efficient testing operations.

3.0 FACILITIES PROVIDED

The KC-135A aircraft is equipped to provide electrical power, breathing air or nitrogen sources, communications equipment (intercom), overboard vent system, and photo lights. (See section 6 for detailed description

of the aircraft.) NASA/JSC will provide photographers, 16 mm movie, 35 mm slides, and prints, as required for test documentation purposes. Work space is available on the ground for buildup and checkout of test equipment to insure its operation before installation in the airplane. Test Directors from the Reduced Gravity Office will supervise testing operations in flight and will review the test documentation submitted by the using organization to insure the inherent safety of the hardware and test procedures. All necessary rigging and moving equipment for heavy or large equipment is available.

4.0 USER REQUIREMENTS

4.1 Test Request Procedure

Requests for reduced gravity test support must be submitted in writing to:

NASA Johnson Space Center
CA/Director of Flight Operations
Houston, Texas 77058.

The request should be submitted no less than 6 months prior to the desired flight date for incorporation into the long-range aircraft flight schedule. The flight schedule is determined at the Reduced Gravity Semiannual Users' Conference, normally held each May and October. This conference allows the users to meet and discuss past testing experiences with the other users, enhancing the development of testing techniques, and to discuss future flight requirements.

The initial test request should contain general information describing the following:

- 0 Test objectives.
- 0 Desired schedule (Exact flight dates will be determined later.)
- 0 Brief description of the test and associated test equipment.
- 0 Number of test personnel required for flight.
- 0 Special support or constraints.
- 0 Identifiable hazards.
- 0 Names, addresses, and phone numbers of contacts.

Contact will be established by the Reduced Gravity Office with the requesting organization to formalize the test program.

4.2 Test Equipment Fabrication Requirements

It is important for the users to design and construct their test equipment in accordance with the following guidelines.

4.2.1 Structural - All test equipment provided by the using organization must be stressed for the ultimate gravity forces given below:

- 0 Forward - 9 g's (eyeballs out)
- 0 Aft - 2 g's (eyeballs in)
- 0 Lateral - 3 g's
- 0 Up - 2 g's (eyeballs up)
- 0 Down - 6 g's (eyeballs down)

These forces should be calculated for the test equipment in its take-off and landing configuration. The in-flight test configuration should be designed for a possible 2.5-g force at maneuver entry and exit.

4.2.2 Floor Loading - The following maximum floor loadings should be considered in the design of test hardware:

- 0 Concentrated floor load of 25 pounds per square inch.
- 0 Contact pressure load of 200 pounds per square foot.
- 0 Loads above these limits must have shoring underneath (e.g., plywood sheets) to spread the loading.
- 0 Rigid test fixtures longer than 10 feet must be designed so as to not interfere with the normal flexure of the aircraft.

*4.2.3 Electrical Power and Interfaces - The following electrical power is available in the test section of the aircraft:

28 volt DC	80 amps
110 volt AC, 400 Hz, single phase	50 amps
110 volt AC, 400 Hz, three phase	50 amps
110 volt, AC, 60 Hz	20 amps.

Electrical wiring and interconnect cabling with the aircraft must be fabricated and installed with good workmanship standards. Each piece of test equipment should be self-protected with an incorporated circuit breaker or other current-limiting device to protect against electrical shorts. Normal aircraft vibration, high humidity, handling rates, and higher-than-1-g loads should be considered in connector and wiring selection.

The aircraft electrical test power is distributed to five power distribution panels evenly spaced along the lower side wall of the test section. Moveable power boxes connected to the power distribution panels contain circuit-protected terminals mounted on bus bars. All power and ground leads from test equipment should be 20 feet long with #8 (.163 inch diameter) spade lugs at the end. The exception to this is the 60 Hz AC power leads, which will utilize the standard three-prong plug.

4.2.4 Equipment Mounting - All test equipment should be mounted on baseplates with 3/4-inch holes drilled to match the 20-inch centered grid pattern of nutplates in the floor of the airplane (see figure 2). Aircraft type bolts, supplied by JSC, are used to secure the baseplates to the floor of the airplane. Suitable handles and holes are needed around the baseplates for forklift arms or J-bars.

 4.2.5 Free-Float Packages - Perturbations of the airplane can cause small g forces during a zero-g maneuver ($\pm .02$ g). If a precise zero g is required, the test package can be free-floated inside the cabin, preventing contact with the walls, ceiling, or floor of the aircraft. To provide the maximum free-float time, the package to be floated should be as light and compact as possible. If an umbilical is used between the floating package and tied-down support equipment, it should be at least 30 feet long to allow for drifting of the floating package. Handles the length of the longitudinal axis of the package (in its floating configuration) should be mounted using 3/4-inch tubing approximately 18 inches above the package floorline.

4.2.6 Hazardous Materials - Avoid hazardous liquids and gases where possible, including high pressure, toxic, corrosive, or explosive materials. If such materials are required for a test, the proper container must be used (e.g., high pressure gases are stored in certified K bottles). If such materials are approved for use at the JSC safety review, provisions for dumping and purging in flight will be required.

4.2.7 Miscellaneous Guidelines

- 0 - Avoid sharp corners on all test equipment.
- 0 - Avoid electrolyte type batteries (dry cells are permitted).
- 0 - Avoid flammable materials
- 0 - Consider equipment or procedural failures. Provide backups or workarounds to prevent such conditions from resulting in hazards to personnel or aircraft.
- 0 - Consider the activities required during the 2-g and zero-g portions of the flight.

4.3 Test Equipment Data Package

Four weeks prior to the first test flight, the appropriate documentation must be submitted for review and approval. This documentation, the test equipment data package, includes the test plan, engineering drawings and schematics, structural analysis, electrical load analysis, and an analysis of any identifiable hazards. The test plan contains the following:

- 0 Test objectives.
- 0 Test description.
- 0 In-flight test procedures.
- 0 Parabola requirements, number, and sequencing.
- 0 Test support requirements, ground and flight.
- 0 Data acquisition system.
- 0 Test operating limits or restrictions.
- 0 Test personnel requirements.
- 0 Photographic requirements.

4.4 Test Personnel

All flight personnel must provide certification of a current flight physical (Air Force Class III or FAA Class II) and physiological training. The number of personnel will be held to the minimum required for the safe and efficient conduct of the test. Upon receipt of certification of the physical and physiological training, the Reduced Gravity Office will obtain the required invitational boarding orders for each individual. Approximately 2 weeks is needed to obtain these boarding orders.

4.4.1 Physical and Physiological Training

Both physicals and physiological training are available at JSC, although nonlocal personnel may find it easier to obtain them elsewhere. The physical is conducted in two parts; i.e., laboratory and doctor's examination, with an approximate 2-week interval between the visits. The physiological training is a day and a half class and altitude chamber run. The physicals can be obtained from any Federal Aviation Administration (FAA) flight surgeon, and physiological training classes are offered at several Air Force and Navy installations.

4.4.2 Familiarization Flight - Depending on the nature of the tests and duties planned for the test personnel, a familiarization flight for people inexperienced in reduced gravity flights may be required. Therefore, when the actual flight test of their equipment occurs, the test personnel will be aware of the sensations, body responses, in-flight test procedures, etc.

3 Shipping

The test equipment should be received at least one week prior to the first flight. The address to use for equipment shipment is:

NASA Johnson Space Center
Transportation Office, Bldg. 420
Houston, TX 77058
Attn: Zero Gravity Office
Ellington Air Force Base, Hangar 990

4.6 Preflight

The buildup and checkout of test equipment is solely the responsibility of the using organization. All tools and checkout equipment must also be provided by the user. A JSC safety review will be held prior to installation of equipment into the aircraft to determine if all necessary requirements have been met. A simulated ground run may be required during this review whereby the test personnel will demonstrate normal and contingency in-flight procedures. An emergency egress briefing will be given to all flight personnel who have not previously flown on the aircraft. All flight personnel will attend the preflight briefing where that day's flight test plan will be discussed. All flight personnel will wear approved flight suits and boots, which can be provided on loan from JSC.

7 Flight Phase

All personnel on board the aircraft will be under the direction of the aircraft flight crew and Test Director, both for normal and emergency conditions and for test operations. Strict adherence to the authority of these personnel will be rigidly enforced. Any deviation from the flight test plan must be discussed with the Test Director before implementing.

4.8 Post Flight

A post-flight debriefing will be held immediately after landing to review any problems that occurred during the flight and to discuss possible alterations to the test. Upon completion of the test phase, the equipment will be downloaded and prepared for shipment by the user. Two copies of the finalized test report shall be sent to the Reduced Gravity Office. This data will be maintained in a reduced gravity reference library for use by other interested parties.

5.0 AIRCRAFT DESCRIPTION AND PROVISIONS

5.1 Environment

Cabin pressure is controlled between sea level (14.7 psia) and 11,000 feet (9.7 psia) during the parabolic maneuvers. Loss of cabin pressure would

result in a pressure as low as 2.7 psia, which must be considered in the design of test equipment. Cabin temperature varies from 50° to 80°F in flight normally. The temperature in the cabin is not controlled while the airplane sits on the ground. If necessary, a portable ground air conditioner is available during preflight operations.

5.2 Dimensions (See figures 3 to 5)

Approximately 60 feet of the compartment length is available for test purposes and stowage of a limited amount of aircraft equipment. Typical cross sections at three locations are shown in figures 3 to 5. The cargo hatch, through which the equipment is loaded, is 75 inches high by 118 inches wide. Eighteen inches of width near the top is unusable because of the door actuating mechanism.

5.3 Crew Provisions

There are 24 seats provided aft of the test section for test personnel. Parachutes, emergency oxygen, smoke masks, life preservers, life rafts, first-aid equipment, and other emergency equipment are provided on board the aircraft.

The interior walls of the cargo compartment are covered with foam padding for the protection of personnel and equipment.

5.4 Test Provisions

- a. Interphone - An interphone system is provided for test communications. The number of personnel on the interphone will be controlled to assure clear and efficient communications.
- b. Electrical Power - See section 5.2.3.
- c. Gas Supply System - A cryogenic storage and supply system is available to provide a source of breathing air or nitrogen.
- d. High Pressure Gas System - A high pressure bottle rack for a supply of inert gases.
- e. Overboard Vent System - Plumbing is available to allow venting of liquids and gases overboard in flight.
- f. Photography - Photographic lights are installed in the aircraft test section. These are sufficient to support photography of most open tests. Additional lighting equipment is available to support enclosed tests or special photography.

ORIGINAL PAGE IS
OF POOR QUALITY

6.0 FUNDING

The Reduced Gravity Program is cost reimbursable with the flight hour charge rate based on an annual flight hour projection versus costs of operating the airplane. Reimbursement costs are computed semiannually and published in the minutes of the Reduced Gravity Semiannual Users Conference.

8.0 CONCLUDING REMARKS

The degree of detail, rigor, and formality required in the development and conduct of a reduced-gravity test depends on the complexity, hazard, and uniqueness of the test. Communications with the Reduced Gravity Office are required early and often to eliminate any last minute surprises which will cause delays. The personnel of the Reduced Gravity Office will review and comment on preliminary drawings and plans at any stage of development. It should be noted that a test will be conducted only after cognizant NASA personnel have been assured that a safe, well organized, and productive flight can be achieved.

ANALYSIS OF LOW-G HEAT TRANSFER FOR A
CRYOGENIC OXYGEN PRESSURIZATION HEATER

Jce Rios, Ph. D.

University of Puerto Rico

1981 NASA-ASEE Summer Faculty Fellow

Supervisor:

John M. McGee

Power Generation Branch

Propulsion and Power Division

Abstract - The statement of the problem and its relation to the Orbiter's enhancement program is presented. An analysis of available experimental and analytical data pertaining to the problem is given. A computational technique proposed is discussed. Limitations of the procedure are presented. The result of applying the technique to one set of operating conditions for the heaters is presented.

NATIONAL AERONAUTICS AND SPACE ADMINISTRATION

LYNDON B. JOHNSON SPACE CENTER

HOUSTON, TEXAS

AUGUST 11, 1981

I. STATEMENT OF THE PROBLEM

The fuel cell system of the Orbiter utilizes oxygen and hydrogen as reactants. These reactants are supplied from pressure vessels which at present, are loaded while the vehicle is on the ground and prior to its launch. The location of these tanks can be seen in Figure 1 which shows the Power Reactant Storage and Distribution System (PRSD) of the Orbiter. In particular, the tanks which supply the oxygen are pressurized to a nominal value of 900 psia. This is accomplished by hydraulically pressurizing the reactants after the tanks are fully loaded. This pressurization assures that the state of the oxygen is in the supercritical pressure region.

While on-orbit, and as the oxygen is consumed in the fuel cells, the pressure in the tank is maintained by the use of a set of heaters immersed in the fluid in the tank. However, since the pressure is not allowed to fall below the critical pressure, the fluid is kept supercritical and the heat transfer processes occurring are those related to a single phase component. The location of the heaters and other details of the oxygen tank can be seen in Figures 2 and 3.

As part of the enhancement program for the Orbiter, the following concept has been proposed: after the external tank separates from the Orbiter, about 2000 pounds of residual liquid oxygen remain in the Orbiter in the main propulsion system lines. At present, this liquid oxygen is dumped overboard. To utilize it, and thus be able to reduce the launch weight of the Orbiter, it has been proposed to transfer part of this liquid oxygen to empty PRSA tanks which have been previously prechilled to approximately 163°R during normal ground servicing operations. These tanks would be vented to a low pressure (of about 1 psia) prior to the liquid oxygen transfer. The Orbiter would be pitched at a 2 degree/second rate to ensure settling of the liquid oxygen in the main propulsion system 17-inch manifolds. To carry out the transfer of

NASA-S-78-11803A

FIGURE 1 - PRSD AND FUEL CELL COMPONENTS

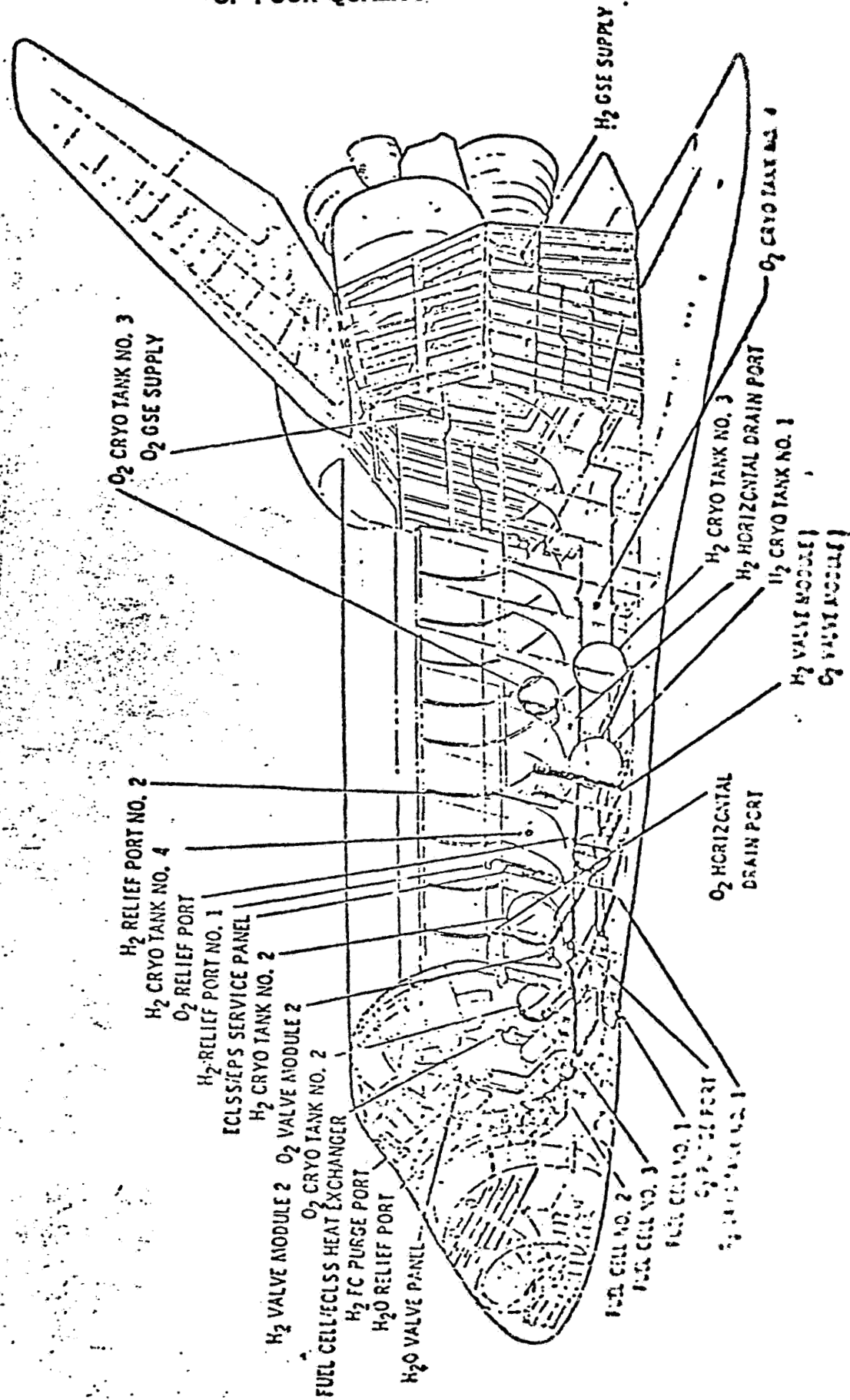
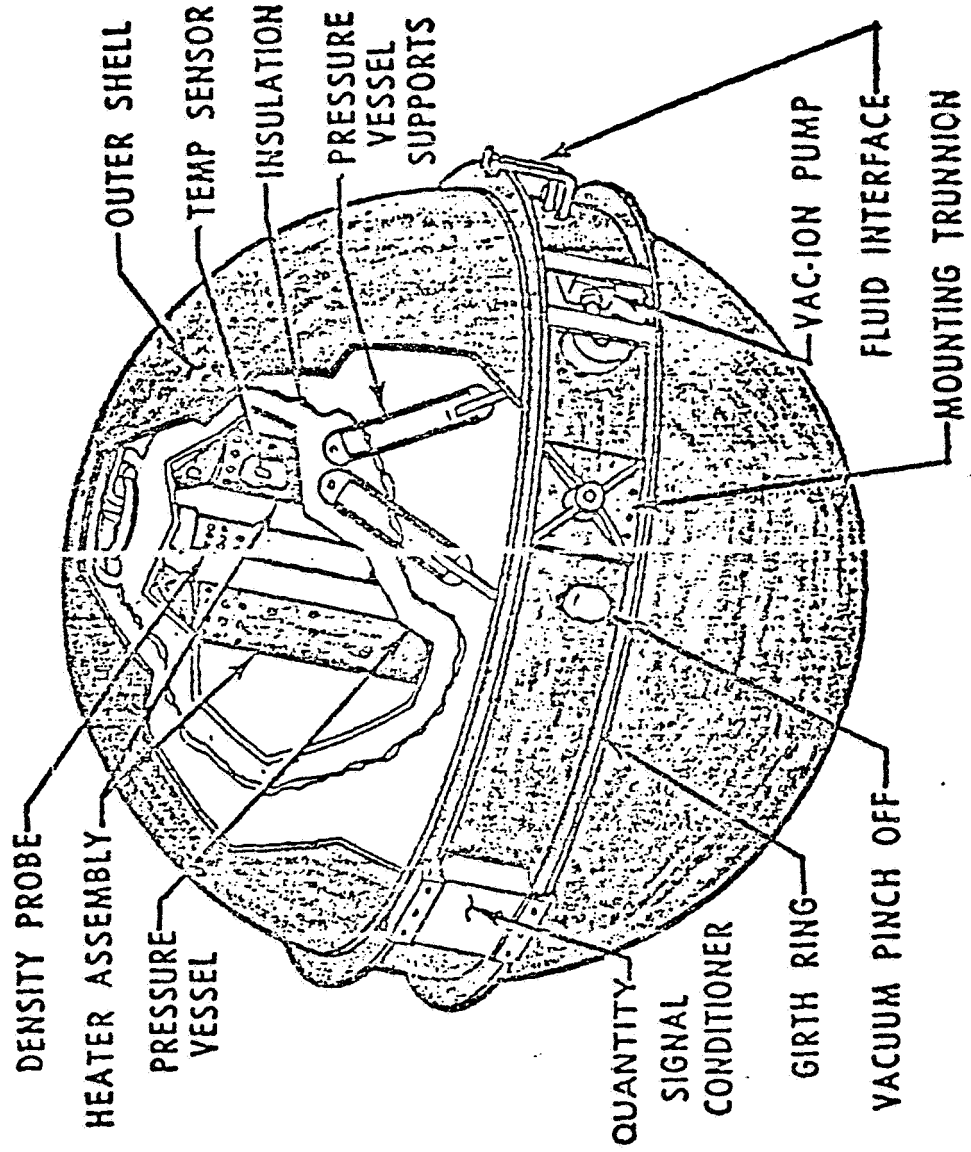


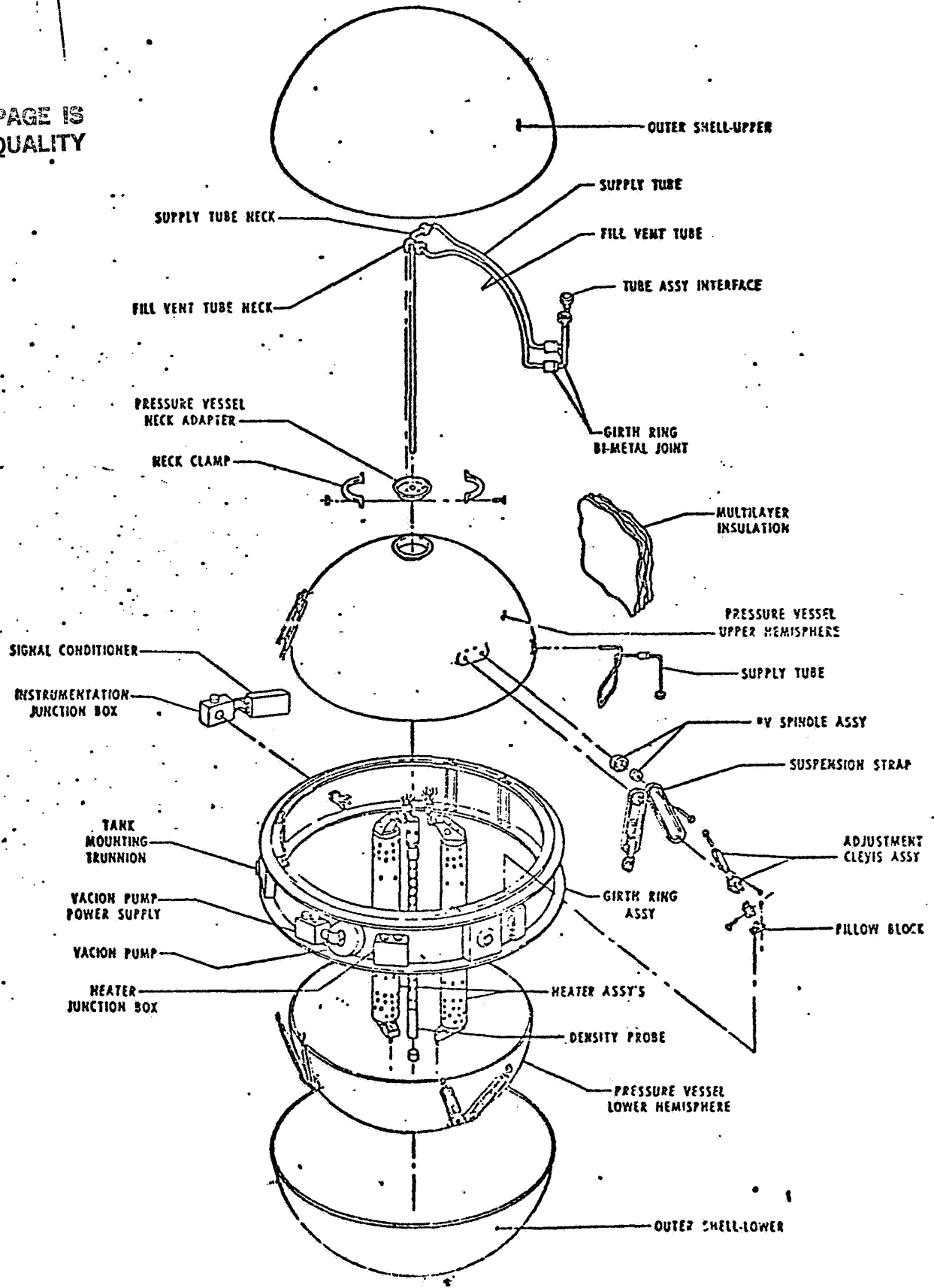
FIGURE 2 · OXYGEN TANK



ORIGINAL PAGE IS
OF POOR QUALITY

FIGURE 3 PRSA O2 TANK CONFIGURATION

ORIGINAL PAGE IS OF POOR QUALITY



the fluid, the manifolds would be pressurized and a nonvented fill of the PRSA tanks would take place. Liquid oxygen remaining in the lines would then be dumped overboard. Figures 4 and 5 show schematically the proposed procedure.

After the transfer of the liquid oxygen to the tanks, its pressure and temperature has been estimated to be 45 psia and 172°R , respectively (for a completely full tank). This corresponds to a slightly subcooled and subcritical state. To bring the pressure in the tank to the system operating pressure of about 900 psia the set of internal heaters would be used. This means bringing the substance from a subcritical state to a supercritical one. At present, this process is unique since it has never been carried out before in a space environment. This study is related to this process. It is desired to predict the performance of the heaters while bringing the state of the substance from the subcritical state to the supercritical one, while in orbit. In particular, it is desired to predict the time the pressurization process will take and the temperature of the heater as the process proceeds. The latter is important to carry out the pressurization process safely since there are materials within the tank which could achieve ignition temperatures if the heaters were allowed to exceed the safety limit of 350°F .

ORIGINAL PAGE IS
OF POOR QUALITY.

FIGURE 4
LO₂ TRANSFER SYSTEM

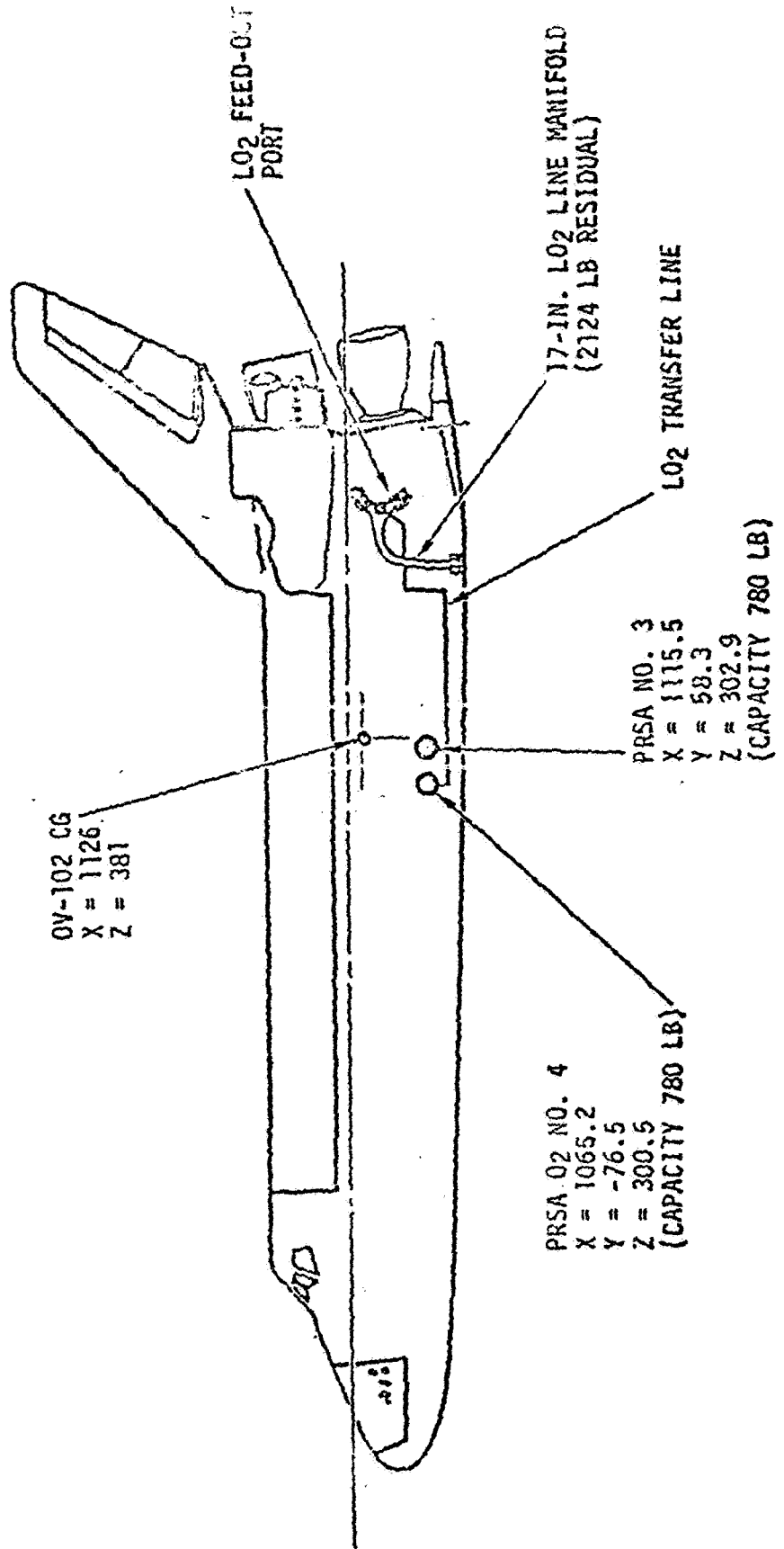


FIGURE 5 LO₂ TRANSFER SCENARIO

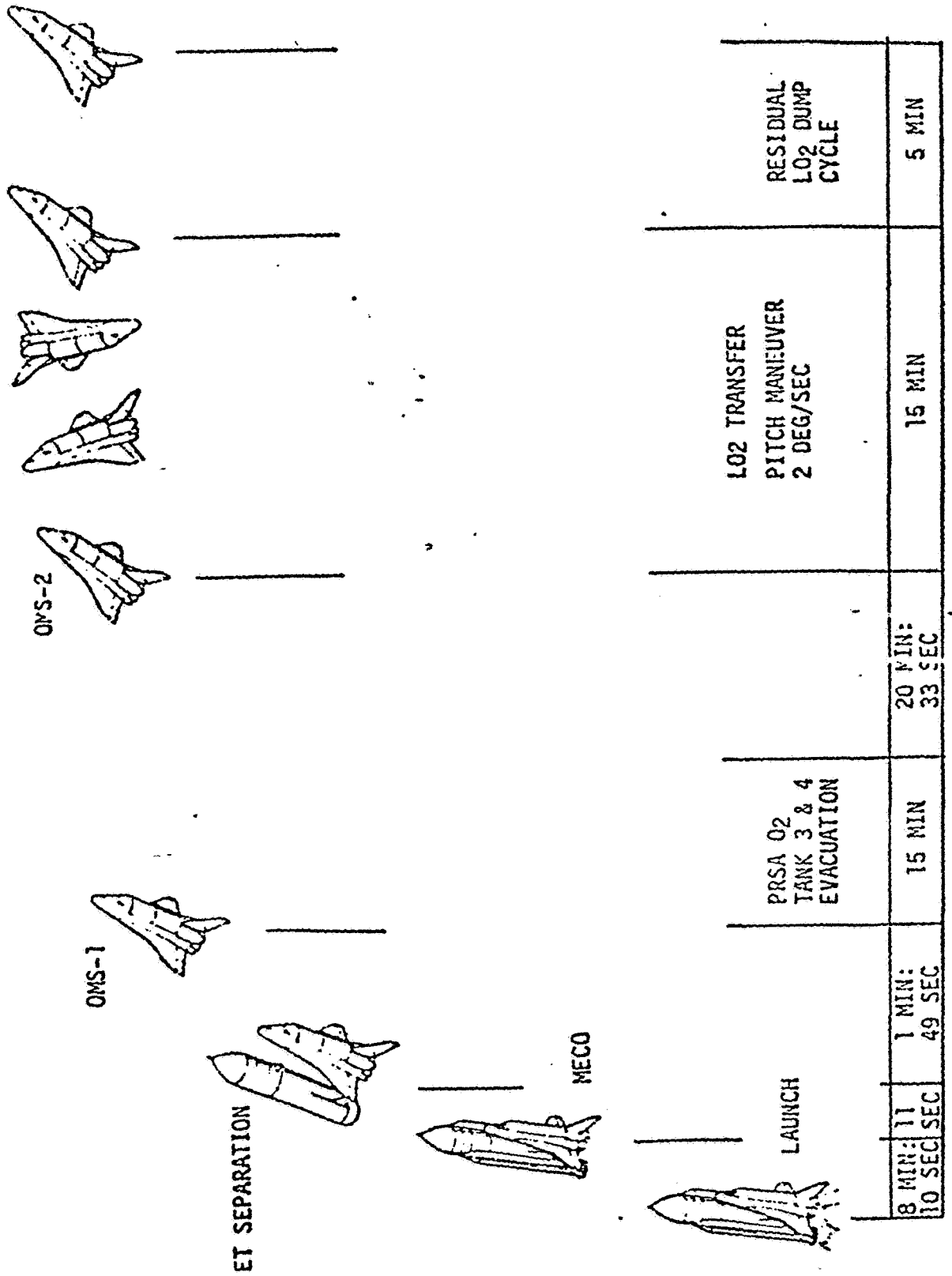
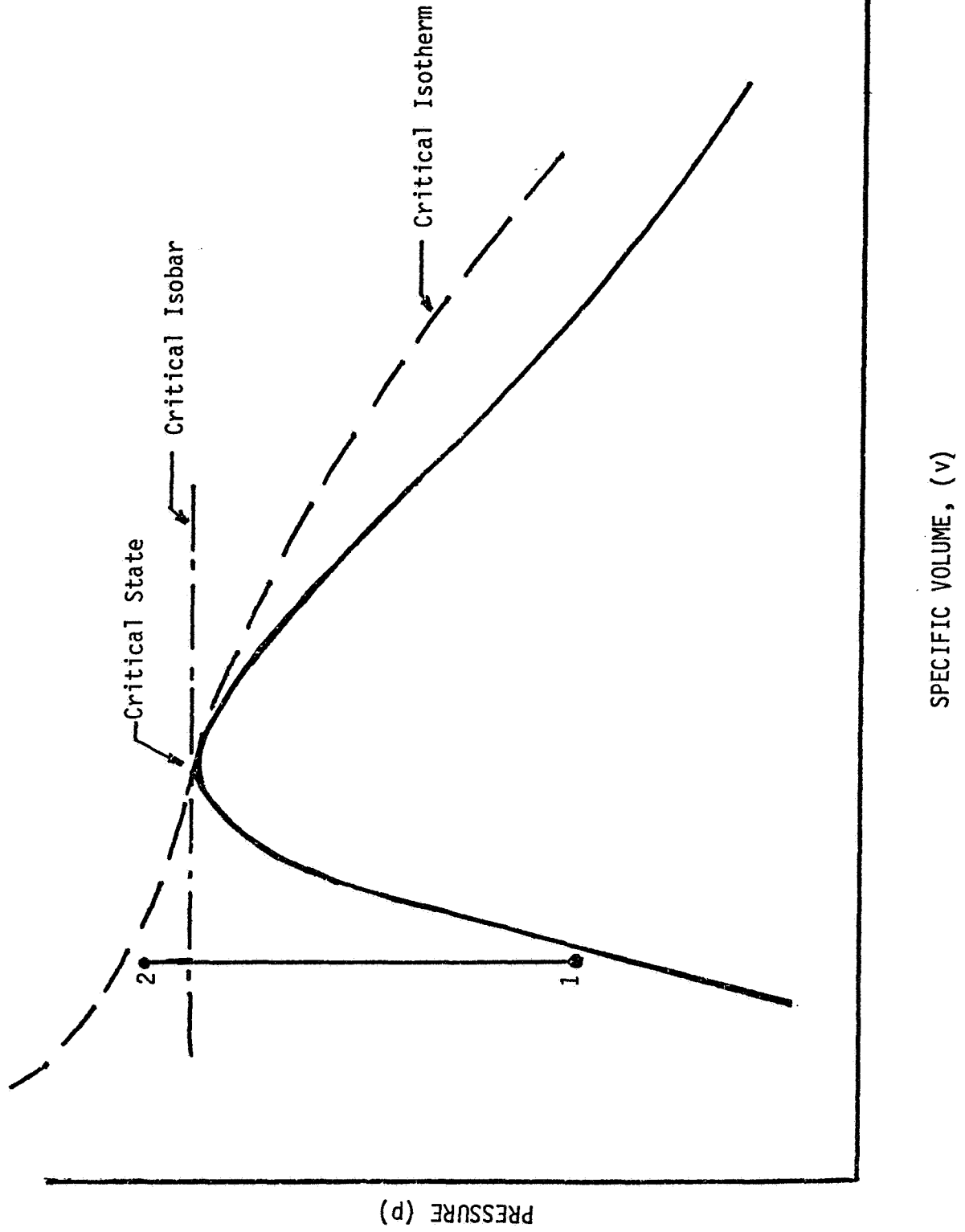


FIGURE 6 PRESSURE SPECIFIC VOLUME' DIAGRAM



II. THEORETICAL CONSIDERATIONS

From a thermodynamic point of view, the process that a closed system undergoes in bringing it from a subcritical to a supercritical state, is one of constant average density for the system as Figure 6 shows. The first law applied to a closed system yields.

$$Q = U_2 - U_1 \quad (1)$$

where Q is the heat input and U_1 , U_2 are the initial and final internal energies of the substance during the process. As can be seen from the figure, the pressure increases from p_1 to p_2 as the process is carried out. At any instant of time, a knowledge of how much energy has been transferred into the fluid would provide the value of its pressure.

While thermodynamics deals with the total energy content of a fluid, it does not provide information as to the rate at which these energy exchanges will occur.

Thus, one has to refer to heat transfer theory to obtain information about the rate of energy transfers and thus on time requirements for the processes involved.

The mechanism for the energy transfer in the form of heat are those of conduction, convection, and radiation and those found on multiphase processes such as boiling and condensation. The study of these processes in reduced and zero gravity environments has been promoted since the middle 1950's by the development of the space technology and research. However, the studies, and the correlations derived from them, has a limiting factor, the inaccuracies associated with the experimental production of reduced gravity. The probable main limitation of the techniques available on earth to produce a reduced gravity environment is the short test time. Tests in a space station may be the only way to finally determine the long-term performance of these processes.

Based on the still limited knowledge that we have at present, an analysis of the performance of the heaters in the oxygen tank of the PRSD system was undertaken in this study.

Initially, before the heaters are turned on, both the heaters and the fluid can be assumed to be at the same temperature. What occurs after the heaters are turned on can be described in the following manner. If the state of the fluid is one of a slightly subcooled liquid, at first, the electrical energy supplied to the heaters and converted as heat by them, will be used to bring the liquid adjacent to the heaters to its saturation temperature at the existing pressure at that moment. The addition of more energy will increase the temperature of the heaters above the saturation temperature of the fluid adjacent to it, and boiling will start.

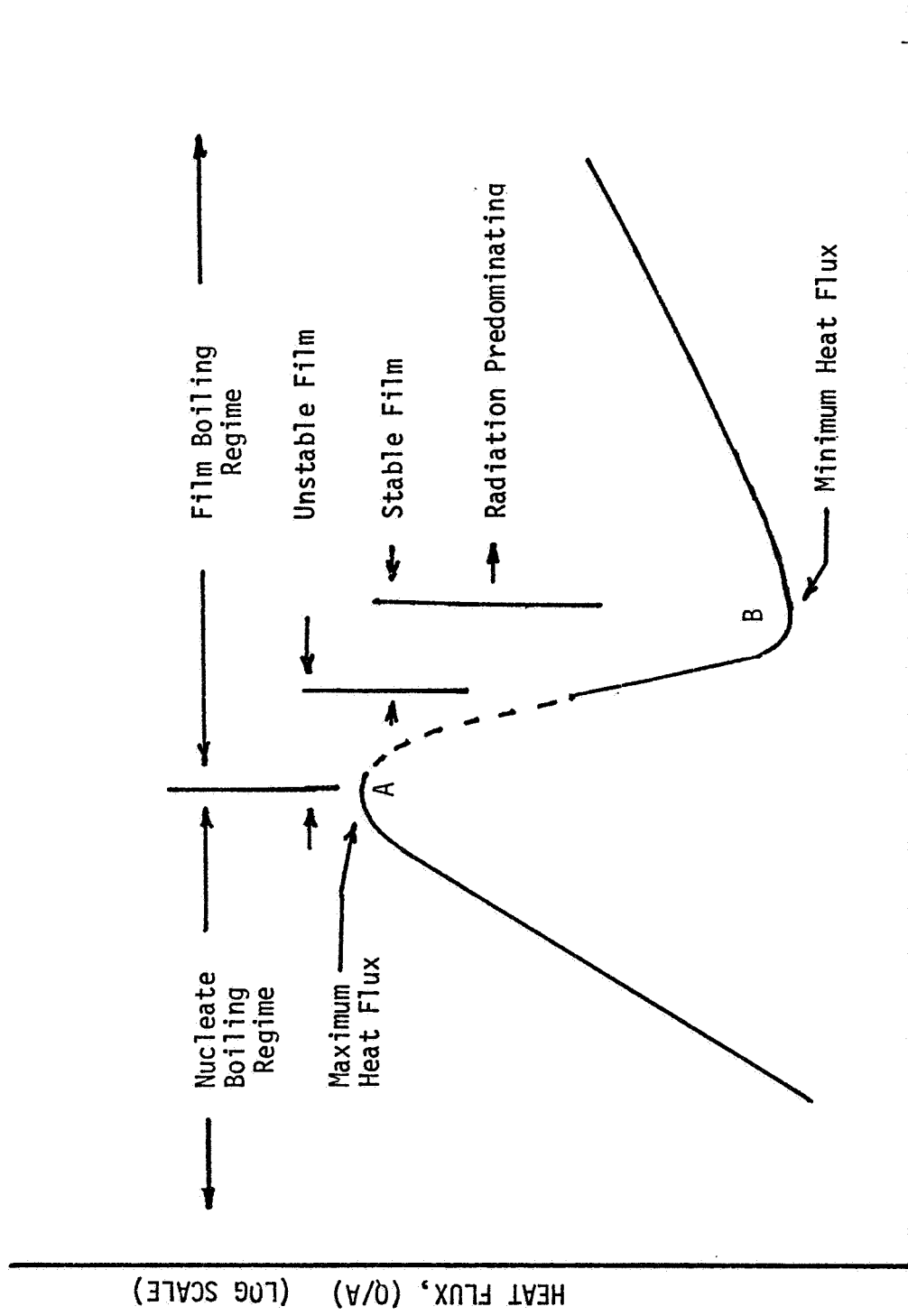
Figure 7 shows a typical boiling curve. It is a representation of heat flux versus excess temperature, where the excess temperature, $(T_w - T_{sat})$, is the difference between the surface temperature of the heater and the saturation temperature of the fluid adjacent to the heater.

Various regimes are indicated in the figure. That of nucleate boiling refers to one in which a vigorous bubble formation at the heater's surface is observed.

The initial portion of the film boiling regime is one in which bubbles form so rapidly that they prevent fresh fluid from moving in close to the heater's surface. Individual bubbles tend to coalesce and form a film of vapor on the surface of the heater. Because the film intermittently forms and disappears, this portion of the film boiling regime is very unstable.

The regime of stable film boiling is one in which the film on the heater surface is stable. Due to the increased thermal resistance of this layer, the heat flux is reduced as the excess temperature increases. It reaches a minimum, and as the excess temperature continues to increase, radiant heat transfer

FIGURE 7 TYPICAL BOILING CURVE



becomes predominant and the heat flux increases again. Point A of the curve is called the critical or maximum heat flux while Point B is called the minimum heat flux. Due to the complexity of the boiling process, most engineering calculations involving it are made from empirical correlations.

There are several factors to consider for the boiling processes in reduced gravity environments. One must consider how the nucleate boiling heat transfer flux is influenced as gravity is reduced. Gravity effect on the upper limit of the nucleate boiling flux regime (known as the critical heat flux) is also important since the latter determines when transition from nucleate to film boiling will occur. Gravity effect on the film boiling regime is also of interest.

Boiling will take place until the pressure of the fluid goes above the critical pressure. From this point on, the fluid will behave as a single phase component. These regimes will be considered in more detail as follows.

An energy balance on the heaters at any instant of time yields the following equation,

$$(\text{rate of energy input} - \text{rate of energy output}) = \text{rate of increase in the internal energy of the heater.} \quad (2)$$

The rate of energy input term refers to the rate of energy input as electrical energy to the heater, while the rate of energy output term refers to the heat transfer process or processes which at that instant are controlling the rate of energy output from the heater. The change in internal energy of the heater causes a change in its temperature. They are related through the equation,

$$\text{rate of change in internal energy of the heater} = \frac{(\text{heat capacity of the heater}) \times (\text{rate of change of the temperature of the heater})}{\text{of the heater}} \quad (3)$$

$$\text{i.e.,} \quad \frac{\Delta U}{\Delta \tau} = (mc) \left(\frac{\Delta T}{\Delta \tau} \right) \quad (4)$$

where

- m - mass of the heater
- c - specific heat of the heater
- τ - time

Consider now the above relations in the case when the fluid adjacent to the heater is initially subcooled and is going to be brought to a saturated liquid state by the conversion of electrical energy into heat energy in the heater, while in a low-g environment. In this case, it is assumed that heat conduction into the layers of fluid adjacent to the surface of the heater is the primary mode of heat transfer.

Gravity reductions primarily affect the convective heat transfer mode since this mode is dependent upon buoyancy forces, which are correspondingly reduced as the gravity field is reduced. Temperature differences are such that the contribution to the heat transfer by radiation is negligible. To solve such a system the temperature gradient should be known or assumed. In the problem under consideration a linear temperature gradient was assumed and an iterative technique was utilized to determine the variation with time of the temperature at the heater's surface. The amount of heat added to the fluid was calculated and from it, the corresponding pressure rise of the system. Properties of the fluid were evaluated at the particular pressure and temperature occurring at a given instant of time. The thermal conductivity of the fluid was evaluated at the temperature of the heater's surface while the density and specific heat were calculated at the mean temperature of the fluid in which conduction had taken place. The difference between using the arithmetic mean temperature and using the bulk temperature was determined to be insignificant and the arithmetic mean temperature was used in this study due to its simplicity.

The iterative model used for this portion of the heating process is described in Appendix A. The iterative process begins by determining the amount of energy converted by the heater into heat energy in a unit of time. This heat energy raises the temperature of the heater above the temperature of the fluid which surrounds it, and thus establishes a temperature gradient. Due to this temperature gradient heat flows into the fluid. A balance is sought between the amount of heat which flows through conduction from the heater into the fluid and the energy stored during that instant in the mass of fluid which has been affected by this energy transfer. The energy which flows into the fluid is subtracted from the initial energy generated at the heater and the one which will be generated in the next period of time is added to determine what amount of energy will be available to increase the heater's temperature at the beginning of the next unit of time. The available energy is related to the heater's temperature increase by the relation $Q = mc(\Delta T)$ from which $\Delta T = Q/mc$. The product mc is the heat capacity of the heater.

When the temperature at the heater's surface reaches the saturation temperature of the fluid at the prevailing pressure, boiling begins. The model then, although following the same energy accounting procedures, changes to account for the multiphase processes involved.

Experiments where nucleate boiling has been studied in reduced gravity fields indicate that, within this regime, the wall heat flux (Q/A) as a function of the difference between the wall temperature and the saturation temperature of the fluid ($T_w - T_{sat}$) do not vary appreciably from the experimental data obtained at 1-g, as gravity is reduced. This can be observed in Figure 8 where the data for boiling liquid nitrogen at a 1-g and at a $10^{-2}g$ levels is shown. The same phenomena is reported for nucleate boiling in increased gravity fields (1,2)*. Some authors (2) have concluded that

* Number in parenthesis refer to the reference number.

"buoyant forces are not of prime significance in the process of nucleate boiling. The role of inertia forces resulting from bubble growth appears to have the principal influence in the process."

On the other hand, the experimental data shows that the maximum heat flux, i.e., the heat flux at which the transition from nucleate boiling to film boiling occurs, as well as the minimum heat flux and the film boiling regime itself are strongly dependent upon gravity levels. This effect can also be observed in Figure 8.

For the pool nucleate boiling regime, the following equation in generalized Stanton Number form was selected, (2)

$$Re = \frac{F(p)}{(St)^a (Pr)^b}$$

It can be expressed as

$$\frac{L^* G^*}{\mu_l} = \frac{F(p)}{[(Q/A)/\Delta T c_p] G^*]^a [Pr]^b}$$

where

$$L^* = \left[\frac{g_0 \sigma}{g(\rho_l - \rho_v)} \right]^{1/2}$$

$$G^* = \frac{(Q/A) \rho_l}{h_{fg} \rho_v}$$

$$F(p) = 3.05 \times 10^{-11} \left[\frac{p}{[\sigma(g/g_0)(\rho_l - \rho_v)]^{1/2}} \right]^{7/3}$$

$$a = 10/3$$

$$b = 6.5/3$$

In the above relations,

p - pressure, psfa

A - area, ft²

g - normal gravitational acceleration, ft/sec²

ΔT - ($T_w - T_{sat}$), °R

T_w - wall temperature, °R

- T_{sat} - saturation temperature, $^{\circ}R$
 c_{pl} - specific heat capacity of the saturated liquid, BTU/ lbm- $^{\circ}R$
 g_0 - conversion factor, $32.2 \frac{lbm-ft}{lbf-sec^2}$
 σ - surface tension, lbf/ft
 ρ_l - density of the saturated liquid, lbm/ft 3
 ρ_v - density of the saturated vapor, lbm/ft 3
 h_{fg} - latent heat of vaporization, BTU/lbm
 Pr - Prandtl number
 $F(p)$ - pressure function
 Re - Reynolds number, properties measured at T_{sat}
 S_t - Stanton number, properties measured at T_{sat}
 μ_l - viscosity of the liquid

The heat flux in this regime was assumed independent of g level as previously explained. When considering the point of maximum heat flux, Kutateladze correlation (2), was selected, which state that

$$(Q/A)_{max} = (0.16) \rho_v h_{fg} \left[\frac{g_0 g_0 \{ \rho_l - \rho_v \}^{1/4}}{\rho v^2} \right] (a/g)^{1/4}$$

In this equation, the parameters are the same as previously described. However, a represents the gravitational acceleration level while g represents the normal (32.2 ft/sec 2) earth gravitational acceleration. This equation postulate that as a/g approaches zero, the heat flux goes to zero. At an a/g level of 10^{-6} , the $(a/g)^{1/4}$ factor would reduce the maximum heat flux by a 0.013 factor while at an a/g level of 10^{-3} (the one prevailing during a pitch maneuver of the Orbiter at a rate of 2 degrees/second), it would be reduced by a 0.178 factor. However, the experimental data deviates from the expected $(a/g)^{1/4}$ behavior. This is shown in Figure 9 taken from reference 2. The figure shows that at low values of a/g, (a/g \sim 0), the maximum flux is about 40 to 60% of the value for an a/g = 1.

The meaning of the reduction in maximum heat flux as a/g \rightarrow 0 is that the fluid goes into the film boiling regime much sooner and for a small value of the excess temperature ($T_w - T_{sat}$).

ORIGINAL PAGE IS
OF POOR QUALITY

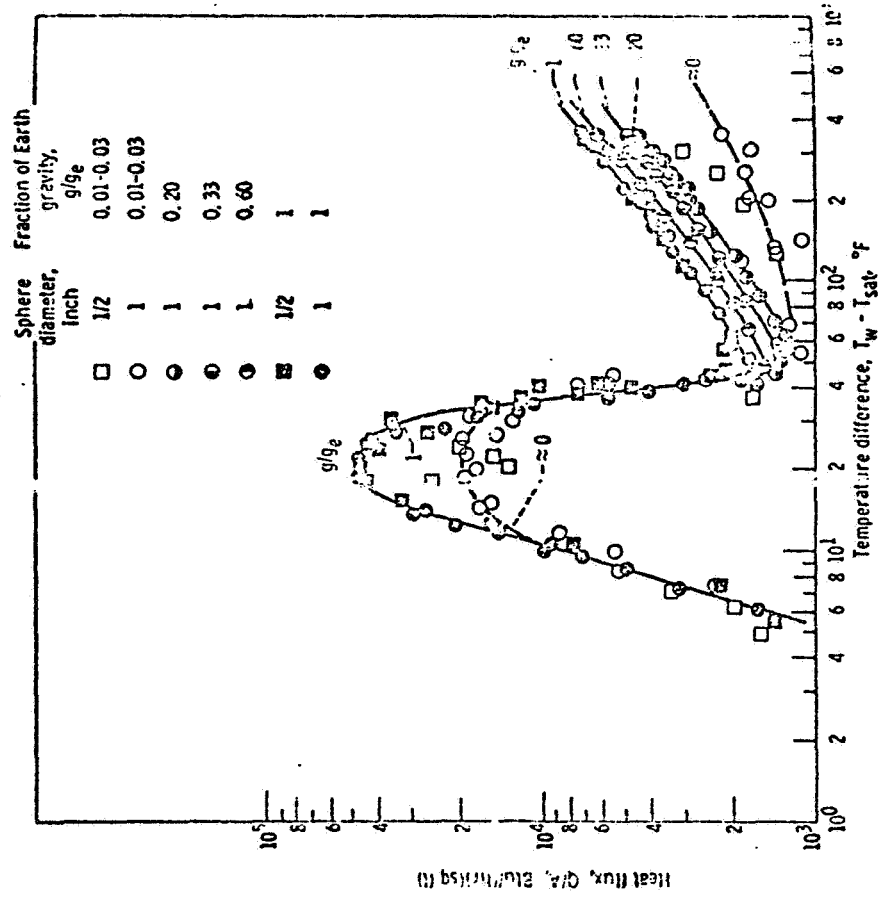


Fig. 8. Nucleate and transition boiling at earth and near zero gravity and film boiling at earth and fractional gravities for liquid nitrogen (Merte and Clark (39)).

ORIGINAL PAGE IS
OF POOR QUALITY

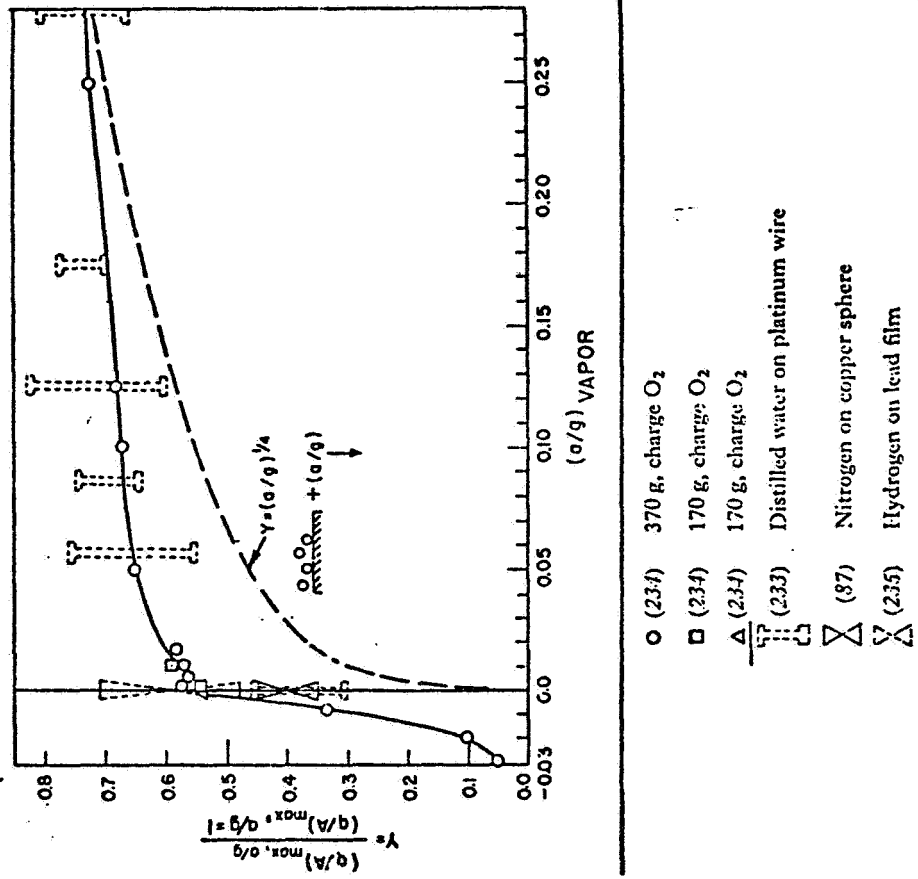


Fig. 9. Normalized maximum heat flux at small relative vapor accelerations (calculated from bulk liquid temperatures) [from Lyon *et al.* (234)].

The point of maximum heat flux at a particular pressure was shown in Figure 7 as point A. It separates the nucleate boiling from the film boiling. As shown in this figure, the initial portion of the A-B portion of the curve corresponds to an unstable film while the final portion corresponds to a stable film. As pointed out before, it is considered to be a region of transition boiling. Little study has been done on this portion of the film boiling regime. Considering now point B of the curve, it represents the point of minimum heat flux in the film boiling regime. From this point on, radiation contributes to the film boiling and must be taken into consideration.

For this study the correlation of Zuber (2) was selected to determine the minimum heat flux. It is given as

$$(Q/A)_{\min} = \frac{\pi}{24} \left[\frac{\sigma g g_0 (\rho_l - \rho_v)}{(\rho_l + \rho_v)^2} \right]^{\frac{1}{4}} (a/g)^{\frac{1}{4}}$$

The $(a/g)^{\frac{1}{4}}$ dependence has been confirmed by certain experimental data for at least $(a/g) > 0.10$. However at very low values, it is not known if the relation will hold. In this case it would predict low film boiling heat fluxes and the heat transfer from the heater would probably be highly dependent upon radiation because of the resulting high surface temperatures.

For the calculation of heat fluxes in the film boiling regime, the method proposed by L. A. Bromley (3) was used in this study. The heat flux would be given by

$$Q/A = \left[h_c + h_r \left(\frac{3}{4} + \frac{1}{4} \frac{h_r}{h_c} \left(\frac{1}{2.62 + \frac{h_r}{h_c}} \right) \right) \right] (T_w - T_{\text{sat}})$$

where, h_r , the radiation contribution is given by

$$h_r = \frac{\sigma \epsilon (T_w^4 - T_{\text{sat}}^4)}{T_w - T_{\text{sat}}}$$

For h_c , Breen and Westwater correlation was used (2). Their correlation is

$$h_c = (0.59 + 0.069 \frac{\lambda_c}{D_o}) F_2 \lambda_c^{-\frac{1}{4}}$$

where,

$$\lambda = 2\pi \left(\frac{g_0 \sigma}{g (\rho_l - \rho_{vf})} \right)^{1/2} \left(\frac{a}{g} \right)^{-1/2}$$

$$F_2 = \left(\frac{k_{vf}^3 \rho_{vf} (\rho_l - \rho_{vf}) g h_{fg}'}{\mu_{vf} (T_w - T_{sat})} \left(\frac{a}{g} \right)^{1/4} \right)$$

$$h_{fg}' = h_{fg} \left\{ 1 + 0.34 \frac{c_{pvf} (T_w - T_{sat})}{h_{fg}} \right\}^2$$

In the above relations,

σ - is the Stefan-Boltzmann constant

ϵ - emissivity of the surface

D_0 - outside diameter of the heating element

The subscript v refers to the vapor and the additional subscript f , indicates that vapor properties are taken at the mean film temperature, $T_f = (T_w + T_{sat})/2$.

**ORIGINAL PAGE IS
OF POOR QUALITY**

III. DEVELOPMENT OF AN ANALYTICAL PROCEDURE

Figure 10 shows the heater used in the oxygen PRSA tank. Two heaters are used per tank, The first task was to model the heater by a suitable geometry.

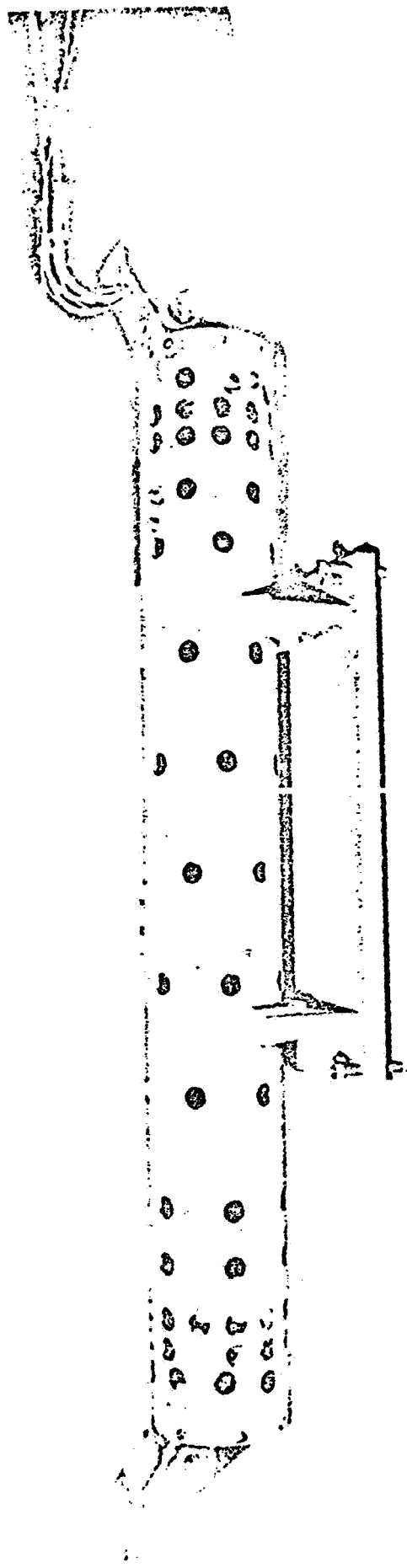
The heating elements are soldered to the inside of a cylindrical pipe of inside diameter 3.46 inches and 0.020 inches thick. The length of the cylinder is 27 inches. The set of heating elements have a total length of 312.75 inches and an outside diameter of 0.187 inches.

The geometry selected to model the heater was that of a cylindrical pipe of the same outside and inside diameters, but with an outside area which accounted for the holes in the wall of the actual heater. The area of the heating element on the inside of the actual heater was considered as equivalent to that of a finned surface so that on the model the inside area was considered to be the sum of the net inside area of the actual cylindrical surface, and the surface area of the heating elements. The length of the cylindrical surface of the model was assumed to be the same as that of the actual heater.

This model was used for the first part of the heating process while the liquid adjacent to the heater surface was being brought to a saturated liquid condition. The surface area of the heating elements was used as the heat transfer area during the boiling process. The value of the thermal capacity of the heater (mc) was determined from tests carried out on the tanks and described in Report No. BR16369 (8). In these tests, the heaters were turned on while the inside of the PRSA tank was held under vacuum. The heaters were started from ambient temperature and the time required for them to reach a temperature of $+350^{\circ}\text{F}$ was noted. Using the information provided by the temperature - time histories, the heat capacity was determined to be $1.1 \text{ BTU}/^{\circ}\text{R}$.

ORIGINAL PAGE IS
OF POOR QUALITY

FIGURE 10. Heater Assembly



The next task was to develop a simple iterative procedure based on an energy balance to describe the heat transfer phenomena while the liquid was being brought from a subcooled state to a saturated one. The worst-case possible was conceived, i.e., one in which neither convective motion nor radiation assist the rate of heat loss from the surface of the heater. Conduction into a fluid surrounding the heater was the only mechanism considered. Details of the procedure are given in Appendix A .

The following task was to select appropriate correlations to determine heat fluxes during the various regimes of the boiling phenomena, while the fluid was being brought from a subcritical condition to pressures above the critical pressure. These were to be used in an iterative procedure similar to the one already mentioned above. The correlations used for the determination of the heat fluxes were discussed in a previous section of this report.

IV. WORK ACCOMPLISHED

The first aspect of the work consisted of becoming oriented with the problem and the details of the tank, heater, etc. This was followed by a literature survey on aspects pertinent to the task.

As already mentioned, an iterative technique based on an energy balance at the heater was devised and used to describe the phenomena occurring while the fluid was being brought from a subcooled state to a saturated one. A computer program was prepared to carry out the iterations. Several subroutines were prepared to interpolate the values for the properties as given in the tables in a manner suitable to the requirements of the equations used. Similarly, a computer program for the nucleate and film boiling regimes of the boiling curve was also prepared with the proper subroutines to evaluate the values of the properties. Partial results from the computer outputs are shown in Figures 11 and 12 for power inputs of 0.58 kw per heater (the two heating elements of the heater on) and 0.29 kw per heater (one heating element of the heater on).

They show that if the tank is completely full of liquid, the pressurization process takes about 15 minutes for the case of full power supplied to the heater and 30 minutes for the case of half power. The temperature of the heater follows closely above the saturation temperature of the fluid at the particular pressure prevailing at a given instant of time. The temperatures during heater operation were well below the safe operating limit 350°F.

Figure 13 shows the results from the computer output for the case of 90% fill by mass. Most of the energy supplied (about 90%) was used to collapse the bubble of vapor. It took about 110 minutes to collapse

FIGURE 11 PRESSURE AND TEMPERATURE TIME HISTORIES

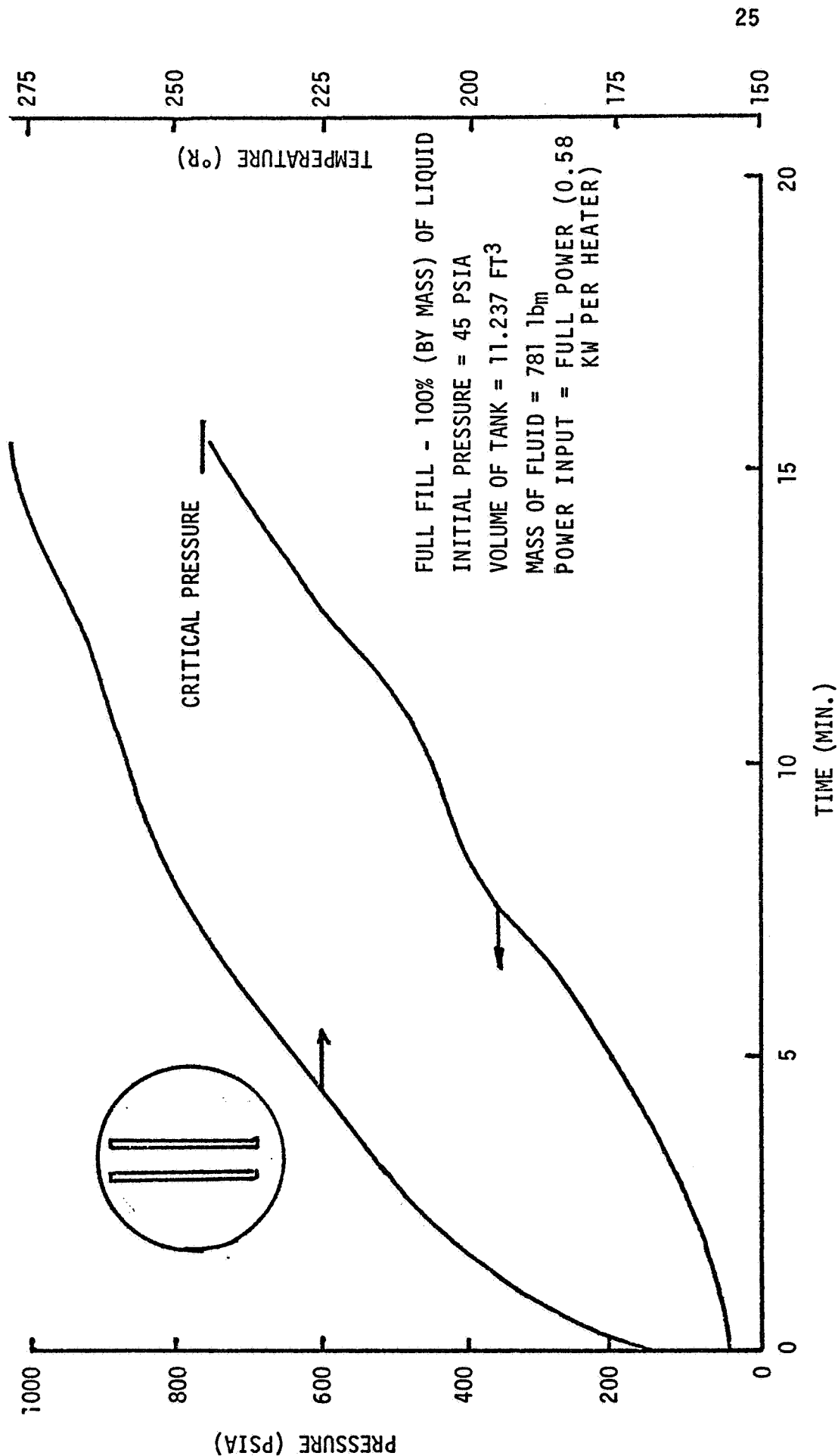


FIGURE 12 PRESSURE AND TEMPERATURE TIME HISTORIES

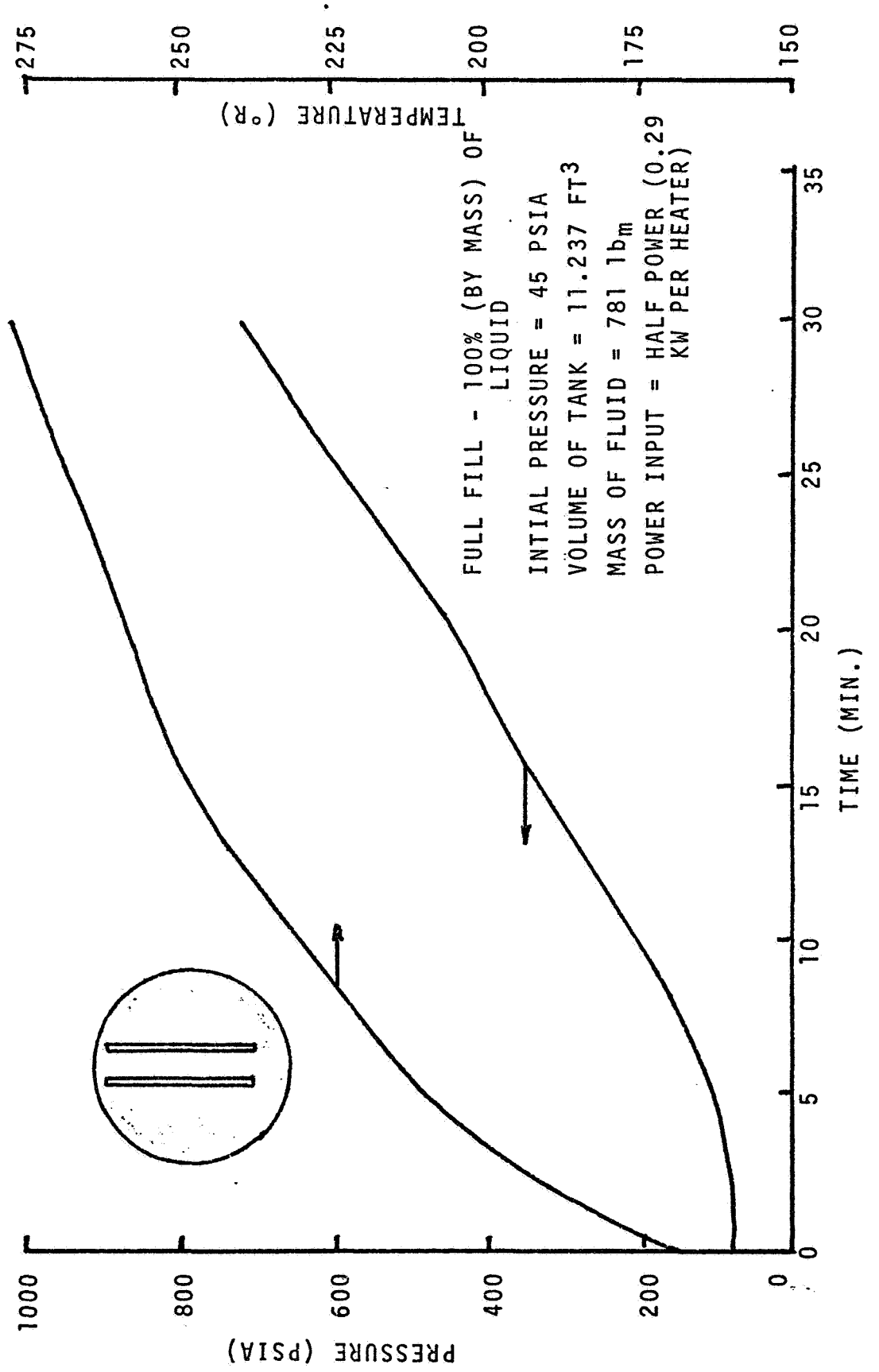
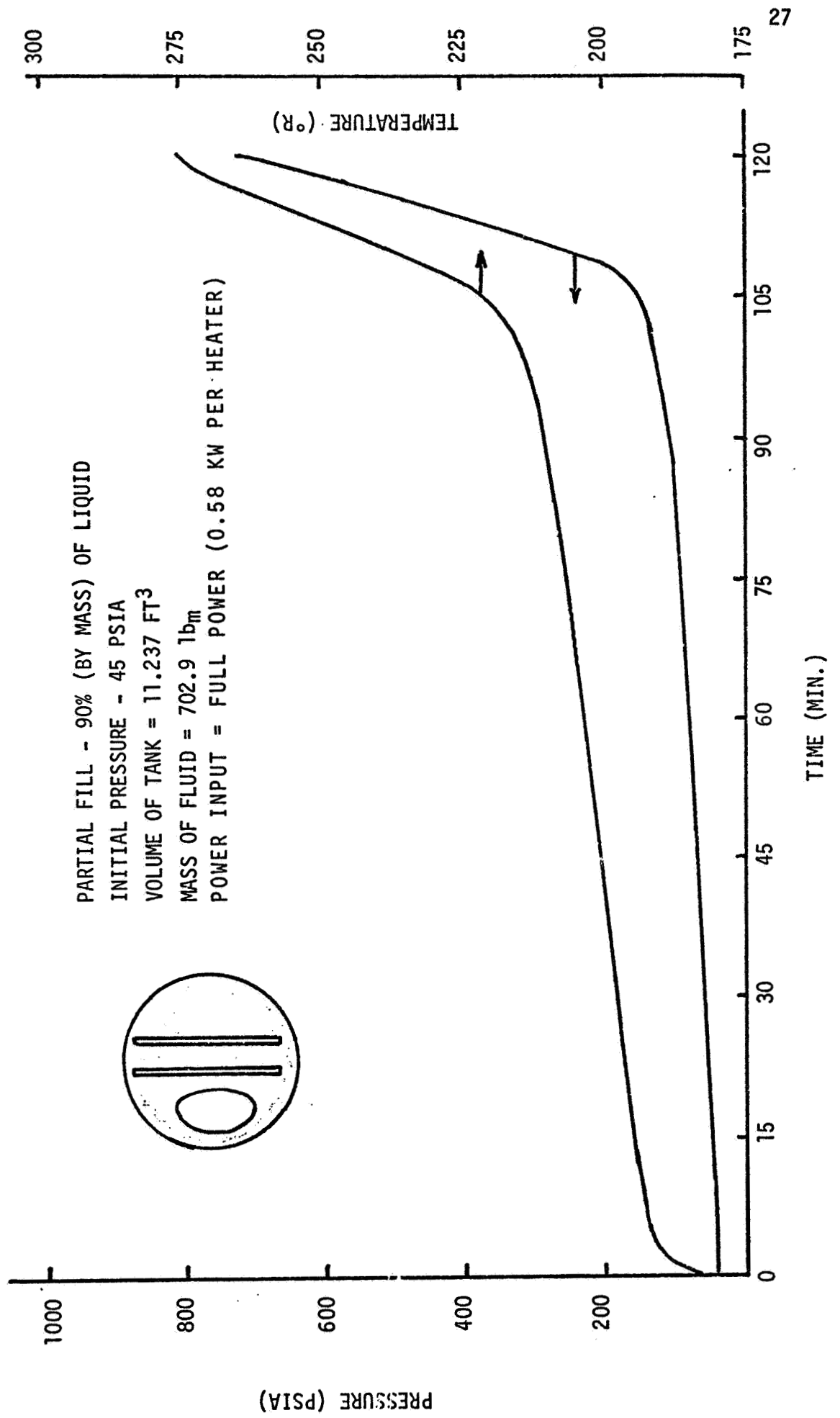


FIGURE 13 PRESSURE AND TEMPERATURE TIME HISTORIES



the bubble and an additional 15 minutes to pressurize the system to the critical state pressure. The maximum temperatures during heater operation were also well below the safe operating limit of 350°F.

V. LIMITATIONS OF THE PROCEDURE

The assumption of a linear temperature gradient during the first portion of the heating process, when the fluid is being brought to saturation was done arbitrarily. However, the thickness of the layer of liquid involved during the process turned out to be small (~ 0.15) so that the assumption is justified.

The heat flux rates for the boiling regimes (and thus their correlations) are for steady state conditions. By taking small intervals of time one expects to approximate the actual process by a quasi-steady one.

Experimental data on heat transfer at low a/g levels is limited, specially as $a/g \rightarrow 0$.

The values of the heat capacity as well as the emissivity of the heaters were assumed constant.

It is recognized that the heat capacity of the heater will be a function of temperature. A refinement to the procedure would be to include its variation throughout the range of temperatures of interest.

Although emissivity is also a function of temperature, analysis of the results indicated the process did not involve a range of temperatures in which radiation is as mayor contributor.

Volumetric changes of the tank and heat leak were not considered.

VI. CONCLUSIONS AND RECOMMENDATIONS

The results of this work indicate that the pressurization of liquid oxygen from a subcritical to a supercritical state by the use of the heaters of the PRSA tanks while in a low-g environment is feasible.

The heat transfer rates observed during the analysis were so high that modeling of the heater as a cylindrical pipe as explained previously could be modified. This model assumed that the heat would be conducted to the cylindrical pipe of the original heater as the heating elements were turned on and from this surface into the fluid. The other extreme case would be to consider that the heat flows from the heating elements into the fluid and that the cylindrical structure to which they are welded be considered just as a supporting structure and not as a heat transfer area. It is recommended that this type of model be adopted and the results compared with the previous one. It is most likely that the actual behavior lies between these two extremes.

It is recommended that the analysis be extended to consider fill percentages less than 100%.

Analytical Model for the Conduction Dependent Heat Transfer Phenomena
While a Subcooled Liquid is Brought to a Saturated State Under a Low-g Environment

Consider a section of cylindrical pipe with a fluid in contact with the outer and inner surfaces as shown in Figure 14. Let r_i and r_o be the inner and outer radii respectively, of the pipe. Consider the fluid to be free of convective motion and radiation heat transfer negligible so that the heat transfer between the surface and the fluid is essentially through conduction. Assume that at time $t = 0$, the pipe and the fluid are at the same temperature, T_0 . Consider that from time $t = 0$ on, heat is generated in the pipe at a rate P by sending an electric current through the pipe. The heat generated within an interval of time t would be Pt . If we assume that initially this energy goes into raising the heater's temperature by an amount ΔT_h , then

$$Pt = (mc)_h \Delta T_h$$

where m is the mass of the heater c its specific heat, and the subscript h denotes heater. From the above equation

$$\Delta T_h = \frac{Pt}{(mc)_h}$$

This increase in temperature of the heater above the temperature of the surrounding fluid will establish a temperature gradient throughout the fluid close to the heater and heat will flow from the heater into the fluid as shown in Figure 15 . The amount of heat flowing into the fluid is given by

$$kA_o \left(\frac{\Delta T_h}{x_o} \right) t$$

for the external surface of the heater. A_o is the external area and x_o is the thickness of the layer of liquid into which heat has been able to flow during the interval of time under consideration. $(\Delta T_h/x_o)$ represents

ORIGINAL PAGE IS
OF POOR QUALITY

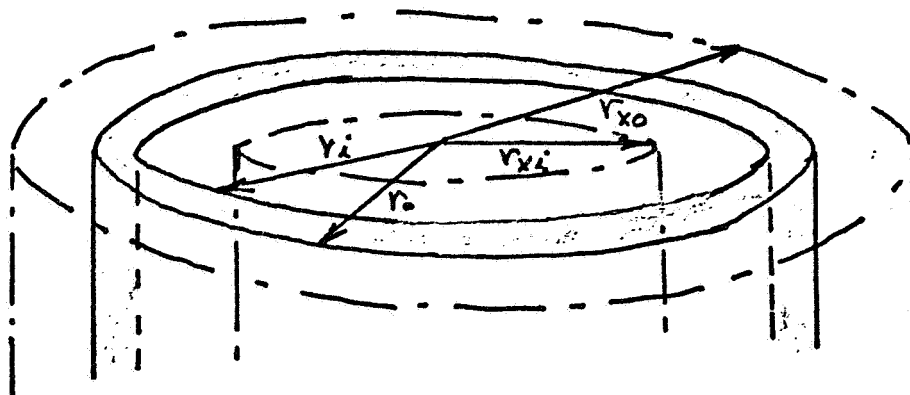


FIGURE 14. Cross section of the cylindrical pipe and fluid cores.

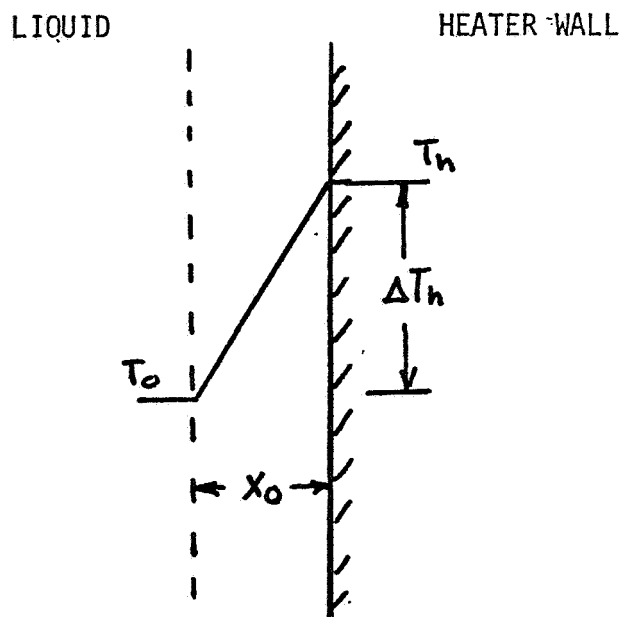


FIGURE 15. Temperature gradient within the liquid.

the temperature gradient within the layer and it has been assumed linear arbitrarily. The temperature gradient at the wall of the heater, when multiplied by the thermal conductivity of the fluid evaluated at the temperature of the heater surface and by the external area of the heater will give the amount of heat that flowed through conduction into the layer of fluid. If this energy is subtracted from the energy generated by the heater during the interval of time, i.e.,

$$Pt - (kA_0 \frac{\Delta T_h}{x_0}) t$$

this energy, in addition to the one generated in the next interval of time will be available to increase the heater's surface temperature in the next interval of time.

To determine the thickness x_0 , an energy balance between the heat flowing through conduction into the layer and its energy content can be written as:

$$\begin{aligned} \text{energy in the layer} &= \text{total heat that has gone into the layer from time} \\ & t = 0 \text{ to the time interval in consideration} \end{aligned}$$

The energy in the layer is given by

$$m_f c_f \Delta T_f$$

where the subscript f refers to the liquid in the layer. The mass m is given by

$$m_f = \pi (r_{x_0}^2 - r_0^2) L \rho_f$$

where r_{x_0} is the radius of the external limit of the layer into which heat energy has gone, L is the length of the heater and ρ_f is the bulk density of the fluid in the layer. Thus, the energy in the layer is given by

$$\pi (r_{x_0}^2 - r_0^2) L \rho_f c_f \frac{(\Delta T_h)}{2}$$

From this balance, r_{x_0} can be determined. x_0 is then,

$$x_0 = r_{x_0} - r_0$$

In the procedure one has to initially assume a value of x_0 for the conduction equation. x_0 is determined from the above equation and if different from the assumed one, an iterative procedure is used to correct for it. The value of x_0 to be used for each cycle of the iteration can be determined from

$$x_{0_{\text{new}}} = x_{0_{\text{old}}} + \frac{(x_{0_{\text{obtained}}} - x_{0_{\text{old}}})}{2}$$

until the difference between the assumed x_0 and the given x_0 is less than a predetermined amount. A similar method can be used to determine the energy in the layer adjacent to the inside surface of the heater. In this case

$$U_i = \pi(r_i^2 - r_{x_i}^2) Lc_{f\rho f} \left(\frac{\Delta T_f}{2}\right)$$

On each cycle, i.e., every time a new interval of time is considered, the pressure and other properties of the fluid are evaluated from the internal energy of the system. In this case it is necessary to consider the total internal energy of the system which is given by the initial internal energy of the fluid plus ΔU where the fact that two heaters are supplying energy must be considered. Thus

$$U = U_{\text{initial}} + 2(U_o) + 2(U_i)$$

As an example of how the procedure works, consider that initially the fluid in the tank as well as the heaters (which are off) are at a temperature of 172°R and a pressure of 45 psia. Assume that at time $t = 0$ the two heating elements on each heater are turned on and that the electric power supplied to one heater is 0.58 kw. Consider a time interval of 1 second.

The energy converted to heat is this second is where r_o = outer radius of heater = 1.75 inches.

$$L = \text{length of heater} = 27/12 \text{ feet}$$

and where ρ_f and c_f are evaluated at $T_o + \frac{\Delta T_h}{2} = 172.25^\circ R$

Solving for x_o gives

$$x_o = 1.76 \text{ inches}$$

and

$$x_o = r_{x_o} - r_o = 1.76 - 1.75 = 0.01 \text{ inches}$$

A new x_o is selected to repeat the procedure

$$x_{o_{\text{new}}} = x_{o_{\text{assumed}}} + \frac{(x_{o_{\text{obtained}}} - x_{o_{\text{assumed}}})}{2}$$

$$x_{o_{\text{new}}} = 0.04 + \frac{(0.01 - 0.04)}{2}$$

$$x_{o_{\text{new}}} = 0.02 \text{ inches}$$

Repeating the above procedure with the new value yields a

$$kA_o \frac{(\Delta T_h)t}{x_o} = 0.010 \text{ BTU} \quad \text{with } r_{x_o} = 1.77 \text{ inches}$$

$$x_o = 1.77 - 1.75 = 0.02 \text{ inches}$$

which checks with the assumed one. By the same procedure, the energy, transfer to the fluid at the inside surface of the cylindrical pipe is determined to be 0.016 BTU with $x_i = 0.026"$. This energy when multiplied by 2 (due to the fact that there are two heaters) represents the increase in internal energy of the fluid within the tank and is used to determine the pressure existing at that instant and the corresponding saturation temperature. The energy remaining in the heater for the next period of time, from the energy generated in the period under consideration is

$$0.55 - (0.010 + 0.016) = 0.52 \text{ BTU}$$

This amount added to the 0.55 BTU which will be generated in the next period gives a total of 1.07 BTU available to raise the temperature of the heater to a new T_h from its initial value of T_o . If one now considers a

period of two seconds, the energy available to raise the heater temperature would be 1.07 BTU giving a $\Delta T_h = \frac{1.07}{1.1} = 0.97$ BTU/ $^{\circ}$ R, a heater temperature $T_h = T_o + \Delta T_h = 172.0 + 0.97 = 172.97^{\circ}$ R, and a fluid bulk temperature = $T_o + \Delta T_h/2 = 172.5^{\circ}$ R. With a gradient $\Delta T_h/x_o$, the heat flowing from the outer surface of the heater during the second interval is determined to be 0.009 BTU with an x_o of 0.025". Similarly, for the inside surface, the heat flow is 0.011 BTU with an $x_i = 0.034$ ". The total energy conducted during the second interval to the fluid is $0.009 + 0.011 = 0.020$ BTU. This amount added to the one of the first interval gives a total of 0.04 BTU which represents the increase in internal energy of the mass of fluid up to that instant. The process is repeated until saturation conditions exist for the fluid adjacent to the heater.

BIBLIOGRAPHY

1. Siegel, R., Effects of Reduced Gravity on Heat Transfer, Advances in Heat Transfer, Vol. 4, pp 143-205, Academic Press, 1967.
2. Clark, J.A., Cryogenic Heat Transfer, Advances in Heat Transfer, Vol. 5, pp 400-468, Academic Press, 1968.
3. Adelberg, M., Effect of Gravity Upon Nucleate Boiling, Advances in Astronautical Sciences, Vol. 14, pp 196-222, The American Astronautical Society, 1963.
4. Clark, J.A., and H. Merte, Jr., Nucleate, Transition and Film Boiling Heat Transfer at Zero Gravity, Advances in Astronautical Sciences, Vol. 14, pp 177-220, The American Astronautical Society, 1963.
5. Incropera, F.P. and David P. DeWitt, Fundamentals of Heat Transfer, John Wiley and Sons, Inc., 1981.
6. Pitts, D.R. and Leighton E. Simmons, Heat Transfer, McGraw Hill Book Co., 1977.
7. Otto, E.W., Liquid Behavior During Weightlessness the Fluid Dynamic Aspects of Space Flight, Vol. 1, pp 31-37, Proceedings of the AGARD-NATO Specialists' Meeting Sponsored by the Fluid Dynamics Panel of AGARD, Marseille, France, April 20-24, 1964, Gordon and Breach Science Publishers, 1966.

1981 NASA-ASEE Summer Faculty Research Fellowship Program
at
NASA Johnson Space Center

EFFECT OF SHEAR STRESS ON CELL CULTURES AND OTHER REACTOR PROBLEMS

Faculty Fellow: Howard Schleier
Norwalk State Technical College

Supervisor: Michael A. Reynolds, Ph. D.
Biomedical Applications Branch
Medical Sciences Division

Abstract:

An experimental method is described for testing anchorage dependent cell cultures in fluidized beds. Feasibility calculations indicate the allowed parameters and estimate the shear stresses therein. In addition, the diffusion equation with first order reaction is solved for the spherical shell (double bubble) reactor with various constraints.

ORIGINAL PAGE IS
OF POOR QUALITY

Certificate of Acceptability

I hereby accept the attached documents as the final report of Howard Schleier, in partial fulfillment of the requirement of his 1981 NASA/ASEE Fellowship.


Michael A. Reynolds, Ph. D./Date

Abstract

The first part of this report consists of a feasibility study on ^{the} utilization of micro-carrier beads in a fluidized bed. Preliminary estimates indicate that HEK might be successfully grown on 150 micron beads near the upper range of fluidization, about 30-50% terminal velocity. Studies also indicate shear rates at approximately 0.1 dyne/cm^2 , Stokes Law governing, and Sherwood numbers of about 2.

The second part of this report is an analysis of the diffusion equation for incompressible flow with first order chemical reaction for a spherical shell. The boundary conditions are peculiar to the problem.

Special Recognition

I wish to grant special recognition to Dr. J. D. Hellums, Dean of Engineering, Rice University. The suggestion that a fluidized bed configuration utilizing micro-carrier beads be investigated was originally his.

ACKNOWLEDGEMENT

I wish to cite M. A. Reynolds, my advisor, for his inspiration, guidance and friendship. I also want to thank him for using his miraculous power of expedition in ironing out the snags I ran into on this project.

I also want to thank all members of the Biomedical Applications Branch and the Bioprocessing Laboratory for their responsiveness and desire to aide me in every aspect of this work.

Last, but not least, I would like to recognize the efforts of our very charming secretary, Nancy Fee, without whose assistance this report could not have been typed.

Preliminary Estimate as to the Feasibility of Fluidizing Spherical Microcarriers

Consider 150×10^{-6} m diameter beads of density 1040 kg/m^3 in a fluid of viscosity $1 \times 10^{-3} \text{ kg/m-s}$ and a density of 1000 kg/m^3 at a "g" of 10 m/s^2 .

Then

$$u_t = g (\rho_p - \rho) D_p^2 / (18\mu) = \frac{10 \text{ m/s}^2 \times (1040 - 1000) \text{ kg/m}^3 \times (150 \times 10^{-6} \text{ m})^2}{18 \times 1 \times 10^{-3} \text{ kg/m-s}} = 5. \times 10^{-4} \text{ m/s}$$

checking $Re = \frac{D_p u_t \rho}{\mu}$

$$= \frac{150 \times 10^{-6} \text{ m} \times 5 \times 10^{-4} \text{ m/s} \times 1000 \text{ kg/m}^3}{1 \times 10^{-3} \text{ kg/m-s}}$$

= .075 supporting the Stokes Law assumption at u_t . Also, the

velocity of incipient fluidization $V_{om} = u_t / 91.7 = 5 \times 10^{-4} \text{ m/s} \div 91.7 =$

$5 \times 10^{-6} \text{ m/s}$ then the maximum shear stress (at u_t) $= \frac{3}{2} \frac{\mu u_t}{R} \sin \theta$

$$= \frac{3 \times (1 \times 10^{-3} \frac{\text{kg}}{\text{m-s}}) \times (5 \times 10^{-4} \text{ m/s}) \sin 90^\circ}{150 \times 10^{-6} \text{ m}}$$

$$= 0.01 \text{ N/m}^2 = 0.1 \text{ dyn/cm}^2, \text{ hence there is}$$

probably no problem with shear in this range.

Now let us analyze shear stress @ V_{om} in a fluidized bed, ref: Unit Operations of Chemical Engineering - McCabe and Smith (1976) 3rd Edition, from Fig. 7-9

$$D_p = 150 \times 10^{-6} \text{ m} \times 39.37 \text{ in/m} = 5.91 \times 10^{-3} \text{ in, say } 0.006''$$

then $\epsilon_m = 0.45$ and $-\frac{\Delta P}{L} = \frac{g}{g_c} (1 - \epsilon_m) (\rho_p - \rho)$

$$= \frac{10 \text{ m/s}^2}{1 \frac{\text{kg m}}{\text{N-s}^2}} (1 - .45) (1040 - 1000) \frac{\text{kg}}{\text{m}^3} = 220 \text{ N/m}^3$$

if $S = X$ -section m^2 and $A =$ surface area of particles m^2 . Assuming

that a shear stress distributed equally over the surface area of the

particles suspends them, and that the pressure drop is due to the viscous

dissipation to the particles then

$$\left(-\frac{\Delta P}{L}\right) LS = \tau A$$

weight of bed = frictional force

consider the volume $V = LS$ then

$$1 - \epsilon_m = \frac{V_p}{V} = \frac{n \pi D_p^3}{6V}$$

where n is the number of spheres then

$$\frac{n}{V} = \frac{6(1 - \epsilon_m)}{\pi D_p^3}$$

and
$$\frac{A}{V} = \frac{n}{V} \times \pi D_p^2 = \frac{6(1 - \epsilon_m) \pi D_p^2}{\pi D_p^3} = \frac{6(1 - \epsilon_m)}{D_p}$$

Since $A = \frac{A}{V} (LS)$

$$\left(-\frac{\Delta P}{L}\right) LS = \tau \frac{[6(1 - \epsilon_m)]}{D_p} LS$$

and
$$\tau = \left(-\frac{\Delta P}{L}\right) \frac{D_p}{6(1 - \epsilon_m)} = 220 \frac{N}{m^3} \times \frac{150 \times 10^{-6} m}{6(1 - .45)}$$

$$= 0.01 N/m^2 = 0.1 \text{ dyn/cm}^2$$

same as $\max \theta u_t$

in fact a range of 5×10^{-6} to 500×10^{-6} m/s seems practicable, now let us consider O_2 supply.

Use H_2O at 300K with a μ of 1 cp $\rho_{O_2} = 1.14$ g/cc re Lange 9th Edition then from eq 22-24 McCabe and Smith

$$D_v = \frac{7.4 \times 10^{-8} (2.6 \times 18)^{1/2} \times 300K}{1 \text{ cp} \times \left(\frac{1 \text{ cc}}{1.14g} \times 32 \frac{g}{\text{mol}}\right)^{.6}}$$

$$= 2.05 \times 10^{-5} \text{ cm}^2/\text{s}$$

$$= 2.05 \times 10^{-5} \text{ cm}^2/\text{s} \times (1m/100 \text{ cm})^2$$

$$= 2.05 \times 10^{-9} \text{ m}^2/\text{s}$$

From Fig. 22-6 McCabe and Smith

$$N'_{RE} = \frac{\sqrt{A_p G}}{\mu}$$

$$= \frac{\pi \times (150 \times 10^{-6} \text{ m})^2 \times 1000 \frac{\text{kg}}{\text{m}^3} \times 5 \times 10^{-6} \text{ m/s}}{1 \times 10^{-3} \frac{\text{kg}}{\text{m-s}}}$$

$$= 1.33 \times 10^{-3} \text{ LOW}$$

consider data for single particle only evaluating the Schmidt number we get

$$S_c = \frac{\mu}{\rho D_v} = \frac{1 \times 10^{-3} \frac{\text{kg}}{\text{m-s}}}{1000 \frac{\text{kg}}{\text{m}^3} \times 2.05 \times 10^{-9} \text{ m}^2/\text{s}} = 488$$

$$Re = \frac{D_p G}{\mu} = \frac{150 \times 10^{-6} \text{ m} \times 5 \times 10^{-6} \text{ m/s} \times 1000 \text{ kg/m}^3}{1 \times 10^{-3} \text{ kg/m-s}} = 7.5 \times 10^{-4}$$

$$Sh = 2 + 6 Re^{1/2} S_c^{1/3} = 2 + 6 (7.5 \times 10^{-4})^{1/2} \times (488)^{1/3} = 2.13$$

taking a conservative stance, we will estimate on the basis of the asymptotic condition of 2.00 over the entire range then

$$\frac{k D_p \bar{M}}{\rho D_v} = 2.0$$

$$\text{and } k = \frac{2.0 \rho D_v}{D_p \bar{M}}$$

$$= \frac{2.00 \times 1000 \text{ kg/m}^3 \times 2.05 \times 10^{-9} \text{ m}^2/\text{s}}{150 \times 10^{-6} \text{ m} \times .018 \text{ kg/mol}}$$

$$= 1.52 \frac{\text{mol}}{\text{m}^2 \cdot \text{s}}$$

$$\text{number of particles in 5 g} = \frac{V_p}{V_u}$$

$$\frac{5 \times 10^{-3} \text{ kg}}{1040 \text{ kg/m}^3 \times \frac{\pi}{6} \times (150 \times 10^{-6} \text{ m})^3 / p} = 2.72 \times 10^6 p$$

area of 5 g of particles

$$= 2.72 \times 10^6 p \times \pi D_p^2 = 2.72 \times 10^6 p \times \pi (150 \times 10^{-6} \text{ m})^2 / p$$

$$= 1.92 \times 10^{-1} \text{ m}^2 \text{ conservatively.}$$

Base absorption on carrier surface.

Using data from Cell Culture and its Application, Acton and Lynn, Academic Press (1977) p. 592 for liver (in vitro) O_2 consumption is (Q)

$$= 6.25 \times 10^{-12} \frac{\text{mol}}{\text{cm}^2 \cdot \text{s}} \times \left(\frac{100 \text{ cm}}{1 \text{ m}}\right)^2 \times 4 \times 1.92 \times 10^{-1} \text{ m}^2$$

$$= 4.81 \times 10^{-8} \text{ mol/s}$$

Assume re above reference $P_{O_2 \text{ in}} = 135T$ $P_{O_2 \text{ (pericellular)}} = 84T$, and that the effective driving force is 10% of the entrance driving force, then $\Delta p = 0.1 (135T - 84T) = 5.1T$, using $H = 5.18 \times 10^4 \text{ atm/mf}$ (Perry 3-98) = $3.94 \times 10^7 \text{ T/mf}$ then

$$\Delta x = \frac{5.1T}{3.94 \times 10^7 T} = 1.30 \times 10^{-7}$$

in this dilution one may assume that mol fraction and mol ratio are nearly equal and

$$N_{O_2} = 1.52 \frac{\text{mol}}{\text{m}^2 \cdot \text{s}} \times 1.92 \times 10^{-1} \text{ m}^2 \times 1.30 \times 10^{-7}$$

$$= 3.79 \times 10^{-8} \text{ mol/s}$$

this is close enough to $4.8 \times 10^{-8} \text{ mol/s}$ to be considered for feasibility; if necessary, compensation can be made later by not inoculating all the beads.

Conservatively estimating that the driving force of the effluent liquid is nearly the average, the $P_{O_2 \text{ (exit)}} = 84T + 5.1T$ say $90T$ then the P_{O_2} loss

in the liquid stream is

$$135T - 90T = 45T$$

and the mol fraction change is

$$45T/3.94 \times 10^7 = 1.14 \times 10^{-6} = \text{mol ratio}$$

then

$$N_{H_2O} = \frac{4.81 \times 10^{-8} \frac{\text{mol } O_2}{s}}{1.14 \times 10^{-6} \frac{\text{mol } O_2}{\text{mol } H_2O}} = 4.22 \times 10^{-2} \frac{\text{mol } H_2O}{s}$$

or

$$Q_{H_2O} = 4.22 \times 10^{-2} \frac{\text{mol } H_2O}{s} \times \frac{.018 \text{ kg } H_2O}{\text{mol } H_2O} \times \frac{1 \text{ m}^3}{1000 \text{ kg } H_2O}$$

$$= 7.60 \times 10^{-7} \text{ m}^3/\text{s}$$

$$= 7.60 \times 10^{-7} \text{ m}^3/\text{s} \times \left(\frac{100 \text{ cm}}{\text{m}}\right)^3 \times \frac{60 \text{ s}}{1 \text{ min}}$$

$$= 45.5 \text{ cm}^3/\text{min} \text{ in range of pump. Velocity in } 2.5 \text{ } \emptyset \text{ cm tube is } Q/S$$

$$\frac{7.60 \times 10^{-7} \text{ m}^3/\text{s}}{\frac{\pi}{4} \times (2.5 \text{ cm})^2 \times \left(\frac{1 \text{ m}}{100 \text{ cm}}\right)^2} = 1.54 \times 10^{-3} \text{ m/s}$$

This is again borderline in nature, we can still try the experiment in the range $5-500 \times 10^{-6}$ m/s. The chances that all the conservative assumptions come to fruition simultaneously is slight, and we still have the option of not innoculating all of the beads. It will require experimentation to resolve the problem.

NOMENCLATURE

<u>Symbol</u>	<u>Definition</u>	<u>SI Units</u>
A	Total area of particles in bed	m^2
A_p	Area of individual particle	m^2
D_p	Particle diameter	m
D_v	Volumetric diffusivity	m^2/s
G	Mass rate	kg/m^2-s
g	Acceleration of gravity	m/s^2
g_c	$= 1 \frac{kg-m}{N-s^2}$	$\frac{kg-m}{N-s^2}$
H	Henry's constant	N/m^2
k	Mass-transfer coefficient	mol/m^2-s
L	Length of bed	m
\bar{M}	Average molecular mass	kg/mol
N_{H_2O}	Molar flow of water	mol/s
N_{O_2}	Molar flow of oxygen	mol/s
P_{O_2}	Partial pressure of oxygen	N/m^2
Q_{H_2O}	Volumetric flow of water	m^3/s
R	Radius of particle	m
Re	Reynolds number	none

ORIGINAL PAGE IS
OF POOR QUALITY

S	Cross-sectional area of empty pipe	m^2
S_c	Schmidt number	none
Sh	Sherwood number	none
u_t	Terminal settling velocity	m/s
V	Volume of bed	m^3
\bar{V}_{om}	Velocity of incipient fluidization	m/s
V_p	Volume occupied by particles	m^3
V_u	Volume of individual sphere	m^3
$-\Delta p$	Pressure drop	N/m^2
Δx	mol fraction difference	none
ϵ_m	Porosity at incipient fluidization velocity	none
μ	Viscosity	$kg/m-s$
Π	3.1416 ---	none
ρ	Density of fluid	kg/m^3
ρ_p	Density of particle	kg/m^3
τ	Shear stress	N/m^2
θ	Latitudinal spherical coordinate	rad

C-4

ORIGINAL PAGE IS
OF POOR QUALITY

Steady-state Radial Diffusion with First-order Irreversible Chemical Reaction
in a Spherical Shell for Dilute in Compressible media

Let us consider:

$$\frac{\partial C_a}{\partial t} + (v \cdot \nabla C_a) = D_a \nabla^2 C_a + R_a \quad (1)$$

then $\frac{\partial C_a}{\partial t} = 0$ because of the steady state constraint, dilution forces

$(v \cdot \nabla C_a)$ to zero and $A \xrightarrow{k} B$ requires $R_a = -kC_a$. Since $C_a = C_a(r)$ only

$$D_a \nabla^2 C_a = \frac{D_a}{r^2} \frac{d}{dr} \left(r^2 \frac{dC_a}{dr} \right) \quad (2)$$

$$\text{and } \frac{D_a}{r^2} \frac{d}{dr} \left(r^2 \frac{dC_a}{dr} \right) - kC_a = 0 \quad (3)$$

$$\text{let } x = \sqrt{\frac{k}{D_a}} r \text{ and } \vartheta = \frac{C_a}{C_{a1}} \quad (4) \ \& \ (5)$$

$$\text{then } \frac{1}{x^2} \frac{d}{dx} \left(x^2 \frac{d\vartheta}{dx} \right) - \vartheta = 0 \quad (6)$$

$$\text{let } \vartheta = f(x)/x \quad (7)$$

$$\text{then } \frac{1}{x^2} \frac{d}{dx} \left(x^2 \frac{d \left(\frac{f(x)}{x} \right)}{dx} \right) - \vartheta = 0 \quad (8)$$

$$\text{and } \frac{1}{x^2} \frac{d}{dx} \left(x^2 \frac{\left(x \frac{df}{dx} \right) - f}{x^2} \right) - \frac{f}{x} = 0 \quad (9)$$

$$\text{or } \frac{1}{x^2} \frac{d}{dx} \left(x \frac{df}{dx} - f \right) - \frac{f}{x} = 0 \quad (10)$$

differentiating

$$\frac{1}{x^2} \left[x \frac{d^2 f}{dx^2} + \frac{df}{dx} - \frac{df}{dx} \right] \frac{f}{x} = 0 \quad (11)$$

$$\text{solving } \frac{d^2 f}{dx^2} - f = 0, \ x \neq 0 \quad (12)$$

~~_____~~

$$\text{and } f = C_1 \exp(x) + C_2 \exp(-x) \quad (13)$$

$$\text{then } \theta = C_1 \frac{\exp(x)}{x} + C_2 \frac{\exp(-x)}{x} \quad (14)$$

BC:1

$$x = X_1, \theta = 1$$

$$\text{then } 1 = \frac{C_1 \exp(X_1)}{X_1} + \frac{C_2 \exp(-X_1)}{X_1} \quad (15)$$

BC:2

$$\text{@ } x = X_2, \frac{d\theta}{dx} = 0$$

implying that no A crosses R_2 boundary

$$\frac{d\theta}{dx} = C_1 \left[\frac{x \exp(x) - \exp(x)}{x^2} \right] + C_2 \left[\frac{-x \exp(-x) - \exp(-x)}{x^2} \right] \quad (16)$$

$$\text{and } 0 = C_1 [X_2 \exp(X_2) - \exp(X_2)] + C_2 [-X_2 \exp(-X_2) - \exp(-X_2)] \quad (17)$$

$$\text{then } 0 = C_1 [\exp(X_2)][X_2 - 1] - C_2 [\exp(-X_2)][X_2 + 1] \quad (18)$$

$$\text{or } C_1 = C_2 \frac{[\exp(-X_2)][X_2 + 1]}{[\exp(X_2)][X_2 - 1]} \quad (19)$$

$$C_1 = \frac{C_2}{\exp(2X_2)} \left(\frac{X_2 + 1}{X_2 - 1} \right) \quad (20)$$

substituting into (15)

$$1 = \frac{C_2}{\exp(2X_2)} \left(\frac{X_2 + 1}{X_2 - 1} \right) \frac{\exp(X_1)}{X_1} + \frac{C_2 \exp(-X_1)}{X_1} \quad (21)$$

$$\text{or } 1 = C_2 \left(\frac{(X_2 + 1) \exp(X_1 - 2X_2) + (X_2 - 1) \exp(-X_1)}{(X_2 - 1) X_1} \right) \quad (22)$$

then

$$C_2 = \frac{(x_2-1) x_1}{(x_2+1) \exp(x_1-2x_2) + (x_2-1) \exp(-x_1)} \quad (23)$$

substituting in (20)

$$C_1 = \frac{(x_2-1) x_1}{(x_2+1) \exp(x_1-2x_2) + (x_2-1) \exp(-x_1)} \cdot \left(\frac{x_2+1}{x_2-1}\right) \cdot \frac{1}{\exp(2x_2)} \quad (24)$$

or

$$C_1 = \frac{(x_2+1) x_1}{(x_2+1) \exp(x_1) + (x_2-1) \exp(2x_2-x_1)} \quad (25)$$

Now let us consider C_b ,

$$\frac{D_a}{r^2} \frac{d}{dr} \left(r^2 \frac{dC_a}{dr} \right) - kC_a = 0 \quad (3)$$

$$\frac{D_b}{r^2} \frac{d}{dr} \left(r^2 \frac{dC_b}{dr} \right) + kC_a = 0 \quad (26)$$

Since $A \rightarrow B$

$$\text{then } - \frac{D_a}{r^2} \frac{d}{dr} \left(r^2 \frac{dC_a}{dr} \right) = \frac{D_b}{r^2} \frac{d}{dr} \left(r^2 \frac{dC_b}{dr} \right) \quad (27)$$

letting $\rho = D_a/D_b$, $\theta = C_b/C_{a1}$ $x = \sqrt{\frac{k}{D_a}} r$ (28), (29),
and (30)

and multiplying by x^2 we get

$$-\rho \frac{d}{dx} \left(x^2 \frac{d\theta}{dx} \right) \equiv \frac{d}{dx} \left(x^2 \frac{d\theta}{dx} \right) \quad (31)$$

$$-\rho x^2 \frac{d\theta}{dx} = x^2 \frac{d\theta}{dx} + C_3 \quad (32)$$

$$-\rho \frac{d\theta}{dx} = \frac{d\theta}{dx} + \frac{C_3}{x^2} \quad (33)$$

$$-\rho \theta = \theta - \frac{C_3}{x} + C_4 \quad (34)$$

$$\text{BC:1 } x = x_1, \frac{d\theta}{dx} = 0$$

implying that no B crosses the R_1 boundary.

A material balance at steady state then requires that

$$D_a 4\pi R_1^2 \left(\frac{dC_a}{dr} \right) \Big|_{r=R_1} = D_p 4\pi R_2^2 \left(\frac{dC_b}{dr} \right) \Big|_{r=R_2} \quad (35)$$

or

$$\rho x_1^2 \frac{d\theta}{dx} \Big|_{x=x_1} = x_2^2 \left(\frac{d\theta}{dx} \right) \Big|_{x=x_2} \quad (36)$$

$$\begin{aligned} \rho C_1 [x_1 \exp(x_1) - \exp(x_1)] + \rho C_2 [-x_1 \exp(-x_1) - \exp(-x_1)] \\ = \rho x_1^2 \left(\frac{d\theta}{dx} \right) \Big|_{x=x_1} \end{aligned} \quad (37)$$

$$= C_3 \quad (38)$$

$$-\rho\theta = \theta_1 - \frac{C_3}{x_1} + C_4 \quad (39)$$

hence

$$C_4 = \frac{C_3}{x_1} - \theta_1 - \rho \quad (40)$$

The rate of production is then

$$N_{a1} = 4\pi R_1^2 D_a \left(\frac{dC_a}{dr} \right) \Big|_{r=R_1} \quad (41)$$

$$= 4\pi \frac{x_1^2}{\left(\sqrt{\frac{k}{D_a}}\right)^2} D_a C_{a1} \left(\frac{d\theta}{dx} \right) \Big|_{x=x_1} \quad (42)$$

$$= \frac{4\pi x_1^2}{\sqrt{\frac{k}{D_a}}} D_a C_{a1} \left[C_1 \frac{(c_1 \exp x_1 - \exp x_1)}{x_1^2} + C_2 \frac{(-x_1 \exp(-x_1) - \exp(-x_1))}{x_1^2} \right] \quad (43)$$

$$N_{a1} = \frac{4\pi D_a C_{a1}}{\sqrt{\frac{k}{D_a}}} C_1 [x_1 \exp x_1 - \exp x_1] + C_2 [-x_1 \exp(-x_1) - \exp(-x_1)] \quad (44)$$

$$C_1 = \frac{(x_2+1) x_1}{(x_2+1) \exp x_1 + (x_2-1) \exp (2x_2-x_1)} \quad (25) \quad (25)$$

$$C_1 = \frac{(x_2+1) x_1 \exp (-x_1)}{(x_2+1) + (x_2-1) \exp (2x_2-2x_1)} \quad (45)$$

$$C_1 \exp(x_1) [x_1-1] = \frac{[x_2+1] \cdot [x_1-1] x_1}{[x_2+1] + [x_2-1] \exp [2x_2-2x_1]} \quad (46)$$

$$C_2 = \frac{(x_2-1) x_1}{(x_2+1) \exp (x_1-2x_2) + (x_2-1) \exp (-x_1)} \quad (25)$$

$$C_2 \exp(-x_1) [x_1+1] = \frac{(x_1+1) (x_2-1) x_1}{(x_2+1) \exp (2x_1-2x_2) + (x_2-1)} \quad (47)$$

then

$$N_{a_1} = N_a + N_b = N_{b_2}$$

$$= \frac{4\pi D_a C_{a_1}}{\sqrt{\frac{k}{D_a}}} \left\{ \begin{array}{l} \frac{(x_2+1)(x_1-1) x_1}{(x_2+1) + (x_2-1) \exp (2x_2-2x_1)} \\ \frac{(x_1+1) (x_2-1) x_1}{(x_2+1) \exp (2x_1-2x_2) + (x_2-1)} \end{array} \right\} \quad (48)$$

NOMENCLATURE

C_1, C_2, C_3, C_4	Constants of integration
C_a	Concentration of A, mol/L ³
C_{a_1}	C_a @ $r=R_1$
C_b	Concentration of B, mol/L ³
D_a	Volumetric diffusivity of A, L ² /T
D_b	Volumetric diffusivity of B, L ² /T
d	Total differential operator
f	$x\phi$
k	First order rate constant, T ⁻¹
N	Molar flow, mol/T
N_a	Molar flow of A, mol/T
N_{a_1}	N_a @ $r=R_1$
N_b	Molar flow of B, mol/T
N_{b_2}	Molar flow of B @ $r = R_2$
R_a	Generation of A, $\frac{\text{mol}}{\text{L}^3\text{T}}$
R_1	Inside radius of spherical shell
R_2	Outside radius of spherical shell
R	Radius
x	$\sqrt{k/D_a} r$
x_1	$\sqrt{k/D_a} R_1$

ORIGINAL PAGE IS
OF POOR QUALITY

x_2

$$\sqrt{k/D_a} R_2$$

∂

Partial differential operator

∇

"del" operator, L^{-1}

\emptyset

$$C_a/C_{a_1}$$

θ

$$C_b/C_{a_1}$$

θ_1

$$\theta [r = R_1]$$

ρ

$$D_a/D_b$$

π

3.14 ---

ORIGINAL PAGE IS
OF POOR QUALITY

N82 23132

D10

1981 NASA-ASEE Summer Faculty Research Fellowship Program

at

NASA Johnson Space Center

THE TECTONICS OF ANORTHOSITE MASSIFS

Faculty Fellow: Carl K. Seyfert
Department of Geosciences
Buffalo State University College
Buffalo, NY 14222

Supervisor: Dr. Jeffery Warner
Geology Branch
Planetary and Earth Sciences Division
NASA Johnson Space Center
Houston, TX

Abstract:

I propose that anorthosite massifs developed approximately 1.4 to 1.5 billion years ago along an arch which developed parallel to a zone of continental separation as a block which included North America, Europe, and probably Asia separated from a block which included parts of South America, Africa, India, and Australia. Anorthosite massifs also formed at the same time along a belt which runs through the continents which comprise Gondwanaland (South America, Africa, India, Australia, and Antarctica). I propose that this was a zone of continental separation which subsequently became a zone of continental collision about 1.2 billion years ago. The northern anorthosite belt also parallels an orogenic belt which was active between 1.8 and 1.7 billion years ago. Perhaps heat generated during this mountain building period helped in the formation of the anorthosites.

There are several other times in earth history when mountain building was followed by continental rifting, but no large anorthosite massifs developed during these times. The formation of anorthosite massifs may have required an additional input of heat from an outside source. It has been suggested that the moon made a close approach to the earth 1.4 to 1.5 billion years ago. This approach may have been the time of capture of the moon by the earth, or more likely represented the time when the moon's orbit changed from retrograde to prograde. Tidal heating of the solid earth by the moon when it was within a few tens of earth radii of the earth may have provided additional heat required for the formation of anorthosite massifs.

**ORIGINAL PAGE IS
OF POOR QUALITY**

Introduction:

An anorthosite massif is a large, intrusive body consisting of more than 90% plagioclase feldspar, and which generally has the following properties:

- a) It has few if any compositional layers (Wiebe, 1978).
- b) The plagioclase ranges from An₄₅ to An₆₅ (Anderson, 1968).
- c) Their size ranges from less than 100 sq. km to 30,000 sq. km (Anderson, 1968).

This paper will first describe the tectonic environment of emplacement of the massifs, then discuss the possible relationship of the emplacement of anorthosite massifs to the capture of the moon, and finally will describe my current thinking on the formation of anorthosite massifs.

Tectonics of Emplacement of Anorthosite Massifs:

A number of different tectonic environments have been proposed for the emplacement of massifs. These include:

- a) Adjacent to subduction zones (Emslie, 1973; Dewey and Burke, 1973)
- b) Along an orogenic belt following the peak of metamorphism and deformation (Bridgwater and Windley, 1973)
- c) Along an aborted (Morse, 1981) or incipient (Berg, 1977; Wynne-Edwards, 1976; Bridgwater et al., 1974) continental rift.
- d) Parallel to a zone of continental separation prior to the actual separation (Emslie, 1978)
- e) Parallel to a zone of continental separation during the actual separation

Some of the difficulties with the above environments for the emplacement of anorthosites are:

- a) There is no evidence for the presence of a subduction zone during the time of emplacement of most anorthosites (approximately 1.4 billion years ago as will be discussed later). Furthermore, some anorthosites (such as the Labrieville, Quebec anorthosite) are much too K-rich, have too high a TiO₂ content, and have too high an Fe/Mg ratio to be related to calc-alkaline magmatism (Emslie, 1978).
- b) Anorthosites occur in two great belts when they are plotted on a Pangaea-type reconstruction of the continents (Herz, 1969). The more northerly of these belts runs from Southern California through the Adirondacks, southeastern Ontario, Quebec, and Labrador to Norway and the Ukraine of southern Russia (Fig. 1). This belt parallels a 1.7 to 1.8 billion year old orogenic belt (the Penokean fold belt and its equivalents) (Fig. 2). However, there is a

ORIGINAL PAGE IS
OF POOR QUALITY

large area between the Superior and Slave provinces and within the Labrador trough (both part of the Churchill Province) which was also part of a 1.7 to 1.8 billion year orogenic belt, and this area contains no anorthosite or related rocks. This indicates that while a recently active orogenic belt may have assisted in the formation of anorthosites, there must have been some additional factor or factors controlling the emplacement of the anorthosite massifs.

- c) An aulacogen is one type of aborted or incipient continental rift. Aulacogens generally intersect a continental margin at a high angle, usually at a plume. Igneous activity along aulacogens, therefore, is generally along linear belts which may parallel each other, but which would not parallel the edge of the continent. However, anorthosite massifs appear to be in a belt which parallels the edge of the continent formed by separation of North America and Europe from Gondwanaland (discussed below). Anorthosite massifs could have formed parallel to a zone along which a continent attempted to rift, but as will be discussed below, rifting did occur either during or just after emplacement of the anorthosites.
- d) and e) It is very difficult to determine which of these might be correct, but I believe that one of the two represent the environment in which anorthosite massifs were emplaced.

A comparison of apparent polar wander (APW) paths for North America and Gondwanaland recalculated for a Pangaea-type reconstruction of the continents (Fig. 3) indicates that North America and Gondwanaland were in contact with each other 1.8 billion years ago and began to separate between 1.7 and 1.4 billion years ago (Seyfert and Sirkin, 1979). The exact time of the beginning of separation is not possible to determine from paleomagnetic studies because of the scarcity of paleomagnetic data in that time interval.

When two continents begin to separate from each other, sediments are deposited in geoclinal basins bordering those continents. The sedimentary rocks of the Grand Canyon Sequence may have been deposited in such an environment when North America and Gondwanaland began to separate. The oldest sedimentary rocks in the Grand Canyon Sequence are approximately 1.4 billion years old (Seyfert and Sirkin, 1979). This date probably provides a minimum date for the beginning of separation of North America and Gondwanaland.

This date is consistent with paleomagnetic data, and it is close to that of most anorthosites (Table 1). Thus, it is evident that the time of separation of the continents approximates the time of emplacement of most anorthosites. It is not possible at this time, however, to determine if the anorthosites were emplaced just prior to or during rifting apart of the continents.

Support for the idea that the separation of North America from Gondwanaland was associated with the emplacement of anorthosite massifs comes from the observation that the northern belt of anorthosites parallels the zone along which these continents were presumed to have separated. Direct evidence of the location of the zone along which the continents separated is very difficult to obtain. However, because the continents were joined together again following their separation, the zone of collision produced by their joining will approximately parallel the zone along which the continents separated. The boundary between rocks deformed during the Grenville Orogeny as the continents collided (Seyfert, 1980) is located along the northwestern boundary of the Grenville Province (Fig. 4), which is more or less coincident with the Grenville Front. The northern belt of anorthosite massifs approximately parallels this boundary and its continuation in Europe (Fig. 5).

Radiometric Dating of Anorthosite Massifs:

Radiometric dates on anorthosite massifs range from 540 million years to 1650 million years (Table 1). However, it is quite likely that a number of these dates do not reflect the actual time of emplacement of the anorthosites. A large number of the anorthosite massifs are located within the Grenville Province, a broad band of rocks which was metamorphosed and deformed about 1200 million years ago (Seyfert, 1980). These anorthosites were apparently affected by this deformation and were recrystallized and granulated in some areas. Other areas, particularly within the larger bodies, show little if any effects of the deformation. It is possible that the anorthosites were emplaced during deformation (see e.g. Michot, 1968), but I believe that it is more likely that the anorthosites were emplaced prior to the Grenville Orogeny (Emslie, 1978; Bridgewater and Windley, 1973; Stockwell, 1964). Well dated anorthosites in the Nain Structural Province have dates averaging approximately 1430 million years, but anorthosites which appear to be part of the same belt, but which are located in the Grenville Province give mostly younger dates, averaging about 1100 million years. It seems likely that these dates are not the time of initial emplacement of the anorthosites, but represent a time of later heating. However, the date on the Mealy

Mountains Anorthosite in Labrador (this anorthosite is located within the Grenville Province) is older than the other anorthosites within the Grenville Province, and it is older than the other massifs outside of the Grenville Province as well (Table 1). Its date of 1650 could be older than its emplacement, but it is difficult to understand how this might occur. Possibly zircon which was used in the dating was inherited from its wall rock. Anorthosites and related rocks are notoriously hard to date by the whole-rock rubidium-strontium method, so the 1650 million year old date by that method on the Mealy Mountains Anorthosite might not be too reliable. It is interesting to note that the anorthosites of the Larimie Range give a 1430 ± 20 million year old date using the uranium-lead method on zircon (which agrees with other dates on associated rocks - see Table 1), but the rubidium-strontium whole-rock dates on the monzonites range from 1290 to 1950 million years (Table 1). Radiometric dates on European anorthosites from Norway may well have been affected by an orogenic event correlative with the Grenville Orogeny (Table 1). However, anorthosites in areas not affected by Grenville deformation (such as the Nain region, Larimie Range, and Chilka Lake India) all seem to give consistent dates of 1430 million years. It is my belief that anorthosite massifs were all emplaced within a very narrow time range at about 1430 million years. Even if they were emplaced over a broader time range, say 1200 to 1650 million years, it is still very difficult to understand why anorthosites massifs were not emplaced before or after that time, a time restricted to the Middle Proterozoic.

The Southern Anorthosite Belt:

A belt of anorthosites in the Southern Hemisphere extends from southern South America across southern Africa, Antarctica, Madagascar, and India to central Australia (Fig. 6) on a Pangaea reconstruction of the continents. If, as it appears likely, the anorthosite belt in the Northern Hemisphere formed as a result of continental separation which was followed by a continental collision, the anorthosite belt in the Southern Hemisphere may have had a similar origin. I propose that a zone of separation of the continents ran through the southern anorthosite belt, and that the separation occurred approximately 1430 million years ago, at the same time as the anorthosite belt in the Northern Hemisphere. This age agrees well with the date on the Chilka Lake Anorthosite (Table 1) of 1404 million years.

Closure of the ocean formed as a result of this continental separation occurred approximately 1100 million to 1200 million years ago judging by radiometric dates on metamorphic rocks along this belt (Craddock, Geologic Map of Antarctica; Seyfert and Sirkin, 1979). Presumably, a mountain belt formed along this zone at about

**ORIGINAL PAGE IS
OF POOR QUALITY**

the same time as the Grenville Orogeny in the Northern Hemisphere. It should be pointed out, however, that there is not sufficient paleomagnetic data from the southern continents to test the hypothesis of an opening and closing of an ocean within Gondwana and during the Middle Proterozoic 1430 to about 1150 million years ago.

Relation of Anorthosite Massifs to Lunar Capture:

Herz (1969) proposed that the emplacement of anorthosite massifs represented a unique event in geologic history. Radiometric dating of anorthosites since the publication of his paper in 1969 (Table 1) has lent further support to his proposal. If, as has been suggested by Emslie (1978), anorthosite massifs were emplaced in association with a rifting apart of two continents, why then are anorthosite massifs so restricted in time? Why were they only emplaced during the Middle Proterozoic during a time interval lasting at most 450 million years (10% of geologic time).

Herz (1969) suggested that the emplacement of anorthosites represented a unique cataclismic event or a thermal event restricted to the Precambrian. He proposed that the birth of the earth-moon system or a series of meteorite impacts may have triggered the rise of anorthosites. I propose that the unique event was caused not by the birth of the earth-moon system, but a close approach of the earth and moon as the moon's orbit changed from retrograde to prograde.

Gerstenkorn (1955), based on a careful study of the moon's present orbit and calculating what its past orbit must have been, proposed that the moon was once orbiting the earth in a retrograde orbit. Such an orbit would require that the moon spiral into the earth as a consequence of tidal interaction between the earth and moon. Gerstenkorn calculated that the moon's orbital plane increased in inclination as it approached the earth and that its orbital plane became inverted after becoming vertical with respect to the ecliptic. This "flip" of the moon's orbital plane would result in a change of the moon's orbit from retrograde to prograde.

Goldreich (1968) showed some flaws in Gerstenkorn's original calculations, and Gerstenkorn (1968; 1969) made new calculations indicating the possibility of capture from a polar or even a prograde orbit with very small perigee. Singer (1968; 1970) made similar calculations with similar results. However, Alfven and Arrhenius (1976) state that "formal objections to Gerstenkorn's original model do not necessarily mean that this is less likely to describe the general type of evolution ." (p. 461)

Alfven and Arrhenius (1976) predict that if a spin-orbit resonance is established

ORIGINAL PAGE IS
OF POOR QUALITY

between the earth and moon, the moon will not reach the Roche limit, which might have resulted in the disruption of the moon. Rather, a spin-orbit resonance would result in a minimum earth-moon distance of about 7 earth radii (Alfven and Arrhenius, 1976, p. 463).

The effects of such a close approach between the earth and moon would almost certainly be evident on the earth. Some of the effects expected would be an increase in igneous activity (due to tidal heating of the solid earth) and a strong increase in ocean tides. The generation of anorthosite massifs may have resulted from tidal heating by the moon during its close approach to the earth. There are a number of other examples of igneous activity at approximately the same time as the emplacement of anorthosite massifs. Many large charnockites were intruded at about this same time, and these show evidence of having been emplaced into areas with an unusually high geothermal gradient (Saxena, 1977). This high geothermal gradient may have been produced, at least in part, by the close approach of the earth and moon. Furthermore, a very large number of large granite bodies were intruded in a belt extending from Arizona to western Ohio (Herz, 1969; Seyfert and Sirkin, 1979). What is remarkable about these granitic rocks is that they were emplaced into an anorogenic environment (Silver et al, 1977). Almost all batholithic size granitic bodies are emplaced in orogenic environments, either at or near a plate margin, or where two continents collide. In at least one area, the St. Francois Mountains of central Missouri, very large volumes of rhyolite were extruded at the same time (1400 to 1500 million years ago) as the anorogenic granites and anorthosites were emplaced.

There are no well-dated sedimentary sequences known anywhere in the world to have been deposited between 1400 and 1500 million years ago (Seyfert and Sirkin, 1979). It is possible that very large tides produced by the moon during its close approach may have prevented accumulation of sedimentary rocks on the continents. It may be that most sediment was simply swept off the continents and deposited in the deep ocean basins. It is interesting to note that there is fairly good evidence for unusually high tides during the Cambrian. In northwestern Wyoming, there are large thicknesses of flat-pebble (limestone) conglomerates in Middle to Late Cambrian deposits. These may have been produced as a result of high tides churning up recently deposited limestone beds.

I may be worth mentioning here that there is excellent evidence that large moons in the solar system have probably been captured. The evidence comes from the retrograde rotation of a number of moons of the giant planets. In the solar system, there are six retrograde satellites (Alfven and Arrhenius, 1976).

These include Jupiter 8, Jupiter 9, Jupiter 11, Jupiter 12, Phoebe, and Triton. Triton has a mass of 135×10^{24} grams, almost twice the mass of the earth's moon. However, it should be pointed out that Neptune, about which Triton orbits, is much larger than the earth, and therefore it would be much easier for Neptune to have captured Triton than the earth to have captured its moon.

Formation of Anorthosites:

I have done a considerable amount of reading on the origin of anorthosites in the hope that their origin might be of help in the understanding of what sort of heating the moon might have produced on the earth during the close approach of the earth and moon. In this regard, I have been only partially successful. It soon became evident that there was not the slightest bit of consensus on the origin of anorthosite in anorthosite massifs. There were at least 10 different groups of theories on their origin as of 1968 (Fig. 7).

I will not review here the various theories for the origin of anorthosite massifs, but will refer to the publication of the papers presented at the Second Annual George H. Hudson Symposium held in Plattsburg, New York in 1966 (Isachsen, 1968) and to several recent reviews (Duchesne and Demaiffe, 1978; Emslie, 1978; Ashwal and Seifert, 1980; Morse, 1981).

To give some idea of the various possible origins for anorthosites, I have prepared a list of "Problems associated with anorthosites." (Table 2). The number of possible combinations of factors which make up the formation of anorthosites is very large. I will not attempt to describe or discuss the various possibilities, but I would like to present my current thinking on the origin of anorthosite massifs. I have found that it corresponds very closely to the ideas of Buddington (1968). Some of the observations supporting my views are given in Table 3.

I believe that anorthosite massifs originated by partial melting of the lower crust. This view contrasts with the views of most of the geologists working on anorthosites, but it is in agreement with Buddington's (1968) views. In support of this origin, I would point out that the Sr^{87}/Sr^{86} ratios for anorthosite massifs are in the range from .703 to .706 (See e.g. Heath and Fairbairn, 1968). These values are higher than one would expect for mantle rocks of chondritic composition evolving for approximately 3 billion years (the age of the earth minus the age of anorthosites). This led Ashwal and Seifert (1980) to suggest crustal contamination of magma of mantle origin as a way of increasing the Sr^{87}/Sr^{86} ratios. However, a major amount of crustal contamination would have to have been involved. The initial Sr^{87}/Sr^{86} ratios of rocks from the upper crust would probably have been higher than

ORIGINAL PAGE IS
OF POOR QUALITY

anorthosite massifs, but it is quite likely that the lower crust had a lower initial ratio. One problem with a crustal origin for anorthosite massifs is that the Rb content of most anorthosites is very low, too low in fact to have produced an initial ratio of .703 to .706. The low Rb content might be explained by removal of a granitic component from the lower crust before formation of the anorthosites. The granitic component must have remained in the lower crust long enough to have increased the initial strontium ratio to its observed value.

The Marcy Anorthosite has an ϵ Nd of +5 (Ashwall and Wooden, unpublished manuscript). A positive ϵ Nd indicates that the anorthosite was derived from a source which was depleted in light rare earth elements (DePaolo, 1981). Therefore, the Nd data is consistent with the model suggested here of depletion of the lower crust in a granitic component, a component which would have been relatively enriched in light rare earths. It should be pointed out that because the density of the lower mantle is higher than that of the upper crust, it is generally assumed that the lower mantle is richer in iron and magnesium than the upper crust. It is quite likely that it got that way as a result of the removal of a granitic component. In fact, the intrusion of granitic batholiths into orogenic belts is a very common event, and it is likely that these granites were derived from the lower crust by partial melting. It should be pointed out, however, that the initial $\text{Sr}^{87}/\text{Sr}^{86}$ ratios of many granitic rocks indicates that they were not formed by the partial melting of old crust, but the ratios are compatible with partial melting of sedimentary and volcanic rocks which were subducted shortly before partial melting of these deposits. The granitic rocks of the Klamath Mountains and the Sierra Nevada Mountains in California are excellent examples of granites formed in this way. Presumably, the lower crust beneath these granitic rocks has been depleted in a granitic component and has been enriched in iron and magnesium. It is also likely that the lower crust would be enriched in calcium and aluminum if the original crust (before partial melting) was rich in plagioclase, such as would be the case if the protolith were largely composed of metamorphosed graywackes.

Crystals of plagioclase in many anorthosite massifs are bent and broken. Anorthosites in the Grenville Province may have been brecciated and sheared during the Grenville Orogeny, but this characteristic texture is also present in unmetamorphosed anorthosites. It is quite likely that the plagioclase crystals were bent and broken in part during emplacement of the anorthosites. This suggests that the magma was largely crystalline during its emplacement. The magma may have been a crystal mush, a widely accepted model for anorthositic magmas. Separation of crystals from liquid magma might occur during rise of a crystal mush by a process of flow dif-

ferentiation (Bhattacharji and Smith, 1964). It is also likely that considerable fractionation by floatation of plagioclase crystals occurred within the lower crust prior to rise of the anorthositic magma. At pressures of the lower crust (approximately 10 to 12 kilobars for the crust in which the anorthosite massifs were generated), plagioclase of composition An_{50} is considerably less dense than a gabbroic liquid. At a pressure of 10 kb, plagioclase of An_{50} has a density of about 2.61 g/cc, while at the same pressure, a basaltic melt has a density of about 2.74 g/cc (Kushiro, 1980). Many anorthosites have a margin (often chilled) of gabbroic or gabbroic anorthosite composition. These rocks may represent the melt phase associated with a rising anorthositic diapir composed largely of plagioclase crystals. Gabbroic intrusions associated with anorthosites may also represent liquids squeezed out or separated by flow differentiation from a rising anorthositic diapir. Most workers now believe that the associated granitic and syenitic rocks commonly found with anorthosites are not genetically related to the anorthosites, but rather were generated by partial melting of crustal rocks as a result of heating by the anorthositic magmas (see e.g. Buddington, 1968).

Summary and Conclusions:

I believe that anorthosites form within the lower crust by partial melting of rocks previously depleted in a granitic component. Heating of the lower crust sufficient to melt such depleted rocks is rather uncommon in earth history, certainly on the scale represented by anorthosite massifs. A unique heating event was needed, and this event was a close approach between the earth and moon. This close approach produced tidally induced heating, which may have been concentrated at the crust-mantle boundary (Ashwal, personal communication).

Rifting of North America and Europe from Gondwanaland may have somehow assisted in either the melting or emplacement of the anorthosite massifs. An additional factor may have been heat generated during the orogenic event 1700 to 1800 million years ago, assuming that it takes more than about 300 million years for the heat from an orogenic event to be completely dissipated.

The magma generated in the lower crust was either an anorthositic gabbro or a gabbroic anorthosite. Fractionation by floatation of plagioclase crystals while the magma was in the lower crust produced a magma of gabbroic anorthosite or anorthosite composition. The magma was largely crystalline as it began to rise, and there was additional fractionation by flow differentiation on the way up. When the anorthosite or gabbroic anorthosite reached the site of emplacement, it was largely crystalline, but it was surrounded by a more mafic border which was largely liquid on emplacement.

References Cited

- Alfvén, H and G. Arrhenius, 1976, Evolution of the Solar System: NASA SP-345, 599 p.
- Anderson, A.T., 1968, Massif-type anorthosite: A widespread Precambrian igneous rock, in Y.U. Isachsen, ed., Origin of Anorthosite and Related Rocks: Memoir 18, New York State Museum and Science Service, Albany, N.Y., p. 47-55.
- Ashwal, L.D., and J.L. Wooden, unpublished manuscript, Age and origin of the Marcy Massif, Adirondack Mountains, New York: Evidence from Nd and Sr Isotopes.
- Ashwal, L.D. and K.E. Seifert, 1980, Rare-earth-element geochemistry of anorthosite and related rocks from the Adirondack New York, and other massif-type complexes: Geol. Soc. Amer. Bull., Part II, v. 91, p. 659-684.
- Ashwal, L.D., J.L. Wooden, and C.-Y. Shih, 1980, Nd and Sr isotope geochemistry of the Marcy Massif, Adirondacks, New York Geol. Soc. Amer. Abs. with Programs, v. 12, p. 380.
- Berg, J.H., 1977, Regional geobarometry in contact aureoles of the anorthositic Nain Complex, Labrador: Jour. Petrology, v. 18, Part 3, p. 399-430.
- Bhattacharji, S. and C.H. Smith, 1964, Flowage differentiation: Science, v. 145, p. 150-153.

Bridgwater, D. and B.F. Windley, 1973, Anorthosites, post-orogenic granites, acid volcanic rocks and crustal development in the North Atlantic shield during the Mid-Proterozoic: Spec. Publ. Geol. Soc. S. Afr. 3, p. 307-317.

Bridgwater, D., J. Sutton, and J. Watterson, 1974, Crustal Downfolding associated with igneous activity: Tectonophysics, v. 21, p. 57-77.

Buddington, A.F., 1968, Adirondack anorthositic series, in Y.W. Isachsen ed., Origin of Anorthosite and Related Rocks: Memoir 18, New York State Museum and Science Service, Albany, N.Y., p. 215-231.

DePaolo, D.J., 1981, Nd isotopic studies: Some new perspectives on earth structure and evolution: EOS, v. 62, p. 137-140.

Dewey, J.F. and K. Burke, 1973, Tibetan, Variscan, and Precambrian basement reactivation: Products of continental collision: J. Geol., v. 81, p. 683-692.

de Waard, D., J.C. Duchesne, and J. Michot, 1974, Anorthosites and their environment: Géologie des Domaines Cristallins, Centenaire de la Société Géologique de Belgique, Liège, p. 323-346.

Duchesne, J.C., and D. Demaiffe, 1978, Trace elements and anorthosite genesis: Earth Planet. Sci. Lett., v. 38, p. 249-272

Emslie, R.F., 1978, Anorthosite massifs, rapakivi granites, and late Proterozoic rifting of North America: Precambrian Res., v. 7, p. 61-98.

Emslie, R.F., 1973, Some chemical characteristics of anorthosite ^{suites} and their significance: Can. J. Earth Sci., v. 10, p. 57-69

Fountain, J.C., D.S. Hodge, and F.A. Hills, 1981, Geochemistry and petrogenesis of the Laramie anorthosite complex, Wyoming: Lithos, v. 14, p. 113 -

Gerstenkorn, ^{H.} 1955, Gezeitenreibung beim Zweikörperproblem: Z. Astrophys., v. 36, p. 245 -

Goldreich, P., 1968, On the controversy over the effect of tidal friction upon the history of the earth-moon system. A reply to comments by H. Gerstenkorn, Icarus, v. 9, p. 391 -

Heath, S.A., and H.W. Fairbairn, 1968, Sr^{87}/Sr^{86} ratios in anorthosites and some associated rocks, in Y.W. Isachsen, ed., Origin of Anorthosite and Related Rocks: Memoir 18, New York State Museum and Science Service, Albany, N.Y., p. 99-110.

Herz, N., 1964, Anorthosite belts, continental drift, and the anorthosite event: Science, v. 164, p. 944-947.

Isachsen, Y.W., ed., 1968, Origin of Anorthosites and Related Rocks: Memoir 18, New York State Museum and Science Service, Albany, N.Y., 466 p.

Kushiro, I., 1980, Viscosity, density, and structure of silicate melts at high pressures, and their theoretical applications, in R.B. Hargraves, ed., Physics of Magmatic Processes: Princeton University Press, Princeton, N.J., p. 93-120.

Morse, S.A., unpublished manuscript, ^{1981,} A partisan review of anorthosites.

Sarkar, A., L. Bhanumathi, and M.N. Balasubrahmanyam, 1981, Petrology, geochemistry, and geochronology of the Chilka Lake igneous complex, Orissa state, India: Lithos, v. 14, p. 93-111.

Saxena, S.K., 1977, The charnockite geotherm: Science: v. 198, p. 614-617.

Seyfert, C.K., 1980, Paleomagnetic evidence in support of a Middle Proterozoic (Helikian) collision between North America and Gondwanaland as a cause of the metamorphism in the Adirondacks: Summary: Geol. Soc. Amer. Bull., v. 91, p. 118-120.

Silver, L.T., and S.B. Lammers, 1966, Geol. Soc. Amer. Spec. Paper 87, p. 156.

Silver, L.T., 1968, A geochronological investigation of the anorthosite complex, Adirondacks Mountains, New York, in Y.W. Isachsen, ed., Origin of Anorthosite and Related Rocks: Memoir 18, New York State Museum and Science Service, Albany, N.Y., p. 233-251.

Spooner, C.M., and H.W. Fairbairn, 1970, Strontium 87/Strontium 86 initial ratios in pyroxene granulite terrains: Jour. Geophys. Res., v. 75, p. 6706-6713.

Stockwell, C.H., 1964, Forth report on structural provinces, orogenies, and time-classification of rocks of the Canadian Precambrian shield: Geol. Surv. Can. Prof. Pap. 64-17, p. 1-21.

Wiebe, R.A., 1978, Anorthosite and associated plutons, southern Nain complex, Labrador: Can. J. Earth Sci., v. 15, p. 1326-1344.

ORIGINAL PAGE IS
OF POOR QUALITY

Wynne-Edwards, H.R., 1976, Proterozoic ensialic orogenesis:
The millipede model of ductile plate tectonics: Amer.
Jour. Sci., v. 276, p. 927-953.

FIGURE CAPTIONS

Figure 1 - Anorthosites in the Northern Hemisphere. From Herz (1969).

Figure 2 - Anorthosites, rapakivi granites, and related rocks in the Northern Hemisphere. From Emslie (1973).

Figure 3 - Apparent polar wander paths for North America and Gondwanaland recalculated for a Pangaea reconstruction of the continents. From Seyfert and Sirkin (1979).

Figure 4 - Geologic Provinces for Ancestral North America. From Seyfert and Sirkin (1979).

Figure 5 - Reconstruction of the continents showing that the belt of anorthosite massifs parallels the Grenville Front and its equivalent in Europe. The suture along which the continents of North America and Europe were joined to Gondwanaland 1.2 billion years ago is assumed to parallel this front. It is further assumed that this suture is essentially coincident with the zone along which the continents of North America and Europe separated from Gondwanaland about 1.4 billion years ago. After Emslie (1973).

Figure 6 - Reconstruction of Gondwanaland showing the Middle Proterozoic anorthosite massifs along with the location of a proposed suture formed when the northern half of Gondwanaland joined (collided with) the southern half of Gondwanaland 1.2 billion years ago. It is assumed that this suture is essentially coincident with the zone along which northern and southern Gondwanaland separated from each other about 1.4 billion years ago. After Seyfert and Sirkin (1979).

Figure 7 - A summary of some of the principal theories proposed for the formation of anorthosite massifs. From Anderson (1968).

ORIGINAL PAGE IS
OF POOR QUALITY

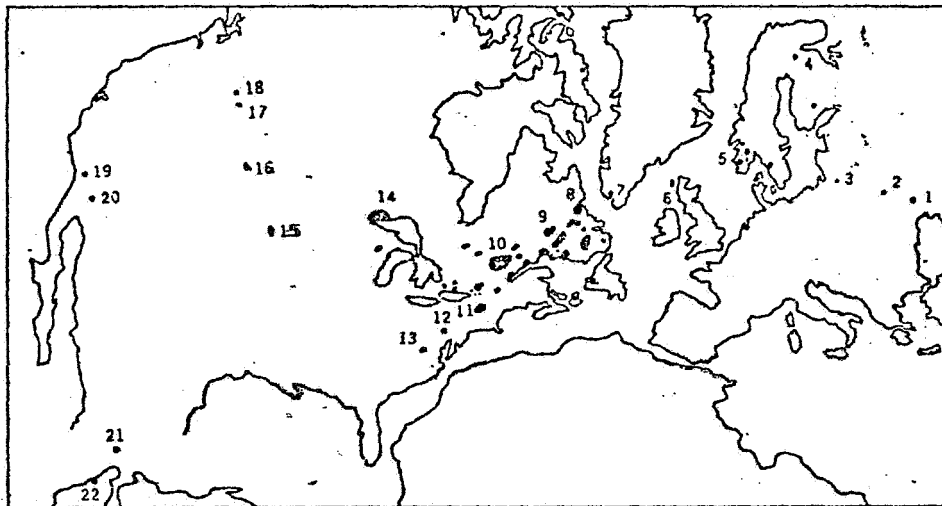
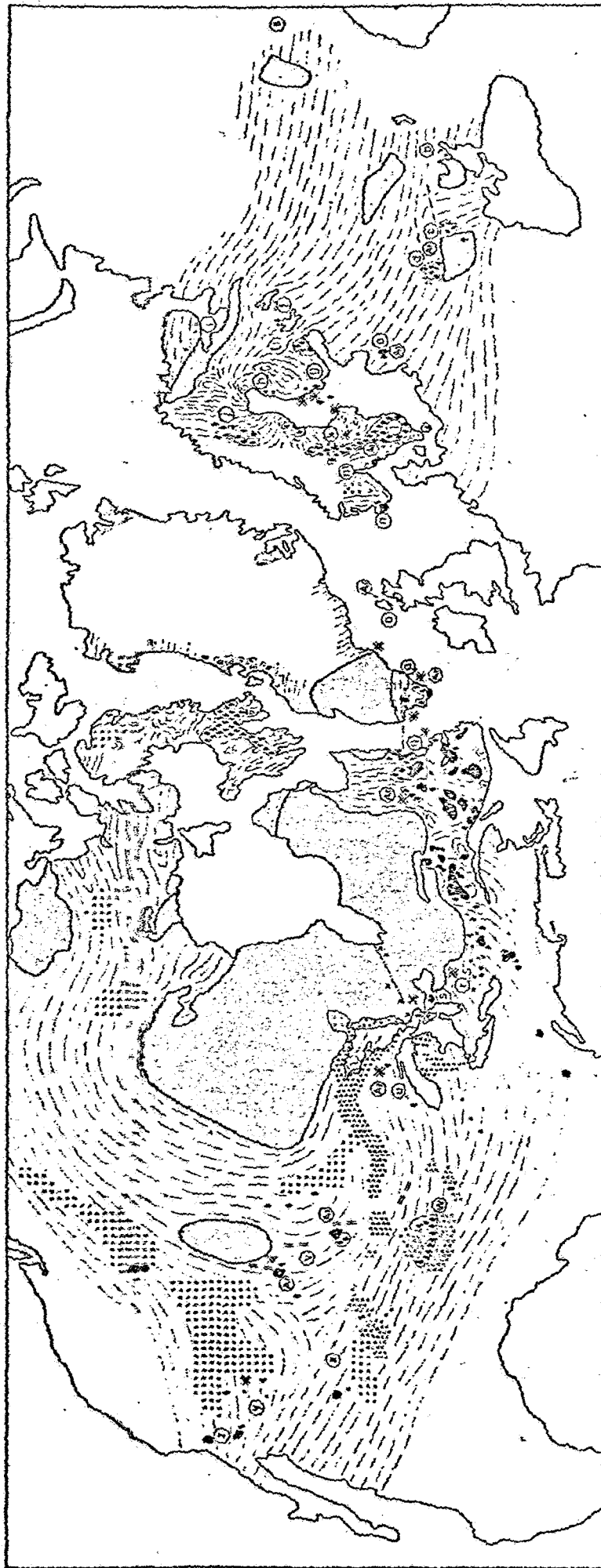


Fig. 1. Anorthosites of the Northern Hemisphere plotted on the North Atlantic reconstruction of Bullard and others (2). Anorthosites referred to in the text: 1, Korosten, Ukraine; 2, Korsun-Novomyrgorod, Ukraine; 3, Suwalki, Poland; 4, Utsjoki, Finland; 5, southern Norway; 6, South Harris, Outer Hebrides; 7, Gardar, Greenland; 8, Kiglapait-Nain, Labrador; 9, Mechikamau, Labrador; 10, Lac St. Jean, Quebec; 11, Adirondacks, New York; 12, Honeybrook, Pennsylvania; 13, Roseland, Virginia; 14, Duluth Minnesota; 15, Cambridge Arch, Nebraska; 16, Laramie Range, Wyoming; 17, Bitterroot Range, Montana; 18, Boehls Butte, St. Joe, Idaho; 19, San Gabriel Range, California; 20, Orocoopia Range, California; 21, Pluma Hidalgo, Oaxaca, Mexico; and 22, Sierra de Santa Marta, Colombia.

Figure 1.

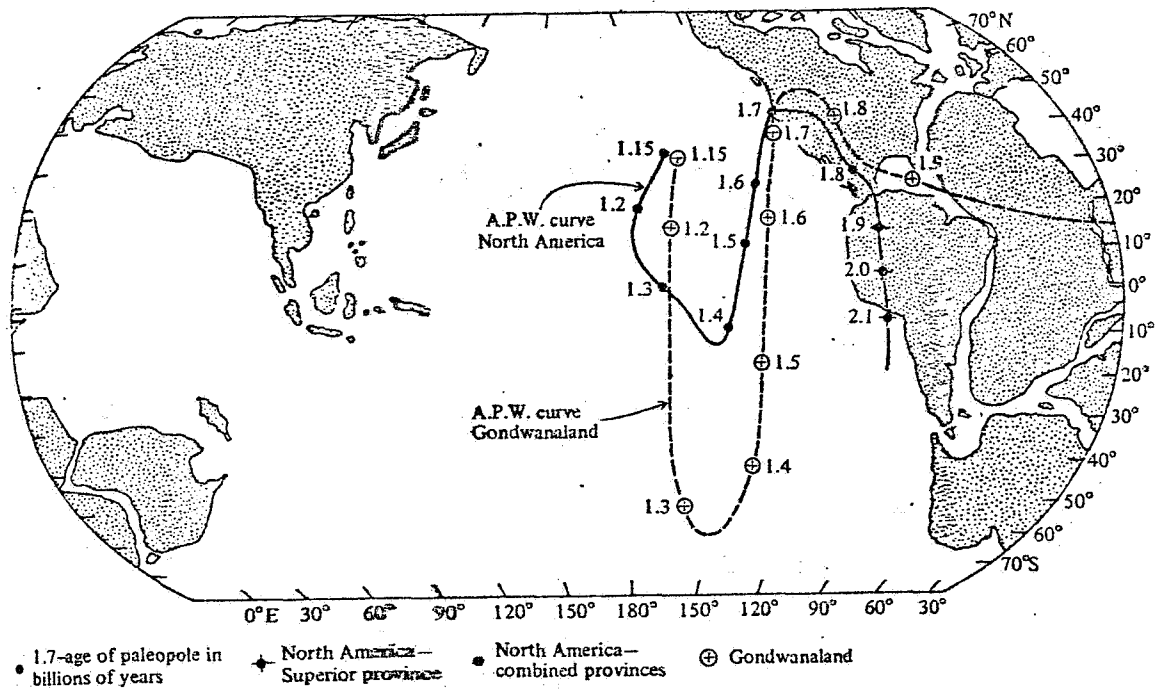


- Archaean dykes unaffected by Proterozoic metamorphism
- Minimum area affected by Proterozoic thermal activity 1500-2000 m.y. ago
- Anorthites and related basic intrusions
- ▨ Repetitive granites, quartz syenites and related granitic or intermediate intrusions
- ▧ Acid volcanics estimated 1000-1700 m.y. ago
- ▩ Sedimentary sequences (with some volcanics) deposited 1000-1700 m.y. ago
- ▦ Basic intrusives and associated sediments deposited 1000-1200 m.y. ago
- ▧ Alkali intrusives emplaced 1000-1700 m.y. ago
- ⊙ Archaean white K/Al or Rb/Sr mineral ages are markedly discordant to Rb/Sr whole-rock isochron ages
- ⊛ Dykes
- ⊞ Cataclasis
- ⊟ Faults
- ⊠ See text

Figure 2.

ORIGINAL PAGE IS
OF POOR QUALITY

FIGURE 9.4 Apparent polar wander (A.P.W.) curves for North America, Gondwanaland, and Europe are recalculated for a Pangaea reconstruction of the continents by moving these continents along with their A.P.W. curves to the positions which they occupied prior to the beginning of separation of the continents during the Mesozoic: (a) Comparison of the recalculated A.P.W. curves based on samples 1.15 to 0.2 billion years old from North America and Gondwanaland indicates that these continents were together (or at least were not widely separated) 1.15 billion years ago, separated soon thereafter, and were rejoined about 400 million years ago. (b) Comparison of the recalculated A.P.W. curves based on samples 1.7 to 1.15 billion years ago from North America and Gondwanaland indicates that these continents were joined together (or at least were not widely separated) 1.7 billion years ago, separated soon thereafter, and were rejoined about 1.2 billion years ago. (c) Comparison of recalculated A.P.W. curves based on samples 2.75 to 1.7 billion years old from North



b)

Figure 3.

ORIGINAL PAGE IS
OF POOR QUALITY

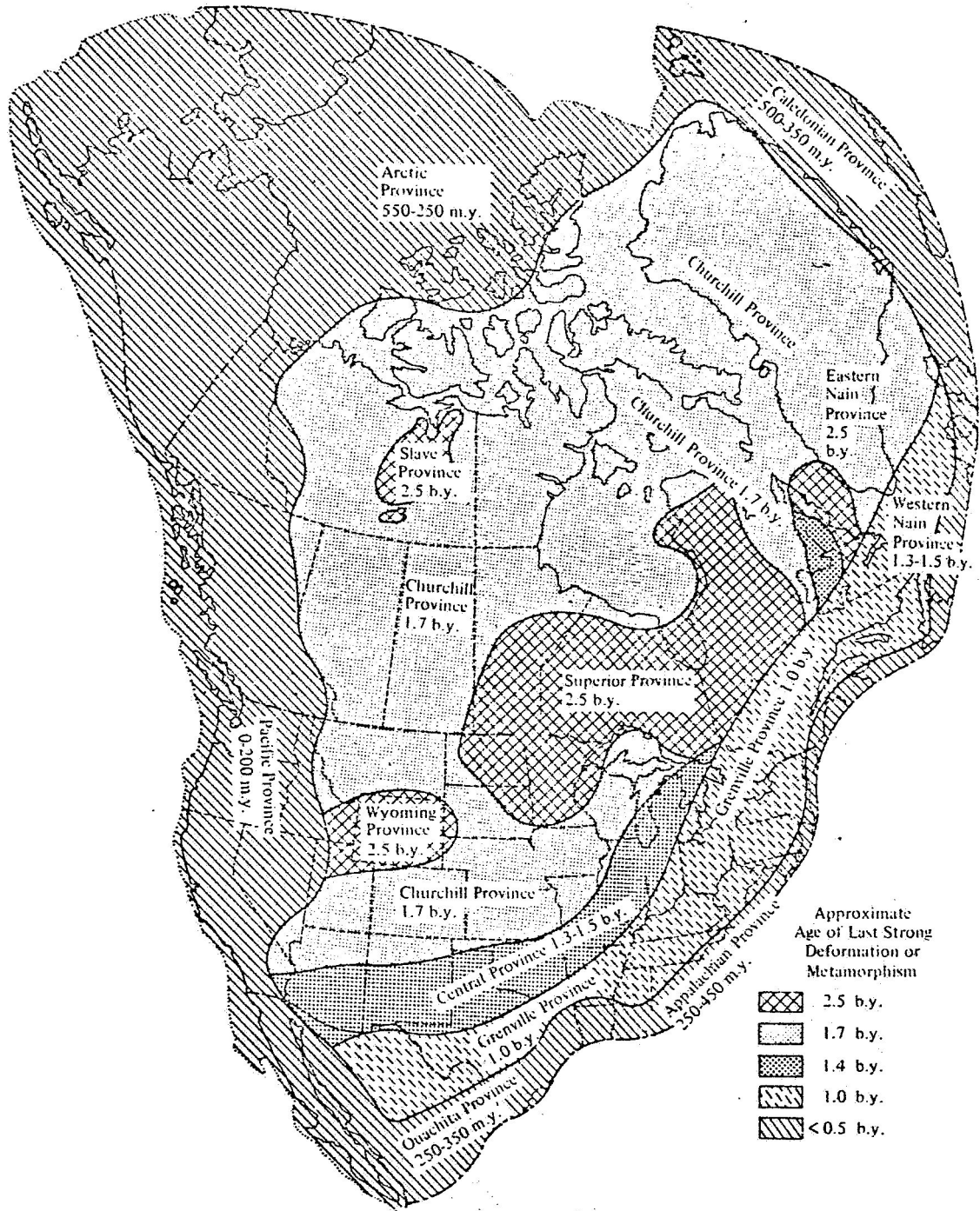
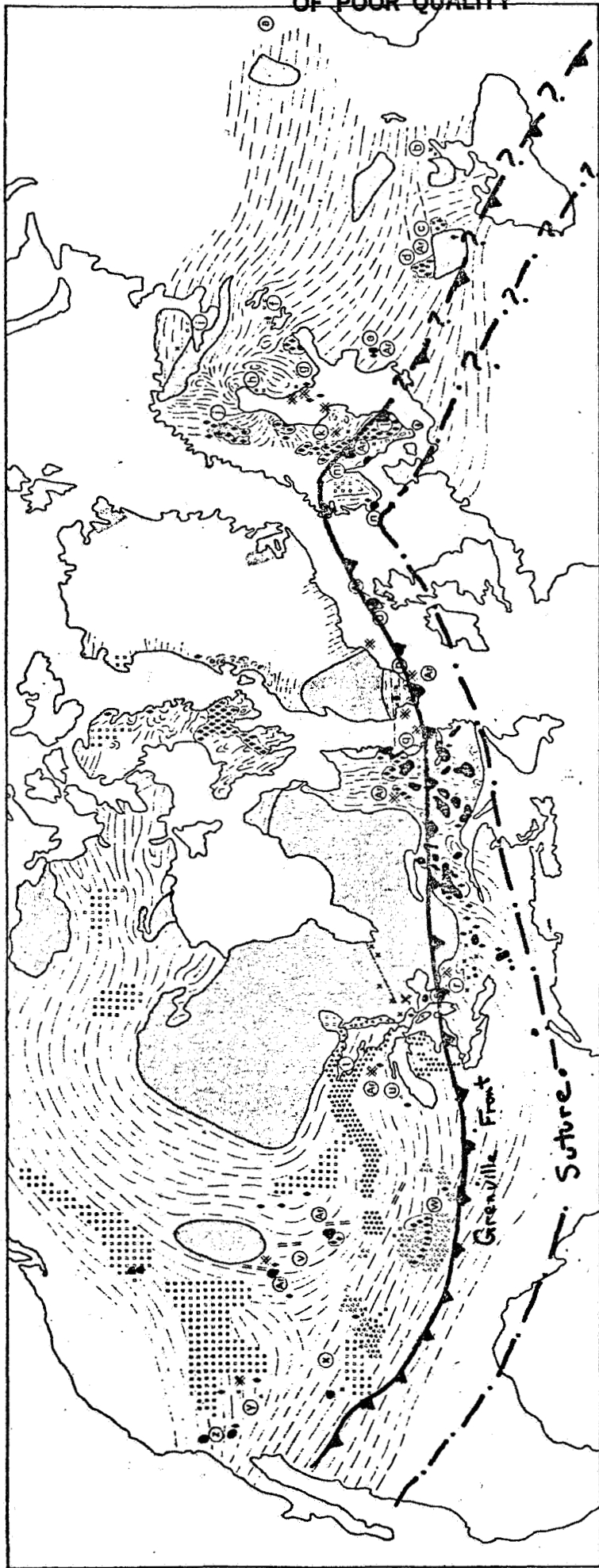


FIGURE 9.9 Geologic provinces of Ancestral North America.

Figure 4.



- Achaean areas unaffected by Proterozoic metamorphism
- ▨ Minimum area affected by Proterozoic thermal activity 1600-2000 m.y. ago
- ▩ Aenotholites and related basic intrusions
- ▧ Repetitive granites, monzonites, quartz syenites and related granitic or intermediate intrusions
- ▦ Acid volcanics extruded 1000-1700 m.y. ago
- ▥ Sedimentary sequences (with some volcanics) deposited 1000-1700 m.y. ago
- ▤ Basic extrusives and associated sediments deposited 1000-1200 m.y. ago
- ▣ Alkali intrusives emplaced 1000-1700 m.y. ago
- ▢ Areas where K/Ar or Rb/Sr mineral ages are markedly discordant to Rb/Sr whole-rock isochron ages
- ✱ Dykes
- ▬ Calciclasts
- Faults
- ⊙ ⊚ See text

Proposed suture formed during collision of North America and Europe with Gondwanaland

Figure 5.

Grenville Front and equivalents - Separates rocks metamorphosed 1.0 - 1.2 billion years ago from older rocks.

ORIGINAL PAGE IS
OF POOR QUALITY

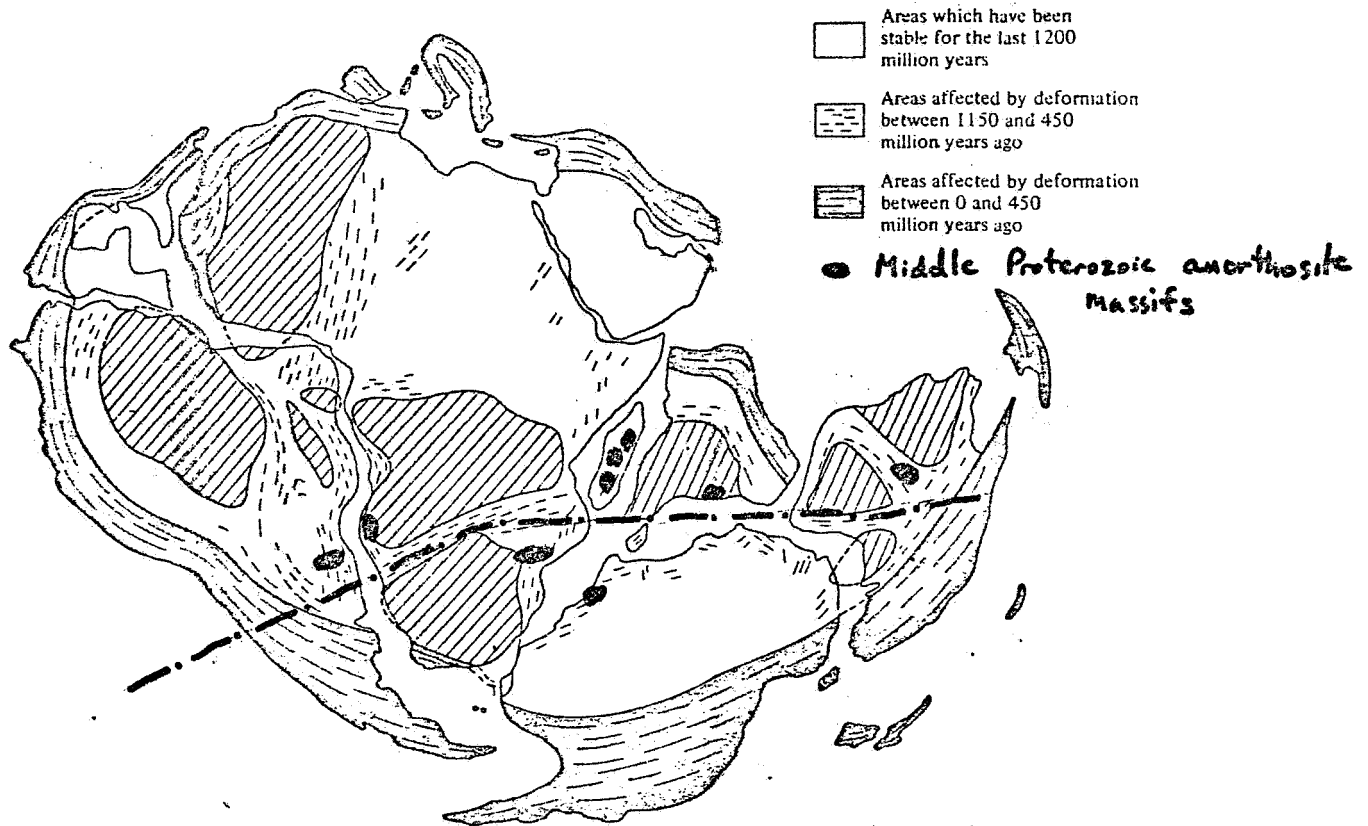


FIGURE 7.15 Matching of geological provinces in South America with those in Africa. (After Hurley, Ref. 12 Copyright © 1963 by Scientific American, Inc., all rights reserved.)

Figure 6.

Table 1 - Radiometric Dates of Anorthosites and Related Rocks.

Site Location/Name	Analysis #	Date, M.Y.	Method	Mineral	Rock	Primary Reference	Secondary Reference	Comment
Adirondack Mts, N.Y.	1	1485 ± 85	WR-Rb/Sr	Zircon	Pyroxene Gneiss	Spooner + Fairbairn, 1970		Dated on Well Rocks SW of Many Anorthosite outcrops - Recrystallized by granulite age??
"	(Many)	1070 ± 10	U/Pb Con.	"	Anorthosite Pyroxite	Silver, 1968		11th metamorphic event (granulite) Silver, 1968
"	(Many)	1100 ± 15	"	"	Spinel Pyroxite	"		Spinel cuts + ... younger than anorthosite
"	(Some Mts)	1080 ± 10	"	"	Micaschale	"		with anorthosite??
"	(Many)	1070 ± 20	"	"	Anorthosite Pyroxite	"		Metamorphed (silica) - Recrystallized Anorthosite
"	(Many)	1020 ± 10	"	"	Thionium Magnetite Ore	"		Possibly post date and/or anorthosite
Adirondack Mts, N.Y.	1	1130 ± 10	"	"	Pyroxene Gneiss	"		Date on Well rocks 410 m SE of ...
Nain, Labrador	42	1480	K-Ar			Morse, 1964		de wind, etc, 1974
Nain, Labrador	42	1400				Wheeler, 1960		Anorthite, 1968
Mt. Chikoman, Labrador	36	1400	K-Ar			Emms, 1964		de wind pt of, 1974
"	38	1460		Zircon		Krogh et al, 1973		"
Adirondack Mts, N.Y. (Many)	1	932 ± 40	WR-Rb/Sr		Leucocratic	Ashard et al, 1980		Leucocratic assumed co-magmatic with anorthosite
"	1	1213 ± 25	WR-Rb/Sr		Leucocratic + Pyroxite	"		"
Leucocratic Range, N.Y.	27	1430 ± 20	WR-Rb/Sr		Shaw's Granite	Souboureydou et al, 1975		Leucocratic Pyroxite assumed co-magmatic with anorthosite
"	27	1420 ± 20	207Pb/206Pb	Zircon?	"	"		Foundation et al, 1981 - Shaw's Granite probably anorthite - this estimated to be a same age
"	27	1432 ± 15	"	"	Hypoxene Monzonite	"		"
"	27	1450	WR-Rb/Sr		"	"		Magmatic is assumed to be for Shaw's
"	27	1665	"		"	"		"
"	27	1290	"		Amphibole	"		"
"	27	1424 ± 15	207Pb/206Pb	Pb Zircon?	"	"		"
Egersund, Norway	18	1000 ± 35		Zircon		Pasteads + Nichol, 1975		de wind et al, 1974 Date on outcrops
"	18	957 ± 43		Spinel	Farsundite	Pasteads et al, 1970		" Date on outcrops only after this date
"	18	993 ± 18		Zircon	"	Nichol + Pasteads, 1972		" Assumed to be contemporaneous or
"	18	1200	U-Pb + Rb/Sr		"	Pasteads + Nichol, 1975		"
"	18	1470 ± 78	WR-Rb/Sr		Gneiss	Versteeg, 1970		Date on Well Rocks
"	18	1404 ± 89	"		Anorthite + Quartz	Sarker et al, 1981		"
C. Ka Lake, India	121	1312	"		Rapakivi Gneiss	"		"
"	121	540	WR-Rb/Sr		"	Higgins + Digg, 1977		Reynolds - Assumed to be associated in time
Syrt, IB, Quebec	63	1650	WR-Rb/Sr and U/Pb		"	Emms, Present Emmons		Emms, 1978
Medby Mountains, Labrador	36					Morse, 1970		Morse, 1970

ORIGINAL PAGE IS
OF POOR QUALITY

FOLDOUT FRAME

FOLDOUT FRAME

Table 1 (cont'd) - From Herz (1969).

Table 1. Age determinations on anorthosites and related rocks; m.y., million years.

Site	Age (m.y.)	Notes
<i>Africa - Asia - Australia</i>		
Southern Angola (22)	1260 ± 90	By Nicolaysen on muscovite in pegmatite with Rb/Sr. Considered minimum age for anorthosite.
Upangwa, Tanzania (23)	1712 ± 70	K/Ar date on muscovite (1720); and biotite (1705) from leucocratic gneiss at Igawa; considered correlative with Ubendian. Anorthosite complex about 100 km away is also part of Ubendian system. Dating is thus tenuous.
Eastern Ghats, India (24)	1300-1520	Emplacement of charnockites using whole-rock Rb/Sr ages.
Musgrave Ranges, Australia (25)	1390 ± 130	Nine pyroxene granulites for Rb/Sr isochron.
Stanovoi Region, Aldan shield, Siberia (26)	< 1800-2000 > 1550-1600	Intrusion of anorthosites and syenites.
Dzhugdzhur Massif, Siberia (27)	2250 ± 150	Pb ²⁰⁷ /Pb ²⁰⁶ on two apatites from anorthosite, 2260 and 2240 m.y.; Pb ²⁰⁶ /U ²³⁸ , 1580 and 1650 m.y.; Pb ²⁰⁷ /U ²³⁵ , 1900 and 1930 m.y.; 2250 m.y. is from Concordia plot.
Anabar Massif, Siberia (28)	1734	K/Ar on hornblende from gabbro anorthosite Irkutsk.
<i>North America - South America</i>		
St. Joe (Boehls Butte), Idaho (29)	1200	Age of sill amphibolite considered comagmatic with anorthosite.
San Gabriel Range, California (30)	> 1200	Pb/U on zircon from cross-cutting pegmatite.
Laramie Range, Wyoming (31)	> 1335 ± 30 < 1715 ± 60	Sherman granite (1335) intrudes anorthosite which in turn intrudes gneiss complex (1715). Whole-rock Rb/Sr isochrons.
Cambridge Arch, Nebraska (6)	> 1170, < 1700 prob. 1300-1360	1170 is age of cataclasis, 1700 is age of basement rock; 1300-1360 is thermal event.
Duluth Gabbro Complex, Minnesota (32)	1115 ± 15	Pb/U concordia on zircon concentrates.
Canada (33)	1370	Date of Elsonian orogeny and anorthosite emplacement.
Adirondacks, New York (34)	1125 ± 10	Pb/U ages on zircon.
Roseland, Virginia (35)	1100	Date on charnockitic rock about 110 km northeast of Roseland, considered equivalent to charnockite at Roseland (16). Pb/U ages on zircon are from 1070-1150; Rb/Sr and K/Ar on biotite are 890 and 800.
Michikamau, Labrador (36)	1400 ± 80	K/Ar on biotite in cross-cutting granite gave 1360 ± 80 and on intruded metasedimentary rocks 1520 ± 85.
Kiglapait, Labrador (37)	1480 ± 50	K/Ar on biotite in granodiorite intrusive.
Sierra de Santa Marta, Colombia (38)	1380	Rb/Sr isochron on Dibulla gneiss, granulite facies.
Gardar, Greenland (39)	1150-1335	K/Ar on biotite from granite and on phlogopite-talc from ultrabasic rocks.
and (40)	1250-1300	Anorthosite xenoliths in Narrsaq gabbro of Mid-Gardar period of dike formation. Anorthosite itself gave 1025 on K/Ar in biotite and 1075 on K/Ar in augite which represents a later thermal event.
<i>Europe</i>		
South Harris, Outer Hebrides (41)	1450 ± 30 1530 ± 30	Date is Sr/Rb on biotite from pegmatite intruding metagabbro about 300 m from metagabbro-anorthosite gneiss contact.
Southern Norway (42)	> 1000	Emplacement of para-anatectic anorthosites and cogenetic rocks.
Podlasic region, Poland (43)	1250-1350	Charnockitic localities not given, but this is same region as the anorthosite of Suwalki.
Korosten Complex, Ukraine (44)	1750	Gabbro and rapakivi granites; "Labradorites" grade into both.
Korun-Novomirgorod, Ukraine (44)	1300-1500	Alkaline gabbro and granite. "Labradorites" grade into monzonites and gabbros.

ORIGINAL PAGE IS
OF POOR QUALITY

TABLE - 2

PROBLEMS CONNECTED WITH ANORTHOSITE MASSIFS

- 1) Where did they come from?
 - a) Crust
 - 1) Anorthositic primary crust
 - 2) Mafic lower crust
 - 3) Anorthositic gabbro primary crust
 - 4) Gabbroic anorthosite primary crust
 - 5) Garnet-plagioclase-pyroxene granulite residue from partial melting
 - b) Mantle
 - 1) pyrolitic lherzolite (such as garnet peridotite, spinel peridotite)
 - A) Garnet peridotite
 - B) Spinel peridotite
 - C) Plagioclase Peridotite
 - 2) Eclogite (garnet-pyroxene)
 - A) Total melt forming basaltic liquid
 - B) Partial melt forming liquid of composition
 - I) Anorthositic gabbro
 - II) Gabbroic anorthosite
 - III) Anorthosite
- 2) What was the composition of the parent liquid?
 - a) Basaltic (gabbroic)
 - b) Anorthositic gabbro
 - c) Gabbroic anorthosite
 - d) Anorthosite
- 3) to what degree was there fractionation due to crystal settling near the site of melting (origin)
 - a) Extensive
 - b) Moderate
 - c) Minor
 - d) None
- 4) To what degree was there fractionation due to differing amounts of partial melting near the site of melting (origin)
 - a) Extensive
 - b) Moderate
 - c) Minor
 - d) None
- 5) To what degree was there fractionation due to crystal settling between the site of melting and the site of emplacement (such as at the crust-mantle boundary)
 - a) Extensive
 - b) Moderate
 - c) Minor
 - d) None
- 6) To what degree was there fractionation due to flow differentiation between the site of melting and site of emplacement
 - a) Extensive
 - b) Moderate
 - c) Minor
 - d) None

* Liquid, solid, or mixture - whatever rises

- 7) To what degree did the formation of anorthosite (more than 90% Plagioclase) form as a result of fractionation by crystal settling after emplacement?
- Extensive
 - Moderate
 - Minor
 - None
- 8) What was the composition of the liquid, solid, or mixture immediately after emplacement
- Basaltic (gabbroic)
 - Anorthositic Gabbro
 - Gabbroic anorthosite
 - Anorthosite
- 9) What is the tectonic environment of emplacement of anorthosites?
- Rift zone
 - Aulacogen associated with continental separation
 - Intercontinental rift not connected with continental separation
 - Subduction Zone - on the margin of a shrinking ocean
 - Above a plume, below a hot spot
 - Rift zone parallel to a developing continental margin formed as two continents separate
 - Collisional zone where two continents are colliding
- 10) Why are anorthosite massifs restricted to the Middle Proterozoic (1.7 to 1.2 billion years ago) for the most part - This is 10% of geologic time
- Related to close approach of the moon to the earth following lunar capture
 - Higher heat flow during the Precambrian and therefore a thinner lithosphere
 - Other
- 11) What is the depth of emplacement of anorthosites?
- 0 10 20 30 40 50 60 70 km
- 12) In what crustal level are anorthosites emplaced?
- Upper crust
 - Middle Crust
 - Lower Crust
- 13) What is the relationship between anorthosites and these associated rocks:
- Granite-Charnockite rocks
 - Anorthosites fractionated from Granite
 - Granites fractionated from Anorthosite
 - Anorthosites caused melting of gr.
 - Syenite-Monzonite-Mangerite
 - Anorthosites fractionated from syenite
 - Syenites fractionated from anorthosite
 - Anorthosites caused melting of syenites
 - Gabbro-Troctolite-Nortite
 - Anorthosites fractionated from gabbro
 - Gabbro fractionated from anorthosites
 - Anorthosites caused melting of gabbros
 - Gabbros caused melting of anorthosites

TABLE - 3

IMPORTANT "FACTS" TO CONSIDER WHEN WORKING ON ORIGIN, EMPLACEMENT ETC. OF ANORTHOSITES

- 1) The average composition of anorthosite massifs is either an anorthosite (An_{48}) or gabbroic anorthosite (An_{54})
- 2) Chilled margins have been reported for some massifs - sometimes composed of gabbroic anorthosite or anorthositic gabbro??
- 3) Little layering (compositional layering) is present, and cryptic layering is generally (always?) absent
- 4) Crystals of plagioclase and pyroxene are often very large - up to 1 meter across
- 5) Crystals of plagioclase are often bent and broken, apparently during emplacement
- 6) Crystals of plagioclase often show a strong preferred orientation (foliation)
- 7) Anorthosite massifs are often very large up to 20,000 or 30,000 sq km
- 8) Ti and Fe/Mg ratios do not resemble calc-alkaline andesites
- 9) Many massifs are 1.4 to 1.5 billion years old
- 10) Rapikivi granites are associated in time and space with anorthosite massifs
Most are 1.4 to 1.5 billion years old - Many rapikivi granites are very large
- 11) There was no known orogenic (mountain building, deformation, metamorphism) episode 1.4 to 1.5 billion years ago
- 12) Anorthosites generally contain only anhydrous mafic minerals such as pyroxene and olivine. Furthermore, the apparently late differentiates (such as olivine gabbros) are also anhydrous
- 13) The density of liquid and/or solid anorthosite will tend to be fairly high - certainly higher than a granite - This is important in the rate of rise of liquid or crystal/liquid mixtures
- 14) The Marcy Anorthosite has an ϵ Nd of +5
- 15) Typical anorthosite massifs have an initial $^{87}\text{Sr}/^{86}\text{Sr}$ of .703 - .706

ORIGINAL PAGE IS
OF POOR QUALITY

N82 23133

D11

A COMPARISON OF STRATIFIED VS. REGRESSION ESTIMATORS

Helen Calvert Takacs
Mississippi State University
1981 NASA-ASEE Summer Faculty Fellow

Supervisor:

Dr. Richard P. Heydorn
Pattern Recognition Section
Scene Analysis Branch
Earth Resources Research Division

ABSTRACT

One can use Landsat data acquired over an agricultural area along with ground enumeration of the same area to obtain crop acreage estimates which are better (as measured in terms of bias and variance) than can be obtained from either data source alone. Two basic approaches have been considered within the AgRISTARS program. One is a stratified crop acreage estimator, and another is a regression estimator. One would like to know which procedure is better for a given sample size of ground acquired data. A statement of the problem has been mathematically formulated and some theorems have been proved which relate to the variance of the two estimators. For a particular set of data, the regression and stratified estimators are compared in terms of certain easily computed parameters.

National Aeronautics and Space Administration
Lyndon B. Johnson Space Center
Houston, Texas
August 20, 1981

Introduction

This report describes the problem of comparing two methods of combining Landsat data with ground enumerations to improve the precision of crop area estimates. The United States Department of Agriculture (USDA) has proposed a regression estimator obtained by regressing ground truth data against Landsat derived area estimates. Experimental results obtained with this approach over several states suggest that the variance of this estimator is 2-3 times smaller than that of the ground-enumerated estimator. Working with USDA, National Aeronautics and Space Administration (NASA) researchers have experimented with stratified crop area estimators, where again Landsat data is used to increase the precision of an ordinary ground survey estimator.

While some comparisons between the two estimators have been done experimentally, an insufficient amount of theoretical investigations has been done to understand the fundamental characteristics of the two approaches. A good understanding of this problem should be a significant step forward in deciding how best to use satellite data in domestic crop acreage surveys.

In the present work the problem is formulated mathematically and some theorems are presented which relate to the variance of the two estimators. In addition, the two methods are compared in terms of certain easily computed parameters for a particular set of data.¹

This is a preliminary study, and much additional work will be done on this problem. A model can be formulated which will allow comparison of the stratified and regression estimators. This model can be implemented on a computer so that various simulation studies will contribute numerical insight. This approach should reveal important differences and similarities between the two estimates and thereby motivate further theoretical investigations.

Statement of the Problem

Suppose that we have allocated N one-square-mile segments, each segment containing m pixels to the region to be sampled. Further consider that n of these segments have been enumerated by a ground observer; i.e., for those segments we know the class identity of each pixel. We assume that n is much smaller than N .

¹The data set used consists of thirty-three segments in Northern Missouri. It is further described in Amis, et al., 1981a and 1981b.

Each segment is classified by classifying the pixels in a segment as being of crop 1 (the crop of interest) or of crop 0 (not the crop of interest). Also, for those n segments that have been observed from the ground we know, in fact, that each pixel is a crop 1 or a crop 0 pixel. The segments have been allocated using a simple random sample allocation rule.

Keeping this sampling frame in mind, let us introduce some formal notation.

Let X be a random variable of Landsat observations on a pixel contained within some segment. That is, we consider the multispectral measurements obtained using Landsat from a given pixel as being a realization of the random variable X . We denote an observation (realization) on X as $X(w) \triangleq \chi$, where χ is vector valued, i.e., $\chi \in \mathbb{R}^k$.

Let H be a random variable of crop class labels. We denote a particular label as $\mathbb{H}(w) \triangleq \theta \in \{0,1\}$. Whenever we have an observation $X(w)$, we also have an associated label, $\mathbb{H}(w)$, i.e., we have the pair $(X(w), \mathbb{H}(w))$. However, we can always observe $X(w)$, but we cannot always observe $\mathbb{H}(w)$. The values $\mathbb{H}(w)$ are only known from field observations, i.e., they are known in the n one-square-mile segments which have been enumerated by a ground observer, but not elsewhere.

We assume that we have a classifier that can classify each pixel as either crop 1 or crop 0. We denote that classifier by the symbol Φ . Given χ we have $\Phi(\chi) \in \{0,1\}$. We can think of $\Phi(X)$ as an estimator of \mathbb{H} based on Landsat observations.

We are now in a position to formulate our estimators of the proportion of crop 1 in the sampling frame.

We will call the estimator denoted \hat{P}_S the poststratified estimator, since stratification takes place after selection of the segments of the simple random sample. Given the sample (X_i, \mathbb{H}_i) , $i=1, 2, \dots, n$ from the ground observed segments and given the sample X_j , $j=1, 2, \dots, N$ including the rest of the segments, let

$$\hat{P}_S = \left[\frac{\sum_{i=1}^{n \cdot m} \Theta_i \phi(X_i)}{n \cdot m} \cdot \frac{1}{N \cdot m} \sum_{j=1}^{N \cdot m} \phi(X_j) + \frac{\sum_{i=1}^{n \cdot m} \Theta_i (1 - \phi(X_i))}{n \cdot m \sum_{i=1}^{n \cdot m} (1 - \phi(X_i))} \cdot \frac{1}{N \cdot m} \sum_{j=1}^{N \cdot m} (1 - \phi(X_j)) \right] \Delta + \left(\frac{1}{n \cdot m} \sum_{i=1}^{n \cdot m} \Theta_i \right) (1 - \Delta) \quad (1)$$

where $\Delta(w) = \begin{cases} 1 & \text{when } \phi(X_i(w)) = 1 \text{ for some } i \text{ and } \phi(X_i(w)) = 0 \text{ for some } i, \\ & i = 1, 2, \dots, n \cdot m \\ 0 & \text{otherwise.} \end{cases}$

Here the random variable Δ is intended to take care of the case where the classifications are all either 1 or 0. Those are the cases where we have to redefine our estimator because our small sample (of size n) all fell into one strata or another. We shall assume N is so large that the classifier working on the large sample will create two nonempty strata.

We will call the estimator denoted \hat{P}_R the regression estimator, and we develop its formula as follows. Given the n segments which have ground observations, let

$$Q_k = \frac{1}{m} \sum_{\ell=1}^m \Theta_{\ell k}, \quad k = 1, 2, \dots, n$$

where we have introduced the additional index k to keep track of the segment. For the k th segment, Q_k represents the proportion of that segment that is the crop of interest using field observations. We can consider $Q_k, k = 1, 2, \dots, n$ as an independent identically distributed (iid) sequence of random variables.

Similarly define

$$S_k = \frac{1}{m} \sum_{\ell=1}^m \phi(X_{\ell k}), \quad k = 1, 2, \dots, n.$$

For the kth segment, S_k represents the estimate of the proportion of that segment that is the crop of interest using the classifier.

Thus for each ground observed segment we have the pair of random variables (Q_k, S_k) , $k = 1, 2, \dots, n$ where Q_k is the exact proportion of the crop of interest and S_k is the classified proportion of the crop of interest.

We shall assume that the following linear regression model holds.

$$Q_k = a + bS_k + \epsilon_k, \quad k = 1, 2, \dots, n \tag{2}$$

where $\epsilon_k \sim N(0, \sigma^2)$. Let \hat{a} and \hat{b} be the usual least squares estimators of a and b respectively (computed over the n ground observed segments.) Then we define the estimator of the proportion of crop 1 in the sampling frame to be

$$\hat{P}_R = \hat{a} + \hat{b} \frac{1}{N} \sum_{t=1}^N S_t. \tag{3}$$

Note that \hat{P}_R is formed by summing over all of the segments, and \hat{a} and \hat{b} are formed from just the ground observed segments.

Questions of Interest

Now that the statement of the problem has been mathematically formulated, here are some of the questions of interest.

1. Are the estimators \hat{P}_S and \hat{P}_R biased or unbiased?
2. Is $\text{var}(\hat{P}_S) < \text{var}(\hat{P}_R)$ or $\text{var}(\hat{P}_S) > \text{var}(\hat{P}_R)$ or $\text{var}(\hat{P}_S) = \text{var}(\hat{P}_R)$?
3. How do these variances compare with the simple random sample estimator variance, i.e.--the variance of

$$\frac{1}{n} \sum_{k=1}^n Q_k ?$$

4. Can we compare the variance of \hat{P}_R and $\frac{1}{n} \sum_{k=1}^n Q_k$ in terms of the omission and commission error rates of the classifier and the proportion of the crop of interest present? That is, can we say that

$$\text{var}(\hat{P}_R) = R \text{var}\left(\frac{1}{n} \sum_{k=1}^n Q_k\right)$$

where $0 \leq R \leq 1$ and R is a function of the crop 1 proportion and classifier errors only.

In addressing these questions we will begin by considering two simple cases. The first assumes that the segments come from the same statistical population, that is, there are no statistical segment-to-segment differences. This case will be called the homogeneous stratum case. With this assumption pixel observations drawn randomly from any one segment are distributed the same as those drawn without regard to their segment location. In the second case we allow the segments to come from separate populations. This will be called the heterogeneous stratum case.

Homogeneous Stratum with Known Regression

In this case we draw n iid random variables \textcircled{H}_i , (X_i) , $i=1, 2, \dots, n$ and form the means

$$\overline{\textcircled{H}} = \frac{1}{n} \sum_{i=1}^n \textcircled{H}_i \quad \text{and} \quad \overline{\phi(X)} = \frac{1}{n} \sum_{i=1}^n \phi(X_i).$$

It can be shown (Heydorn, 1981b) that for this case the correlation coefficient, R , relating the mean value \textcircled{H} to the mean value $\overline{\phi(X)}$ is related to the omission and commission error probabilities of the classifier and the proportion of the class of interest in the sampling frame.

The variance of the regression estimator is

$$\begin{aligned} \text{var}(E(\hat{Q})) &= (1 - R^2) \text{var}(Q) \\ &= \frac{(1 - R^2) \text{var}(\textcircled{H})}{m} \end{aligned}$$

The following results (Heydorn, 1981b) are stated without proof.

Given the stratified estimator, \hat{P}_S , it can be shown that

$$\lim_{N \rightarrow \infty} \text{var}(\hat{P}_S) = R_1 \text{var}(\textcircled{H})$$

where

$$R_1 = \frac{\Pr(\phi(X) = 0 | \textcircled{H} = 1) \Pr(\phi(X) = 0 | \textcircled{H} = 0)}{\Pr(\phi(X) = 0)} + \frac{\Pr(\phi(X) = 1 | \textcircled{H} = 1) \Pr(\phi(X) = 1 | \textcircled{H} = 0)}{\Pr(\phi(X) = 1)}$$

and that

$$\text{var}(\hat{E}(Q)) = R_1 \text{var}(\textcircled{H})/n.$$

Indeed

$$(1 - R^2) = R_1 \tag{4}$$

or

$$R = \sqrt{1 - R_1}$$

where letting

$$\begin{aligned} \text{omission probability } \triangleq \Pi_{10} &= \Pr(\phi(X) = 0 | \textcircled{H} = 1), \\ \text{comission probability } \triangleq \Pi_{01} &= \Pr(\phi(X) = 1 | \textcircled{H} = 0), \end{aligned}$$

and

$$\lambda = \Pr(\textcircled{H} = 1)$$

we can write

$$R_1 = \frac{(1 - \Pi_{01})\Pi_{10}}{\Pi_{10}\lambda + (1 - \Pi_{01})(1 - \lambda)} + \frac{\Pi_{01}(1 - \Pi_{10})}{(1 - \Pi_{10})\lambda + \Pi_{01}(1 - \lambda)} \tag{5}$$

Another point to make in the homogeneous case with known regression is that we started with the model

$$\textcircled{H} = \alpha + \beta\phi(X) + \delta$$

showing that

$$E(\textcircled{H} | \phi(X)) = \alpha + \beta\overline{\phi(X)}$$

which means that in the homogeneous case we have a linear regression when we group pixels into segments and consider segment averages.

Heterogeneous Stratum

Consider the statement of the problem with the assumption that random observations from one sample segment can have a different probability distribution from observations from another sample segment.

It can be shown (Heydorn, 1981b) that to have a linear regression

$$Q = a + bS + \epsilon$$

$\phi(X)$ has to be a sufficient statistic for P, the set of all probabilities of \textcircled{H} given we are in a particular segment. We can denote a member of P as

$$\Pr(\textcircled{H} = i | \Delta = j), \quad i = 0, 1; \quad j = 1, \dots, n$$

where Δ indexes the segments. This means that a linear regression depends upon the classifier being able to take a region in which the proportions of crop across that region are "uneven" and stratify it so that within the stratum the proportions are "evenly" distributed. That is

$$\Pr(\cdot | \phi(X) = i, \Delta = j) = \Pr(\cdot | \phi(X) = i).$$

Another point is that when we specify a value of S, we assume that this value gives us some information with regard to the sample segment that we have been observing. If we know a segment proportion, as given by a classifier, then certain portions of the region have a higher probability than others of containing the segment. We call this condition an "uneven sample."

We now consider the variance of the regression estimator, $E(\hat{Q})$. It can be shown (Heydorn, 1981b) that for a sample of size n

$$\text{var}(E(\hat{Q})) = \frac{R_2 \text{var}(\textcircled{H})}{n}$$

where

$$R_2 = \frac{1}{J} \sum_S (nS) \frac{\sum_k \Pi_{10}(k)^{nS} \Pi_{00}(k)^{n-nS} \sum_k \Pi_{11}(k)^{nS} \Pi_{01}(k)^{n-nS}}{\sum_k \Pi_{10}(k)^{nS} \Pi_{00}(k)^{n-nS}}$$

and

$$\Pi_{ji}(k) = \Pr(\phi(X) = j | \textcircled{H} = i, \Delta = k)$$

$$\Pi_j(k) = \Pr(\phi(X) = j | \Delta = k).$$

A Numerical Example Comparing the Stratified Estimator with the Regression Estimator

In a recent study (Amis, et al., 1981b), the regression estimator was calculated for six different crops of interest using 33 segments in Northern Missouri. There were 12 different regression runs for each crop. The runs differed in that there were three classifier procedures (Editor, CLASSY, MSG), cases where all 33 segments were used for both training the classifier and estimating, cases where the 33 segments were divided into 25 for training and 8 for estimating, cases where a jackknifed test set was used, and cases where single date satellite acquired data is compared with estimates from multiple date data.

Using the true proportion (λ), omission error probability (Π_{10}), commission error probability (Π_{01}) and R^2 values computed in the Amis study, we used formulas (4) and (5) to compute $(1-R^2)$, the empirical variance reduction factor for a regression estimator, and R_1 , the theoretical variance reduction factor for a stratified estimator relative to a simple random sample variance. R_1 was then adjusted to reflect a variance reduction relative to the segment proportion variances. We call this adjusted number R_1^* and compute it according to the following formulas.

In the stratified case we have:

$$\text{var} (\hat{P}_S) = R_1 \frac{\text{var} (\hat{H})}{m} .$$

In the regression case we have:

$$\text{var} (\hat{E}(Q)) = (1-R^2) \text{var} (Q) .$$

Therefore to adjust R_1 so that it will be relative to $\text{var} (Q)$, let

$$R_1^* = R_1 \frac{\text{var} (\hat{H})/m}{\text{var} (Q)} .$$

Then our comparison is in terms of

$$\frac{\text{var} (\hat{P}_S)}{\text{var} (\hat{E}(Q))} = \frac{R_1^*}{1-R^2} .$$

The results as tabulated in the appendix indicate that for this set of data the stratified estimator results in a greater reduction in variance. This example is not typical however. A look at Table 8 in the appendix shows us that there is a large variation in the number of pixels per segment, which means that we have lost efficiency in the regression case, where pixels are clustered into segments. In another case where there was not such a large variation between strata, stratified estimation might not be better.

Furthermore, for this numerical example, we did not have time to go back to the original data and using an average value for m when m varied may not have been legitimate. We would have liked more time to look at this example and others.

Suggestions for Further Study

Further studies will begin by developing a simulation model to investigate topics such as:

- a) Cases where linear regressions hold and cases where they do not.
- b) The variance reduction of the stratified and regression estimators as a function of segment-to-segment differences and classifier omission and commission probabilities.

Hopefully, those studies will provide insight as to the major differences between the two estimators, and, perhaps, how to improve their performance. This will also provide a logic basis for further theoretical studies. Later theoretical studies should consider the more difficult realistic cases where the regression parameters and the classifier parameters are estimated rather than assumed to be known.

ORIGINAL PAGE IS
OF POOR QUALITY.

TABLE 1 - CURRENT PROCEDURE - TRAIN AND ESTIMATE ON 33 SEGMENTS

(A) EDITOR MULTITEMPORAL PERFORMANCE MEASURES

	<u>True Pro- portion</u>	<u>Omission Error</u>	<u>Comission Error</u>	<u>1-RSQ</u>	<u>R₁</u>	<u>R₁' = R₁ *Factor</u>	<u>R₁' / (1-R²)</u>
Corn	0.101	0.27	0.37	0.20	0.95	0.024	0.122
Wheat	0.030	0.71	0.56	0.62	0.99	0.069	0.111
Pasture	0.392	0.21	0.46	0.21	0.89	0.012	0.058
Soybeans	0.275	0.21	0.33	0.15	0.82	0.011	0.077
Woodland	0.080	0.53	0.54	0.38	0.99	0.021	0.057
Other Hay	0.092	0.78	0.60	0.80	0.95	0.030	0.037

(B) EDITOR AUGUST PERFORMANCE MEASURE

Corn	0.101	0.48	0.55	0.58	0.99	0.025	0.044
Wheat	0.030	0.66	0.68	0.73	0.98	0.068	0.093
Pasture	0.392	0.27	0.52	0.26	0.95	0.013	0.050
Soybeans	0.275	0.26	0.37	0.25	0.89	0.012	0.049
Woodland	0.080	0.58	0.58	0.56	0.97	0.021	0.037
Other Hay	0.092	0.92	0.79	0.98	0.78	0.024	0.025

(C) EDITOR MAY PERFORMANCE MEASURE

Corn	0.101	0.74	0.76	0.93	0.88	0.022	0.024
Wheat	0.030	0.98	0.88	0.99	0.82	0.057	0.058
Pasture	0.392	0.32	0.51	0.42	0.97	0.013	0.032
Soybeans	0.275	0.33	0.52	0.39	0.98	0.013	0.035
Woodland	0.080	0.67	0.65	0.56	0.96	0.021	0.037
Other Hay	0.092	0.84	0.64	0.95	0.92	0.029	0.030

TABLE 2 - CLASSY PROCEDURE - TRAIN AND ESTIMATE ON 33 SEGMENTS

	<u>True Pro- portion</u>	<u>Omission Error</u>	<u>Comission Error</u>	<u>1-RSQ</u>	<u>R₁</u>	<u>R₁ˆ = R₁ *Factor</u>	<u>R₁ˆ / (1-R²)</u>
Corn	0.101	0.27	0.29	0.07	0.92	0.023	0.339
Wheat	0.030	0.61	0.58	0.56	0.99	0.069	0.123
Pasture	0.392	0.24	0.45	0.16	0.91	0.012	0.079
Soybeans	0.275	0.18	0.34	0.11	0.81	0.011	0.104
Woodland	0.080	0.50	0.51	0.28	0.99	0.021	0.077
Other Hay	0.092	0.73	0.63	0.52	0.95	0.030	0.057

TABLE 3 - MSS CLASSIFIER PROCEDURE - TRAIN AND ESTIMATE ON 33 SEGMENTS

Corn	0.101	0.34	0.24	0.15	0.92	0.023	0.157
Wheat	0.030	0.79	0.40	0.62	0.99	0.069	0.111
Pasture	0.392	0.14	0.50	0.24	0.87	0.012	0.050
Soybeans	0.275	0.16	0.35	0.15	0.81	0.011	0.076
Woodland	0.080	0.66	0.47	0.43	0.99	0.021	0.050
Other Hay	0.092	0.98	0.47	1.00	0.93	0.029	0.029

TABLE 4 - CURRENT EDITOR CLUSTERING AND CLASSIFICATION PROCEDURE

(A) TRAIN ON 25 SEGMENTS

Corn	0.101	0.25	0.31	0.09	0.92	0.023	0.264
Wheat	0.030	0.64	0.66	0.50	0.98	0.068	0.137
Pasture	0.392	0.33	0.44	0.12	0.95	0.013	0.110
Soybeans	0.275	0.16	0.31	0.14	0.77	0.010	0.077
Woodland	0.080	0.45	0.50	0.34	0.99	0.021	0.063
Other Hay	0.092	0.67	0.71	0.63	0.94	0.029	0.047

(B) TEST ON AN INDEPENDENT SET (8 SEGMENTS)

Corn	0.101	0.45	0.42	0.39	0.99	0.025	0.065
Wheat	0.030	0.67	0.71	1.00	0.97	0.068	0.068
Pasture	0.392	0.48	0.47	0.61	0.99	0.013	0.022
Soybeans	0.275	0.28	0.63	0.60	0.99	0.013	0.023
Woodland	0.080	0.72	0.55	0.12	0.97	0.021	0.176
Other Hay	0.092	0.60	0.88	0.76	0.85	0.026	0.035

TABLE 5 - CLASSY PROCEDURE

	<u>True Pro- portion</u>	<u>Omission Error</u>	<u>Comission Error</u>	<u>1-RSQ</u>	<u>R₁</u>	<u>R₁[^] = R₁ *Factor</u>	<u>R₁[^]/(1-R²)</u>
(A) TRAIN ON 25 SEGMENTS							
Corn	0.101	0.22	0.30	0.08	0.91	0.023	0.293
Wheat	0.030	0.64	0.67	0.42	0.98	0.068	0.163
Pasture	0.392	0.26	0.44	0.16	0.92	0.012	0.079
Soybeans	0.275	0.15	0.31	0.13	0.77	0.010	0.083
Woodland	0.080	0.49	0.42	0.23	0.99	0.021	0.094
Other Hay	0.092	0.67	0.62	0.42	0.96	0.030	0.072

(B) TEST ON AN INDEPENDENT SET (8 SEGMENTS)

Corn	0.101	0.44	0.48	0.60	0.99	0.025	0.042
Wheat	0.030	0.58	0.53	0.66	0.99	0.069	0.105
Pasture	0.392	0.35	0.48	0.56	0.97	0.013	0.024
Soybeans	0.275	0.29	0.59	0.29	0.99	0.013	0.047
Woodland	0.080	0.80	0.55	0.17	0.96	0.020	0.122
Other Hay	0.092	0.73	0.87	0.79	0.79	0.025	0.031

TABLE 6 - MSE CLASSIFIER PROCEDURE

(A) TRAIN ON 25 SEGMENTS

Corn	0.101	0.28	0.24	0.08	0.90	0.023	0.289
Wheat	0.030	0.83	0.44	0.51	0.99	0.068	0.135
Pasture	0.392	0.12	0.46	0.21	0.82	0.011	0.054
Soybeans	0.275	0.13	0.32	0.13	0.77	0.010	0.083
Woodland	0.080	0.67	0.49	0.44	0.99	0.021	0.048
Other Hay	0.092	0.197	0.59	0.93	0.89	0.028	0.030

(B) TEST ON AN INDEPENDENT SET (8 SEGMENTS)

Corn	0.101	0.45	0.45	0.60	0.99	0.025	0.042
Wheat	0.030	0.67	0.36	0.95	0.99	0.069	0.073
Pasture	0.392	0.23	0.47	0.61	0.91	0.012	0.020
Soybeans	0.275	0.25	0.59	0.33	0.97	0.013	0.041
Woodland	0.080	0.81	0.53	0.12	0.96	0.020	0.174
Other Hay	0.092	0.97	0.70	0.99	0.83	0.026	0.026

**TABLE 7 - CURRENT EDITOR CLUSTERING AND CLASSIFIER PROCEDURE
RESULTS FOR JACKKNIFED TEST SET OF 33 SEGMENTS**

	<u>True Pro- portion</u>	<u>Omission Error</u>	<u>Comission Error</u>	<u>1-RSQ</u>	<u>R₁</u>	<u>R₁' = R₁ *Factor</u>	<u>R₁'/(1-R²)</u>
Corn	0.101	0.32	0.37	0.25	0.96	0.024	0.099
Wheat	0.030	0.76	0.74	0.87	0.96	0.066	0.076
Pasture	0.392	0.37	0.51	0.44	0.98	0.013	0.031
Soybeans	0.275	0.21	0.37	0.29	0.86	0.012	0.041
Woodland	0.080	0.51	0.59	0.41	0.99	0.021	0.052
Other Hay	0.092	0.85	0.80	0.98	0.80	0.025	0.026

TABLE 8 - PURE PIXELS OF GROUND TRUTH BY SEGMENT

Segment Number	Corn	Winter Wheat	Permanent Pasture	Soybeans	Dense Woodland	Other Hay
6034	5	7	45	13	0	38
6085	0	0	165	22	0	72
6015	31	19	30	81	0	8
6038	0	0	0	0	0	0
6098	0	0	310	0	0	0
6073	27	0	41	17	77	33
9046	0	0	99	0	47	36
6064	0	7	46	76	40	0
6065	29	3	28	1	0	15
6095	0	0	0	0	0	0
9061	86	0	0	183	0	0
9036	5	3	36	125	0	0
6053	0	0	40	104	4	4
6058	12	0	0	171	2	35
9057	0	0	108	17	14	45
9037	17	26	79	67	2	2
9062	8	0	251	18	30	16
9066	0	8	0	79	0	0
6045	6	0	340	13	0	0
9047	59	43	42	152	3	0
6048	53	0	7	0	62	0
9097	6	0	12	82	1	62
9096	37	0	0	26	39	28
6040	9	2	124	22	8	55
6060	0	0	0	10	3	6
6035	51	5	84	125	0	34
9016	93	0	0	85	0	0
9051	0	35	145	9	115	0
6063	22	2	31	76	16	0
6050	34	0	182	0	0	79
9052	39	19	26	137	0	0
6059	0	0	115	18	44	14
9017	22	13	141	46	7	10

ORIGINAL PAGE IS
OF POOR QUALITY

REFERENCES

- Amis, M.L., Lennington, R.K., Martin, M.V., McGuire, W.G., and Shen, S.S. (1981a). "Evaluation of Large Area Crop Estimation Techniques Using Landsat and Ground-Derived Data," DC-L1-04051, JSC-17116, Johnson Space Center, Houston, Texas.
- _____ (1981b). "Evaluation of USDA Large Area Crop Estimation Techniques," Seventh International Symposium on Machine Processing of Remotely Sensed Data, West Lafayette, Indiana.
- Cochran, William G. (1977). Sampling Techniques, Third Edition, New York: John Wiley & Sons.
- Dalenius, Tore (1950). "The Problem of Optimum Stratification," Skandinavisk Aktuarietidskrift, 33, 203-213.
- _____ and Hodges, J.L., Jr. (1959). "Minimum Variance Stratification," JASA, 54, 88-101.
- Feiveson, A.H. (1979). "Estimating Crop Proportions from Remotely Sensed Data," Proceedings of Technical Sessions, Vol. II, The LACIE Symposium, October 1978, Lyndon B. Johnson Space Center, Houston, Texas (JSC-16015).
- Fuller, Wayne A. (1966). "Estimation Employing Post Strata," JASA, Vol. 61, No. 316, pp. 1172-1183.
- Ghosh, S.P. (1963). "Optimum Stratification with Two Characters," The Annals of Mathematical Statistics, 34, pp. 866-872.
- Heydorn, R.P., Bizzell, R.M., Quirein, J.A., Abotteen, K.M., and Sumner, C.A. (1979). "Classification and Mensuration of LACIE Segments," Proceedings of Technical Sessions, LACIE Symposium, (JSC-16015), Vol. 1, October 1978 Johnson Space Center, Houston, Texas, pp. 73-86.

ORIGINAL PAGE IS
OF POOR QUALITY

Heydorn, R.P. (1981a). "Post-stratified and Pre-stratified Estimators,"
unpublished notes.

_____ (1981b). Private communication.

Raj, Des (1964). "On Forming Strata of Equal Aggregate Size," JASA, 59,
481-486.

ORIGINAL PAGE IS
OF POOR QUALITY

N82' 23134

D12

OPTIMAL USE OF ELECTROPHYSIOLOGICAL INDICATORS
OF MUSCULAR EFFORT AND FATIGUE

Otis L. Updike, Ph.D.

University of Virginia

1981 NASA-ASEE Summer Faculty Fellow

Supervisors:

James L. Lewis, Jr., Ph.D., Chief
Crew Station Design Section

Michael M. Thomas, Manager
Design Performance Laboratory

Barbara J. Woolford, Manager
Anthropometric Measurements Laboratory

(Crew Station Branch
Spacecraft Design Division)

NATIONAL AERONAUTICS AND SPACE ADMINISTRATION

LYNDON B. JOHNSON SPACE CENTER

HOUSTON, TEXAS

August 21, 1981

ACKNOWLEDGEMENTS

Many associates deserve the appreciation of the writer for assistance, subtle and gross, on this summer project. Among these are my supervisors, James Lewis, Barbara Woolford, and Michael Thomas, who gave encouragement and assistance in time of need; fellow Fellows Charles Bennett, Charles McKinley, and David Chesak, who exchanged with me helpful information; colleague Milton Adams at the University of Virginia, who called attention to aspects of neuromuscular physiology; and librarian Martin McDonough, who put up with my flood of requests for reference copies. I am grateful to all these, and to others at JSC whose assistance was chiefly patient and cordial hospitality.

- *CLM*

ABSTRACT

Electromyograms (EMG) from working muscles convey information on effort and fatigue. Their application, e.g. to assess the demands of vehicle control tasks, is complicated by the cooperative action of sets of muscles, by both intrinsic and imposed filtering, and by numerous other sources of variation. Fourier analyses of these noise-like signals offer one approach to interpretation; downward spectral shifts accompany fatigue. Techniques are being sought (in both time and frequency domains) for further condensing the wideband EMG signals, while retaining essential information, into a concise "state vector" usable in comparing control system designs. Moments of the spectral distribution of power (computed from improved estimates of the spectrum), descriptors from zero-crossing analyses, and mechanical and systemic stress indicators warrant further investigation as contributors toward an optimal index of muscle performance.

INTRODUCTION

The Crew Station Design Section, in particular the Design Performance Laboratory, is charged with anticipating the demands which tasks performed during weightlessness and in spacesuits will impose on Shuttle crews. Tools and equipment -- for example, controls -- will need to be optimally human-engineered for safe, efficient use. Further in the future, space construction or repair during EVA will impose demands still more stringent -- and harder to specify.

Simulated space tasks can yield information for the system designers on the demands and effects to be expected. Obviously needed are measures of effort, fatigue, and alertness; as these conditions suggest, both physical and psychological effects should be monitored. Variables appropriate for indicating such conditions are electrophysiological activity, mechanical forces, and systemic stress indicators like galvanic skin response and heart rate. These primary measurands can be picked up from such unobtrusive sensors as surface electrodes while subjects perform simulated -- or actual -- work. They should prove useful not only in design-oriented tests but also, later, in feedback training and perhaps in providing early warnings of physiological limits during arduous space work.

The primary measurands are, however, not directly usable. Instead they will yield derived variables, as discussed below. The objective is a versatile physiological index. Such an index is unlikely to be a single number; it will typically be a "state vector", analogous to the state vectors used in control system design. Its components (or their weighting) will be selected optimally for the application of interest, so its dimensionality will match each intended use.

PHYSIOLOGICAL BACKGROUND

History

Myoelectric studies -- investigation of electrical activity of muscles -- date back two centuries to Galvani's demonstrations (1786). DuBois-Reymond, in

1843, first clearly demonstrated electrical signals from human muscles; and this work was continued by such notables as von Helmholtz and Duchenne. Muscle physiology reached the point of recognition of the motor unit and its neuromuscular interactions just over 50 years ago (e. g., with Adrian and Bronk). The foundation for electromyography was laid, and with more sophisticated electronics in the 1950s myoelectric research accelerated. By 1960 several groups had reported changes in EMG amplitude and waveform indicative of fatigue, and several workers reported correlations of integrated EMG signals (IEMG) with force of contraction.

The following decade saw rising interest in the spectral analysis of EMGs -- first with filter-type analyzers and later with the fast Fourier transform (FFT). In the 1970s emphasis increased on elucidating the mechanisms for myoelectric changes and on applying the EMG to ergometric questions of effort and fatigue (as well as to diagnosis of neuromuscular disorders and to prosthetic rehabilitation).

Basic Neuromuscular Physiology

The muscles of current concern are skeletal (voluntary, or striated) in type. Their cellular units, the muscle fibers, are under 100 micrometers in diameter; though usually smaller, they may be as long as 300 mm. Two chief kinds of fiber occur, in differing proportions, in various skeletal muscles. One, the "pale", "fast", or "phasic" fibers, shows rapid but brief twitch responses and is used for precise movements. The "red", "slow", or "tonic" fibers respond slowly but with large twitches and are important for posture maintenance and other more leisurely contractions. Their high myoglobin content gives them superior endurance. (Intermediate types also exist.)

Groups of fibers, called motor units (MU), are innervated from a single motor neuron. A "spike" of electrochemical activity (wave of membrane depolarization) arriving down this nerve fiber evokes a similar response of depolarization in all the fibers belonging to one motor unit, resulting in a mechanical twitch. Since hundreds of MUs cooperate in even a small muscle the twitches, milliseconds in duration, blend into an effectively continuous contraction.

The electrical activity of a single MU firing -- the MUAP (motor unit action potential) -- arises from ion fluxes causing a reversal of polarity across the cell membrane, followed by a prompt return to the original state (depolarization and repolarization). These events propagate as a wave along each muscle fiber at 2 - 6 m/s. Electrodes in the vicinity of the moving wave of a single fiber sense the resulting currents as a diphasic voltage pulse; the potential swings up, then down, to perhaps +200 and -200 μ V, before returning to baseline levels. Similar pulses are being generated, concurrently, on the other fibers of the MU, and there is both spatial and temporal dispersion. Signals picked up by electrodes not actually penetrating the fiber, therefore, are a summation which appears as a mono-, di-, or polyphasic pulse of 5 - 20 ms duration (typically \sim 9 ms)[DeLuca, 1979]*. When a muscle is contracting, developing sustained force, action potentials occur repetitively as "trains", or MUAPTs.

At significant force levels, hundreds of motor units are producing MUAPTs. Remote electrodes (e. g., surface electrodes perhaps \sim 10 mm from the muscle) pick up the summation of myriads of pulses in an "interference pattern". A physicist or engineer, viewing this activity on a scope, recognizes broadband noise. (Amplified and reproduced by a loudspeaker, the sound is like rain on a roof.) The frequency spectrum and amplitude probability density carry information as to strength of contraction and as to the population distribution of motor units.

EMG Changes with Increasing Force

It is instructive to consider the changes in the EMG as the neural spike frequency increases (to increase the force of contraction)[Bouisset, 1973]. The initially sparse MUAPTs become more frequent, as more MUs go into action; this is "spatial recruitment". Pulse intervals of the different MUAPTs are randomly distributed, so spatial recruitment makes the amplitude distribution of the EMG more nearly gaussian. When the "interference pattern" is fully established, there is both cancellation and reinforcement among overlapping MUAPs, and the net distribution of amplitudes is quite gaussian.

*References cited in this report are a selected, minimal set from a compilation of over 160 sources. This collection, with brief annotations as to coverage, can be supplied on request.

As more force is neurally commanded, many MUs increase their firing rate; this change in the MUAPT pulse interval is "temporal recruitment". Often the proportion of larger MUAPs from the slow fibers increases. Some investigators cite evidence for increasing synchronization -- additive interference -- among MUAPTs at high force levels. All these force-augmenting mechanisms have only minor effects on the EMG signal spectrum but increase the average amplitude (measured as increased IEMG -- integrated full-wave-rectified EMG voltage -- or as EMG power). Several models whose behavior mimics that described lend support to this account of events [e. g., Person and Libkind, 1970; DeLuca, 1979; Piotrkiewicz, 1978; Miyano and Sadoyama, 1979].

The EMG Spectrum and Fatigue Effects

Fatigue develops with sustained or repeated strong contractions; the time scale depends on the force level, the muscle types, subject motivation, responsibility, and boredom. A quantitative index of physical fatigue, distinct from the poorly quantifiable psychological factors, has been a goal of many investigators [e. g., Kadefors et al., 1973; Hjorth, 1973; Viitasalo and Komi, 1977; Drosin, 1977; Lindström et al., 1977; Kadefors et al., 1978; Petrofsky, 1979]. Spectral changes (or their time-domain equivalents) are the best indicators thus far recognized.

The EMG signal is band-limited, non-white (and, during fatiguing exertions, non-stationary) noise with a power spectrum dependent on

- muscle size, composition, and distance from the pickup electrodes;
- electrode size, spacing, and placement relative to the fiber axes;
- temperature and chemical factors of the tissue environment.

Most of these variables can be held constant or chosen (as can amplifier input impedance) in a range where they have negligible effect on the spectrum. As a result, EMG spectral analysis is a practical approach to fatigue monitoring.

The power spectrum of the EMG signal extends from <10 Hz to >10 kHz, but most of its power (and information) lies between perhaps 20 and 300 Hz. As the source is distributed in space and time -- phase-dispersed, traveling waves on spatially dispersed muscle fibers -- surface electrodes act as if

a filter is interposed between the summed-MUAPT source and the output. This both gives surface electrodes a low-pass characteristic, relative to intramuscular (needle or wire) electrodes, and produces a differentiating effect which enhances high frequencies but reduces amplitude from closely spaced (e. g., 1 mm) differential electrodes [Kadefors, 1973].

With strip-form surface electrodes transverse to the muscle fibers, a further spectral feature may appear: a series of dips at harmonically related intervals in the power spectrum. These arise from nulls in the response of a differentially connected electrode pair to moving-wave sources, and their frequencies yield information on wave velocity [Lindström and Magnusson, 1977; Lynn, 1979].

When all the interfering variables are held constant, fatigue is found to skew the EMG spectrum toward lower frequencies. Several causes have been proposed:

- wave-velocity decreases due to ischemic effects (blood flow restriction), which causes depletion of oxygen and glucose plus accumulation of metabolic products (e. g., lactic acid);
- shift of activity to the slow, tonic fibers which contribute lower frequencies; or
- velocity changes of thermal origin.

Experiments best support the first two of these.

Modifying and Interfering Effects

Numerous factors complicate the use of EMG characteristics to indicate fatigue and effort.

- Mammalian muscles are very diverse in size of fibers, in numbers of fibers per motor unit, in proportions of slow and fast fibers, and probably in thresholds for recruitment and synchronization.
- Muscles occur in groups, with the result that (a) three or more muscles must be monitored for almost any task, and (b) the redundancy allows load-shifting among "equivalent" group members as a fatigue response.

- Muscles may be loaded isometrically (constant-length), isotonically (constant-tension), or neither, with quite different sensitivities of indicator variables.
- Available force (maximum voluntary contraction) and fatigability depend strongly on degree of muscle extension and on velocity of contraction.
- Beyond the filtering effect of distance, the character of signal picked up by surface electrodes varies with their location (on the belly or near the ends of a fusiform muscle) and on location relative to fiber axes.
- Intersubject variations occur, especially with training but also with motivation and other psychological factors.

The consequences of these effects are extreme requirements for standardization in tests aimed at developing indicators of muscle performance, disparity among published results for different systems, and lengthy experimental programs yielding data of restricted applicability.

SIGNAL INTERPRETATION

Directly Observable Characteristics

With a minimum of processing, several features of the EMG signal are evident. The integrated absolute value (IEMG) and the power (proportional to amplitude squared) are both readable, in a semiquantitative sense, from the oscilloscope pattern; and both tend to correlate with force. The ratio of a-c to d-c components can be observed roughly. The spectral distribution is crudely readable, especially at high sweep speeds, from the "jaggedness" of the pattern; as low frequencies become dominant, the trace gets smoother. Rhythmic effects, associated with tremor and perhaps synchronization, may be evident. All these effects may be quantitated, where useful, by analog or digital computation and may be presented as real-time indicators.

Spectral Analyses

The downward skew in EMG power spectrum is a widely accepted fatigue indicator.

It has been summarized in several low-dimensional descriptors. One is the H/L ratio: the ratio between power in a high band of frequencies (e. g., 62 - 100 Hz) to that in a low band (e. g., 12 - 50 Hz). This descriptor decreases steadily with isometric fatigue. Another one-dimensional descriptor is the mean power frequency (MPF), which splits the spectral power into equal high and low bands [Viitasalo and Komi, 1977, 1978]. It, too, decreases monotonically with fatigue. More detail has been sought by dividing the myoelectric power spectrum into 4 - 6 bands whose trends with work-time are compared. Commonly observed has been a falling trend in the highest band, a rise in the lowest as fatigue develops, and relative constancy for intermediate bands. Except for random fluctuations, the result provides a discrete approximation to "spectral shape" [Komi and Viitasalo, 1976].

All these ways of characterizing spectral skew suffer (a) from sensitivity to filter characteristics -- for both the band-defining filter, whether physical or computational, and the inescapable filtering effect of the muscle-tissue-electrode system -- and (b) from artifact, chiefly the power-line frequency (and harmonics), which require further band-rejection filters to "notch them out". Better digital analysis and filtering schemes will improve these approaches.

A further spectral technique is "dip analysis" [Lindström and Magnusson, 1977]. It employs the quasi-nulls mentioned above to estimate propagation velocity of the wave in the muscle fibers, which declines with fatigue. The main drawback of dip analysis is its requirement for optimal placement of electrodes and for very "clean", high-resolution spectra. It, too, will benefit from improved analysis and filtering schemes.

Time-Domain Analyses

A time series such as the EMG signal may be searched for a concise set of descriptors in the time domain, the frequency domain, or both. Characteristics in each domain, of course, have counterparts in the other; so choice of domain depends on computational convenience, utility of the descriptors, and the user's preference. Time-domain descriptors, common in ECG and EEG interpretation, were more common a decade ago than now -- owing, in part,

to the convenience of producing the FFT with computers specialized toward integral transforms. (The autocorrelation, a time-domain function, is now usually computed by a discrete Fourier transform followed by an inverse transformation.) In the writer's view, a combination of descriptors from both domains may well yield the optimal state vector to characterize muscle condition.

Several time-domain approaches have been used on EMGs. Individual MUAPTs, picked up by intramuscular electrodes, have been analyzed on-line for rise time, peak amplitude, and amplitude/rise time ratio; an averaged MU potential (AMUP) has usually been so treated [Komi and Viitasalo, 1976; Viitasalo and Komi, 1977, 1978]. On interference patterns peak height distribution, peak count, and "turn count" (slope reversals per unit time) have been used, notably in ergonomic studies [Johnson, 1978] and diagnosis [Fusfeld, 1978]. Zero-crossings per unit time, preferably computed on a drastically amplified and clipped EMG signal, have had adherents [Hjorth, 1970, 1973; Saltzberg and Burch, 1971]. Zero-crossing rate has also been used as a quality-control check on signals which were subjected to spectral analysis [Kadefors et al., 1978].

These time-domain descriptors tend to suffer from sensitivity to system noise (often artifactual) and distortion, particularly when they require local differentiation or equivalent operations. Descriptors derived through integration -- transforms and correlation or coherence functions -- are more resistant to such error sources. Zero-crossing counts and intervals are moderately error-resistant among the non-integral descriptors.

The time-domain methods for analyzing time-series data used by statistical analysts [Box and Jenkins, 1976] -- autoregressive (AR), moving-average (MA) and ARMA techniques -- deserve consideration for EMG interpretation. These focus on the random fluctuations, stripping off systematic trends. They prove to be equivalent to certain new frequency-domain techniques which are discussed below [Childers, 1978].

Options for Exploration

Several approaches hold promise for improved EMG analyses. It appears that most simple descriptors have received attention; but better computational capabilities, now available at affordable costs, justify further consideration of selected cases.

Such a case is spectral moments. The MPF, mentioned above, is the lowest moment of the power spectral density; and higher moments of course exist. A complete set of moments would fully characterize the spectrum "shape". (Symmetry makes alternate moments zero, and the lowest few may suffice.) This viewpoint has been applied to two moments by Kadefors et al. [1977, 1978] to yield a "fatigue index".

These workers related the index to wave velocity, providing a link to a clearly-defined physical variable and thus adding confidence as to the significance of these descriptors. The data were normalized, compensating out some errors. Adding to the attractiveness of velocity is its capability of being estimated by dip analysis [Lindström, 1977] and by an on-line method using digital filters [Lynn, 1979], so that alternate check methods are available.

Enhanced spectrum estimation methods -- the maximum-entropy and maximum-likelihood methods (MEM, MLM) have recently been developed [Childers, 1978]. These are intimately related to AR and MA techniques, as developed in the reference cited (a compilation of recent papers presenting advances in spectrum-analytic techniques). They should yield improved spectra, possibly ones in which the noise-prone higher moments are significant enough for use. The possibility that phase, available from some spectral estimates, carries useful information is unexplored. (Spectral power is phase-independent.)

The zero-crossing, or period-analytic, methods described by Hjorth [1970] and applied by him to EEGs, have been related to spectral moments [Hjorth, 1973; Saltzberg and Burch, 1971] and give similar information by a different computational route. In the time domain they are quite simple to apply, on-line, and they promise both direct utility and the possibility of checking spectrally derived moments.

Systemic and biomechanical indicators should usefully complement the descriptors derived from the EMG. Force variations -- tremor and step changes -- obviously correlate with fatigue. Indicators of autonomic nervous system activity -- galvanic skin response (GSR) and heart rate (HR) -- and possibly respiratory variables and even electroencephalographic activity

may indicate general stress. These are known to respond to fatigue, but often in nonlinear and nonrepresentative ways. They have the merit, though, of bringing in the psychological factors that are so hard to quantify. They should therefore be considered -- with care -- as contributors toward a "muscular state vector".

Finally, serendipitous spinoffs from work on myoelectric prosthesis control [e. g., Hogan and Mann, 1980] may advance the goal of fatigue and force evaluation. There is a remote chance that "cepstral" techniques [Childers et al., 1977] -- which have been applied to EEG signals -- may have some use; though these are usually associated with sound propagation, they may prove to have some capability of educing the periodicities in MUAPTs. They are largely untried.

RECOMMENDATIONS

As a result of extensive critical review in the fields of muscle physiology, related biotechnology, and applicable signal processing, the writer offers the following recommendations for extending the work at the Crew Station Design Section [v. Lewis, 1979] toward a state vector which is both useful and feasible for evaluation. This direction should lead to the optimal index needed for spacecraft design -- though optimality may be hard to prove!

- The applicability of spectral moments toward a fatigue index should be further investigated, with appropriate computation on existing data followed by further experiments.
- The time-domain, period-analytic approach to moments should be compared with the frequency-domain estimation now permitted with the new MEM and MLM spectral estimation techniques.
- Systemic indicators, especially GSR, HR, and force variations, should be monitored in any further fatigue studies.
- Recurring reassessments of the adequacy of currently accessible state vectors should be planned as new data continue to be gathered.

REFERENCES

- Bouisset, S., "EMG and Muscle Force in Normal Motor Activities", in New Devel. Electromyog. Clin. Neurophysiol. (Desmedt, J. E., ed.) Vol. 1, pp. 547-583 (Karger, Basel, 1973)
- Box, G. E. P. and Jenkins, G. M., "Time Series Analysis: Forecasting and Control" (Holden-Day, San Francisco, 1976)
- Childers, Donald G. (ed.), "Modern Spectral Analysis" (IEEE Press and John Wiley, New York, 1978). N. B.: This book is a collection of recent reprints of papers on the topic, most of which are relevant where cited in this text; it is the most convenient place to refer to these related papers, hence is cited in toto.
- Childers, D. G., Skinner, D. P., and Kemerait, R. C., "The Cepstrum: a Guide to Processing", Proc. IEEE 65: 1428-43 (1977)
- DeLuca, Carlo J., "Physiology and Mathematics of Myoelectric Signals", IEEE Trans. Biomed. Eng. BME-26: 313-25 (1979)
- Drosin, Allain B., "Mechanical and Electrical Manifestations of Fatigue in the Muscles of Pronation and Supination", Bull. N. Y. Acad. Med. 53: 615-27 (1977)
- Fusfeld, R. D., "Instrument for the Quantitative Analysis of the EMG", Med. Biol. Eng. 16: 290-95 (1978)
- Hjorth, Bo, "EEG Analysis Based on Time-Domain Properties", Electroencephal. Clin. Neurophysiol. 29: 306-10 (1970)
- Hjorth, Bo, "The Physical Significance of Time-Domain Descriptors in EEG Analysis", Electroencephal. Clin. Neurophysiol. 34: 321-25 (1973)
- Hogan, N., and Mann, R. W., "Myoelectric Signal Processing: Optimal Estimation Applied to EMG: I. Derivation of the Optimal Myoprocessor. II. Experimental Demonstration of Optimal Myoprocessor Performance", IEEE Trans. Biomed. Eng. BME-27: 382-410 (1980)
- Johnson, J. C., "Comparison of Analysis Techniques for EMG Data", Aviat. Space Envir. Med. 49 (1 Pt. 1): 14-18 (1978)
- Kadefors, R., "Myo-Electric Signal Processing as an Estimation Problem", in New Devel. Electromyog. Clin. Neurophysiol. (Desmedt, J. E., ed.) Vol. 1, pp. 519-32 (Karger, Basel, 1973)
- Kadefors, R., Petersén, I., and Broman, H., "Spectral Analysis of Events in the Electromyogram", in New Devel. Electromyog. Clin. Neurophysiol. (Desmedt, J. E., ed.) Vol. 1, pp. 628-37 (Karger, Basel, 1973)
- Kadefors, R., Lindström, L., Petersén, I., and Örtengren, R., "EMG in Objective Evaluation of Localized Muscle Fatigue", Scand. J. Rehabil. Med. 6: 75-93 (1978)
- Komi, P. V., and Viitasalo, J. H. T., "Signal Characteristics of EMG at Different Levels of Muscle Tension", Acta Physiol. Scand. 96: 267-76 (1976)
- Lewis, James L., "Operator Performance and Localized Muscle Fatigue in a Simulated Space Vehicle Control Task", NASA Tech. Memo. 58 220 (June 1979)

- Lindström, L., Kadefors, R., and Petersén, I., "An Electromyographic Index for Localized Muscle Fatigue", J. Appl. Physiol.: Resp. Envir. Exer. Physiol. 43: 750-54 (1977)
- Lindström, Lars H., and Magnusson, R. I., "Interpretation of Myoelectric Power Spectra: a Model and Its Applications", Proc. IEEE 65: 653-62 (1977)
- Lynn, P. A., "Direct On-line Estimation of Muscle Fiber Conduction Velocity by Surface Electromyography", IEEE Trans. Biomed. Eng. BME-26: 564-71 (1979)
- Miyano, H., and Sadoyama, T., "Theoretical Analysis of Surface EMG in Voluntary Isometric Contraction", Europ. J. Appl. Physiol. 40: 155-164 (1979)
- Person, R. S., and Libkind, M. S., "Simulation of Electromyograms Showing Interference Patterns", Electroencephal. Clin. Neurophysiol. 28: 625-32 (1970)
- Petrofsky, J. S., "Frequency and Amplitude Analysis of the EMG During Exercise on the Bicycle Ergometer", Europ. J. Appl. Physiol. 41: 1 - 15 (1979)
- Piotrkiewicz, M., "A Study of Surface Electromyograms by Means of Digital Simulation. I. The Principles of a Model of Surface Electromyogram", Electromyog. Clin. Neurophysiol. 18: 83-94 (1978)
- Saltzberg, B., and Burch, N. R., "Period-Analytic Estimates of Moments of the Power Spectrum: a Simplified EEG Time-Domain Procedure", Electroencephalog. Clin. Neurophysiol. 30: 568-70 (1971)
- Viitasalo, Jukka H. T., and Komi, P. V., "Signal Characteristics of EMG During Fatigue", in Applied Physiology and Occupational Physiology, pp. 111-21 (Springer-Verlag, 1977)
- Viitasalo, J. T. et al., "Interrelationships of EMG Signal Characteristics at Different Levels of Muscle Tension and During Fatigue", Electromyog. Clin. Neurophysiol. 18: 167-78 (1978)

P13

MEASUREMENT OF TRACE LEVELS
OF CHLORINE IN THE STRATOSPHERE

EN82 23135

Doris C. Warren, Ph.D.

Houston Baptist University

1981 NASA-ASEE Summer Faculty Fellow

Supervisor:

Donald E. Robbins

Space Environment Office

Earth and Planetary Sciences Division

Abstract - Mathematical models of stratospheric ozone have predicted a reduction in the total ozone due to chlorofluoromethanes released into the atmosphere. Analytical procedures for the collection of air in the stratosphere and for analysis of these air samples for trace levels of chlorine, irregardless of the state of chemical composition, have been developed. Calibration experiments are being conducted in order to validate all methods and procedures. Results of neutron activation analysis calibration procedures using standard chlorine gases are included.

NATIONAL AERONAUTICS AND SPACE ADMINISTRATION

LYNDON B. JOHNSON SPACE CENTER

HOUSTON, TEXAS

AUGUST 21, 1981

INTRODUCTION

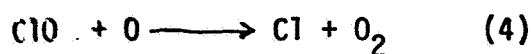
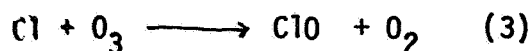
In 1981 the controversy surrounding chlorofluoromethanes (CFC's) and the reduction of stratospheric ozone continues. A potentially serious problem with CFC's was identified and received major public attention in 1974, when Dr. F. Sherwood Rowland and Dr. Mario J. Molina at the University of California, Irvine presented their theory of ozone destruction by CFC gases (1) at a National American Chemical Society meeting.

The compounds of main concern in the continuing ozone debate are fluorocarbon-11 (CFCl_3) and fluorocarbon-12 (CF_2Cl_2). The problem with CFM's is that the compounds are extremely inert. When used as aerosol propellents or refrigerants-probably the best known are the DuPont Freons-the compounds escape to the lower atmosphere. Since the compounds are inert, they do not decompose in the lower atmosphere but eventually find their way into the stratosphere.

Ozone is formed in the stratosphere according to the following reactions:



According to the Rowland-Molina hypothesis, chlorine, in the stratosphere, may participate by means of a catalytic process in a cycle which will break down ozone, O_3 , into diatomic oxygen, O_2 . It has been proven by laboratory measurements that the CFC's absorb ultraviolet radiation (190-225 nm) and decompose to atomic chlorine and other products. Then according to the hypothesis the following reactions occur:



Several other reactions, involving species such as HO, HO₂, NO and NO₂, may also contribute to ozone destruction. The question to be answered is whether chlorine atoms react in the stratosphere as they do in the laboratory.

Early experiments centered around the measurement of ozone, C10 and CFM's in the stratosphere. Mathematical models of stratospheric ozone were developed and predicted reductions in the total ozone (amount in a unit vertical column) from CFC's released in the atmosphere. These reductions were first predicted to be several percent, building up over a few decades. Since much concern developed over whether human activity might seriously reduce the earth's protective layer of ozone, in 1979, fluorocarbon 11 and 12 aerosol products were banned from interstate commerce in the United States.

In a new report (2), released in late 1979, a panel of the National Academy of Science warns that it foresees many thousand of additional cases of skin cancer, if the ozone layer, which filters the sun's ultraviolet rays, continues to be eroded by fluorocarbon. The forecasts for stratospheric ozone eventual losses have been revised upward to 18.5%.

As a result of these new warnings, in October 1980, the Environmental Protection Agency announced that it was considering further measures to reduce the level of fluorocarbons released into the atmosphere (3). EPA's intention is to limit production of CFC's in the U.S. to 30% of their present levels. This production limit could seriously affect the refrigeration market.

THE PROBLEM

The National Academy of Sciences stressed the desirability of obtaining "a direct check on ozone reduction predicted for the CFM's" (4). This appears to be a difficult task because the total ozone varies, from apparently natural processes, by as much as 50% at mid-latitudes in a year's time. The

-3-

relationship of the earth's position to the sun causes a variation of the electromagnetic radiation reaching the earth's atmosphere, therefore causing a change in the amount of ozone formed. Secondly, during one year's time the amount of mixing of the air between the troposphere (layer next to the earth) and the stratosphere varies.

Results of modelling calculations have shown (4,5) that the greatest percentage reduction in ozone from CFM's occurs in the upper stratosphere from 35 to 45 km. The limited measurements of ozone in the upper stratosphere available indicate that the natural variations of ozone concentration are smaller at altitudes of 35 - 45 km. Direct in-situ measurement of ozone in the region of interest are thus necessary. Instrumentation, previously used with demonstrated accuracy, is available for collection of data to construct ozone concentration profiles. The ozone concentrations are being measured by U V absorption from balloon platform, satellites, rockets and ground-based instrumentation.

During the past five years, analytical models of the stratosphere have shown a greater sensitivity of ozone photochemistry to the chlorine catalytic cycle. At the same time measurements have produced questions about the accuracy of the model predictions (6). The questions concern differences in measured and predicted concentrations of the more reactive chlorine species. There is reasonably good agreement for the more inert chlorine constituents. Values from initial measurements of the HCl profile above about 30 km, the ratio of HCl to HF, and the ratio of ClO to ozone do not follow from current models. The sum of the chlorine concentrations measured (HCl, CF₂'s and ClO) is higher than what is predicted by the models. These discrepancies are not trivial and suggest that something is missing from the chemistry used in

Present models. The models agree more or less closely with one another, of course, because they are all based on essentially the same reactions and rate constants. The predicted value for total chlorine concentration in the stratosphere is approximately 3 parts per billion (ppb).

Because of these conflicting views, it becomes apparent that more experimental measurements are needed. The recent NAS report (2) states that "a total chlorine concentration measurement would be of great value." This recommendation is further emphasized by the recent NASA report on the same subject. The NASA report lists total chlorine as one of "a few species for which new and improved techniques must be developed." (7)

TOTAL CHLORINE MEASUREMENTS

We, at NASA-Johnson Space Center, are developing analytical procedures for the collection of air in the stratosphere and for analysis of these air samples for trace levels of chlorine, irregardless of the state of chemical composition.

Accurate measurement of trace levels of organics such as the CFM's and reactive inorganic species such as Cl, ClO and HCl in the stratosphere provide a complicated problem in analytical methodology. An even more complex task to accomplish is the determination of total stratospheric chlorine. The total chlorine mixing ratio is believed to approach a constant value around 25 to 30 km and remain constant above that. Hence NASA stratospheric chlorine experiments are concentrating their effort on the region above 25 km.

In our experiment, whole air samples will be collected from a balloon platform in the stratosphere by using a cryopump that operates at liquid neon temperature (27°K). The whole air samples will be returned to ground where total chlorine content will be measured by neutron activation analysis (NAA). Flights will originate from the NCAR balloon facility located at Palestine,

Texas. The NAA part of the experiments are conducted at the Texas A & M Nuclear Science Center in College Station, Texas,

Most of the effort to date has concentrated on proving the experiment's feasibility by developing procedures to avoid contaminating the sample or losing the chlorine. In addition, absolute calibration of the system must be obtained. The experiment is an arduous undertaking because the mixing ratios of total chlorine in the stratosphere are expected to be about 3 ppbV. The atmospheric species consist of highly reactive forms, such as HCl, ClO, ClO, NO₂, and Cl in addition to the chlorofluoromethanes. Furthermore, contamination of the air sample by the comparatively large concentrations of chlorine compounds at ground level must be avoided. In spite of these difficulties, significant progress has been made.

In Figure 1 the general outline of laboratory measurements is shown. Experiments have been conducted at each step of the general plan of analysis in order to validate the precision and accuracy of the measurement and to determine any problems with the procedure. A calibration gas (an air sample containing a known concentration of contaminant, HCl or CFM) was necessary. A permeation instrument was obtained (Kin Tek Laboratories, Texas City, TX) to prepare dynamically blended, calibrated, low concentration gas mixtures (air or liquid nitrogen boil-off and HCl or CFM). "Zero" grade air is further purified by cooling the air to approximately 107°K in a mixture of isopentane and liquid N₂. Any residual chlorine contaminants is frozen out of the air before use as a diluent in preparation of the standard gas mixture.

A cryogenic pumping system employing liquid neon is used to freeze the samples of air in the collection containers. This is done in order to obtain

a larger volume of air for sampling at one time. The selection of a suitable container for sample collection and storage is a real problem. Almost any surface, with which air sample comes in contact, such as residues on glass, metal or plastic collection apparatus, becomes a potential source of contamination. Thus careful cleaning procedures for all surfaces the air sample contacts must be followed. We have found that glass surfaces cleaned with 1%HF solution followed by evacuation at least overnight is sufficient. Metal surfaces are cleaned by baking under vacuum for an appropriate period of time.

Loss of trace concentrations of chlorine containing compounds on container surfaces is by far the most serious experimental problem. Loss of Freon from quartz vessels was about 11%, while loss of ppb levels of HCl in stainless steel collection bottles was about 65%. Inexpensive collection methods employing pre-evacuated grab sample containers, condensation traps, adsorption tubes and/or plastic grab bags, commonly used for atmospheric gas analysis are not suitable because of sample loss during collection and storage. We have fabricated two collection bottles which are now ready to be evaluated. One bottle is stainless steel coated with a layer of gold and the other bottle is constructed from tantalum, which should be inert enough that chemisorption will not occur to any large extent.

Neutron activation analysis (NAA) was chosen as the method of Cl analysis. The two reasons for this choice are, first, that radioactive measurements give elemental analysis results at lower limits of detection over any other analytical technique available today. NAA has a high degree of sensitivity for the majority of elements. Secondly, with NAA the number of Cl atoms present in a sample can be measured without regard to the state of chemical combination of the Cl. Another advantage of NAA is that it is essentially a non-destructive method of analysis. Non-destructive analysis involves minimum sample manipulation and,

therefore, a trace analysis sample is not contaminated by reagents and containers as in conventional destructive wet-chemical techniques.

NAA involves bombarding the sample with neutrons (in a nuclear reactor) and measuring the radioactivity induced in the sample using gamma-ray spectrometry. A method of calibration for the element of interest must be developed. The standard should preferably be internal to the sample taken for analysis or, if not, the standard should contain a known amount of the element of interest. It is important that the irradiation assembly must provide the same neutron flux for both sample and standard or appropriate correction factors must be determined. The main thrust of this summer's work has been to obtain an absolute calibration of quartz rod flux monitors. The number of chlorine atoms in nine flux monitors were measured in comparison to a known Freon 12 standard. The results are shown in Table 1. When the data is combined the average number of chlorine atoms per mg of quartz is 2.156 ± 0.083 with a 3.8% error.

One limitation of NAA is that like most analytical methods it suffers from possible matrix effects and interferences. Preliminary examination of NAA results from irradiation of air samples containing chlorine indicated that the presence of argon gave rise to Compton Scattering which produced a large background in the region of the spectrum where the 1.6 and 2.2 MEV peaks of Cl occur. Because of this the Ar levels in the air must be reduced. The Ar concentration in the air sample is reduced by distillation. Each air sample (at liquid neon temperature) is warmed to liquid N₂ temperature. Most of the Argon in the air is thus removed while the chlorinated compounds remain. During this procedure, the pressure of the air sample taken is measured and the volume then calculated.

It would be ideal to irradiate the air sample in the collection bottle, but a material such as quartz which is penetrated easily by the neutrons must be used. Our air samples are transferred to quartz bottles cryogenically before irradiation (Figure 1). The quartz bottles must be sealed shut with a torch after the transfer. We have experimented with bottles having teflon stopcocks and quartz stopcocks. But these sample bottles could not withstand the irradiation conditions. The teflon stopcocks leaked and the quartz stopcocks were frozen closed.

The isotope activated is Cl^{37} which has an abundance of 24.47% of naturally occurring chlorine. Irradiating Cl^{37} with thermal neutrons produces the reaction $\text{Cl}^{37} + \text{N} \longrightarrow (\text{Cl}^{38})^*$. The resulting compound nucleus $(\text{Cl}^{38})^*$ decays to Ar^{38} with a 38.2 minute half-life emitting a beta particle and either one or two gamma rays (2167.5 or 1642.4 keV).

After the irradiated sample cools sufficiently to be handled, unfortunately, another step must be added to our analytical procedure (Figure 1) before counting can occur. The quartz bottles have a large enough chlorine content that the chlorine content of the sample cannot be measured while in the irradiated bottle. This requires a transfer of the air sample to a counting bottle. The counting bottle, which has a stopcock, is connected via a teflon tubing tee connection to the irradiated sample bottle. A scavenger gas, ethylene oxide, is connected to the third position in the tee. We found that it was necessary to use the ethylene oxide to react with and sweep the chemisorbed chlorine from the quartz bottle. The procedure is as follows: (1) the quartz bottle neck is scored and connected to the tee; (2) the neck is broken; (3) the radioactive

chlorine gas is transferred by cryopumping to the counting bottle; (4) the stopcock, to the counting bottle is closed; (5) the ethylene oxide is allowed to sweep through the quartz sample bottle; and (6) the resulting mixture is transferred cryogenically to the counting bottle. The radioactivity of each sample is measured and the number of chlorine atoms present can be calculated.

The analytical procedures have been developed and tested to the point at which a calibrated HCl sample can be introduced into the flight container. We must await the results of those experiments to consider this procedure feasible for accurate measure of chlorine in stratospheric air samples.

ORIGINAL PAGE IS
OF POOR QUALITY

REFERENCES

- (1) Chemical and Engineering News, Sept. 23, 1974, p. 27.
- (2) National Academy of Sciences Report, Stratospheric Ozone Depletion by Halocarbons: Chemistry and Transport (Washington, D.C., 1979), p. 134.
- (3) The Houston Post, June 14, 1981, Sec. C, p. 20.
- (4) National Academy of Sciences Report, Halocarbons: Effects of Stratospheric Ozone, (Washington, D.C., 1976).
- (5) NASA-GSFC, Chlorofluoromethane Assessment Workshop Report, March, 1977.
- (6) Chemical and Engineering News, Oct. 15, 1979, p. 26.
- (7) Robert D. Hudson and Edith I. Reed, ed., The Stratosphere: Present and Future, NASA Reference Publication 1049 (December, 1979).

ORIGINAL PAGE IS
OF POOR QUALITY

FIGURE 1

GENERAL PLAN OF ANALYSIS-LABORATORY MEASUREMENTS

Calibrated Gas Sample Prepared

Sample Collected in Tantalum Bottle
(cryogenic pumping)

Argon Interference Removed

Sample Transferred Cryogenically
to a Quartz Bottle

Chlorine Determined
by Neutron Activation Analysis

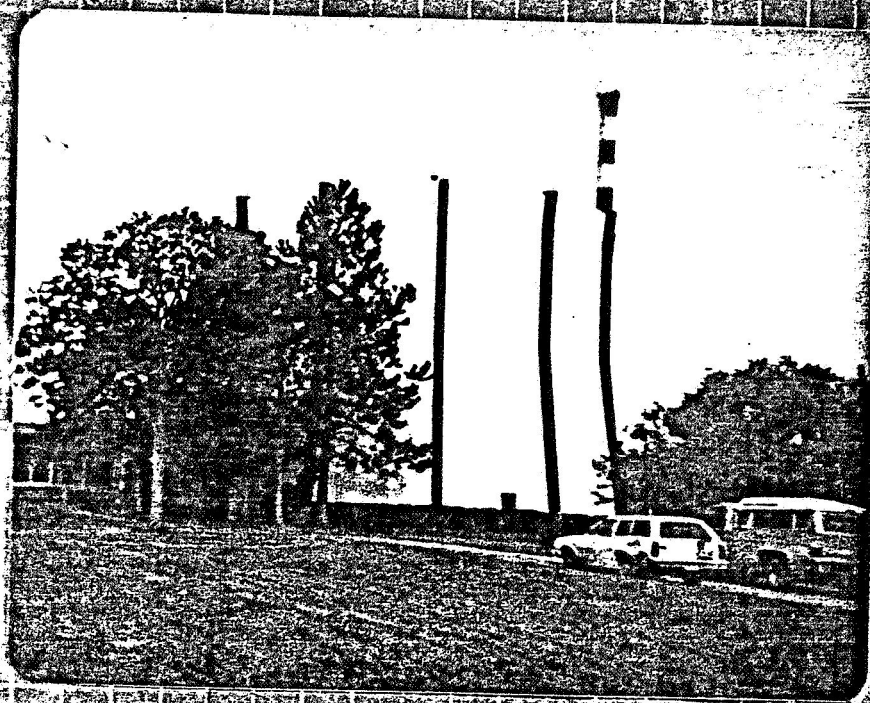
- A. Irradiation
- B. Cryogenic Transfer for Counting
- C. Sample Counted

ORIGINAL PAGE IS
OF POOR QUALITY

TABLE 1
ATOMS OF CHLORINE FOUND PER MILLIGRAM OF QUARTZ (SiO₂) CALIBRATOR TUBE

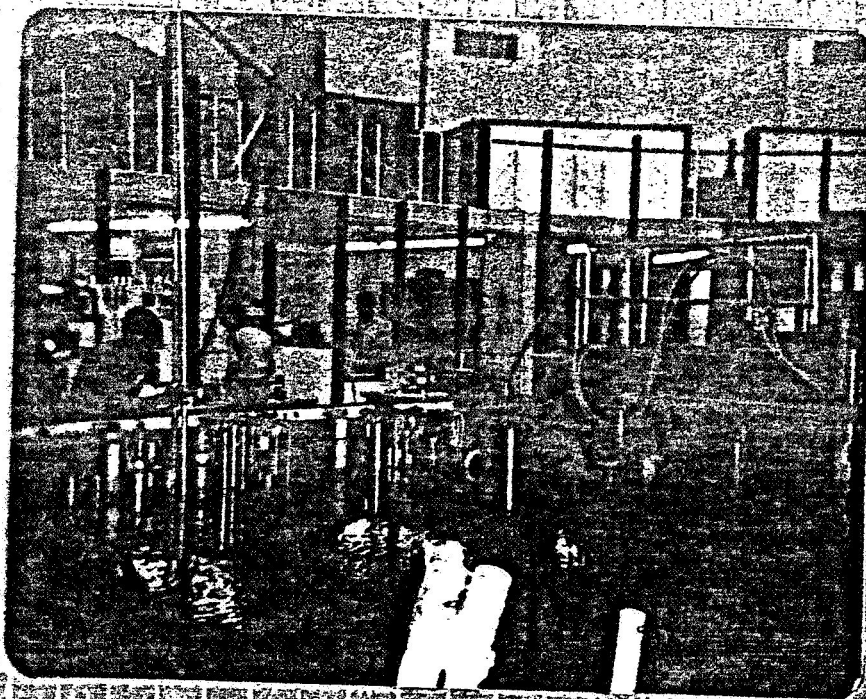
Calibrator Tube Number	Atoms of Chlorine Per mg of Quartz ($\times 10^{17}$)	
	Trial 1	Trial 2
1	2.174	2.320
2	2.202	2.327
3	2.103	2.173
4	2.122	2.132
5	2.112	2.118
6	2.099	2.112
7	2.061	2.211
8	2.084	2.211
9	2.039	--
\bar{X} (Individual trial)	2.111 ± 0.051	2.200 ± 0.085
\bar{X} (combined results)	2.156 ± 0.083	

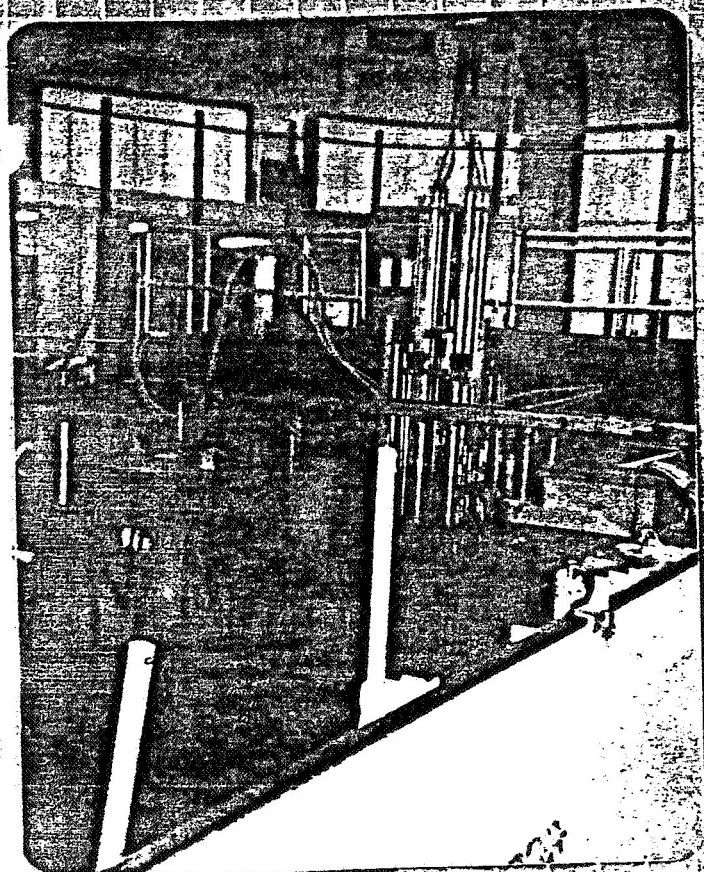
ORIGINAL PAGE
BLACK AND WHITE PHOTOGRAPH



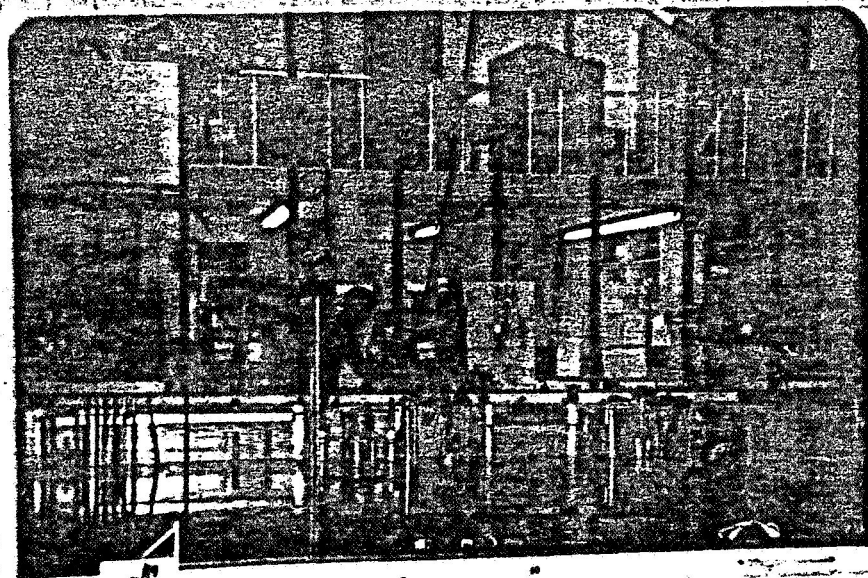
TEXAS A & M
NUCLEAR SCIENCE CENTER

ORIGINAL PAGE
BLACK AND WHITE PHOTOGRAPH





ORIGINAL PAGE
BLACK AND WHITE PHOTOGRAPH



ORIGINAL PAGE IS
OF POOR QUALITY

N82 23136

D14

COMPUTER SIMULATION OF CURRENT
COLLECTION IN A PLASMA ENVIRONMENT

Dino Zei, Ph.D.
Ripon College
1981 NASA-ASEE Summer Faculty Fellow

Supervisor
Bernard McIntyre, Ph.D., A.S.T.
Test Development Office
Space Environment Test Division

NATIONAL AERONAUTICS AND SPACE ADMINISTRATION
LYNDON B. JOHNSON SPACE CENTER
HOUSTON, TEXAS

August 20, 1981

During the summer of 1980, working as a NASA-ASEE Summer Faculty Fellow, Dr. Raj M. ^{KRISHNAN}~~Kushman~~ of North Texas State University considered the problem of the pattern of current collection by a biased strip of stainless steel (3' x 30' x 1/32") placed in the plasma environment produced by a 30cm Kaufman ion thruster.¹ The experiments were performed in Chamber "A" at the Johnson Space Center.

Two positions of collector relative to ion source were used: Edge-on (Figure 1) in which case currents were measured on both sides of the collector, and "Face-on" (Figure 2) in which case currents were again measured on both sides of the collector. In the latter case, the surface of the collector that faces the ion thruster is referred to as the "front" face, the other side as the "back" face.

A qualitative summary of the experimental results is as follows: For edge-on operation, there was no significant difference in the current collected by the two faces. For "Face-on" operation, the current collected by the two faces was different. In particular, for the back face, a focusing effect was observed.

1. 1980 Summer Faculty Fellow Report

As the bias voltage on the collector was increased, current was collected more toward the center of the panel. (The bias voltage was negative to collect positive ions. "Increasing" bias voltage means more negative.)

Solving the actual three-dimensional problems, with space charge present, is difficult and has not been accomplished to date. However, by assuming an infinite strip, the problem is reduced to a two-dimensional one, while still being a reasonably faithful reproduction of the experimental problem. If, in addition, one ignores the presence of space charge as a first approximation, the solution is of a standard form:

$$-\Phi = V_0 \left[\frac{1}{k} \cosh^{-1} \frac{1}{2a} \left(\sqrt{(x+a)^2 + y^2} + \sqrt{(x-a)^2 + y^2} \right) - 1 \right] \quad (1)$$

2a is the width of the plate (3 ft.)

X is measured parallel to the face, from the center line of the collector

Y is measured perpendicular to the face from the center line of the collector

-V₀ is the bias potential of the collector

$$k = \cosh^{-1} \sqrt{A^2 + Y_s^2}$$

Y_s is the distance along the Y-axis measured from the from face to where $\Phi = 0$

2. Kyrala, Ali; 1981 NASA-ASEE Summer Faculty Fellow Report

This solution represents a series of equipotential surfaces of elliptical cross-section. The particular ellipse representing zero potential has semi-minor axis equal to Y_s (the "sheath thickness"). The ellipse at potential V₀ degenerates into a straight line segment of width 2a. Thus the distance between foci for all ellipses representing equipotential surfaces is also 2a. From the geometry of the ellipse, the semi-major axis, X_s = $\sqrt{A^2 + Y_s^2}$.

A first modification to this idealized solution is to take into account the presence of space charge with the "Langmuir-Childs" law. This law states that the saturation current collected from a space charge is proportional to the 3/2 power of the potential of the collector. As a corollary to this law, the sheath thickness associated with the collector varies as the 3/4 power of the collector potential.² Thus a first modification made to the solution is:

$$-\phi = V_0 \left[\left\{ \frac{1}{k} \cosh^{-1} \frac{1}{2a} \left(\sqrt{(x+a)^2 + y^2} + \sqrt{(x-a)^2 + y^2} \right) \right\}^{4/3} - 1 \right] \quad (2)$$

The parameter 2a is 3 ft. (a = .457 meters)

The sheath thickness, $Y_s \propto (V_0)^{.75}$. From visual observations of the plasma, the thickness of the sheath when $V_0 = 2500$ volts, is approximately equal to the width of the plate. Thus, for any bias voltage on the collector, the sheath thickness is $Y_s = 2a \left(\frac{V_0}{2500} \right)^{.75}$, with V_0 measured in volts. Then, the semi-major axis of the ellipse at potential 0 is $X_s = \sqrt{A^2 + Y_s^2}$. Finally, $k = \cosh^{-1} \sqrt{1 + \frac{(Y_s)^2}{a^2}}$. This defines the parameters needed and also identifies a starting point for ion trajectories -- viz., the ellipse whose semi-minor axis is Y_s , and whose semi-major axis is X_s .

This modification by itself made no significant difference.

A typical result using equation (2) is shown in Figure 3. Because ions left the thruster with an energy of 15-20eV, each ion was given an initial velocity of 10,000 M/Sec toward the collector since this velocity corresponds to about 20eV for Argon.

Virtually every ion that strikes the back face goes through one of two points located at $(\pm .45a, -.19a)$. All trials at various bias potentials of the collector showed the same behavior, i.e., all ions striking the back surface go through one of two points. Furthermore, the two points did not appreciably vary in location with different bias potentials of the collector.

This suggests that after a very short time after the ion flow pattern is being established, succeeding ions will encounter a repulsive force -- the equivalent of positive charges located at the two points, $(\pm .45a, -.19a)$. However, since this represents a cross-section through an assumed infinitely long collector, this effect should be simulated by line charges parallel to the collector rather than by point charges. The field due to a line charge varies as $1/r$. By trial and error, the most reasonable strength to choose for a collector potential of 2500 volts turned out to be $\frac{50}{r}$ in M.K.S. units. For other potentials, the strength was chosen to be $(50/r) (V_0/2500)$. This was the second modification made to the idealized solution.

A third modification is arrived at by considering the expected difference between the sheath on the front face and that on the back face. The idealized solution gives complete symmetry. However, it is more reasonable to suppose that the sheath is considerably larger on the back side. Once the ions have gotten past the collector, they encounter different ambient conditions. The simplest way to simulate this effect, without introducing continuity problems at the boundary between two different sheath edges, is to assume that there is a grounded semi-infinite plate that continues from the sheath edge where it crosses the plane of the collector (Figure 4). Specifically, this modification was accomplished by standard imaging techniques.

A fourth modification is arrived at by considering that those ions which have gotten past the collector will have their initial speeds decreased. The greater the distance behind the collector from which ions are collected, the smaller their initial speed will be. Therefore, the initial velocity of the ions was gradually decreased until it was zero at the point directly below the edge of the collector (Figure 5).

Finally, a few ions were assumed to come from the region in the "shadow" of the collector (Figure 5).

The results of all these modifications is shown in Figures 6, 7, and 8.

Figure 6 (500 volts) shows that current is "focused" at a point 8% of the plate width from the edge. Figure 7 (1500 volts) shows that current is "focused" at a point 15% of the plate width from the edge. And finally, Figure 8 (2500 volts) shows that current is "focused" at a point 26% from the edge.

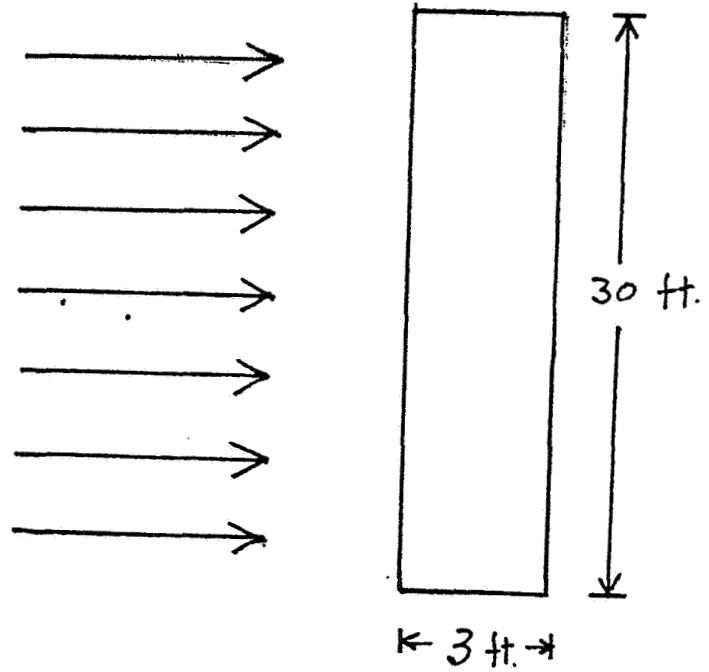
Thus, qualitatively, the experimental fact of current focusing as well as the variation of position of focusing with bias potential may be simulated by starting with an idealized solution for an infinite strip, and making the modifications listed above.

It seems clear that the focusing phenomena is due to ions that skirt past the collector and get drawn back in to the back side of the plate.

A copy of the program used on the HP 9830 is attached to the end of this report.

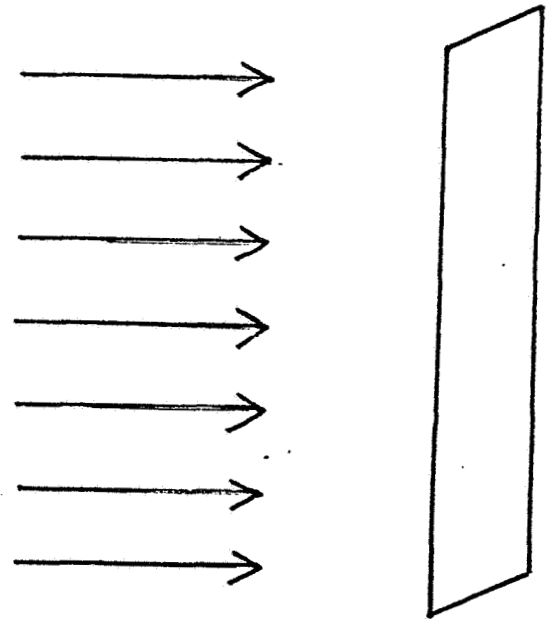
ORIGINAL PAGE IS
OF POOR QUALITY

PLASMA
FROM
THRUSTER



ORIGINAL ION DIRECTION PARALLEL TO FACE OF COLLECTOR

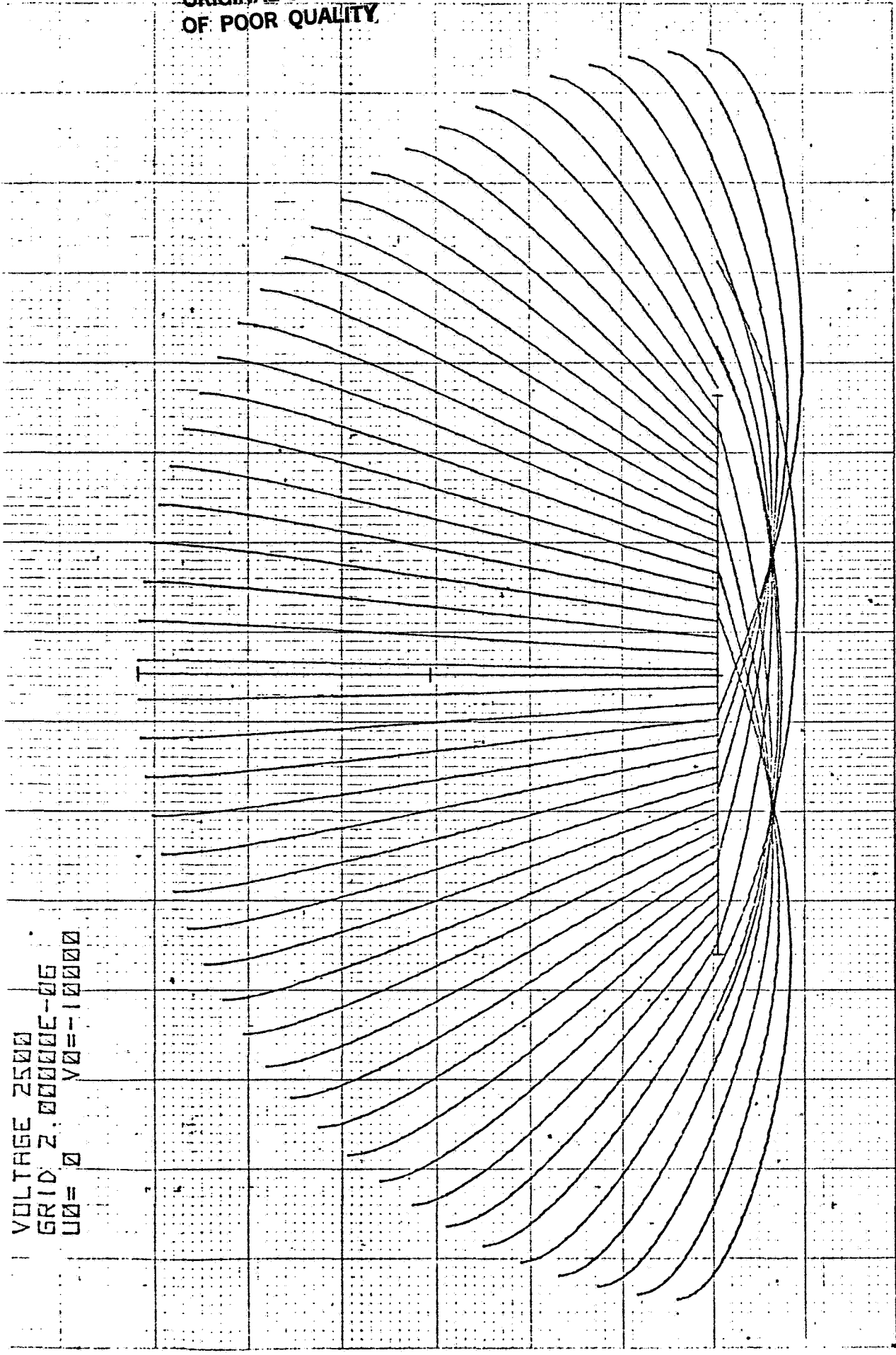
FIGURE 1



ORIGINAL ION DIRECTION PERPENDICULAR TO FACE OF COLLECTOR

FIGURE 2

ORIGINAL PAGE IS
OF POOR QUALITY



VOLTAGE 2500
GRID 2.00000E-06
U0 = 0 V0 = -10000

FIGURE 3

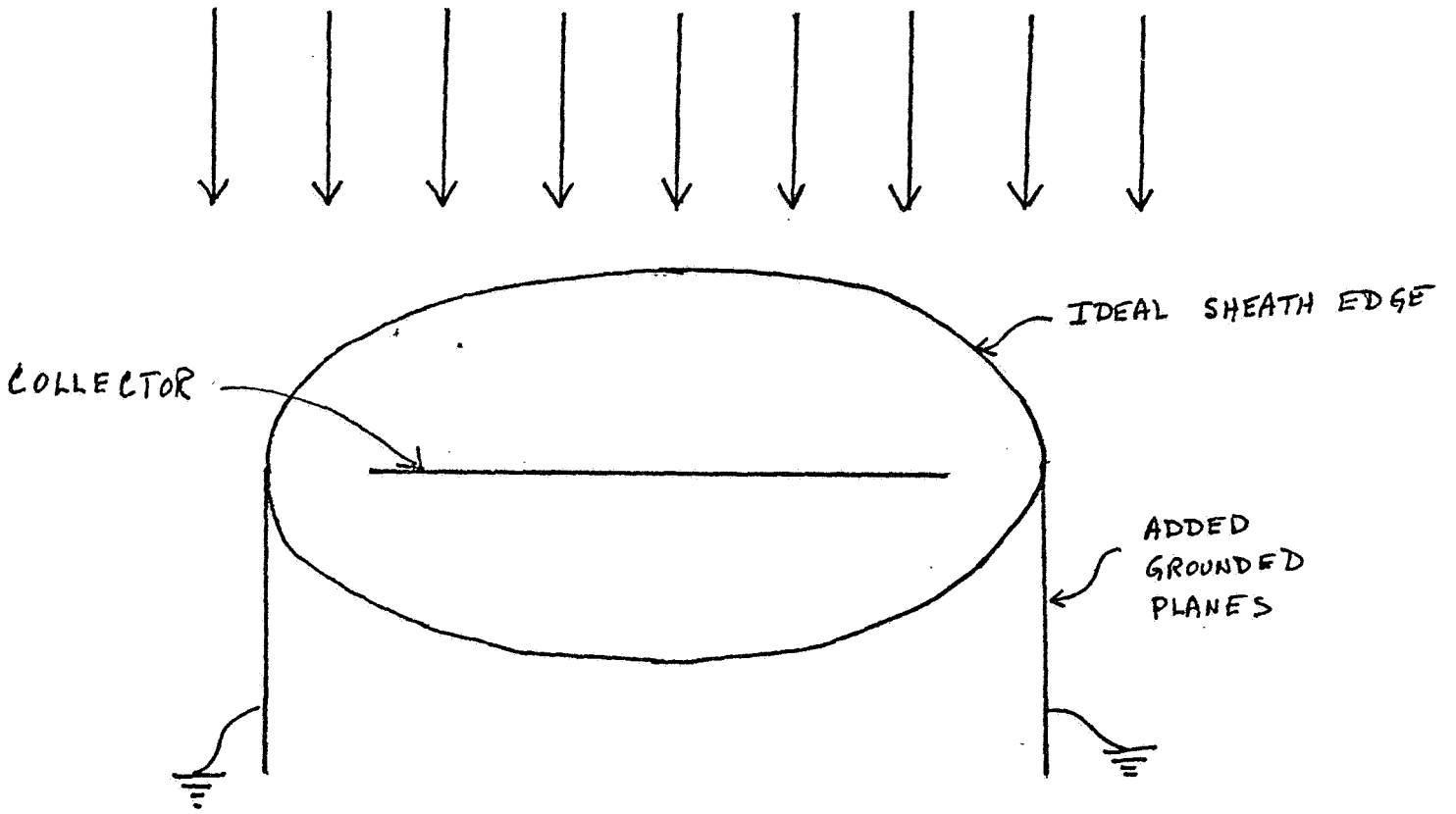
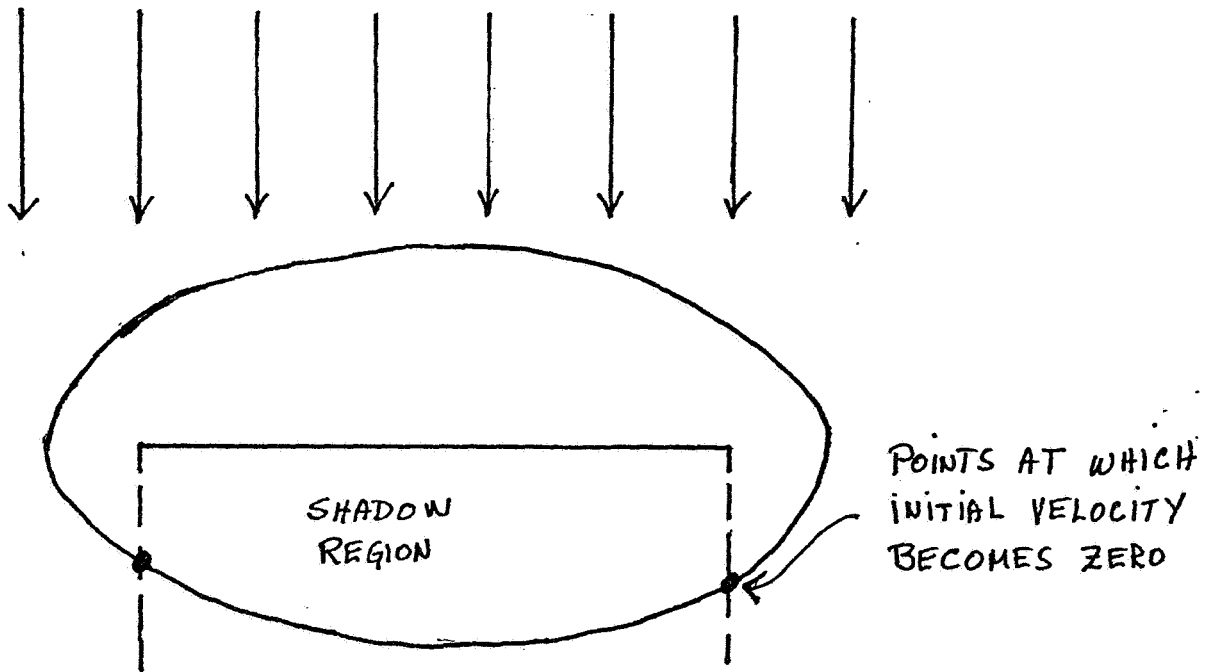


FIGURE 4



ORIGINAL PAGE IS OF POOR QUALITY

FIGURE 5

C-5

ORIGINAL PAGE IS
OF POOR QUALITY

VOLTS 500
HOURS 100
GRID 1000000E-05
LID= 0
V0=-10000

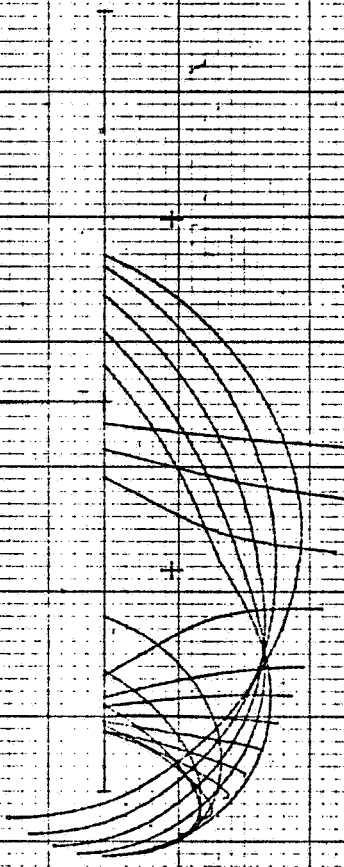


FIGURE 6

55

ORIGINAL PAGE IS
OF POOR QUALITY

14-0000
VOLTAGE 1500
GR 0.1 10000-06
L10= 10000

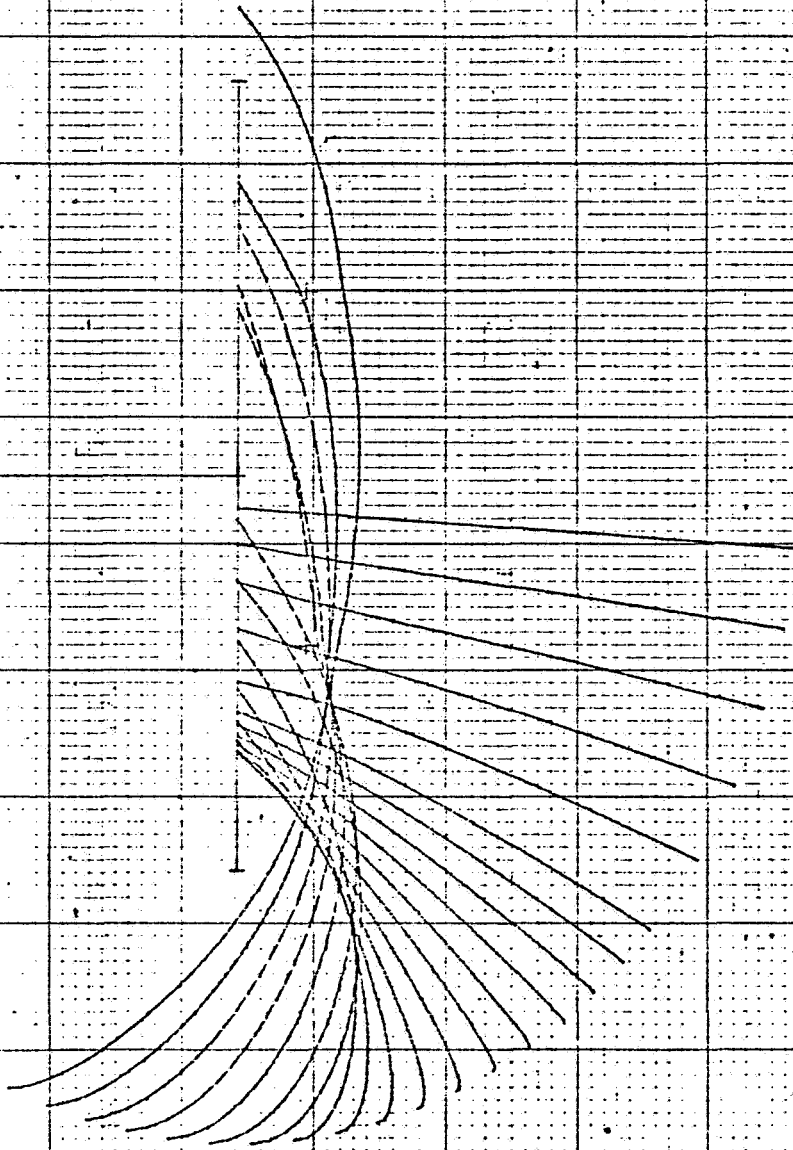


FIGURE 7

